Control of HCl Emission from Cement Plants

Pachitsas, Stylianos

Publication date:
2018

Document Version
Publisher's PDF, also known as Version of record

Control of HCl Emission from Cement Plants

Stylianos Pachitsas

PhD Thesis

2018

DTU Chemical Engineering
Department of Chemical and Biochemical Engineering

TECHNICAL UNIVERSITY OF DENMARK

Department of Chemical and Biochemical Engineering

Control of HCl Emission from Cement Plants

STYLIANOS PACHITSAS

Ph.D. Thesis

June 2018

Preface

This Ph.D. project has been carried out to improve the prediction of HCl emission from cement plants, to optimize the control methods of HCl emission, and to decrease the operating expenses of HCl reduction methods based on the understanding of the mechanism of HCl absorption by cement raw meal.

The Ph.D. project was part of the advanced technology platform 'Minerals and Cement Process Technology - MiCeTech' and funded by the Innovation Fund of Denmark, FLSmidth A/S, Hempel A/S, and Technical University of Denmark. The project supervisor team consisted of: Professor Kim Dam-Johansen, Associate Professor Stig Wedel and Senior Advisor Jytte Boll Illerup, from the Department of Chemical and Biochemical Engineering of Technical University of Denmark, and Lars Skaarup Jensen and Martin Hagsted Rasmussen from the R & D Department of FLSmidth A/S.

Firstly, I would like to express my acknowledgements to MiCeTech platform parties for making this project possible. I would like to thank the supervisor team for its guidance. In addition, a number of people in Technical University of Denmark and FLSmidth A/S contributed to this project. In particular, I would like to thank the Master and Bachelor students, who did their theses in association with this work, and the employees in the different departments of FLSmidth A/S, who had valuable contributions to this project. Furthermore, I gratefully acknowledge DTU - Center of Electron Nanoscope and Chemistry Department of DTU which made the SEM-EDS analysis and XRD analysis, respectively.

Stylianos Pachitsas
Kgs. Lyngby, June 2018

A few minor errors in the Thesis submitted for defence have been corrected in this printed version.

Stylianos Pachitsas
Kgs. Lyngby, November 2018

Abstract

A number of cement plants face problems in their compliance with the HCl emission regulations. This work is focused on the study of the mechanism of HCl absorption by cement raw meal at conditions similar to those of post-preheater tower units. The main goals of the project were the understanding of the mechanism of HCl absorption at industrial conditions and development of industrial models that are able to predict the HCl emission and optimize the control of HCl emission from cement plants.

The first four chapters provide the framework of this study and present the cement manufacturing process, available literature, and industrial data that are related to the HCl formation and absorption mechanisms. In particular, the HCl formation mechanism is not completely understood; however, industrial measurements showed the presence of two formation zones: one in the low temperature (360-600°C) preheater tower cyclones, and one in the rotary kiln. Furthermore, strong HCl scrubbing phenomena were detected in the particle filters and raw mill units. Therefore, the understanding of the mechanism of HCl absorption is a key issue for the optimization of HCl emission control and prediction of the HCl emission from cement plants.

Chapter 5 comprises the description of the used experimental set-ups, experimental procedures and materials characterization. A fixed-bed reactor - FTIR set-up and a standard TGA-FTIR system were used for the conduction of isothermal and ramping temperature tests, respectively. The fixed-bed set-up was used for the experimental study of the mechanism of HCl absorption by raw meal in the temperature range 100-180°C, using gas phase HCl concentration between 52 ppmv and 200 ppmv. The effects of gas phase composition (0 or 5% v/v H_2O, 0 or 30% v/v CO_2, and 0 or 3% v/v O_2) and particle moisture content were also studied using fixed-bed tests. TGA-FTIR tests were conducted to study the effects of raw meal compounds on HCl absorption in the temperature range 90-350°C, using reagent grade $CaCO_3$, simulated raw meal, two industrial raw meals, and the thermally degradable $AlCl_3 \cdot 6H_2O$ as HCl source. Furthermore, the TGA-FTIR tests were used for the fast screening of HCl absorption by different raw meals.

Chapter 6 presents the interpretation of the obtained experimental data. Fixed-bed tests showed that the HCl absorption by raw meal is consistent with a surface saturation phenomenon that is characterized by a certain HCl absorption capacity of raw meal and extremely low active compound conversion (less than 1%). Furthermore, HCl absorption tests using moist gas phase with 5 % v/v H_2O showed increase of HCl absorption capacity of raw meal by 25% at 180°C and 61% at 100°C relative to the absorption capacity from dry gas phase tests. It is noteworthy that the raw meal moisture content strongly promotes the HCl absorption in the case of dry gas phase tests. On the other hand, it was concluded that the presence of 30% v/v CO_2 and 3% v/v O_2 in gas phase has no significant effect on HCl absorption in the range of operating temperatures of post-preheater tower units. Agglomeration of the raw meal particles and flow channelling significantly decrease the apparent HCl absorption capacity. The HCl absorption capacity of raw meals increased

almost 10 times when raw meal samples were diluted using inert material with larger particles size, due to breaking up of agglomerates and elimination of flow channelling. TGA-FTIR tests showed that the industrial raw meals have higher HCl absorption capacity than reagent grade $CaCO_3$ and simulated raw meal. Furthermore, they indicated that Fe_2O_3 promotes $CaCO_3$ chlorination. The obtained results showed that TGA-FTIR system is probably inappropriate for the fast screening of HCl absorption by different raw meals.

Chapter 7 comprises the modelling work on fixed-bed experimental data. The fixed-bed model assumes that the HCl absorption is a surface saturation phenomenon characterized by a specific HCl absorption capacity that depends on temperature, gas phase moisture content and raw meal moisture content. HCl absorption is controlled by HCl mass transfer to the particle surfaces (through the gas film) and active surface conversion. The use of an appropriate Sherwood number expression for multiparticle fixed-beds (mixtures of active and inert particles) and a numerical solution method for the model equations allowed the simulation of the experimental data.

Chapter 8 presents the HCl absorption industrial models for the post-preheater tower units. These models simulate the mechanism of HCl absorption using the same principles, e.g., surface saturation phenomenon, as the aforementioned fixed-bed model. The applied modelling approach for particle filters assumes that the HCl absorption occurs in the dispersion before filtration bags and not in the dust layer on filtration bags. This claim is based on the lab results (fixed-bed tests) which showed that the HCl absorption is a very fast reaction and raw meal particles tend to be strongly agglomerated when they form cake layers (low apparent HCl saturation capacity). Furthermore, the developed model assumes that the HCl absorption approximates a reaction in entrained flow reactor similar to plug flow reactor (PFR) characterized by gas phase residence time equal to 1.9s. The entrained flow reactor model was also used in the simulation of HCl absorption in the raw mill. The application of the entrained flow reactor model to the raw mill showed complete HCl absorption in the raw mill. Generally, it is concluded that the industrial models can simulate the HCl scrubbing phenomena in particle filters and raw mill sufficiently well. The entrained flow reactor model was not evaluated in the case of gas conditioning tower due to the lack of industrial data.

Resumé

Et antal cementfabrikker har udfordringer med at overholde emissionsreglerne for HCl. Denne afhandling undersøger mekanismen for cementråmelets absorption af HCl ved forhold svarende til enhederne efter forvarmeretårnet. Projektets hovedformål var forståelsen af mekanismen for HCl absorption under industrielle forhold samt udvikling af industrielle modeller, der kan forudsige HCl udledningen og optimere kontrollen af HCl udledning fra cementfabrikker.

De første fire kapitler sætter rammerne for denne undersøgelse og præsenterer cementfremstillingsprocessen, tilgængelig litteratur og industrielle data relateret til HCl dannelses og absorptionsmekanismer. HCl dannelsesmekanismen er ikke fuldstændigt forstået, men industrielle målinger viste tilstedeværelsen af to dannelseszoner ved lave temperaturer, 360-600°C: en i forvarmercyklonerne og en i rotérovnen. Desuden blev stærke HCl skrubningsfænomener detekteret i partikelfilteret- og råmølleenhederne. Derfor er forståelsen af mekanismen for HCl absorption et centralt spørgsmål for optimeringen af HCl emissionskontrollen og forudsigelse af HCl frigivelsen fra cementfabrikker.

Kapitel 5 beskriver det eksperimentelle udstyr, forsøgsprocedurer og materialekarakterisering. Der blev anvendt et fixed-bed-reaktor-FTIR system og et standard TGA-FTIR system til udførelse af test ved henholdsvis isoterme betingelser og ved jævnt stigende temperaturer. Fixed-bed opstillingen blev anvendt til at undersøge mekanismen for råmels absorption af HCl i temperaturområdet 100-180°C ved anvendelse af mellem 52 ppm og 200 ppm HCl i gasfasen. Endvidere blev virkningerne af gassammensætning (0 eller 5% v/v H_20, 0 eller 30% v/v CO_2 og 0 eller 3% v/v O_2) og partikelfugtindholdet undersøgt ved forsøg med fixed-bed-reaktoren. TGA-FTIR tests blev anvendt ved undersøgelsen af råmelkomponenternes virkning på HCI absorption i temperaturområdet 90°C-350°C ved anvendelse af rent $CaCO_3$, simuleret råmel, to forskellige industrialle råmel og det termisk nedbrydelige $AlCl_3 \cdot 6H_2O$ som HCl kilde. Derudover blev TGA-FTIR-tests anvendt til en hurtig screening af HCl absorption af forskellige råmel.

Kapitel 6 præsenterer fortolkningen af de eksperimentelle data. Fixed-bed-reaktorforsøgene viste, at HCl absorptionen med råmel er et overflademætningsfænomen, der svarer til en bestemt HCl absorptionskapacitet af råmelet og ekstremt lav omdannelse af den aktive komponent (mindre end 1%). Desuden viste HCl absorptionsforsøg med anvendelse af en gas med et fugtindhold p ˚ 5% v / v H_2O en stigning i HCl absorptionskapaciteten af råmelet med 25% ved 180^{o}C og 61% ved 100^{o}C i forhold ved en tr gas. Det er bemærkelsesværdigt, at råmelets fugtindhold fremmer HCl absorptionen betydeligt i tilfælde af en vandfri gasfase. På den anden side blev det konkluderet, at tilstedeværelsen af 30% v/v CO_2 og 3% v/v O_2 i gasfasen ikke har nogen virkning på HCl absorptionen i intervallet af driftstemperaturer relemante for enhederne efter forvarmeren. Agglomerering af råmelspartikler og kanaldannelse reducerer signifikant den tilsyneladende HCl absorptionskapacitet. Fortynding af råmelsprøver med inert materiale med større partikelstørrelse gav næsten 10 gange højere HCl absorptionskapacitet for råmelet på grund af nedbrydningen af agglomerater og eliminer-

ing af kanaldannelse. TGA-FTIR-tests viste, at ægte råmel, har en højere HCl absorptionskapacitet end rent $CaCO_3$ og simuleret råmel. Desuden indikerede de, at Fe_2O_3 fremmer chlorering af $CaCO_3$. TGA-FTIR systemet er tilsyneladende ikke egnet til hurtig screening af HCI absorption af forskelligt råmel.

Kapitel 7 omfatter modelleringsarbejdet for fixed-bed-reaktor dataene. Modellen er baseret på antagelse af at HCl absorptionen er et overflademætningsfænomen, der er kendetegnet ved en bestemt specifik HCl absorptionskapacitet, der afhænger af temperatur, samt gasfasens fugtindhold og råmelets fugtighed. HCl absorptionen styres af HCl masseoverførslen til partikeloverfladen (gennem gasfilmen) og mætning af den aktive overflade. Anvendelsen af et Sherwoodtal bestemt ved en korrelation for multipartikelsystemer (blandinger af aktive og inerte partikler) og en numerisk løsningmetode til modelligningssystemet tillod simulering af de eksperimentelle data.

Kapitel 8 præsenterer industrimodellerne for HCl absorption i enhederne efter forvarmeren. Disse modeller simulerer mekanismen for HCI absorptionen under anvendelse af de samme principper, fx overflademætningsfænomen, som den førnænte fixed-bed-reaktor model. Partikelfiltermodelleringsmetoden antager, at HCl absorptionen forekommer i dispersionen før filterposerne og ikke i støvlaget på filterposerne. Denne antagelse er baseret på laboratorieresultaterne (test med fixed-bed reaktor), som viste, at HCl absorptionen er ekstremt hurtig, og råmelspartikler har en tendens til at være stækt agglomereret, når de danner kagelag (lav HCl mætningskapacitet). Desuden antages det i den udviklede model, at HCl absorptionen approximerer en reaktion i medstrømsreaktor svarende til PFR karakteriseret ved en gasfase opholdstid p til 1.9s. Denne medstrømsreaktormodel blev også anvendt i simuleringen af HCl absorption i råmelsmøllen. Modellen viste fuldstændig HCl absorption i råmelsmøllen. Generelt konkluderes det, at industrimodellerne i tilstrækkelig grad kan simulere HCl absorbtions fænomerne i partikelfilter og råmelsmøllen. Medstrømsreaktormodellen blev ikke evalueret for et gaskonditioneringstårnet på grund af manglen på industrielle data.

Table of Contents

Preface i

Abstract i

Resumé iv

1 Introduction 1
- 1.1 Background . . . 1
- 1.2 Project Objectives . . . 2
- 1.3 Thesis Outline . . . 3
- 1.4 References . . . 4

2 Cement & Industrial Cement Clinker Production 5
- 2.1 Cement Clinker and Raw Materials . . . 5
- 2.2 Production Process of Portland Cement . . . 9
- 2.3 References . . . 11

3 HCl Emission from Cement Plants 14
- 3.1 HCl Release Zones . . . 15
  - 3.1.1 Preheater Tower . . . 15
  - 3.1.2 Rotary Kiln . . . 17
- 3.2 HCl Absorption Zone . . . 17
  - 3.2.1 Gas Conditioning Tower (GCT) . . . 18
  - 3.2.2 Raw Mill . . . 19
  - 3.2.3 Particle Filters . . . 21
- 3.3 Conclusions on HCl Emission from Cement Plants . . . 22
- 3.4 References . . . 23

4 Literature Review on HCl Release & Absorption at Industrial Conditions 25
- 4.1 HCl Release . . . 25
  - 4.1.1 Salts and Salt Hydrates Thermal Decomposition . . . 26
  - 4.1.2 Organic Matter Reaction with Inorganic Chlorides . . . 27
  - 4.1.3 Inorganic Chlorides - Gas Phase Reactions . . . 28
  - 4.1.4 HCl Release from Fuel Combustion in Kilns . . . 29
  - 4.1.5 Conclusions on HCl Release . . . 30
- 4.2 HCl Absorption . . . 31
  - 4.2.1 Temperature Effect on HCl Absorption . . . 34
  - 4.2.2 Gas Phase Moisture Effect on HCl Absorption . . . 35
  - 4.2.3 Sulphur Dioxide Effect on HCl Absorption . . . 35
  - 4.2.4 Carbon Dioxide and Oxygen Effects on HCl Absorption . . . 36
  - 4.2.5 Particle Size and Surface Area Effects on HCl Absorption . . . 37

4.2.6 Absorption Mechanism - Reaction Limiting Step . . . 37
4.2.7 Conclusions on HCl Absorption . . . 38
4.3 Overall Conclusions on Literature Review . . . 38
4.4 References . . . 39

5 Used Set-ups, Experimental Methods and Materials in HCl Absorption Study 45
5.1 Experimental Activities - Isothermal Tests . . . 45
5.1.1 Fixed-bed Set-up . . . 45
5.1.2 Experimental Procedure of Fixed-bed Tests . . . 50
5.1.3 Materials and Experimental Conditions of Fixed-bed Tests . . . 50
5.2 Experimental Activities - Ramping Temperature Tests & In-situ HCl Release . . . 53
5.2.1 TGA-FTIR Set-up . . . 53
5.2.2 Experimental Procedure of TGA-FTIR Test . . . 54
5.2.3 Materials and Experimental Conditions of TGA-FTIR Tests . . . 55
5.2.4 Data Processing of TGA-FTIR Tests . . . 57
5.3 References . . . 57

6 Experimental Results on HCl Absorption 59
6.1 Fixed-bed Experimental Results . . . 59
6.1.1 Experimental Set-up Behaviour and Test Methodology . . . 59
6.1.2 Determination of HCl Absorption Mechanism and Capacities . . . 64
6.1.3 Evaluation of Parameters Affecting HCl Absorption Capacity . . . 67
6.1.4 Conclusions on Fixed-bed Data . . . 71
6.2 TGA-FTIR Results . . . 71
6.2.1 Experimental Set-up Behaviour . . . 71
6.2.2 Fast Screening of HCl Absorption Capacity of Raw Meals . . . 73
6.2.3 Evaluation of Raw Meal Compounds' Effects . . . 75
6.2.4 Conclusions on TGA-FTIR Data . . . 80
6.3 References . . . 81

7 Modelling of HCl Absorption in Fixed-bed Tests 84
7.1 Fixed-bed Model Principles . . . 84
7.2 Mathematical Model Description . . . 86
7.3 Calculation of Mass Transfer Coefficient . . . 87
7.3.1 Flow Dynamic Parameters . . . 87
7.3.2 Selection of Sherwood Number Expression . . . 88
7.4 Fixed-bed Model Evaluation . . . 89
7.4.1 Model Performance at 100^{o}C - Dry Gas Phase . . . 89
7.4.2 Model Performance Using Moist Gas Phase . . . 91
7.4.3 Model Sensitivity to Sherwood Number and Discretization Grid . . . 93
7.5 Conclusions on Fixed-bed Model . . . 96
7.6 References . . . 96

8 Industrial HCl Absorption Models for Cement Plants 98
8.1 Basic Principles of Cement Plant Unit Models . . . 98
8.1.1 Particle Filters . . . 98
8.1.2 Vertical Raw Mill . . . 101
8.1.3 Gas Conditioning Tower . . . 105
8.2 Entrained Flow Reactor Model Description . . . 106
8.3 Industrial Models Evaluation . . . 108
8.3.1 Particle Filters . . . 110
8.3.2 Vertical Raw mill . . . 113

8.3.3 Sensitivity Analysis of the Entrained Flow Reactor Model 116
8.4 Conclusions on Industrial Models Evaluation 118
8.5 References 119

9 Conclusions & Recommendations **120**
9.1 Understanding of HCl Absorption Mechanism 120
9.2 Fixed-bed Model 121
9.3 Simulation of Industrial HCl Scrubbing Phenomena 121
9.4 Method for Fast Screening of HCl Absorption Capacity 122
9.5 Recommendations for Future Work 122
9.6 References 123

Notation **124**

Appendix A TGA-FTIR Calibration Examples **128**
A.1 HCl Calibration 128
A.2 CO_2 Calibration 131
A.3 $AlCl_3 \cdot 6H_2O$ Dissociation Tests 132

Appendix B XPS Analysis Results **136**
B.1 RM-A Samples Unexposed and Exposed(fixed-bed) to HCl 136
B.2 Fe_2O_3 Samples Unexposed and Exposed to HCl 139

Appendix C XRD Analysis of RM-B and RM-B-$AlCl_3 \cdot 6H_2O$ Samples Heated at 310^oC and 380^oC **142**
C.1 Detection of $CaCl_2$ Formation 142
C.2 Detection of $Ca(MgFe)(CO_3)_2$ Formation 143

Appendix D Mass Balance & Numerical Solution of Fixed-bed Model **145**
D.1 Mass Balance 145
D.2 Numerical Solution Using Explicit Discretization 147

Appendix E Mass Balance - Entrained Flow Reactor Model **148**
E.1 Mass Balance 148

Appendix F Scientific Article on HCl Absorption by Raw Meal (Draft) **150**

Chapter 1

Introduction

This chapter gives a brief description of the project background and objectives. Additionally, the four main structural sections of the thesis are presented.

1.1 Background

The use of hydraulic binding materials in construction activities was known to ancient civilizations in Mediterranean and Mesopotamia [1, 2]. In modern times, the most widely used cement type is Portland cement, which was invented in mid 19th century. The Portland cement manufacturing process has been optimized significantly in the last two centuries in order to meet the market needs and specifications. The current global cement production is close to 3.4 billion tones/year and is anticipated to reach 4 billion tones/year in 2050 [3].

Cement manufacturing processes have a considerable environmental impact [4]. Table 1.1 shows the reported emission ranges of typical air pollutants from cement kilns. The air pollutants can be categorized into three groups based on the affected geographical area [5]: (i) global pollutants, e.g., CO_2, whereby 5% of global anthropogenic CO_2 emission comes from cement industry [6], (ii) regional pollutants (NO_x and SO_2, which are responsible for the acid rain, and CO) [6], and (iii) local pollutants, such as Hg, HF, volatile organic compounds (VOCs), and particulate matter $<$ 10μm (PM10) [5-7]. The high solubility of hydrogen chloride (HCl) in water allows for its washing out by rain and moisture in the air, and consequently, it can be considered both a local and regional pollutant [8, 9].

The continuous increase of cement consumption in developing countries [10] requires production increase and minimization of the environmental impact from cement manufacturing processes. Consequently, the emission issues have great significance for cement producers and equipment suppliers. The interest is mainly focused on the utilization of emission control through the optimization of emission reduction methods with the minimum capital and operating costs. Furthermore, the ability to predict emissions is useful for the designing of new or reconstruction of existing cement plants that must be compliant with the environmental regulations.

Table 1.1: Emission ranges of typical air pollutants from European cement kilns [4].

Air pollutant	Emission range per tonne of clinker
NO_x	0.33-4.67 kg
SO_2	up to 11.12 kg
Dust	$0.062 \cdot 10^{-2}$ - 0.522 kg
CO	0.46 - 4.6 kg
CO_2	$\sim$ 850 kg (total) [5]
TOC/VOCs	$0.023 \cdot 10^{-1}$ - 0.138 kg
HF	0.021 - 2.3 g
HCl	0.046 - 46 g
Hg	0 - 69 mg

1.2 Project Objectives

HCl is considered a gaseous pollutant of concern in the cement industry with serious environmental impact due to its high toxicity. In humans, HCl inhalation can result in respiratory system irritation, and death in the case of high HCl concentrations [8, 11]. A number of cement plants are facing problems in their compliance with the current HCl emission limits, e.g., 3 ppmv in dry flue gas at 7% v/v O_2 - U.S. limit [12] and 10mg/Nm^3, dry gas, 10% v/v O_2 - E.U. limit [13]. Therefore, the cement manufacturing companies and equipment suppliers show interest in the minimization of the HCl emission control cost and optimization of the prediction of HCl emission.

HCl formation mechanisms in cement manufacturing processes are not completely understood. However, industrial scale measurements have identified the presence of two HCl formation zones in cement production process: in the low temperature (360-600°C) preheater tower cyclones, and in the rotary kiln [14, 15]. Industrial tests, using fuels with varying chlorine content, supported that the HCl concentration at the preheater outlet is not directly related to the fuel chlorine content and HCl formation in the kiln [15]. Strong HCl scrubbing phenomena were detected in particle filters and raw mill units in the temperature range 90-220°C [14, 15]. These observations indicated a significant HCl absorption by raw meal and preheater dust at low temperatures in presence of moist gas phase.

This work contributes to the control of HCl emission from cement plants through the study of HCl absorption by raw meals at conditions similar to those of post-preheater tower units. The understanding of the mechanism of HCl absorption gives valuable information about absorption parameters and optimal operating conditions. Furthermore, the development of industrial models that simulate the scrubbing phenomena in post-preheater tower units allows the prediction of HCl concentration at the stack and evaluation of the emission control methods. It is noteworthy that the by-pass system is not part of this study.

The project objectives can be summarized as follows:

- The understanding of the mechanism of HCl absorption by raw meal comprising the determination of the absorption affecting parameters and optimal operating conditions.

- The development a fixed-bed model for the simulation of lab data and study of the absorption mechanism in a consistent way.

- The development of industrial models that simulate the scrubbing phenomena in post-preheater tower units. These models can be used for the prediction of HCl concentration in stack flue gas and evaluation of the emission control methods.

- The suggestion of a test method for the fast screening of HCl absorption by different raw meals.

1.3 Thesis Outline

The thesis is split into the following three structural units:

Literature Study

The literature study is divided into 3 chapters. It comprises the description of cement clinker manufacturing process, presentation of the industrial measurement data (HCl formation and absorption zones in cement plants), and presentation of literature data relative to HCl absorption by Ca-based sorbents and HCl release from raw meal compounds at industrial conditions. The framework of the experimental study was determined to a great extent by the literature study.

Experimental Study

This structural unit consists of Chapter 5 and Chapter 6. Chapter 5 presents the experimental set-ups (fixed-bed-FTIR and TGA-FTIR), experimental procedures, and materials characterization in the study of HCl absorption by raw meal and raw meal compounds. Chapter 6 presents the interpretation of experimental results.

HCl Absorption Models

The developed HCl absorption models are described in Chapter 7 and Chapter 8. Chapter 7 presents the fixed-bed model and its evaluation. The industrial models are presented in Chapter 8. Furthermore, the industrial models' evaluation, using the available industrial data, is also included in Chapter 8. The models are developed based on the assumption that HCl absorption is a surface saturation phenomenon characterized by a specific HCl absorption capacity that depends on the physical and chemical properties of sorbent, temperature, gas phase moisture content, and moisture content of sorbent. The models for industrial equipment assume that the flow of particles and gas in the equipment corresponds to an entrained flow reactor.

This thesis comprises parts related to the HCl absorption by raw meal and Ca-based sorbents which are intended to be published in a scientific article (see Appendix F) with the title: "Experimental evaluation of hydrogen chloride (HCl) absorption by cement raw meal at low temperatures, using fixed-bed tests", written by Pachitsas, S., Wedel, S., Skaarup Jensen, L., Boll Illerup, J., and Dam-Johansen, K.. These parts are the literature study on HCl absorption by Ca-based sorbents, and the

experimental evaluation of HCl absorption by raw meal which are presented in Chapter 4 (section section 4.2) and Chapter 6 (section 6.1), respectively.

1.4 References

[1] Bhatty, J., Kosmatka, F., and Miller, S., Innovations in Portland Cement Manufacturing, Portland Cement Association, 2004, ISBN:0-89312-234-3.

[2] Moropoulou, A., Bakolas, A., and Anagnostopoulou, S., Composite Materials in Ancient Structures, Cement & Concrete Composites, vol. 27, pp. 295-300, 2005.

[3] Schneider, M., Romer, M., Tschudin, M., and Bolio, H., Sustainable Cement ProductionPresent and Future, Cement and Concrete Research, vol. 41, pp.642-650, 2011.

[4] Best Available Techniques (BAT) Reference Document for the Production of Cement, Lime and Magnesium Oxide, European Commission, [22 April 2018], http://eippcb.jrc.ec.europa.eu/reference/BREF/CLM_Published_def.pdf.

[5] Cote, I., Samet, J., and Vandenberg, J.J., U.S. Air Quality Management: Local, Regional and Global Approaches, Journal of Toxicology and Environmental Health Part A, vol.71, pp.63-73, 2008.

[6] Habert, G., Environmental Impact of Portland Cement Production, Eco-Efficient Concrete, pp.3-12, 2013, ISBN: 978-0-85709-424-7.

[7] Hydrogen Fluoride as Air Pollutant, Agency of Toxic Substances and Disease Registry (ATSDR), [22 June 2018], https://www.atsdr.cdc.gov/toxprofiles/tp11-c6.pdf

[8] Hydrogen Chloride as Air Pollutant, Scottish Environment Protection Agency, [22 April 2018], http://apps.sepa.org.uk/spripa/pages/substanceinformation.aspx?pid=5

[9] Chow, W. and Connor, K., Managing Hazardous Air Pollutants-State of Art, CRC Pres. Inc., pp.175, 1993, IBSN: 0-87371-866-6.

[10] International Energy Agency World Business Council for Sustainable Development, Cement Technology Roadmap 2009: Carbon Emissions Reductions up to 2050, [22 June 2018], https://www.iea.org/publications/freepublications/publication/Cement.pdf

[11] Medical Management Guidelines for Hydrogen Chloride (HCl), Agency for Toxic Substances and Disease Registry, [22 April 2018] https://www.atsdr.cdc.gov/mmg/mmg.asp?id=758&tid=147.

[12] U.S. Environmental Protection Agency (EPA), National Emission Standards for Hazardous Air Pollutants from the Portland Cement Manufacturing Industry, 40 CFR Part 63, §63.1343, pp.405, 2013.

[13] Directive 2010/75/EU of the European Parliament and of the Council of 24 November 2010 on industrial emissions (integrated pollution prevention and control) (Recast), European Union (EU), [22 April 2018] http://eur-lex.europa.eu/LexUriServ/LexUriServ.do?uri=OJ:L:2010:334:0017:0119:EN:PDF

[14] Emission Measurements at Cement Plant A,Internal report FLSmidth A/S, Copenhagen, 2012.

[15] Emission Measurements at Cement Plant B,Internal report FLSmidth A/S, Copenhagen, 2013.

Chapter 2

Cement & Industrial Cement Clinker Production

Portland cement is a hydraulic binder used for building and in concrete products. It is made up of a mixture of finely ground clinker minerals with gypsum. Cement clinker is produced by burning a mixture of raw materials (cement raw meal) containing $CaCO_3$, SiO_2, Fe_2O_3 and Al_2O_3 in kiln systems. In particular, cement raw meal can be described as a blend of different raw materials, such as limestone, sand, and shale or clay (aluminosilicates)[1]. In the case of stoichiometric needs unfulfillment by primary components, corrective materials, such as bauxite, laterite and iron ore are added [1]. This chapter gives a brief description of cement clinker manufacturing process and some typical examples of raw meal and cement clinker compositions. Cement plants' geographical distribution is usually connected with raw materials availability [1]. Typically, cement plants are placed close to their source of calcium oxide [1]. It is commonly accepted that raw materials' impurities are causing the emission of different air pollutants, e.g., SO_2 [2, 3], organic compounds [4, 5] and NH_3 [6]. Consequently, a connection between cement plant emissions' profile and composition of raw materials is anticipated. Thus, the effect of composition of raw materials on HCl emission from cement plants should be investigated.

2.1 Cement Clinker and Raw Materials

A simplified example of Portland cement clinker composition is shown in Table 2.1. It is clearly seen that the principal compounds (90% w/w) of cement clinker are alite (C_3S), belite (C_2S), tricalcium aluminate (C_3A) and tetracalcium aluminoferrite (C_4AF). Typical examples of Portland cement clinker, raw meal and raw material compositions, in terms of oxides content, are shown in Table 2.2. Cement clinker mainly consists of CaO, SiO_2 and Al_2O_3. Furthermore, MgO content of clinker is an important parameter, which is determined by final product specifications (clinker $<$4.5 % w/w [7, 10]) [1, 7-10] and mainly affected by limestone composition [1]. Therefore, limestone suitability for Portland cement production is largely defined by its MgO content [1, 7-10]. The high content of MgO in final product results in a slow reaction with water that can lead to the destructive expansion of hardened concrete [10]. The analysis of raw materials composition (see Table 2.2) shows that shale is the raw material with the highest content of organic matter, SiO_2, Fe_2O_3, and chlorine. Consequently, the shale or clay fraction of raw meal is a topic of special interest in the study of HCl release from raw meal in cement preheaters. Limestone is the source of CaO and characterized by having a low content of chlorine and organic matter. The high loss on ignition (LOI), in the case of cement raw meal and limestone, can be explained by $CaCO_3$ calcination (endothermic reaction), which occurs between 700^{o}C and 900^{o}C [11].

Table 2.1: Simplified composition of Portland cement clinker [10].

Mineral	Chemical formula	Abbreviation	Content (% w/w)
Tricalcium silicate (Alite)	$3CaO \bullet SiO_2$	C_3S	50-70
Dicalcium silicate (Belite)	$2CaO \bullet SiO_2$	C_2S	15-30
Tricalcium aluminate	$3CaO \bullet Al_2O_3$	C_3A	5-10
Tetracalcium aluminoferrite	$4CaO \bullet Al_2O_3 \bullet Fe_2O_3$	C_4AF	5-15

Table 2.2: Typical composition of Portland cement clinker, raw meal and raw materials.

Component	Limestone % w/w [1]	Shale % w/w [1]	Raw meal % w/w [1]	Clinker [1] % w/w
SiO_2	0.25-9.05	59.9	14.4	22.6
Al_2O_3	16.66	19.6	3.2	5.2
Fe_2O_3	1-1.15	17.79	1.8	2.9
CaO	48.83-55.31	4.01	42.3	65
MgO	0.4-0.85	2.28	1.3	2
K_2O	0.04-0.35	0.93	0.6	0.9
Na_2O	0.03-0.11	1	0.17	0.3
TiO_2	0.10-0.15	0.89	0.17	-
LOI 975°C	38.85-43.66	9.1	35.5	0
Cl	0.001-0.01	0.017-0.048 [12]	0.003-0.02 [1, 12]	0.1
Org.C	0.08-0.1 [12]	0.4-0.8 [12]	0.1-0.21 [1, 12]	-

Calcium Oxide Source

There is a wide variety of raw materials which can be used as calcium oxide source in cement manufacturing processes. In particular, limestones, marble, chalk, and natural cement (naturally occurring argillaceous limestones [13]) are used in cement industry [7, 8]. This work focuses on limestones which are the most widely used calcium oxide sources in the production of Portland cement [1].

Limestone is a naturally occurring carbonate sedimentary rock abundant in earth's crust [14]. It is characterized based on its inorganic or organic origin [1, 14]. Generally, limestone formation mechanisms require the presence of Ca ions and CO_2 in the terrestrial system and appropriate physico - chemical conditions for the deposition and diagenesis stages (geological transformation)[1, 14]. The inorganic deposition mechanism is based on the direct precipitation and crystallization of carbonate in aquatic environments (marine and inland waters) [14]. Characteristic examples are the travertine, oolitic limestones, stalactites and stalagmites [1]. The majority of commercially viable limestone deposits have organic origin, where aquatic organisms (bivalves, gastropods, corals, brachiopods, algeals etc.) are $CaCO_3$ sources [1, 14]. The diagenetic process (lithification) transforms the carbonate deposit to limestone-sedimentary rock [1, 14]. The limestone aquatic origin can explain the presence of inorganic chloride salts and salt hydrates, e.g., NaCl, KCl, $MgCl_2 \cdot 6H_2O$, etc., as impurities.

Limestones can be classified according to the carbonate content as follows: (i) ultra-high-calcium (>97% w/w $CaCO_3$), (ii) high calcium (>95% w/w $CaCO_3$), (iii) high purity carbonate (>95% w/w $CaCO_3$ + $MgCO_3$), (iv) calcitic (<5% w/w $MgCO_3$), (v) magnesian (5 to 20% w/w $MgCO_3$), (vi) dolomitic (20-40% w/w $MgCO_3$), and (vii) high magnesium dolomite (40-46% w/w $MgCO_3$) [14]. The limitations on MgO content of final product [1, 7-9] restricts utilization to the first four categories [9].

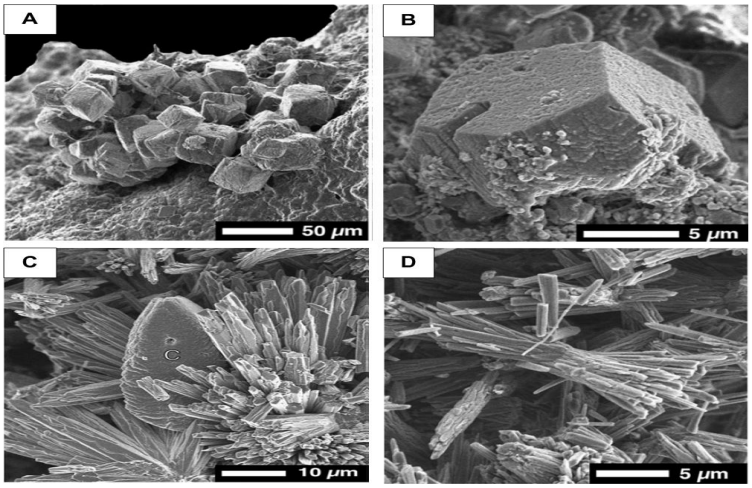

Figure 2.1: A) SEM picture of a cluster of euhedral rhombic calcite crystals; B) SEM picture of a euhedral calcite crystal; C) SEM picture of bundles of radiating aragonite crystals surrounding a calcite crystal (C: calcite); and D) SEM picture of aragonite crystals in wheat-sheaf arrangement.[15]

Calcite and aragonite limestones which combine high $CaCO_3$ content 95-97 % w/w and low $MgCO_3$ content are used in the production of Portland cement [9]. Figure 2.1 illustrates SEM pictures of calcite (Figure 2.1 A-B) and aragonite (Figure 2.1 C-D) crystals. The rhombohedral crystal habit of calcite [1] and orthorhombic[1]-acicular crystal habit of aragonite are clearly seen. It is noteworthy that the limestone crystal size (4-1000μm), shape and impurities can affect limestone calcination behaviour and sintering mechanism in various ways [9, 16, 17].

Argillaceous Materials

The term argillaceous materials corresponds to all fine-grained natural earth materials known as clays [1]. It includes shales (clay rich sedimentary rocks - fissile claystones [18]) and argillites (claystone: indurated clays [18]) [1]. As it is illustrated in Table 2.2, argillaceous materials (shales) are the main source of aluminosilicates, iron oxides, organic matter and chlorine in raw meal. These materials mainly consist of hydrous aluminum silicates with iron and magnesium substitution for aluminum in certain minerals [1]. Furthermore, in some cases they contain water soluble salts and organic substances, which are related to genesis mechanism, source origin, topology, etc.[1, 19]. Soluble salts content consists of chlorides, sulfates and carbonates of alkalies, alkaline earths, aluminium and iron [19].

Worrall [20] categorized clays based on the genesis mechanism to residual and sedimentary. The sedimentary clays have been removed form the place of origin to their current location by natural agencies [1]. In contrast with this, the residual clays lie at the place of origin. The composition of clays is strongly affected by different parameters, e.g., the genesis mechanism, source origin, topology and vegetation [1]. Figure 2.2 illustrates characteristic structures of clay minerals and basic cells bonding.

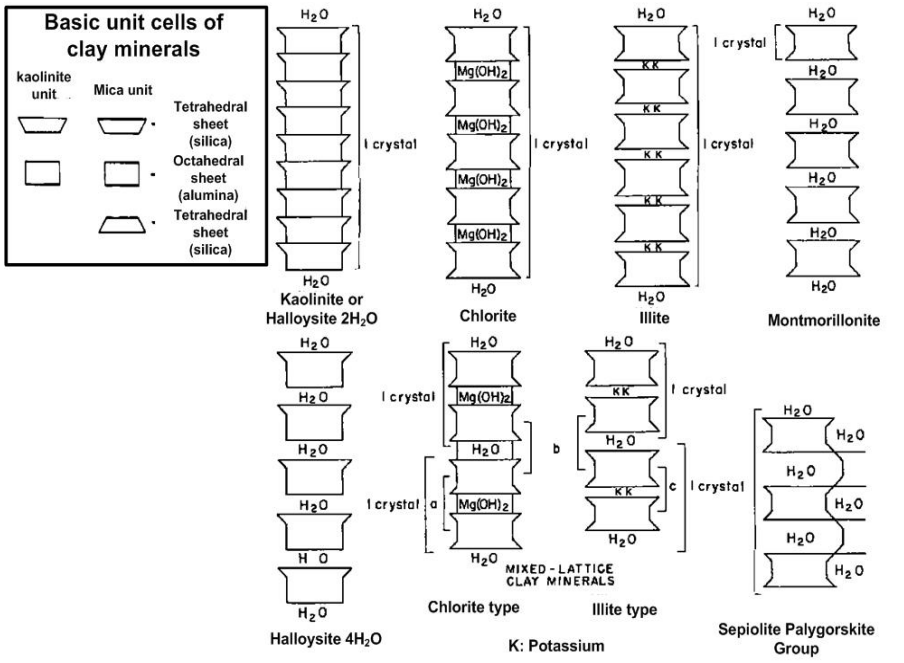

Figure 2.2: Schematic illustration of the structures of clay minerals and basic cells bonding (adapted) [21].

Clay minerals which belong in the groups of kaolin, attallpulgite, allite-mica, and montmorillonite are able to absorb certain anions (SO_4^{--}, Cl^-, PO_4^{-3}, NO_3^-, OH^-, etc.) and cations (H^+, K^+, NH_4^+, etc.), and retain them in an exchangeable state [19]. The organic material occurs as: (i) discrete particles of wood, leaves, etc., (ii) absorbed organic molecules, e.g., humic acids, on clay minerals' surfaces, and (iii) intercalated between the silicate layers [19]. The hydration and dehydration abilities of clay minerals are documented [21, 22]. White and Pichler [21] reported variations in water sorption characteristics within a clay mineral group and between the various clay mineral groups. They supported that montmorillonite absorbs more water than kaolinite, illite, and chlorite. On the other hand, chlorites and illites have similar water sorption properties. Typical maximum dehydration and dehydroxylation temperatures of clay minerals are 550^{o}C and 550-950^{o}C, respectively [1, 22]. The aforesaid characteristics of argillaceous materials implicate their potential involvement in HCl release and absorption mechanisms.

2.2 Production Process of Portland Cement

The cement production process is a multi-stage procedure, which comprises the quarrying, raw materials preparation, fuels preparation, clinker burning, mineral additives preparation, cement grinding, and cement dispatch [23]. Furthermore, the cement production method is classified according to raw materials state as wet, semi-wet, semi-dry, and dry [24]. The majority of cement production lines are based on the dry method due to the availability of dry raw materials and relatively low energy consumption (low production cost)[24].

A simplified flow diagram of cement plant for dry cement production method is shown in Figure 2.3. The main cement plant structural units are: raw mill, cement preheater, calciner, rotary cement kiln, gas conditioning tower, and particle filters. Cement plants in regions where the local raw materials have high content of chloride, sulphur or alkalis are equipped with a kiln to stack by-pass system to reduce chlorine recirculation and corrosion phenomena in calciner and rotary kiln [25], and maintain product quality [26]. Furthermore, the use of alternative fuels with high chlorine content increases the chlorine concentration in kilns to a point that the by-pass installation may be required [26]. By-pass system can remove from 0 to 100% of the kiln flue gas [27]. Typically, it extracts 5-15% of the kiln flue gas [23]. However, the by-pass system contribution to HCl emission from cement plants is not part of this study despite its potential significance.

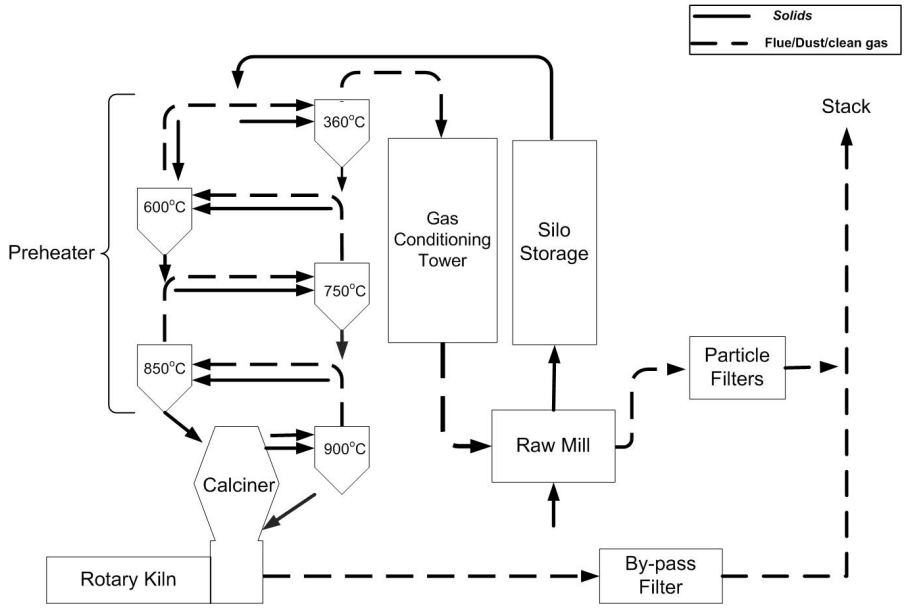

Figure 2.3: Simplified cement plant layout for dry cement production.

The cement manufacturing process can be divided into four main stages as follows:

Materials Preparation

The materials preparation stage comprises the activities occurring from the quarries to preheater tower inlet. Firstly, the quarried raw materials are crushed, using external mechanical forces (crushers) and starts the initial phase of homogenization [1]. In the next stage, the semi-homogenized raw materials mixture goes to raw mill, where the final mixture homogenization, grinding (less than 15 % w/w consists of particles with diameter $>90\mu m$) and drying, using hot kiln flue gas, take place [28]. The raw meal in the form of a dispersion goes to the raw mill cyclone, where the solid particles are separated from the flue gas, solids are stored in raw meal silos, and flue gas goes to particle filter units.

Preheating and Calcination

The homogenized raw meal goes to the preheater tower, where the final drying occurs. The preheater tower comprises a number of cyclones, where the hot klin flue gas (300-900^{o}C [7, 23]) transfers heat to the raw meal, using a non-ideal counter current flow [9]. The solid material and flue gas are mixed and separated in every cyclone, the residence times of solids and flue gas in each cyclone are close to 8s and 2s, respectively [7, 29]. In this stage, the chemically bound water is removed. Hot meal calcination (2.1) occurs in the calciner and is completed in the early stages of rotary kiln. The sustaining of the endothermic calcination reaction (+1780 kJ/Kg) requires fuel combustion in calciner [1]. Typically, the calcination efficiency is close to 90% and temperature of calciner outlet flue gas is kept between 870^{o}C and 900^{o}C [7, 23]. The raw meal and flue gas retention times in the calciner are 5s and 3s, respectively [23].

$$CaCO_{3_{(s)}} \rightleftharpoons CaO_{(s)} + CO_{2_{(g)}} \quad (700 - 900^oC) \tag{2.1}$$

Cement clinkering

Cement clinkering is the last stage of pyroprocessing and comprises the formation of C_3S, C_2S, C_3A and C_4AF, and final clinker formation [7]. The cement clinkering occurs in the rotary kiln at temperatures between 900^{o}C and 1500^{o}C in a continuous process [23]. Rotary kilns are refractory-lined tubes with a diameter up to 6m and varying length, angle of incline 3-4^o and rotating speed 1.2-2 rpm [7]. Figure 2.4 shows raw meal components transformation with temperature. The formation of C_2S, aluminates and aluminoferrites occurs between 800^{o}C and 1250^{o}C, liquid phase appears above 1250^{o}C, and C_3S is formed between 1300^{o}C and 1450^{o}C [1]. Solidification of liquid phase is obtained by cooling from 1300^{o}C to 1240^{o}C and the final clinker microstructure is frozen at temperatures less than 1200^{o}C [1]. The residence time of raw meal in the rotary kiln is from 20 up to 60 min, depending on kiln dimensions [23].

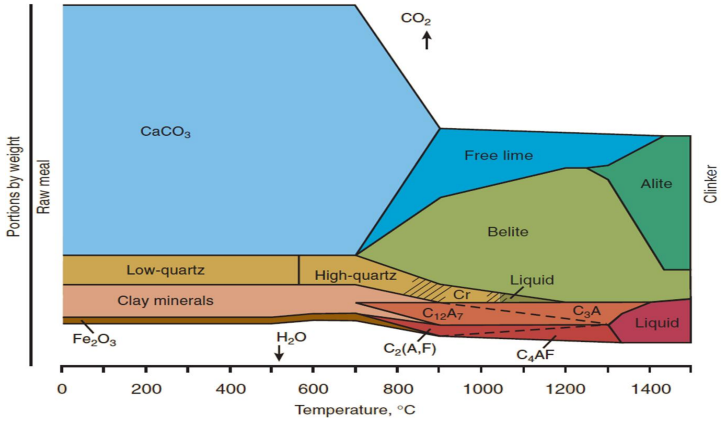

Figure 2.4: Raw meal components transformation with temperature [1].

Clinker Cooling and Finish Grinding

The clinker leaving the rotary kiln is cooled in a clinker cooler, using atmospheric air for the reduction of process energy consumption (combustion air heating) and fast clinker cooling [23]. The clinker cooler outlet hot gas stream is utilized in the fuel combustion in calciner and rotary kiln [23]. The last stage in cement manufacturing process is finish grinding, where the cooled clinker is mixed with 4-6 % w/w gypsum and enters the finish mills. The final product is an homogeneous powder, where 85-96 % w/w consists of particles with diameter less than $45\mu m$ [30].

The analysis of cement manufacturing process presented an overview of the operating conditions of cement plant's units and changes in solid material composition. The aforementioned information in conjunction with industrial data (see Chapter 3) provided the framework of the further literature and experimental studies.

2.3 References

[1] Bhatty, J., Kosmatka, F., and Miller, S., Innovations in Portland Cement Manufacturing, Portland Cement Association, 2004, ISBN:0-89312-234-3.

[2] Hansen, J.P., SO_2 Emissions from Cement Production, Ph.D. Dissertation, Technical University of Denmark, 2007, ISBN: 978-87-91435-50-1.

[3] Jøns, E. and Rabia, O., Laboratory Simulation of Preheater Emissions, World Cement, vol. 30, pp.95-99, 1999.

[4] Sindu, S., Kasti, N., Edwards, P., and Dellinger, B., Hazardous Air Pollutants Formation from Reactions of Raw Meal Organics in Cement Kilns, Chemosphere, vol.42, pp. 4999-506, 2001.

[5] Karstensen, K.H., Formation Release and Control of Dioxins in Cement Kilns, Chemosphere, vol.70, pp. 543-560, 2008.

[6] Cheney, J.L. and Knapp, K.T., A study of Ammonia Source at a Portland Cement Production Plant, Journal of the Air Pollution Control Association, vol.37, pp.1298-1302, 2012.

[7] Sprung, S., Cement and Concrete, Ullmann's Encyclopedia of Industrial Chemistry, Wiley-VCH Verlag GmbH & CO., pp.1-64, 2005, ISBN: 9783527303854.

[8] Cement Raw Materials, British Geological Survey, Natural Environment Research Council, 2005, Available online: [24 April 2018] https://www.bgs.ac.uk/downloads/start.cfm?id=1408.

[9] Rasmussen, M.H., Low SO_2 Emission Preheaters for Cement Production, Ph.D. Dissertation, Technical University of Denmark, 2012, ISBN: 978-87-92481-59-7.

[10] Taylor, H.F.W, Cement Chemistry, 2nd Edition, Thomas Telford Publishing, pp.1-29, 1997, ISBN: 0-7277-2592-0.

[11] Kumar, G.S., Ramakrishman,A., and Hung,Y.T., Advanced Physico-Chemical Treatment Technologies - Handbook of Environmental Engineering, Humana Press, vol.5, pp.611-633, 2007, eISBN: 1-59745-173-8.

[12] Raw Materials and Raw meals Composition, Internal Data Base FLSmidth A/S, Copenhagen, 2015.

[13] Edison, M.P., Natural Cement in 21st Century, Journal of Astm International, vol.4, pp.1-10, 2007.

[14] Oates, J.A.H., Lime and Limestone: Chemistry and Technology, Production and Uses, Wiley-VCH, pp.9-17, 2007, ISBN: 3-527-29527-5.

[15] Jones, B. and Peng, X., Mineralogical, Crystalloraphic, and Isotropic Constraints on the Precipitation of Aragonite and Calcite at Shiqiang and other Hot Springs in Yunnaa Province, China, Sedimentary Geology, vol.345, pp.103-125, 2016.

[16] Chatterjee, A.K., Chemico-mineralogical Characteristics of Raw Materials, Advances in Cement Technology, Pergamon Press, pp.39-68, 1983, ISBN: 0-08-028670-4.

[17] Boyton, R., Chemistry and Technology of Lime and Limestone, 2nd Edition, John Wiley and Sons,1980, ISBN: 978-0-471-02771-3.

[18] Weaver, C.E. (editor), Clays, Muds, and Shales, Developments in Sedimentology 44, Elsevier Science Publisher B.V., pp.7, 1989, ISBN: 0-444-87381-3.

[19] Grim, R.E., Clay Mineralogy, McGraw-Hill Company Inc., 2nd Edition, 1968, ISBN-10: 0070248362.

[20] Worral, W.E., Clays, Their Nature, Origin and Great Properties, Maclaren and Sons, London, 1968, ISBN: 978-0853340218.

[21] White, W.A. and Pichler, E., Water-Sorption Characteristics of Clay Minerals, Division of the Illinois State Geological Survey, 1959.

[22] Grim, R.E. and Brandley, W.F., Rehydration and Dehydration of the Clay Minerals, American Mineralogist, vol.33, pp.50-59, 1948.

[23] Best Available Techniques for the Cement Industry, Cembureau BAT Reference Document, December, 1999. [4 February 2018] URL: www.ztch.umcs.lublin.pl/materialy/batcement.pdf.

[24] Production of Cement, Lime and Magnesium Oxide, BAT Reference Document-European Commission, 2013. [4 February 2018] URL: https://ec.europa.eu/jrc/en/publication/reference-reports/best-available-techniques-bat-reference-document-production-cement-lime-and-magnesium-oxide.

[25] Jøns, E.S., and Østergård, M.J.L., Investigation into Shell Corrosion of Rotary Cement Kilns, ZKG International, vol.52, pp.68-79, 1999.

[26] Kiln Gas Bypass System, Product Brochure, FLSmidth A/S, Copenhagen, 2011. [26 April 2018] http://www.flsmidth.com/ /media/Brochures/Brochures%20for%20kilns%20and%20firing/Kiln_ Gas_ Bypass.ashx

[27] Personal communication: Skaarup Jensen, L., R & D Specialist, FLSmidth A/S, Copenhagen, 2018.

[28] Brundiek, H. and Poeschl, H.J., Roller Mill Application for High Moisture Feed, IEEE Cement Industry Technical Conference Record XXXVIIII, pp.213-225, 1997, ISBN: 0-7803-3962-2.

[29] Strauss, F., Steinbiss, E., and Wolter, A., Measurement of Retention Times in Cement Burning Systems with the Aid of Radio Nuclides, Zement-kalk-gips, vol.40, pp.441-446, 1987.

[30] Kosmatka, S. (Updated by Staff), Cement, In Kirk-Othmer Encyclopedia of Chemical Technology, John Wiley and Sons, 2000, ISBN: 9780471238966.

Chapter 3

HCl Emission from Cement Plants

This chapter gives an overview of the HCl emission from cement plants based on the available industrial data. The HCl release and absorption zones in cement manufacturing process are presented. Emphasis is given to the description of HCl scrubbing phenomena in cement plant units. This is consistent with the main focus of this work.

Industrial measurements [1-3] had given valuable information related to HCl release and absorption zones, and flue gas composition change in cement plant units (raw mill, particle filters, etc.). The industrial data from cement plants with high HCl emissions showed the formation of HCl in the low temperature (360-600^{o}C) preheater tower cyclones and rotary kiln. Furthermore, industrial tests indicated that the HCl concentration in stack gas was not directly dependent on fuel chlorine content and kiln formation zone in the absence of a by-pass stream from kiln to stack; This supports that the HCl release from raw materials in the preheater towers is a primary HCl source.

HCl scrubbing phenomena have been identified in raw mill and particle filters in the temperature range 90-220^{o}C [1, 2]. Moreover, the industrially determined HCl scrubbing efficiencies [1] of particle filters and raw mill corresponded to conversions of the assumed active compound ($CaCO_3$ content of the preheater dust and raw meal) close to $4{\cdot}10^{-2}$ % and $5{\cdot}10^{-3}$ %, respectively.

Figure 3.1 gives a schematic illustration of the HCl release and absorption zones in cement manufacturing process, considering a simplified cement plant layout for dry cement production. The HCl release zones are the preheater tower upper cyclones and rotary kiln. The HCl absorption zone comprises the gas conditioning tower, raw mill, and particle filters with operating temperatures between 94^{o}C and 360^{o}C.

The next sections will present a detailed description of the operating conditions of cement plant units and flue gas composition change in HCl release and absorption zones.

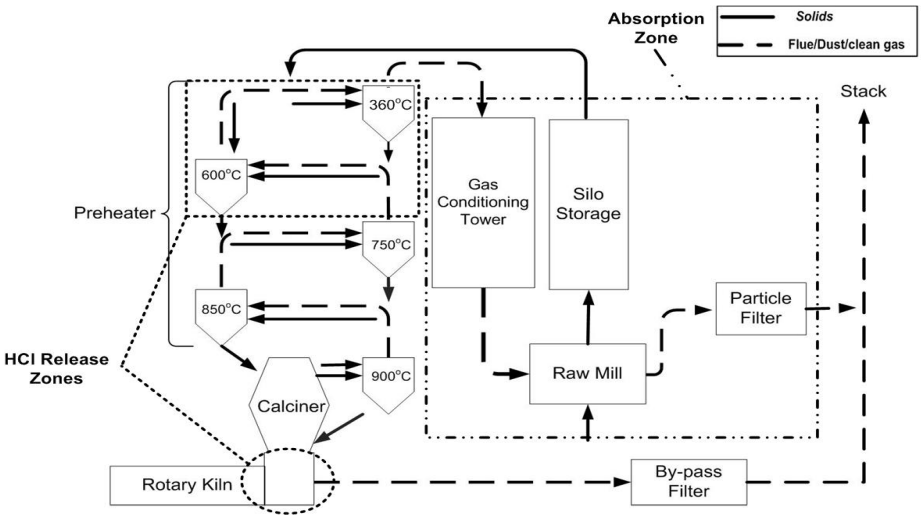

Figure 3.1: HCl release and absorption zones in dry cement manufacturing process.*

3.1 HCl Release Zones

This section presents industrial data related to HCl release in the preheater tower and rotary kiln. Emphasis is given to the HCl release in preheater tower that determines to a great extent the HCl concentration at the preheater outlet. The HCl concentration in by-pass stream is related to the HCl formation in rotary kiln [4]. Therefore, the potential contribution of by-pass stream to the HCl concentration in flue gas at the stack depends on the HCl concentration and volumetric flow in by-pass line.

3.1.1 Preheater Tower

The cement preheater tower comprises a number of cyclones, where the hot klin flue gas transfers heat to the raw meal, using non-ideal counter current flows [5]. The solid material and flue gas are mixed and separated in every cyclone [5]. The residence times of solid material and flue gas in each cyclone are close to 8s and 2s, respectively [6, 7]. Typically, the operating temperatures of preheater tower is between 360^oC (upper cyclone) and 900^oC (lower cyclone) [1-2, 6].

The determination of the mechanisms of HCl release in preheater towers is difficult due to the simultaneous absorption of chlorine species, low raw meal chlorine content, e.g., 0.019% w/w [8], and complex raw meal composition. A number of potential HCl release sources and mechanisms will be presented in Chapter 4. Figure 3.2 shows the measured flue gas composition, temperature and mass flows in the preheater tower of cement plant B. It is clearly seen that the concentrations of NH_3, HCl, SO_2 and total organic carbon (TOC) in flue gas increase significantly after the entry point

*This figure is intended to be published in a scientific article with the title: "Experimental evaluation of hydrogen chloride (HCl) absorption by cement raw meal at low temperatures, using fixed-bed tests", written by Pachitsas, S., Wedel, S., Skaarup Jensen, L., Boll Illerup, J., and Dam-Johansen, K..

of raw meal in preheater tower. This observation indicates that the aforementioned compounds are released from raw meal in the temperature range 395-605^{o}C. In contrast with this, the concentrations of CO_2, H_2O and O_2 in flue gas vary to a limited extent in the preheater tower.

The measured concentrations of HCl and SO_2 are very low in the calciner and high temperature cyclones (cyclone 3 and cyclone 4) of preaheater tower [1, 2]. This can be explained by the high reactivities of $CaCO_3$ and CaO with HCl and SO_2 in the temperature range 600-900^{o}C which allow for the scrubbing of kiln flue gas.

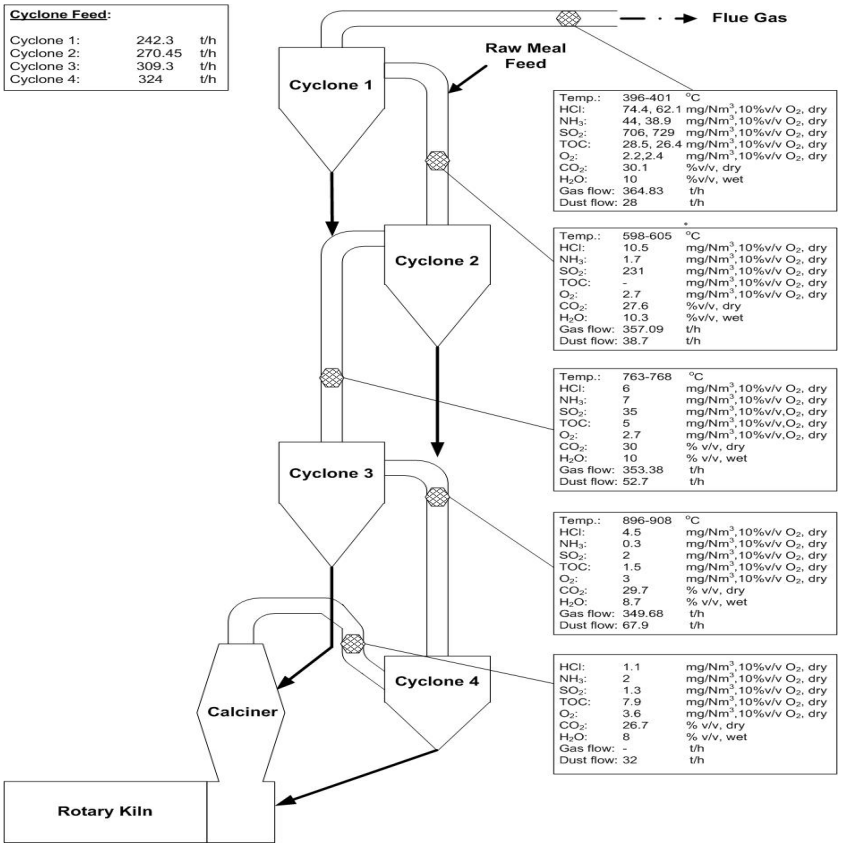

Figure 3.2: Flue gas composition, temperature profile and mass flow data in preheater tower based on the FLSmidth measurements in cement plant B (adapted) [2].

These observations imply that the HCl concentration in flue gas at preheater tower outlet is not directly related to kiln - burner operating conditions, but it may be dependent on raw materials composition. Furthermore, the HCl concentration in flue gas at the preheater outlet corresponds to a release close to 40% of the chlorine content of raw meal feed [2, 9]. It is noteworthy that the conducted industrial measurements in cement plants with high HCl emissions are consistent with the

HCl release in low temperature preaheater cyclones [1, 2]. However, the detected HCl concentrations vary significantly from cement plant to cement plant. As it is illustrated in Figure 3.2, NH_3 and TOC are also released in the low temperature cyclones of preheater tower. The simultaneous release of these compounds with HCl may be related to the mechanism of HCl release (see Chapter 4, section: 4.1.1 - 4.1.2).

The internal mass flow data of preheater towers are useful in the study of HCl release mechanism and source species identification.The designing of cyclones with low pressure drop depresses separation efficiency and allows solids recirculation in preheater tower [10]. The solids flow analysis showed that a flow of solids with high chlorine content (hot raw meal - 1.1 % w/w Cl [11]) from Cyclone 3 and 4 to the upper cyclones is possible. This can increase the actual chlorine content in low temperature cyclones during plant operation.

3.1.2 Rotary Kiln

The reaction of alkali chlorides with kiln flue gas compounds is considered a primary HCl formation source in rotary kilns at temperatures above 900^oC [12]. As it was presented in Chapter 2 (section 2.2), a number of cement plants are equipped with a kiln to stack by-pass system which usually extracts 5-15% of the chlorine rich kiln flue gas [6]; however, it can remove from 0 to 100% of the kiln flue gas [13].

The industrial measurements in cement plant A detected HCl concentrations in by-pass stream (before by-pass filter) almost 10 times higher than those of the preheater outlet flue gas stream [1]. However, the contribution of the by-pass stream ($\sim$ 5% of kiln gases) to the HCl concentration in stack flue gas was limited considering that by-pass contributed $\sim$5mg/Nm^3, 10% v/v O_2, dry and preheater outlet stream contributed $\sim$ 16mg/Nm^3, 10% v/v O_2, dry (By-pass: OFF) [1]. It is noteworthy that on other kilns the HCl concentration and volumetric flow in the by-pass line can be significantly higher than those of cement plant A, and consequently they can lead to an important contribution to HCl concentration at the stack [1]. Therefore, the HCl concentration and volumetric flow in by-pass line determine the potential contribution of by-pass stream to the HCl emission.

3.2 HCl Absorption Zone

This section presents industrial data that are related to the determined HCl absorption zone in cement plant manufacturing process. HCl scrubbing phenomena were identified in particle filters and raw mill units. The HCl reduction in GCT have not been investigated in industrial scale. However, GCT operating principles and conditions (temperature and moisture profiles) indicate the potential presence of HCl scrubbing phenomena in this unit.

3.2.1 Gas Conditioning Tower (GCT)

GCTs are used for flue gas temperature control and humidification before the inlet of particle filters, not all cement plants have GCT. The control of flue gas temperature and moisture content is mainly based on the water injection. The phase transition of water droplets with sizes between $120\mu m$ and $250\mu m$ is used in the flue gas conditioning [14]. The basic operating principles of GCT units are shown in Figure 3.3. The hot flue gas from the preheater tower enters the GCT, where water and air are injected from a system of nozzles. Then, there is the evaporation zone where the droplets evaporation and flue gas cooling occur. Finally, the cooled and moist flue gas leaves the GCT and goes to the particle filters.

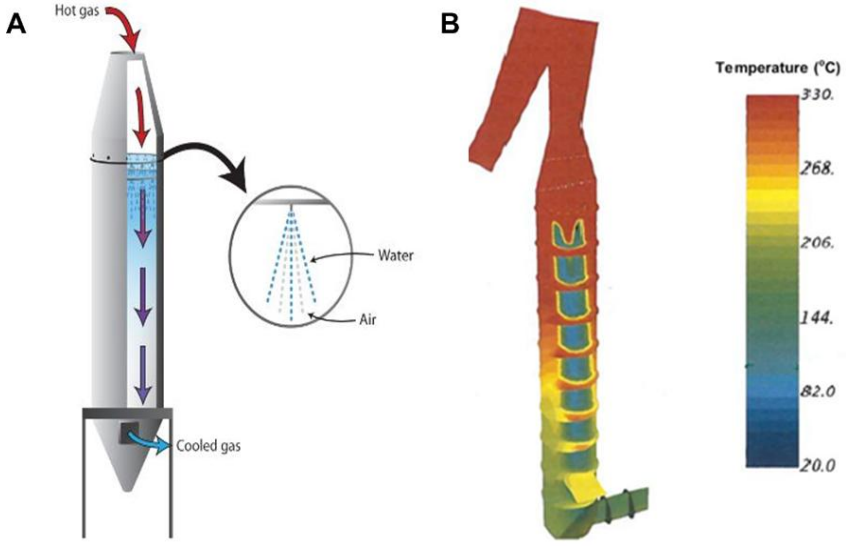

Figure 3.3: A) Schematic drawing of a GCT [15]; B) Indicative CFD simulations of the temperature profile at different GCT cross sections [16].

Table 3.1 shows the flue gas compositions and temperatures at the inlet and outlet of GCT in the case of cement plant B when raw mill is not in operation. The simultaneous flue gas moisture content increase and temperature decrease can significantly promote the HCl absorption by preheater dust particles in GCTs. It is anticipated that the flue gas moisture increase enhances HCl reaction with Ca-based sorbents at temperatures close to the outlet temperatures of GCTs [18-20]. Furthermore, the chemical analysis of GCT dust samples from cement plant B showed that the chlorine content of GCT dust is higher than that of raw meal (GCT dust: $\sim$ 0.22 %w/w (raw mill OFF) - raw meal: 0.019 % w/w) [2]. This indicates the potential presence of HCl scrubbing phenomena in GCTs. However, the potential change of HCl concentration in GCTs has not been investigated using industrial measurements. The GCT effect on HCl concentration in flue gas may be important for the prediction and control of HCl emission from cement plants.

Table 3.1: Flue gas compositions and temperatures at the inlet and outlet of GCT in cement plant B when raw mill is OFF [17].

Parameter	Inlet	Outlet
Temperature (^{o}C)	388	150
Dust flow (t/h)	26	24
H_2O (%v/v, wet)	10.4	23.2
O_2 (%v/v, dry)	3.9	4.6
CO_2 (%v/v, dry)	31	29.7

3.2.2 Raw Mill

The raw meal drying, homogenization, and grinding finalization occur in raw mill units. Figure 3.4 shows the raw mill structure and internal solid material flows in the case of a vertical roller raw mill. The raw mill is split into three main parts: the separator, grinding - drying compartment, and drive unit. The internal solid material flows show that the mass flow of solids coming out grinding table is 15 to 30 times larger than the mass flow of fine dust leaving separator. Furthermore, the mass flow of the recirculating intermediate size particles is 1.5 times larger than the mass flow of fine dust leaving separator. These data clearly show that the dust load of dispersion significantly varies from the grinding table plane towards the separator.

The feed material is ground on a grinding table, using grinding rollers. The solid materials are carried by the hot flue gas to the particle separator, where the fine particles leave the raw mill in the form of a dispersion while the large particles return on grinding table for further processing. Industrial tests showed that the raw meal drying and flue gas temperature drop were instantaneous at the grinding table plane [22]. The final solid material - flue gas separation occurs in a cyclone after the raw mill outlet. It is noteworthy that during raw mill operation a significant amount of water is injected for the stabilization of grinding system (grinding disc - rollers). Table 3.2 presents typical values of the flue gas temperature and moisture content at the inlet and outlet of vertical raw mills. The high flue gas moisture content in conjunction with the solids recirculation and relatively low temperature in this unit gives auspicious conditions for the HCl absorption by raw meal in raw mill units.

Table 3.2: Indicative values of the temperature and moisture content at raw mill inlet and outlet [1, 23].

Parameter	Inlet	Outlet
Temperature (^{o}C)	300	94
H_2O %v/v	6.27	13.14

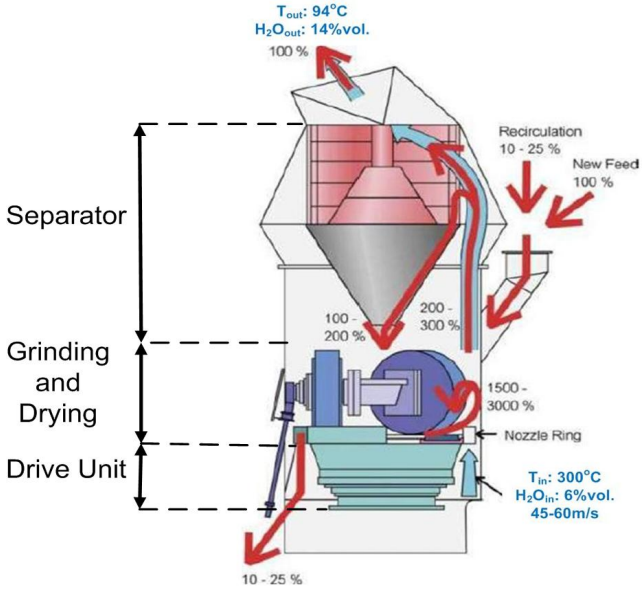

Figure 3.4: ATOX raw mill structure and internal solid material flows (adapted) [21].

The flue gas passing through raw mill (when it is in operation) is an effective method for the reduction of HCl emission from cement plants. However, this method is limited by the process operating flue gas and mass flows (not necessarily all flue gas passes through the raw mill), and raw mill operating time. Industrial measurements verified the importance of the raw mill scrubbing effect for the control of HCl emission from cement plants [1-3]. Moreover, industrial tests on HCl scrubbing efficiency of raw mill in cement plant A with an inlet HCl concentration 25 mg/Nm^{3*} showed that the outlet HCl concentration was ranged from 2mg/Nm^{3*} to 4mg/Nm^{3*} (1-2ppm actual) which corresponded to the used analyzers detection limit (1ppm actual)[1]. Furthermore, it was observed that the HCl scrubbing efficiency of raw mill was not dependent on the operating conditions (temperature and water injection). SO_2 and NH_3 were also effectively scrubbed by raw mill. In particular, up to 94% of the SO_2 and NH_3 were removed. It is noteworthy that only a slight dependence of SO_2 and NH_3 scrubbing efficiencies on operating conditions was observed [1]. A complete HCl absorption in raw mill was also detected in cement plant C with inlet HCl concentration 4.6 mg/Nm^{3*} [3]. On the other hand, a limited study (one measurement) of raw mill scrubbing effect in cement plant B showed HCl reduction close to 77% with an inlet HCl concentration equal to 51mg/Nm^{3*}[2]. However, this measurement is inconsistent with the other data from cement plant B, consequently its validity is questionable.

*in dry flue gas at 10% v/v O_2

3.2.3 Particle Filters

The particle filters are the last cement plant unit before the stack. They are categorized into two main types: the fiber filters (bag filters) and electrostatic precipitators (ESPs). Figure 3.5 shows the operating principals of the particle filters. In the case of bag filters (Figure 3.5 - A) the particles are retained on bag surfaces and form a dust 'cake' layer. The dust layer is periodically removed, using reverse air injection, reverse air pulse injection, or a mechanical shaker. The ESPs (Figure 3.5 - B) use electrostatic attraction for the collection of dust particles on charged metallic plates, where the dust layer is formed. The dust layer is removed from the collection plates by mechanical impulses, vibrations, etc.. The residence times of gas phase in fiber filters (before filtration bags) and ESPs are $\sim$ 1.9s and 20s $\pm$ 5s, respectively [25]. On the other hand, the residence time of particles in filter units is significantly longer, e.g., bag filters: 30-60 min [25].

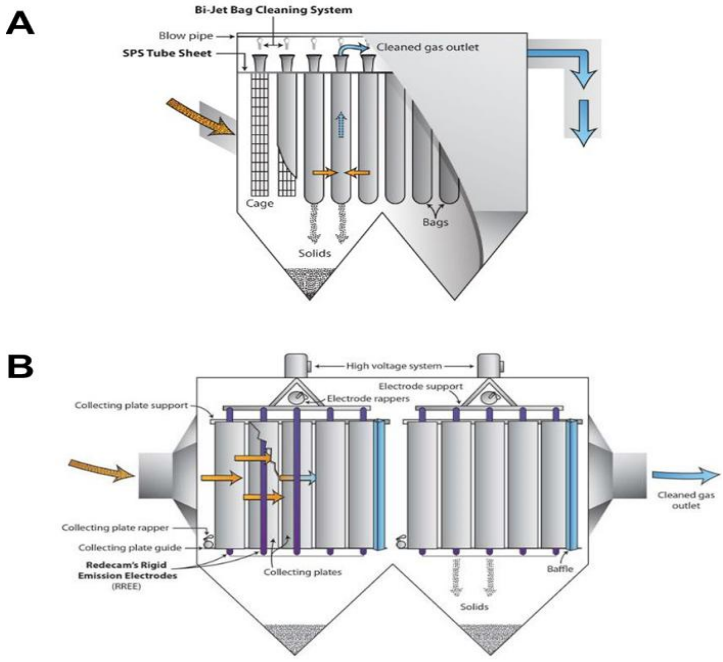

Figure 3.5: A) Schematic drawings of bag filters; B) Schematic drawings of ESPs [24].

The cement plant design typically determines that the flue gas dust load at the filters outlet is about 10 mg/Nm^3 [25]. The flue gas dust load at the inlet of filter units depends on the cement plant operating conditions (raw mill: ON - OFF). For instance, the dust load of filter inlet flue gas is close to 30 g/m$^3_{actual}$ in the case of raw mill operation [23]. The industrial evaluation of the HCl scrubbing efficiency of particle filters (bag filters) when raw mill is OFF was conducted in cement plant A. In particular, the outlet temperature decrease, using water injection and fresh air, from 210^{o}C - 3.5% v/v H_2O to 151^{o}C - 6% v/v H_2O resulted in an increase in HCl reduction from 51% to

63% with inlet HCl concentrations 32mg/Nm^{3*} and 35mg/Nm^{3*}, respectively [1]. It is noteworthy that SO_2 and NH_3 scrubbing phenomena were not observed in particle filters at 210^{o}C. However, a slight reduction (8%) of SO_2 and NH_3 concentrations in flue gas was detected with the temperature decrease [1].

The HCl scrubbing efficiency of ESPs has not been investigated. However, ESP units are sensitive to corrosion phenomena at operating conditions close to the dew point. Therefore, HCl scrubbing in ESP units using operating temperatures close to 100^{o}C is not recommended.

HCl scrubbing phenomena were also detected in by-pass bag filters in cement plant A. In particular, the decrease of the outlet temperature of by-pass filters, using fresh air and water injection, from 164^{o}C - 2.8%v/v H_2O to 91^{o}C - 4% v/v H_2O resulted in an increase in HCl reduction from 20% to 76%, with inlet HCl concentration equal to 225mg/Nm* [1]. The HCl scrubbing efficiency of the by-pass filter unit is not directly comparable to that of the main particle filters due to the significant differences in the compositions of dust (kiln dust: mainly CaO - preheater dust: mainly $CaCO_3$) and flue gas.

3.3 Conclusions on HCl Emission from Cement Plants

The available industrial data from cement plants with high HCl emissions determined the presence of HCl release and absorption zones in cement manufacturing process. Furthermore, they indicated a number of operating parameters that can affect the HCl absorption by raw meal and preheater dust.

The industrial data indicate that the low temperature cyclones (360-600^{o}C) of preheater tower and rotary kiln are the HCl release zones. The HCl formation in rotary kiln is directly connected with the HCl concentration in by-pass gas stream. On the other hand, no direct connection between the HCl formation in kiln and HCl concentration in flue gas at the preheater outlet was detected. Hence, the HCl concentration in flue gas at the preheater outlet is mainly determined by the HCl release in preheater tower.

Strong HCl scrubbing phenomena in the particle filters and raw mill units at temperatures between 94^{o}C and 220^{o}C were detected. These indicated the presence of HCl absorption by preheater dust and raw meal at the usual operating conditions of GCT, raw mill, and particle filters. In addition, the observed enhancement of the HCl scrubbing efficiency of particle filters with the operating temperature decrease showed that temperature can significantly affect the HCl absorption by preheater dust in presence of moist flue gas.

The analysis of the HCl emission from cement plants determined the conditions of interest (HCl release/absorption) which will be studied in next the chapters.

*in dry flue gas at 10% v/v O_2

3.4 References

[1] Emission Measurements of Cement Plant A,Internal report FLSmidth A/S, Copenhagen, 2012.

[2] Emission Measurements of Cement Plant B, Internal report FLSmidth A/S, Copenhagen, 2013.

[3] Emission Measurements of Cement Plant C, Internal report FLSmidth A/S, Copenhagen, 2013.

[4] Kiln Gas Bypass System, Product Brochure, FLSmidth A/S, Copenhagen, 2011. [26 April 2018] http://www.flsmidth.com/ /media/Brochures/Brochures%20for%20kilns%20and%20firing/ Kiln_ Gas_ Bypass.ashx

[5] Rasmussen, M.H., Low SO_2 Emission Preheaters for Cement Production, Ph.D. Dissertation, Technical University of Denmark, pp.10, 2012, ISBN: 978-87-92481-59-7.

[6] Best Available Techniques for the Cement Industry, Cembureau BAT Reference Document, December, 1999. [4 February 2018] URL: www.ztch.umcs.lublin.pl/materialy/batcement.pdf.

[7] Strauss, F., Steinbiss, E., and Wolter, A., Measurement of Retention Times in Cement Burning Systems with the Aid of Radio Nuclides, Zement-kalk-gips, vol.40, pp.441-446, 1987.

[8] Raw Meals Compositional Analysis, Internal report FLSmidth A/S, Copenhagen, 2016.

[9] Operating Diagram of Cement plant B, Internal report FLSmidth A/S, Copenhagen, 2014.

[10] Helm, A. and Rosholm, P., State of the Art Preheater Design, World Cement, vol.25, pp.26-36, 1994.

[11] Raw Materials and Raw meals Composition, Internal Data Base FLSmidth A/S, Copenhagen, 2015.

[12] Jøns, E.S., and Østergård, M.J.L., Investigation into Shell Corrosion of Rotary Cement Kilns, ZKG International, vol.52, pp.68-79, 1999.

[13] Personal communication: Skaarup Jensen, L., R& D Specialist, FLSmidth A/S, Copenhagen, 2018.

[14] Personal communication: Elholm, P., Senior Process Engineer, Fabric Filter Product Management, Airtech-FLSmidth, Copenhagen, 2016.

[15] Gas Conditioning Tower Schematic Drawing, Redecam Group, [3 June 2016] http://www.redecam.com/conditioning-products/

[16] GCT CFD Operating Simulations, Internal report FLSmidth A/S, Copenhagen, 2016.

[17] Operating Diagram of Cement Plant B - Raw Mill: OFF, Internal report FLSmidth A/S, Copenhagen, 2017.

[18] Weinell, C.E., Jensen, P.I., Johansen, K.D., and Livbjerg, H., Hydrogen Chloride Reaction with Lime and Limeston - Kinetics and Sorption Capacity, Industrial Engineering & Chemistry Research, vol.31, pp.164-171, 1992.

[19] Fonseca, A.M., Órfaõ, J.J., and Salcedo, R.L., Kinetic Modeling of the Reaction of HCl and Solid Lime at Low Temperatures, Industrial & Engineering Chemistry Research, vol.37, pp.4570-4576, 1998.

[20] Jozewicz,W., Chang, J.C.S., and Sedman, C.B., Bench-Scale Evaluation of Calcium Absorbents for Acid Gas Emission Control, Environmental Progress, vol. 9, pp.137-142, 1990.

[21] ATOX Raw Mill Structure and Solid Material Flows, Internal training material, FLSmidth A/S, Copenhagen, 2013.

[22] Personal communication: Folsberg, J., Regional Chief Engineer - Raw Mill Department, FL-Smith A/S, Copenhagen, 2018.

[23] Process Diagrams of Cement Plant A, Internal report FLSmidth A/S, Copenhagen, 2005.

[24] Bag filter and ESP Operating Principles, Redecam - Group, [3 June 2016] http://www.redecam.com/air-filtration-products/.

[25] Personal communication: Andersen, B.O., CFD and Fluid Dynamics Specialist, Airtech-FLSmidth, Copenhagen, 2018.

Chapter 4

Literature Review on HCl Release & Absorption at Industrial Conditions

This chapter presents the literature review on the potential mechanisms of HCl release and absorption at industrial conditions. The analysis of cement manufacturing process (Chapter 2) and available industrial data related to the HCl emission from cement plants (Chapter 3) provided the framework of literature review. This chapter comprises two main structural sections: (i) HCl release in preheater towers and rotary kilns, and (ii) HCl absorption in post-preheater tower units. The section on HCl release is mainly focused on the study of the HCl formation occuring in the upper cyclones of preheater towers at temperatures between 360^oC and 600^oC. However, the HCl formation in rotary kilns is also investigated. The section on HCl absorption gives emphasis to HCl reactions with Ca-based sorbents at the operating conditions, e.g., temperatures between 94^oC and 360^oC, of the post-preheater tower units (gas conditioning tower, raw mill and particle filters).

4.1 HCl Release

This section presents the study of HCl release mechanisms from raw materials in preheater towers and rotary kilns. The suggested three potential HCl release mechanisms in preheater towers are: (i) salts and salt hydrates thermal decomposition, (ii) organic matter reaction with inorganic chlorides, and (iii) inorganic chlorides reactions with flue gas compounds. Alkali chlorides reaction with kiln flue gas compounds is considered as a primary formation mechanism of HCl in rotary kilns [1]. In addition, the potential direct release of HCl from combustion of fuels that are commonly used in cement industry is reported. It is noteworthy that the identification of the HCl release mechanisms from fuel combustion is difficult due to the significant variation of fuels composition and chlorine binding (organically or inorganically bound). A brief discussion about the fuel originated HCl release will be presented in this section.

4.1.1 Salts and Salt Hydrates Thermal Decomposition

Raw meal as a mixture of naturally occurring minerals, e.g., limestone and shales, contains impurities which are related to raw materials geological formation. For instance, in the case of marine sedimentary rocks, e.g., limestone, the presence of salts and salt hydrates that were encountered in the aquatic environments of the formation era is anticipated. Similarly, shales and clays contain impurities, e.g., soluble salts and organic substances, which are related to the genesis mechanism, source origin, topology, and vegetation [2]. Emphasis is also given to the presence of salts that can be formed during the cement manufacturing process and release HCl at the preheater tower conditions.

Ammonium Chloride (NH_4Cl)

The mineral NH_4Cl is mainly formed close to volcanic vents and also by coal combustion gas condensation. Consequently, its presence in raw materials by natural occurrence is unlikely. Nevertheless, NH_4Cl can be formed in cement plant units where HCl and NH_3 co-exist in gas phase at temperatures less than 200^oC [5], e.g., raw mill. The release of NH_3 in raw meal drying stages at temperatures between 100^oC and 220^oC is reported [3, 4]. Furthermore, the raw mill operation utilizes preheater outlet flue gas that contains HCl and NH_3. The thermal decomposition of NH_4Cl (4.1) takes place at temperatures between 200^oC and 430^oC, which are close to the operating temperatures of the upper cyclones of preheater towers [5-7]. The decomposition mechanism comprises two stages: (i) the sublimation that starts above 200^oC and has maximal rate at 345^oC [5, 7], and (ii) the complete dissociation in gas phase [5]. The industrial measurements (Chapter 3, section 3.1.1) detected the simultaneous release of HCl and NH_3 in the low temperature cyclones of preheater towers. Hence, NH_4Cl can be considered as a potential HCl source in preheater towers.

$$NH_4Cl(s) \rightleftharpoons NH_3(g) + HCl(g) \tag{4.1}$$

Carnallite ($KCl \cdot MgCl_2 \cdot 6H_2O$)

Carnallite is a common seawater evaporite [8], and consequently it is considered an impurity of marine sedimentary formations, e.g., limestone and shale. The thermal decomposition of $KCl \cdot MgCl_2 \cdot 6H_2O$ to KCl and MgO has been studied by many researchers. Theoretically, the thermal dissociation can be described by one stage reaction (4.2) [9], but in reality the decomposition is complex and occurs in different stages [9, 10]. The experimental studies showed a temperature dependent decomposition process, which occurs above 300^oC (at 450^oC 90% of magnesium is chlorine free) [9].

$$KCl \cdot MgCl_2 \cdot 6H_2O(s) \rightarrow KCl(s) + MgO(s) + 5H_2O(g) + 2HCl(g) \tag{4.2}$$

Magnesium Chloride Hydrates

$MgCl_2 \cdot 6H_2O$ (Bischofite) is a common sea water evaporate [11, 12], which presence in marine sedimentary rocks is likely. Magnesium chloride hydrates are able to release significant quantities of HCl during their thermal decomposition at temperatures above 200^{o}C (4.3 - 4.6) [13-15].

$$MgCl_2 \cdot 4H_2O(s) \rightarrow \ MgCl_2 \cdot 2H_2O(s) + 2H_2O(g) \quad (110 - 175^oC) \tag{4.3}$$

$$MgCl_2 \cdot 2H_2O(s) \rightarrow \ MgCl_2 \cdot H_2O(s) + H_2O(g) \quad (175 - 210^oC) \tag{4.4}$$

$$MgCl_2 \cdot H_2O(s) \rightarrow \ MgOHCl(s) + HCl(g) \quad (210 - 445^oC) \tag{4.5}$$

$$MgOHCl(s) \rightarrow \ MgO(s) + HCl(g) \quad (445 - 640^oC) \tag{4.6}$$

4.1.2 Organic Matter Reaction with Inorganic Chlorides

The organic matter reaction with inorganic chlorides can release HCl at temperatures between 300^{o}C and 500^{o}C. The presence of organic matter in sedimentary rocks (shales, carbonate rocks, and sandstones) is reported [16-18]. Moreover, shales and clays are considered as the raw materials with the highest concentrations of organic matter and chlorine (Chapter 2, Table 2.1). It is commonly accepted that in the case of shales and clays the organic material occurs as: (i) discrete particles of wood, leaves, etc., (ii) absorbed organic molecules, e.g., humic acids, on the clay minerals, and (iii) intercalated between the silicate layers [16]. Experimental studies on biomass pyrolysis showed that HCl was released at temperatures between 300^{o}C and 500^{o}C based on the organic matter reaction with inorganic chlorides. The organic matter thermal degradation generates carboxylic acid groups that react with KCl and NaCl via ion exchange reactions (4.7 - 4.8) [19-21].

$$R - COOH(s) + KCl(s) \rightarrow \ R - COOK(s) + HCl(g) \tag{4.7}$$

$$R - COOH(s) + NaCl(s) \rightarrow \ R - COONa(s) + HCl(g) \tag{4.8}$$

The organic matter functional groups were ranked based on their reactivity with KCl and NaCl as follows:

Free carboxylic acids > ester in lactone ring-hemiacetal > acetal-open esters- hydroxymethyl on ring or chain >> terminal hydroxymethyl [20]

Organic matter thermal desorption experiments using cement raw meal showed that the raw meal releases different organic compounds including benzene, naphthalene, C14-C18 carboxylic acids, phthalates and their derivatives [22-24]. Furthermore, it was identified that the desorbed organics mainly consist of C14-C18 carboxylic acids with molar weights between 200 amu and 300 amu [22, 23]. It is also important that the organics release takes place at temperatures between 250^{o}C and 500^{o}C, which correspond to the defined temperature range of HCl release in preheater towers [22-25]. Therefore, the raw meal organic matter thermal degradation (formation of carboxylic acids) occurs in the same temperature range with HCl release in preheater tower, and organic matter reaction with inorganic chlorides.

Dechlorination of organic chlorides can also be related to the HCl release in preheater tower. The decomposition of chlorinated hydrocarbons by transition metal oxide catalysts at temperatures between 300^{o}C and 500^{o}C is reported [26-28]. In particular, Sidhu et al.[22] reported formation of organic chlorides, e.g., mono- through tetra-chlorinated methanes and ethylenes, in cement preheaters at temperatures between 300^{o}C and 400^{o}C. The chlorination of organics can be caused by the reaction of organic matter with HCl, Cl_2, $CaCl_2$, $FeCl_3$, KCl, etc., and catalyzed by alkali metal oxides and hydroxides [22, 23]. It is noteworthy that Shigapov et al.[29] presented evidences of methane chlorination above CaO - $CaCl_2$ catalysts at 750^{o}C.

4.1.3 Inorganic Chlorides - Gas Phase Reactions

The presence of inorganic chlorides, e.g., $CaCl_2$, NaCl and KCl in raw meal is indisputable. Furthermore, the fuels combustion in rotary kiln adds inorganic chlorides. Theoretically, inorganic chlorides can release HCl based on solid - gas and gas - gas reactions in the presence of appropriate gaseous phases (SO_3, SO_2, O_2, H_2O, etc.) at differing temperatures. These reactions are strongly affected by the gas phase composition, presence of conjugate reactions with solid particles (SiO_2, Al_2O_3, Fe_2O_3, etc.), and temperature [30-34]. Typically, they are considered feasible at temperatures above 400^{o}C. Furthermore, the reaction of vaporized alkali chlorides with kiln flue gas compounds is considered as a primary HCl release mechanism in kilns at temperatures above 900^{o}C [1].

Calcium Chloride ($CaCl_2$)

$CaCl_2$ is a raw meal compound, which can be present as inclusion in limestone or product of the HCl reaction with $CaCO_3$ and CaO [35]. The HCl release via solid - gas reactions between $CaCl_2$ and O_2 / CO_2 / H_2O gas phase (4.9 - 4.12) at temperatures above 400^{o}C is reported [34].

$$CaCl_2(s) + H_2O(g) \rightarrow\ Ca(OH)Cl(s) + HCl(g) \quad (410 - 740^oC) \tag{4.9}$$

$$Ca(OH)Cl(s) + CO_2(g) \rightarrow\ CaCO_3(s) + HCl(g) \quad (410 - 740^oC) \tag{4.10}$$

$$Ca(OH)Cl(s) \rightarrow\ CaO(s) + HCl(g) \quad (640 - 740^oC) \tag{4.11}$$

$$CaCl_2(s) + H_2O(g) + CO_2(g) \rightarrow\ CaCO_3(s) + 2HCl(g) \quad (< 650^oC) \tag{4.12}$$

The work of Matsuda et al.[30] reported the HCl formation by solid - gas reactions (4.13 - 4.16) of $CaCl_2$ with SO_2 / O_2 / H_2O mixture (SO_2: 0.9% v/v, O_2: 5 % v/v, H_2O: 10 % v/v and N_2 - balance) at relatively low temperatures close to 450^{o}C.

$$CaCl_2(s) + SO_2(g) + 1/2O_2(g) + H_2O(g) \rightarrow\ CaSO_4(s) + 2HCl(g) \tag{4.13}$$

$$CaCl_2(s) + SO_2(g) + H_2O(g) \rightarrow\ CaSO_3(s) + 2HCl(g) \tag{4.14}$$

$$CaCl_2(s) + 2H_2O(g) \rightarrow\ Ca(OH)_2(s) + 2HCl(g) \tag{4.15}$$

$$CaCl_2(s) + H_2O(g) + SiO_2(s) \rightarrow\ CaSiO_3(s) + 2HCl(g) \quad (> 600^oC) \tag{4.16}$$

Sodium Chloride (NaCl)

Sodium chloride is a common inorganic salt and an expected raw materials (limestone, shales, and clays) impurity. Furthermore, NaCl can be added in rotary kilns by fuel. The HCl release from NaCl reactions with differing gas phase in presence of conjugate reactions with solid particles (SiO_2, Al_2O_3, Fe_2O_3, etc.) has extensively been studied [30-33]. It is concluded that the NaCl contribution to HCl release can be important only at temperatures above 600^{o}C (4.17 - 4.19)[30-33]. Therefore, the connection of NaCl with the HCl formation in rotary kilns is reasonable.

$$2NaCl(s) + SO_2(g) + 1/2O_2(g) + H_2O(g) \rightarrow \ Na_2SO_4(s) + 2HCl(g) \quad (> 500^oC) \tag{4.17}$$

$$2NaCl(s) + SiO_2(s) + H_2O(g) \rightarrow \ Na_2SiO_3(s) + 2HCl(g) \quad (700 - 900^oC) \tag{4.18}$$

$$2NaCl(s) + SO_3(g) + H_2O(g) \rightarrow \ Na_2SO_4(s) + 2HCl(g) \quad (450 - 625^oC) \tag{4.19}$$

Potassium Chloride (KCl)

KCl can release HCl via solid - gas reactions (4.20 - 4.24) at temperatures above 500^{o}C. However, HCl release rates from KCl are 18 and 10 times lower than those of $CaCl_2$ and NaCl, respectively [30]. Furthermore, reactions (4.25 - 4.26) of vaporized KCl with the kiln flue gas compounds are reported as a primary release mechanism of HCl in rotary kilns at temperatures above 900^{o}C [1, 36].

$$KCl(s) + 1/2SO_2(g) + 1/4O_2(g) + 1/2H_2O(g) \rightarrow \ 1/2K_2SO_4(s) + HCl(g) \tag{4.20}$$

$$KCl(s) + 1/2SO_2(g) + 1/2H_2O(g) \rightarrow \ 1/2K_2SO_3(s) + HCl(g) \tag{4.21}$$

$$KCl(s) + 1/2H_2O(g) \rightarrow \ 1/2K_2O(s) + HCl(g) \tag{4.22}$$

$$KCl(s) + H_2O(g) \rightarrow \ KOH(s) + HCl(g) \tag{4.23}$$

$$KCl(s) + 1/2SiO_2(s) + 1/2H_2O(g) \rightarrow \ 1/2K_2SiO_3(s) + HCl(g) \tag{4.24}$$

$$KCl(g) + 1/2SO_2(g) + 1/4O_2(g) + 1/2H_2O(g) \rightarrow \ 1/2K_2SO_4(s) + HCl(g) \tag{4.25}$$

$$2KCl(g) + SO_3(g) + H_2O(g) \rightarrow \ K_2SO_4(g) + 2HCl(g) \tag{4.26}$$

4.1.4 HCl Release from Fuel Combustion in Kilns

Cement production is characterized by the use of a great variety of fuels differing in composition and chlorine binding (organically or inorganically bound). This work discusses the HCl release from coal, fuel oil, and alternative fuels, e.g., domestic waste. The content of inorganic chlorine in fuels usually is in the form of NaCl and KCl. The HCl release from the inorganic chlorides (NaCl and KCl) reaction with flue gas compounds was described in section 4.1.3.

Coals contain chlorine both organically and inorganically bound in a varying concentration (500-3000ppmw)[37]. Furthermore, the physical coal cleaning after mining can mainly decrease the inorganically bound chlorine content [38]. The work of Harkov and Ross[37] using Appalachian coals showed that most of the coal chlorine was organically bound. In addition, Chow et al.[39] reported that the 86% of the chlorine content of coals (probably cleaned) was released as HCl in power plant incinerators. Therefore, the available literature data [39-42] indicate that HCl can be released by coal combustion in rotary kilns.

Fuel oil can be contaminated by chlorine species during crude oil processing due to the presence of chlorine ions on cracker catalysts, and crude oil transportation [37]. The chlorine release mechanism from fuel oil combustion is considered similar to that in coals combustion [37]. Hence, the fuel oil combustion can release HCl in kilns.

The use of alternative fuels in cement manufacturing process is growing continuously. Alternative fuels contain organic and inorganic chlorine [43]. The total chlorine content and primary chlorine binding depend on the alternative fuels type and composition. Typical, inorganic chlorides are NaCl (e.g., domestic waste) and KCl [43]. Polyvinyl chloride (PVC) is a common organic chloride in domestic waste which thermal decomposition in the temperature range 200-550^{o}C releases HCl (4.27) [43].

$$(CH_2CHCl)_n \rightarrow \ nHCl + nC_2H_2 \tag{4.27}$$

4.1.5 Conclusions on HCl Release

The study of the HCl release from raw materials at preheater tower conditions has not been reported by other researchers. The experimental study of the mechanism of HCl formation at preheater tower conditions is a challenging issue considering the low chlorine content of raw meal, and co-existence of HCl release and absorption phenomena. This section listed different mechanisms which can be involved in the HCl release in preheater tower. The thermal decomposition of salt hydrates and organic matter reaction with inorganic chlorides seem to be the most likely release mechanisms, due to the presence of the participating compounds at the appropriate conditions, e.g., temperature, etc.. Moreover, a combination of HCl release mechanisms is also possible.

The solid - gas and gas - gas reactions of inorganic chlorides with kiln flue gas compounds are considered as primary HCl formation mechanisms in rotary kilns. A number of HCl releasing reactions of inorganic chlorides contained in raw meal and fuel ($CaCl_2$, NaCl, and KCl) with compounds of kiln flue gas (SO_2, H_2O, O_2 and CO_2) were presented. Furthermore, the direct HCl release from fuel combustion is possible.

4.2 HCl Absorption

This section presents the literature study on HCl absorption by Ca-based sorbents. The main part of this section is intended to be published in a scientific article with the title: "Experimental evaluation of hydrogen chloride (HCl) absorption by cement raw meal at low temperatures, using fixed-bed tests", written by Pachitsas, S., Wedel, S., Skaarup Jensen, L., Boll Illerup, J., and Dam-Johansen, K..

The study of the mechanism of HCl absorption by preheater dust and raw meal in post-preheater tower units is a challenging issue due to the presence of different sorbents ($CaCO_3$, CaO, $MgCO_3$, and $MnCO_3$), multi-compound gas phase, wide particle size distribution, particle agglomerates, and potential surface chemistry effects. This study assumes that $CaCO_3$ is the main HCl sorbent in preheater tower dust and raw meal taking into account the raw meal composition (Chapter 2 - Table 2.2). However, the presence of different potential HCl sorbents and impurities may affect the HCl absorption mechanism. This section presents the literature study on the effects of temperature, sorbent physical properties, and gas phase composition (H_2O, CO_2 , O_2, and SO_2) on HCl absorption by Ca-based sorbents.

The reaction of $MgCO_3$ with gas HCl is thermodynamically possible (according to free Gibbs energy minimization), however, the reaction kinetics are anticipated to be very slow. Therefore, it can be considered that the HCl absorption by $MgCO_3$ through solid - gas reactions is negligible at cement plant conditions. However, $MgCO_3$ reaction with HCl dissolved in water liquid phase is reported [44-46]. Experimental studies on the dolomites dissolution in HCl - aqua solutions showed that Ca/Mg ratio is greater in the solution than solid bulk, which indicates that $CaCO_3$ release is faster than $MgCO_3$ release [45, 46]. Busenberg and Plummer[47] supported the presence of two dissolution stages, where initially the $CaCO_3$ release rate is much greater than $MgCO_3$, and a second stage where components are stoichimetrically released. Furthermore, Hosten and Gulsun[48] and Siagi and Mbarawa[49] reported that a high content of $MgCO_3$ decreases the dissolution rate of limestone. Similarly, Stumpf et al.[50] supported that the presence of $MgCO_3$ as dolomite reduces limestones reactivity in acidic aqueous solutions. However, the $MgCO_3$ content in limestone cannot be directly related to the limestone reactivity with HCl - aqua solutions [49]. Furthermore, the experimental studies concluded that limestone - dolomite reactivity in aqueous solutions is promoted by the large specific surface area, small particle sizes, and high temperature [45-50].

It is well known that the absorption of acidic gases by Ca-based sorbents can be affected by temperature, gas phase composition, and sorbent physical properties, e.g., specific surface area and particle size. Therefore, the analysis of the HCl absorption in cement plan units should be based on data that correspond to the industrial conditions. As shown in Chapter 3, the industrial flue gas in post-preheater tower units is characterized by HCl concentrations less than 100ppmv and moisture content between 5% v/v and 19% v/v [51, 52]. The HCl absorption temperature window is considered to be between 90^oC and 400^oC. However, the main interest is focused on the temperature ranges 90-110^oC and 120-220^oC that correspond to the HCl scrubbing conditions in raw mill and particle filters, respectively. It is noteworthy that the industrial evaluation of particle filters and raw mill HCl scrubbing efficiencies showed active compound ($CaCO_3$ content of preheater dust in particle filters and raw meal in raw mill) conversions close to $4{\cdot}10^{-2}$% and $5{\cdot}10^{-3}$%, respectively. Furthermore, raw meal (sorbent) is a multi-compound mixture of finely comminuted natural products, e.g., limestone, clay, sand, with particle sizes predominantly between $1\mu m$ and $100\mu m$ and large surface area 7-9 m^2/g. The flue gas residence times in particle filters (bag filters - before filtration bags) and raw mill (vertical roller mill) are approximately 2s and 1.5s, respectively. The fine particles are dispersed in flue gas; and consequently, flue gas and particles have approximately

similar residence time in the gas conditioning tower and raw mill units. However, fine particles have significantly longer residence times than flue gas in particle filters.

The previous studies insufficiently account for HCl absorption under conditions relevant to the cement plant absorption zone in terms of temperature, gas phase composition, exposure time, and sorbent composition and physical properties outlined in the previous chapters. Table 4.1 shows studies relevant to HCl absorption by Ca-based sorbents considering direct gas - solid reactions (4.28 - 4.30).

$$CaCO_3(s) + 2HCl(g) \rightleftharpoons CaCl_2(s) + H_2O(g) + CO_2(g) \tag{4.28}$$

$$CaO(s) + 2HCl(g) \rightleftharpoons CaCl_2(s) + H_2O(g) \tag{4.29}$$

$$Ca(OH)_2(s) + 2HCl \rightleftharpoons CaCl_2(s) + 2H_2O(g) \tag{4.30}$$

In the following sections a more detailed review of results from previous studies will be presented with the aim of extracting information of relevance for the present work.

Table 4.1: Studies related to HCl absorption by Ca-absorbents.

T(°C)	HCl(ppmv)	Particle Size Range	BET(m^2/g)	Gas Phase H_2O(% v/v)	Tested Materials	Method	
60-1000	1000	20.5-2.12μm(CaO)	8.8-19.7 $Ca(OH)_2$ 1.2-185 limestone	0,5,15	Limestone,CaO, $Ca(OH)_2$	Fixed-bed	Weinell et al.[53]
350-600	13000-40000	0.2-2mm		0	Limestone	Fixed-bed	Petrini et al.[54]
450-550	20000-24000	<0.25mm	-	0	Limestone	Fixed-bed	Ketov et al.[55]
300-600	2000	46.5-190μm	5	0 and 5	Limestone	Fixed-bed	Mura and Lallai[56]
750	1000	32-75μm 250-355μm 710-1000μm	-	0	Cal. limestone	Fluid. bed	Matsukata et al.[57]
310-600	21000	<10μm-720μm	11-13	0	Cal. limestone	Therm. balance	Daoudi and Walters[58]
300-600	900	125μm-500μm	1-2(limestone) 4.1(CaO) 24($Ca(OH)_2$)	1.8-24.2	$CaCO_3$,CaO, $Ca(OH)_2$	Fixed-bed	Duo et al.[59]
150-250 400-600 150-250	1000	<0.125μm	-	1.3	Limestone Cal. limestone $Ca(OH)_2$	Fixed-bed	Wang et al.[60]
150-350	1000-7500	3-59μm	5	0	Cal. limestone $Ca(OH)_2$	Fixed-bed	Gullett et al.[61]
200-600	1000	0.188-925μm	-	0	CaO	Fixed-bed	Mura and Lallai[62]
650-825	2000	200-250μm	-	0 and 14	Cal. limestone	Therm. balance	Partanen et al.[63]
310-670	5000-50000	<45μm	-	0	Cal. limestone	Therm. balance	Daoudi and Walters.[64]
54-177	1000	-	12.4	0-10	$Ca(OH)_2$	Fixed-bed	Jozewicz et al.[65]
50-127	150-1000	0.05-3μm	10	0-11	$Ca(OH)_2$	Fixed-bed	Fonseca et al.[66]
150-400	630	<0.09mm	-	0-11	$Ca(OH)_2$	Fixed-bed	Karlsson et al.[67]
120	250-1000	92%<45μm	21.1	0-19	$Ca(OH)_2$	Fixed-bed	Chisholm and Rochelle[68]

4.2.1 Temperature Effect on HCl Absorption

The literature data indicates that temperature has a significant effect on HCl absorption by Ca-based sorbents. The study of Weinell et al. [53] on HCl absorption by limestone at temperatures between 60^oC and 1000^oC showed that HCl binding capacity is largest in the range 500-600^oC and decreases above 600^oC. They also reported a similar behaviour from $Ca(OH)_2$ except from an increase of HCl binding capacity below 150^oC in presence of moist gas phase. Petrini et al. [54] using limestone at temperatures between 350^oC and 600^oC, showed increase of $CaCO_3$ chlorination with temperature. Ketov et al. [55] reported an optimal HCl absorption temperature for limestone in the range 450-500^oC under comparable experimental conditions. Furthermore, the works of Daoudi and Walters [58, 64] and Duo et al.[59] on HCl absorption, using different Ca-based sorbents in the temperature range 300-600^oC, showed increase of the conversion levels with temperature. Therefore, the available studies clearly support that the HCl absorption by Ca-based sorbents increases with temperature in the range 300-600^oC. It should be kept in mind that these observations of the temperature effect correspond to much higher HCl concentrations than those present in the absorption zone of cement plants. It should also be considered that only two studies [53, 61] used limestone in the relevant temperature range 90-220^oC.

An interpretation of the HCl absorption enhancement with temperature and detected incomplete active compound conversion between 300^oC and 600^oC was given by Duo et al.[59] and Daoudi and Walters [58, 64]. They suggested that the HCl absorption dependence on temperature and incomplete active compound conversion can be related to changes in reaction kinetics and sintering phenomena. In particular, the temperature increase up to 600^oC results in increase of reaction constant and diffusion coefficient. However, the formation of a solid product with larger molar volume [69] leads to pore closure. Partanen et al. [63] presented a different approach to the enhancement of Ca-based sorbents chlorination at temperatures close to 650^oC. According to this, the gaseous H_2O release from $CaCO_3$ / CaO chlorination opens the solid reactant pores, and consequently enhances the HCl diffusion to the inner particle part.

The attenuation of Ca-based sorbents chlorination above a certain temperature around 600^oC, was reported by many researchers [53, 58, 59, 63, 64]. In particular, Weinell et al.[53] supported that, in the case of limestone, the diminishing HCl binding capacity above 500^oC is related to the chemical equilibrium between gas and solid (4.28, 4.29). Partanen et al.[63] connected the overall conversion decrease at 850^oC with formation of $CaCO_3$ - $CaCl_2$ liquid phase. Daoudi and Walters [58, 64] supported that the reduction of limestone conversion at 650^oC was related to the diffusion resistance increase by sintering phenomena. Duo et al.[59] also suggested that sintering at high temperatures [70] results in increase of diffusion resistance and reduction of particles porosity. Generally, the aforementioned diffusion resistance increasing mechanisms (pore blocking and sintering) and gas-solid phase chemical equilibrium are considered as the most common explanation for the Ca-based sorbents overall incomplete conversion [54, 56, 58, 59, 62, 64]. However, the view of Duo et al. [71] was that the observed incomplete conversion is insufficiently explained by the aforesaid causes.

4.2.2 Gas Phase Moisture Effect on HCl Absorption

The effect of gas phase moisture content on acidic gases absorption by Ca-based sorbents was investigated by many researchers [53, 56, 65, 66, 68, 72, 73]. The presented studies concluded that absorption of acidic gases is enhanced by the presence of moisture at temperatures less than 200^{o}C. In particular, Weinell et al. [53] reported enhancement of HCl absorption by $Ca(OH)_2$ in presence of H_2O in gas phase at temperatures less than 200^{o}C. Moreover, the water effect weakens with temperature and disappears above 200^{o}C. The beneficial effect of gas phase moisture content on HCl absorption by $Ca(OH)_2$ at temperatures between 54^{o}C and 177^{o}C was also found by many other research groups [53, 65, 66, 68]. The absence of gas phase moisture effect on HCl absorption by limestone in the temperature range 300-600^{o}C was confirmed by Mura and Lallai [56].

The mechanism which the gas phase moisture affects the HCl absorption by Ca-based sorbents is not completely understood. Weinell et al. [53] and Fonseca et al.[66] suggested that the moisture effect is based on the fracturing of sorbent crystal lattice by a saturated aqueous phase. Furthermore, Jozewicz et al.[65] reported that calcium silicate sorbents (mixture of flyash - $Ca(OH)_2$) have higher reactivity with acidic gases in presence of moist gas phase in comparison with reagent grade Ca-based sorbents due to the bonding of water molecules on silicates surface. Raw meal contains a significant amount of clay minerals, to which H_2O molecules and OH^- groups can be bonded up to 550^{o}C and 550-950^{o}C, respectively [2, 16, 74]. In Jozewicz's results it is likely that H_2O molecules and OH^- groups contribute to HCl absorption by calcium silicate sorbents at low temperatures.

Available literature data support that SO_2 absorption by limestone at low temperatures, e.g., 80^{o}C , is strongly related to the gas phase moisture content and sorbent moisture [72, 73, 75]. In particular, Klingspor et al.[75] suggested a mechanism for SO_2 absorption that comprises: (i) the physical absorption of H_2O and formation of monolayers of H_2O on sorbent surface, (ii) physical absorption of SO_2, and (iii) formation of SO_2 / carbonate complexes. Moreover, it was claimed that SO_2 is not absorbed if the the number of monolayers of water is less than one [75]. Therefore, a similar mechanism (4.31 - 4.33) for the HCl absorption by raw meal in presence of moist gas phase can be assumed at low temperatures.

$$HCl(g) \xrightarrow{H_2O(l)} H^+(aq) + Cl^-(aq) \tag{4.31}$$

$$2H^+(aq) + CaCO_3(s) \rightarrow CO_2(g) + H_2O(l) + Ca^+(aq) \tag{4.32}$$

$$Ca^{2+}(aq) + Cl^-(aq) \xrightarrow{heat} CaCl_2(s) + H_2O(g) \tag{4.33}$$

4.2.3 Sulphur Dioxide Effect on HCl Absorption

Chisholm and Rochelle [68] studied the simultaneous absorption of SO_2 (0-2000ppmv) and HCl (250-1000ppmv) by $Ca(OH)_2$ at 120^{o}C using relative humidity range 0-19% and SO_2/HCl feed ratios in the range 0.28-3. They showed that the HCl absorption is predominant. Furthermore, the final total sorbent conversion did not depend on the SO_2/HCl feed ratio. However, the increase in SO_2/HCl

feed ratio caused an increase in the solid product fraction of $CaSO_3 \cdot 1/2H_2O$ and a slight decrease in the fraction of $CaCl_2 \cdot 2H_2O$. Jozewicz et al.[65] reported that the absorption of HCl and SO_2 by $Ca(OH)_2$ was enhanced by the increase of gas phase relative humidity at low temperatures. Furthermore, the sorbent reactivity with HCl was unaffected by SO_2 in the case of a feed gas containing 1000ppmv HCl and 500ppmv SO_2.

SO_2 concentration in the preheater outlet flue gas, e.g., 600-700 mg/Nm^{3*}, is significantly higher than the concentration of HCl (25-65 mg/Nm^{3*})[51, 52]. The industrial evaluation of HCl scrubbing effect in particle filters showed that the outlet temperature decrease from 210^{o}C to 151^{o}C, using water injection and fresh air, resulted in an increase of HCl reduction from 50% to 63% [51]. However, the industrial measurements showed that flue gas SO_2 concentration was only slightly affected by the operating temperature [51]. In particular, an 8% reduction of the SO_2 concentration across particle filters unit was detected when the outlet temperature was reduced from 210^{o}C to 151^{o}C. Furthermore, SO_2 concentration was unaffected across the filter unit when the outlet filter temperature was 210^{o}C. Therefore, the mechanism of HCl absorption by preheater dust is not significantly affected by SO_2 in the temperature range 150-210^{o}C with moisture content in flue gas between 3.5% v/v and 6%v/v.

Therefore, the industrial and literature data indicate that SO_2 effect on HCl absorption by raw meal and preheater dust is probably insignificant at the operating conditions of post-preheater tower units. Furthermore, the HCl absorption by raw meal and preheater dust is anticipated to be more important than SO_2 absorption.

4.2.4 Carbon Dioxide and Oxygen Effects on HCl Absorption

CO_2 and O_2 are primary rotary kiln flue gas components. Mura and Lallai [56] reported that limestone reactivity with HCl was unaffected by the presence of 30%v/v CO_2 in gas phase at temperatures less than 500^{o}C. However, reactivity was reduced by CO_2 at temperatures above 500^{o}C. Partanen et al. [63] supported that in the case of calcined limestone the presence of CO_2 enhances chlorination at 650^{o}C due to the simultaneous re-carbonation; on the other hand, HCl absorption was unaffected by CO_2 at 850^{o}C. Theoretically, CO_2 directly affects the $CaCO_3$ speciation at high temperatures. In particular, it is well known that the presence of CO_2 suppresses the $CaCO_3$ calcination at temperatures above 700^{o}C (4.34) [76]. The $CaCO_3$ thermal decomposition occurs at a certain temperature when the CO_2 partial pressure is lower than the CO_2 equilibrium pressure at this temperature. Baker [77] gave an equation (4.35) for the calculation of CO_2 equilibrium pressure (atm) of CaO - CO_2 system as function of temperature (K).

$$CaCO_3(s) \xrightarrow{heat} CaO(s) + CO_2(g) \tag{4.34}$$

$$log_{10}P^e_{CO_2} = 7.079 - \frac{8308}{T} \tag{4.35}$$

Gullett et al.[61] reported that a change of gas phase O_2 content between 0% v/v and 5% v/v did not have any apparent effect on HCl absorption by CaO between 100^{o}C and 350^{o}C.

Although pertaining to higher HCl concentrations than those in the cement plant absorption zone, the aforementioned results point to no or only very small effects on HCl absorption at low temperatures (less than 350^{o}C).

*in dry flue gas at 10% v/v O_2

4.2.5 Particle Size and Surface Area Effects on HCl Absorption

Solid reactant particle size and specific surface area are important parameters for solid - gas reactions. Weinell et al. [53] and Matsukata et al.[57] pointed out that the effect of particle size on CaO and limestone final conversion and chlorination rates was limited. On the other hand, Petrini et al.[54], Daoudi and Walters [58], Wang et al.[60], Gullett et al.[61], Mura and Lallai [56], and Partanen et al.[63] found that small particle size and large specific surface area are beneficial for the HCl absorption. Therefore, the majority of the researchers support that large surface area and small particle size of Ca-based sorbents promote the HCl absorption.

4.2.6 Absorption Mechanism - Reaction Limiting Step

The unreacted grain core model and shrinking unreacted core model are mainly applied in the simulation of HCl absorption by Ca-based sorbents. In particular, Weinell et al.[53], Mura and Lallai [62] and Fonseca et al.[66] studied the HCl absorption mechanism using grain models in the temperature range 60-1000^{o}C. Mura and Lallai [56] proposed the grain model for porous particles, and the shrinking unreacted core model in the case of less porous particles. The shrinking core model is also suggested by Wang et al.[60] and Gullett et al.[61] in the temperature range 150-350^{o}C.

The previous studies report that the sorption rate is very fast initially and decreases with the particle conversion until the reaction rate becomes zero [53, 56, 60-62, 66]. Furthermore, they state that reaction rates are limited by reaction kinetics and HCl diffusion resistance in particles. Solid diffusion [56, 62, 66], pore diffusion [56, 60], and gaseous HCl diffusion through product layer [61] are suggested as potential reaction control resistances. A group of of researchers [53, 61, 62] consider that the reaction is mainly controlled by HCl diffusion in particles. However, Mura and Lallai [56, 62], Wang et al.[60], and Fonseca et al.[66] suggested a combination of chemical reaction and HCl diffusion in particles as control mechanisms depending on reaction stage. In particular, they support that the chemical reaction is the rate controlling step in the initial or early stages of the reaction. Furthermore, they report that the active compound final conversions vary between 0% and 98% depending on the experimental conditions and sorbent.

It is commonly accepted that the HCl absorption by Ca-based sorbents is characterized by first order reaction kinetics with respect to HCl concentration [53(60-1000^{o}C), 56(300-600^{o}C), 58-62(150-600^{o}C), 64(310-670^{o}C), 66-68(50-400^{o}C)]. Furthermore, the works of Gullett et al.[61] and Fonseca et al.[66] on CaO and $Ca(OH)_2$ respectively, found that the HCl absorption is described by first order reaction kinetics relative to HCl concentration.

4.2.7 Conclusions on HCl Absorption

The available information related to HCl absorption by Ca-based sorbents corresponds to experimental conditions and tested sorbents that significantly differ from relevant cement plant conditions (HCl concentration: $\leq$ 100ppmv, temperature: 90-220^{o}C, gas phase moisture: 5-19 %v/v sorbent: raw meal and preheater dust). Furthermore, the given HCl absorption mechanism interpretations cannot explain the industrially detected fast HCl absorption that is characterized by extremely low active compound conversions ($5{\cdot}10^{-3}$ - $4{\cdot}10^{-2}$%). Therefore, a direct utilization of the literature data in the prediction of the HCl emission from cement plants does not seem possible.

The previous studies support that the HCl absorption by Ca-based sorbents is characterized by two steps: a first very fast initial reaction step and a second where the reaction rate decreases down to zero with time. The first step may be controlled by the chemical reaction. The second step is controlled by the HCl diffusion in particles. Furthermore, the available data indicate that the reaction is characterized by first order reaction kinetics with respect to HCl concentration.

Literature references support that the temperature can significantly affect HCl absorption by Ca-based sorbents. In addition, enhancement of HCl absorption in presence of moisture in gas phase was reported for temperatures less than 200^{o}C. Independence of the HCl absorption on O_2 and CO_2 was reported at temperatures up to 350^{o}C.

4.3 Overall Conclusions on Literature Review

This section presents an overview of the literature study and highlights the most important information related to the aims of this project. The industrial measurements specified the HCl release and absorption zones in cement manufacturing process. The effective control of HCl emission from cement plants mainly requires the study of the mechanisms of HCl release from raw materials in low temperature cyclones (360-600^{o}C) of preheater tower and HCl absorption by raw meal and preheater dust in the post-preheater tower units (94-220^{o}C). This work gives emphasis to the investigation and modelling of the HCl absorption in post-preheater tower units.

Three potentially involved mechanisms in the HCl release from raw meal at temperatures between 360^{o}C and 600^{o}C were presented: (i) salts and salt hydrates thermal decomposition, (ii) organic matter reaction with inorganic chlorides, and (iii) inorganic chlorides, e.g., $CaCl_2$, reaction with flue gas compounds. The reported low reaction rates of inorganic chlorides with flue gas compounds at temperatures below 500^{o}C make difficult their contribution to the HCl release in preheater tower. The potential presence of more than one HCl release mechanism should also be considered.

The literature study on the HCl absorption by Ca-based sorbents specified a number of parameters that could affect the HCl absorption by raw meal and preheater dust. In particular, Ca-based sorbents demonstrated increase of HCl binding capacity with temperature in the range 360-600^{o}C. It is reported that the presence of moist gas phase enhances the acid gases (SO_2 and HCl) absorption by Ca-based sorbents at low temperatures (less than 200^{o}C); However, the gas phase moisture effect weakens with temperature and disappears above 200^{o}C. The mechanism of gas phase moisture effect is not completely understood. The formation an aqueous phase that breaks the sorbent crystal structure or a modification of the absorption mechanism via the physical absorption of acid gasses were suggested. The industrial and literature data supported that CO_2, O_2 and SO_2 cannot significantly affect the HCl absorption by Ca-based sorbents in the temperature range 94-220^{o}C. Previous studies reported that the specific surface area of sorbents could affect the HCl absorption and the large surface area is probably a HCl absorption promoting parameter. The literature data described the HCl absorption mechanism as a first order with respect to HCl and characterized by two steps: a first very fast initial reaction step and a second slow reaction step where the reaction rate decreases with time. The first step may be controlled by the chemical reaction. The second step is controlled by the HCl diffusion in solid phase.

The presented works on HCl absorption by Ca-based sorbents correspond to experimental conditions and tested sorbents that significantly differ from the industrial conditions and sorbents of interest. Therefore, the literature data cannot directly be utilized in the control and prediction of HCl emission from cement plants. On the other hand, the literature study suggested a number of parameters which could affect the HCl absorption by preheater dust and raw meal. It is concluded that the understanding and modelling of the HCl scrubbing phenomena in post-preheater tower units (gas conditioning tower, particle filters, and raw mill) require the experimental investigation of the mechanism of HCl absorption by preheater dust and raw meal in the temperature range 100-180^{o}C.

4.4 References

[1] Jøns, E.S., and Østergård, M.J.L., Investigation into Shell Corrosion of Rotary Cement Kilns, ZKG International, vol.52, pp.68-79, 1999.

[2] Bhatty, J., Kosmatka, F., and Miller, S., Innovations in Portland Cement Manufacturing, Portland Cement Association, 2004, ISBN:0-89312-234-3.

[3] Liu, W., Xu, J., Liu, J., Cao, H., Huang, X.F., and Li, G., Characteristics of Ammonia Emission During Thermal of Lime Sludge for Co-combustion in Cement Kilns, Environmental Technology, vol.36, pp.226-236, 2016.

[4] Cheney, J.L., and Knapp, K.T., A Study of Ammonia Source at Portland Cement Production Plant, JAPCA, vol.37, pp.1298-1302, 1987.

[5] Erdey, L., Gal, S., and Liptay, G., Thermoanalytical Properties of Analytical-Grade Reagents: Ammonium Salts, Talanta, vol.11, pp.913-940, 1964.

[6] Emons, H., Voigt, H., Pohl, T., and Naumann, R., Thermoanalytical Investigations on the Decomposition of Double Salts: Part II: The Decomposition of Double Salts $MeCl \cdot MgCl_2 \cdot 6H_2O$ (Me=NH_4, Rb, Cs), Thermochimica Acta, vol.121, pp.151-163, 1987.

[7] Olszak-Humienik, M., On the Thermal Stability of some Ammonium Salts, Thermochimica Acta, vol.378, pp.107-112, 2001.

[8] Carnallite, Handbook of Mineralogy, Mineralogical Society of America, 2018, [6 February 2018] http://www.handbookofmineralogy.org/pdfs/carnallite.pdf.

[9] Ashboren, D., Carnallite Decomposition into Magnesia, Hydrochloric Acid and Potassium Chloride: A Thermal Analysis Study; Formation of Pure Particles, Journal of Applied Chemistry and Biotechnology, vol.23, pp.77-86, 1973.

[10] Emons, E.E., Mechanism and Kinetics of Formation and Decomposition of Carnallitic Double Salts, Journal of Thermal Analysis, vol.33, pp.113-120, 1988.

[11] Turekian, K. and Hollad, H. (Editors in Chiefs), Treatise on Geochemistry, 2nd Edition, Elsevier Science, pp.503-505, 2014, ISBN: 9780080959757.

[12] Horst, E.F., and Barry, L.M., Magnesium Technology: Metallurgy, Design Data, Automotive Applications, Springer, pp.31, 2006, ISBN-10: 3-540-20599-9.

[13] Rammelberg, H.U., Schmidt, T., and Ruck, W., Hydration and Dehydration of Salts Hydrates and Hydroxides for Thermal Energy Storage Kinetics and Energy Release, Energy Procedia, vol.30, pp. 362-369, 2012.

[14] Eon, H.C., Park, H., and Yoon, H.S., Preparation of Anydrous Magnesium chloride from Ammonium Magnesium Chloride Hexahydrate, Advanced Power Technology, vol.21, pp.125-130, 2010.

[15] Huang, Q., Lu, G., Wang, J., and Yu, J., Thermal Decomposition Mechanisms of $MgCl_2 \cdot 6H_2O$ and $MgCl_2 \cdot H_2O$, Journal of Analytical and Applied Pyrolysis, vol.91, pp. 159-164, 2011.

[16] Grim, R.E., Clay Mineralogy, McGraw-Hill Book Company, 2nd Edition, 1968, ISBN-10: 0070248362.

[17] Folk, R.L., Detection of Organic Matter in Thin-Sections of Carbonate Rocks Using a White Card, Sendimentary Geology, vol.54, pp.193-200,1987.

[18] Mattiesen, J., Bovet, N., Hilner, E., Andersson, M.P., Schmidt, D.A., Webb, K.J., Dalby, K.N., Hessenkam, T., Crouch ,J., Collins, I.R., and Stipp, S.L.S, How Naturally Absorbed Material on Minerals Affects the Low Salinity Enhance Oil Recovery, Energy and Fuels, vol.28, pp.4849-4858, 2014.

[19] Rahim, M.U., Gao, X., Wu, H., Release of Chlorine from the Slow Pyrolysis of NaCl-Loaded Cellulose at Low Temperatures, Proceedings of the Combustion Institute, vol.35, pp.2891-2896, 2015.

[20] Bridgwater, A.V. (editor), Progress in Thermochemical Biomass Conversion, Wiley and Sons, pp. 1236-1245, 2008, ISBN: 9780632055333.

[21] Pedersen, A.J., Lith, S.C., Frandsen, F.J., Steinsen, S.D., and Holgersen, L.B., Release to the Gas Phase of Metals, S and Cl During Combustion of Dedicated Wast Fractions, Fuel Processing Technology, vol.91, pp.1062-1072, 2010.

[22] Sidhu, S., Kasti, N., Edwards, P., and Dellinger, B.,Hazardous Air Pollutants Formation from Reactions of Raw Meal Organics in Cement Kilns, Chemosphere, vol.42, pp.499-506, 2001.

[23] Karstensen, K.H., Formation Release and Control of Dioxins in Cement Kilns, Chemophere, vol.70, pp. 543-560, 2008.

[24] Sindu, S. and Dellinger, B., Proceeding of the International Speciality Conference on Waste Combustion in Boilers and Industrial Furnaces, A & WMA, pp.119, 1995.

[25] Saiz-Jimenez, C., Analytic Pyrolysis of Humic Substances: Pitfalls, Limitations and Possible Solutions, Environmental Science and Technology, vol.28, pp.1773-1780, 1994.

[26] Wu, X., Jiang, X.Z., and Zhang, L., Catalytic Decomposition of Methylene Chloride by Sulfate Titania Catalysts, Journal of Wuhan University of Technology, vol.17, pp.39-42, 2002.

[27] Dockner, T., Sauderwald, M., Krug, H., and Irgang, M., Reductive Dehalogenation of Organic Halogen Compounds, U.S. Patent number: 4.943.671, 1990.

[28] Kjerzy, H., Tadeusz, M., Derewinski, M., Janik, R., Krysciak, J., Sadowska, and H., Janas, J., Catalytic Oxidation of CH_2Cl_2 on Sodium Doped Al_2O_3, Catalysis Today, vol.54, pp.47-55, 1999.

[29] Shigapov, A.N., Novozhilova, M.A., Vexeshchagin, S.N., Anshits, A.G., and Sikolovskii, V.D., Peculiarities in Oxidative Conversion of Methane to C2-Hydrocarbons over CaO-$CaCl_2$ Catalyst, Reaction Kinetics and Catalysis Letters, vol.37, pp.397-402, 1988.

[30] Matsuda, H., Ozawa, S., Naruse, K., Ito, K., Kojima,Y., and Yanase, T., Kinetics of HCl Emission from Inorganic Chlorides in Simulated Municipal Wastes Incineration Conditions, Chemical Engineering Science, vol.60, pp.545-552, 2005.

[31] Fielder, W.L., Strearns, C.A., and Kohl, F.J., Reactions of NaCl with Gaseous SO_3, SO_2 and O_2, NASA Technical Memorandum 83423, 1983.

[32] Henriksson, M. and Warnqvist, B., Kinetics of Formation of HCl by Reaction NaCl and SO_2, O_2, H_2O, Industrial & Engineering Chemistry Process Design and Development, vol.18, pp.249-254, 1979.

[33] Uchida, A., Kamo, H., Kubota, H., and Kanaya, K., Reaction Kinetics of Formation of HCl in Municipal Refuse Incinerators, Industrial & Engineering Chemistry Process Design and Development, vol.22, pp.144-149, 1983.

[34] Fraissler, G., Jller, M., Brunner, T., and Obernberger, I., Influence of Dry and Humid Gaseous Atmosphere on the Thermal Decomposition of Calcium Chloride and its Impact on the Remove of Heavy Metals by Chlorination, Chemical Engineering and Processing, vol.48, pp.380-388, 2009.

[35] Garrett, D.E., Handbook of Lithium and Natural Calcium Chloride: Their Deposits, Processing, Uses and Properties, Elsevier, 2004, ISBN: 978-0-12-276152-2.

[36] Iisa, K. and Lu, Y., Sulfation of Potassium Chloride at Combustion Conditions, Energy and Fuels, vol.13, pp.1184-1190, 1999.

[37] Harkov, R. and Ross, J., Hydrogen Chloride (HCl) Emissions from Maryland Utility Boilers, Technical report, Maryland Department of Natural Resources, 1999. [28 May 2018] https://www.yumpu.com/en/document/view/18875366/hydrogen-chloride-hcl-emissions-from-maryland-versar-esm

[38] Akers, D. and Dospoy, R., Role of Coal Cleaning in Control of Air Toxics, Fuel Processing Technology, vol.39, pp.73-86, 1994.

[39] Chow, W., Miller, M.J. and Torrens, I.M., Pathways of Trace Elements in Power Plants: Interim Research Results and Implications, Fuel Processing Technology, vol.39, pp.5-20, 1994.

[40] Guo, S., Yang, H. and Liu, Z., The Fate of Fluorine and Chlorine During Thermal Treatment of Coals, Environmental Science and Technology, vol.40, pp.7886-7889, 2006.

[41] Shao, D., Hutchinson, E.J., Cao, H. and Pan, W.P., Behavior of Chlorine During Coal Pyrolysis, Energy & Fuels. vol.8, pp.399-401, 1994.

[42] Herod, A.A., Hodges, N.J., Pritchard, E. and Smith, C. A., Mass Spectrometic Study of the Release of HCl and Other Volatiles from Coals During Mild Heat Treatment, Fuel, vol.62, pp.1331-1336, 1983.

[43] Ma, W., Hoffmann, G., Schirmer, M., Chen, G. and Rotterk, V.S., Chlorine Characterization and Thermal Behavior in MSW and RDF, Journal of Hazardous Materials, vol.178, pp.489-498, 2010.

[44] Friedrich, H.E. and Mordike, B.L., Magnesium Technology, Metallurgy, Design Data, Applications, Springer, 2004, ISBN-10:3-540-20599-3.

[45] Jarvinen, L., Leiro, J., Bjondal, F., Carletti, C., Lundin, T., Gunnelius, K., Smatt, J.H., and Eklund, O., Characterization of Dolomites Before and After Reactivity Measurements with HCl Solution, Surface and Interphase Analysis, vol.47, pp.284-294, 2015.

[46] Zhang, R., Hu, S., Zaung, X. and Yu, W., Dissolution Kinetics of Dolomite in Water at Elevated Temperatures, Aquatic Chemistry, vol.13, pp.309-338, 2007.

[47] Busenbeng, E. and Plummer, L.N., The Kinetics Dissolution of Dolomite in CO_2-H_2O system at 1.5 degrees ^oC to 65 degrees ^oC and 0-atm to 1atm P_{CO_2}, American Journal of Science, vol.282, pp.45-78, 1982.

[48] Hosten, C. and Gulsun, M., Reactivity of Limestone from Different Sources in Turkey, Mineral Engineering, vol.17, pp.97-99, 2004.

[49] Siagi, Z.O., and Mbarawa, M., Dissolution Rate of South African Calcium-Based Materials at Constant pH, Journal of Hazardous Materials, vol.163, pp.678-682, 2009.

[50] Stumpf, T., Roeder, A., and Hennicke, H.W., The Reaction Behavior of Carbonate Stone Dust in Acid Solutions, more Particularly of Sulphurous Acid. Part II: Important Influence Parameters and Measurement on Various Carbonate Stone Dusts for Flue Gas Desulphurization, ZKG, vol.37, pp.454-461, 1984

[51] Emission Measurements of Cement Plant A,Internal report FLSmidth A/S, Copenhagen, 2012.

[52] Emission Measurements of Cement Plant B, Internal report FLSmidth A/S, Copenhagen, 2013.

[53] Weinell, C.E., Jensen, P.I., Dam-Johansen, K., and Livbjerg, H., Hydrogen-Chloride Reaction with Lime and Limestone-Kinetics and Sorption Capacity, Industrial & Engineering Chemistry Research, vol.31, pp.164-171, 1992.

[54] Petrini, S., Eklund, H., and Bjerle,I., HCl-Absorption Durch Kalkstein, Aufbereit Tech, vol.20, pp.309-315, 1979.

[55] Ketov, A.N., Kostin, L.P., and Terent'eva, E.I., O Vzaimodeistii Razlichnykh Vidov Karbonata Kal'taiya s Khloristym Vodorodom Prinagrevanii, Izv, Vyssh. Uchebn. Zaved, Khim. Khim. Tekhnol., vol.11. pp.680-683, 1968.

[56] Mura, G. and Lallai, A., Reaction Kinetics of Gas Hydrogen Chloride and Limestone, Chemical Engineering Science, vol.49, pp.4491-4500, 1994.

[57] Matsukata, M., Takeda, K., Miyatani, T., and Ueyama, K., Simultaneous Chlorination and Sulphation of Calcined Limestone, Chemical Engineering Science, vol.51, pp.2529-2535, 1996.

[58] Daoudi, M., and Walters, J.K., The Reaction of HCl Gas with Calcined Commercial Limestone Particles: the Effect of Particles Size, Chemical Engineering Journal, vol.47, pp.11-16, 1991.

[59] Duo, W,, Kirby, N.F., Seville, J.P.K., Kiel, H.A., Bos, A., and Den, U.H., Kinetics of HCl Reactions with Calcium and Sodium Sorbents for IGCC Fuel Gas Cleaning, Chemical Engineering Science, vol.51, pp.2541-2546, 1996.

[60] Wang, W., Ye, Z., and Bjerle, I., The Kinetics of the Reaction of Hydrogen Chloride with Fresh and Spent Ca-Based Desulfurization Sorbents, Fuel, vol.75, pp.207-212, 1996.

[61] Gullett, B.K., Jozewicz, W., and Stefanski, L.A., Reaction Kinetics of Ca-Based Sorbents with HCl, Industrial & Engineering Chemistry Research, vol.31, pp.2437-2446, 1992.

[62] Mura, G. and Lallai, A., On the Kinetics of Dry Reaction between Calcium Oxide and gas Hydrochloric Acid, Chemical Engineering Science, vol.47, pp.2407-2411, 1992.

[63] Partanen, J., Backman, P., Backman, R., and Hupa, M., Absorption of HCl by Limestone in Hot Flue Gases. Part I: the Effects of Temperature, Gas Atmosphere and Absorbent Quality, Fuel, vol.84, pp.1664-1673, 2005.

[64] Daoudi, M. and Walters, J.K., A Thermogravimetric Study of the Reaction of Hydrogen Chloride Gas with Calcined Limestone Determination of Kinetic Parameters, Chemical Engineering Journal, vol.47, pp.1-9, 1991.

[65] Jozewicz, W., Chang, J.C.S., and Sedman, C.B., Bench-Scale Evaluation of Calcium Sorbents for Acid Gas Emission Control, Environmental Progress, vol.9, pp.137-142, 1990.

[66] Fonseca, A.M., Órfaõ, J.J., and Salcedo, R.L., Kinetic Modeling of the Reaction of HCl and Solid Lime at Low Temperatures, Industrial & Engineering Chemistry Research, vol.37, pp.4570-4576, 1998.

[67] Karlsson, H.T., Klingspor, J., and Bjerle, I., Absorption of Hydrochloric Acid on Solid Slaked Lime for Flue Gas Clean Up, Air Pollution Control Association, vol.31, pp.1177-1180, 1981.

[68] Chisholm, P.N., and Rochelle, G.T., Dry absorption of HCl and SO_2 with Hydrate Lime from Humidified Flue Gas, Industrial Engineering & Chemistry Reasearch, vol.38, pp.4068-4080, 1999.

[69] Perry, R.H. and Green, D.W., Perry's Chemical Engineer's Handbook, 8th Edition, McGraw-Hill, pp.2-11, 2007, ISBN: 978-0-07-142294-9.

[70] Borgwardt, R.H., Calcium Oxide Sintering in Atmospheres Containing Water and Carbon Dioxide, Industrial Engineering & Chemistry Research, vol.28, pp.493-500, 1989.

[71] Duo, W., Sevill, J.P.K., Kirkby, N.F., and Clift,R., Formation of Product Layers in Solid-Gas Reactions for Removal of Acid Gases, Chemical Engineering Science, vol.49, pp.4429-4442, 1994.

[72] Klingspor, J., Karlsson, H.T., and Bjele, I., A Kinetic Study of the Dry SO_2 - Limestone Reaction at Low Temperature, Chemical Engineering Communication, vol.22, pp.81-103, 1983.

[73] Hansen, P.J., SO_2 Emissions from Cement Plant Production, Ph.D. Dissertation, Technical University of Denmark, 2003, ISBN:87-90142-96-9.

[74] Grim, R.E. and Brandley, W.F., Rehydration and Dehydration of the Clay Minerals, American Mineralogist, vol.33, pp.50-59, 1948.

[75] Klingspor, J., Stromberg, A.M., Karlson, H.T., and Bjerlr, I., Similarities Between Lime in Wet-Dry Scrubbing, Chemical Engineering and Processing, vol.18, pp.239-247, 1983.

[76] Kumar, G.S., Ramakrishman,A., and Hung,Y.T., Advanced Physico-Chemical Treatment Technologies - Handbook of Environmental Engineering, Humana Press, vol.5, pp.611-633, 2007, eISBN: 1-59745-173-8.

[77] Baker, E.H., The Calcium Oxide-Carbon Dioxide System in the Pressure Range 1-300 Atmospheres, Journal of Chemical Society, pp.464-470, 1962.

Chapter 5

Used Set-ups, Experimental Methods and Materials in HCl Absorption Study

This chapter presents the used experimental set-ups, methodologies, and materials in the study of HCl absorption by cement raw meals at low temperatures. This work comprises two experimental approaches: (i) isothermal tests using a fixed-bed reactor with gas flow through the tested sample and analysis of the gas phase using Fourier Transform Infrared Spectroscopy (FTIR), and (ii) temperature ramping tests with in-situ HCl generation and effluent analysis using FTIR. The first method (fixed-bed) was used for the investigation of the mechanism of HCl absorption by raw meals at low temperatures, study of the parameters potentially affecting HCl absorption, and quantification of the HCl absorption capacity of industrial raw meals. The second method (in-situ HCl generation) was used for the study of the effects of raw meal compounds on HCl absorption using a thermally degradable solid source of HCl. Furthermore, the potential use of this method for the fast screening of HCl absorption by different raw meals was evaluated.

5.1 Experimental Activities - Isothermal Tests

This section presents the experimental set-up used in isothermal tests. The purposes of these experimental activities were to determine the basic principles of the HCl absorption mechanism, and to quantify the effects of temperature (100-180^oC), gas phase composition (HCl concentration, moisture content, and presence of CO_2 and O_2), and raw meal moisture content on HCl absorption. The main advantage of this method was the approximation of cement plant conditions, e.g., raw mill, particle filters, in terms of flue gas composition and temperature.

5.1.1 Fixed-bed Set-up

Figure 5.1 illustrates an overall view of the set-up. The main components are: (i) the gas supply system, (ii) the steam supply system, (iii) the fixed–bed reactor, (iv) HCl–FTIR analyzer, and (v) the data recording – control system.

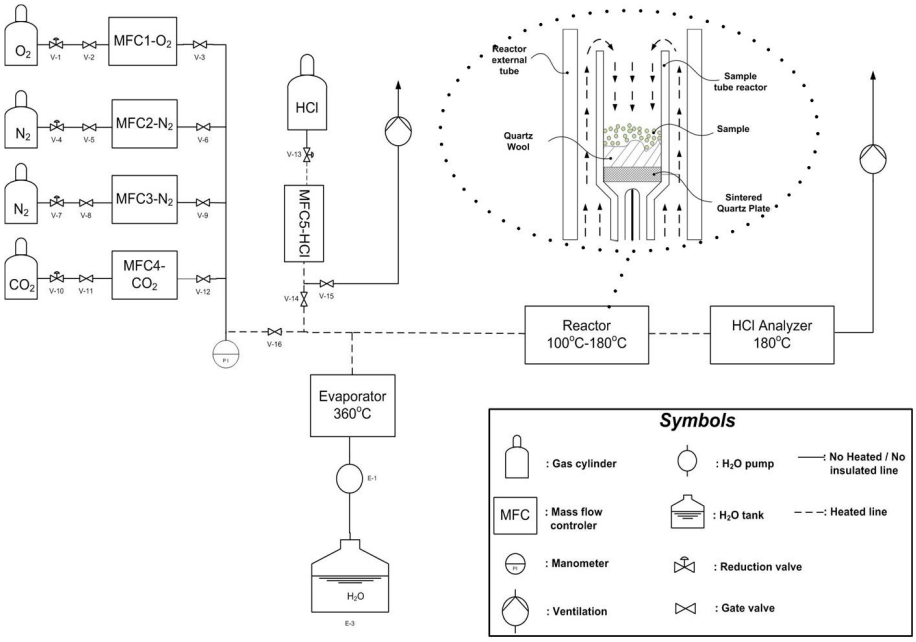

Figure 5.1: Fixed-bed experimental set-up apparatus.*

Gas Supply System

The feed gas stream (except steam) is prepared by mixing of certified O_2/N_2, CO_2/N_2 and HCl/N_2 mixtures supplied by AGA A/S. Each gas supply line comprises: (i) a reduction valve for the pressure reduction to 2 bars which is the minimum operating pressure of Mass Flow Controllers (MFCs), (ii) a MFC (EL-Flow Bronkhost A/S) for the control of dry gas flow, and (iii) two shut-off valves (one before and one after each MFC).

MFCs operate using D.C. signal (0 to 10 V) and are automatically controlled using lab view software (PC). The used MFCs nominal flow ranges at normal conditions 1bar-0^{o}C are: 0-500 Nml/min (MFC-1), 0-1000 Nml/min (MFC-2), 0-1000 Nml/min (MFC-3), 0-1000 Nml/min (MFC-4), and 0-250Nml/min (MFC-5). The nominal MFCs reliability is $\pm$ 2%.

The mixing of dry O_2, N_2 and CO_2 gases occurs in a mixing tube at 25^{o}C. The O_2 / N_2 / CO_2 mixture is heated to 140^{o}C, and then it is mixed with the heated dry HCl/N_2 stream and steam. All the gas supply lines (except of O_2 / N_2 / CO_2 mixing line) are insulated and heated to 140^{o}C to prevent any condensation of H_2O and HCl. The temperature of supply

*This figure is intended to be published in a scientific article with the title: "Experimental evaluation of hydrogen chloride (HCl) absorption by cement raw meal at low temperatures, using fixed-bed tests", written by Pachitsas, S., Wedel, S., Skaarup Jensen, L., Boll Illerup, J, and Dam-Johansen, K..

lines is regulated using heating tapes which are automatically controlled by lab view software (PC).

Steam Supply System

The steam supply system comprises a water evaporator, a high accuracy peristaltic pump (Messgaspumpe N5 Kp18, MC TechGroup A/S), and a water tank. The feed water rate of evaporator is regulated by the control box of peristaltic pump.

The evaporator internal structure comprises a helicoid evaporation tube attached on a cylindrical heating element with operating temperature 360^oC and two thermocouples for the temperature control of the heating element. The evaporator operating temperature is regulated by the control box of evaporator.

The steam supply line is an extension of the evaporation tube. It is insulated and heated to 140^oC to prevent any H_2O condensation. The temperature of steam supply line is regulated using a heating tape which is automatically controlled by lab view software (PC).

Heterogeneous Fixed-bed Quartz Reactor

The fixed-bed experiments were conducted using a fixed-bed reactor made up of quartz with maximum operating overpressure and temperature up to 0.25bar and 1000^oC, respectively. Figure 5.2 illustrates the compartments of fixed-bed reactor. The fixed-bed reactor is based on a standard design used by CHEC group [1-4] and comprises:

- Reactor external tube (Figure 5.2 - B): The reactor external tube is the only non-removable reactor part during the experimental activities. It is placed in a cylindrical electric furnace. The reactor sample tube and reactor bottom are inserted in the reactor external tube. The external reactor quartz - quartz connections are sealed using silica grease and metal clips.

- Sample tube reactor (Figure 5.2 - C): The sample tube is filled with a glass wool layer with the tested sample on the top of it, to prevent porous plate contamination and blocking by sample particles. The gas flow moves from the sample tube top towards the bottom through the sample 'cake layer' and leaves through the reactor bottom. A simplified illustration of flow patterns in the sample tube reactor is presented in Figure 5.1.

- Reactor bottom (Figure 5.2 - D): The reactor bottom part is removable and forms the inlet / outlet gas flow channels. The inlet gas flow moves towards the reactor top through the annular space between the reactor external tube and reactor bottom tube (see Figure 5.2 - A). The outlet flow of sample tube reactor (Figure 5.2 - C) passes through the reactor bottom tube and leaves the fixed-bed reactor.

The electric furnace consists of three heating elements (top, middle and bottom) that give a homogeneous temperature profile along the reactor. The electric furnace temperature is controlled by the control box of furnace.

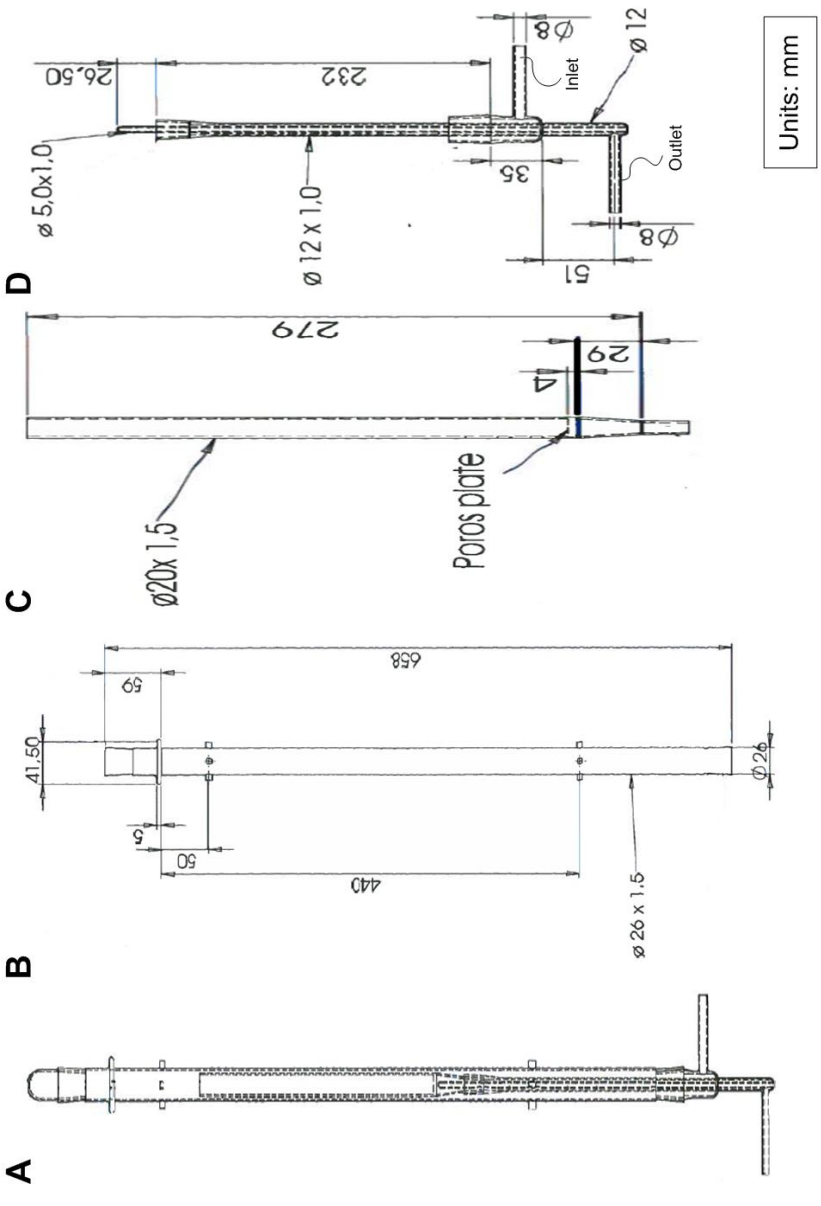

Figure 5.2: Fixed-bed reactor compartments [1]: A) Heterogeneous quartz glass reactor, B) Reactor external tube, C) Sample tube reactor, and D) Reactor bottom.

HCl FTIR Analyzer

The HCl concentration in gas stream is continuously monitored, using an HCl-FTIR analyzer (Servomex - Servotough 2510 series), which gives the HCl concentration in ppmv at normal conditions: 0^oC and $1.01325 \cdot 10^5$ Pa. The data recording frequency is 1Hz. The technical specifications of HCl-FTIR analyzer (Servomex - Servotough 2510 series) are presented in Table 5.1.

Table 5.1: Technical specifications of HCl-FTIR analyzer (Servomex - Servotough 2510 series) [5].

Measuring range - HCl	0-1000 ppmv
Suggested gas stream components	
-N_2	0-80% v/v
-CO_2	0-50% v/v
-O_2	0-20% v/v
-H_2O	0-15% v/v
-SO_2	0-4000 ppmv
Sample temperature	140 ^oC
Cell temperature	180^oC
Cell length	512mm
Cell volume	265.4 cm^3
Sample gas flow	0.2-5 l/min
Measurement uncertainty	$\pm$ 2 ppmv

Data Recording - Control System

The automatically controlled experimental apparatus are: (i) electric furnace, (ii) heating tapes, (iii) MFCs, and (iv) water pump. The shut-off valves are manually controlled. The reactor pressure is not controlled; However, a digital manometer is used for the measurement of reactor overpressure.

The Labview software is used for the data recording and monitoring, and control of the heating tapes and MFCs. The acquired data are saved in excel files. Furthermore, the user can select the recording parameters.

The electric furnace and water pump are controlled by separate control boxes. The operating parameters of these devices are not recorded.

5.1.2 Experimental Procedure of Fixed-bed Tests

The results reliability was ensured by following a standardised experimental protocol. Many tests were conducted for the evaluation of gas flow effect on set-up performance. The experimental protocol can be described by the following steps:

- Calibration of MFCs and HCl-FTIR analyzer:

  The calibration of MFCs and HCl analyzer was carried out in a regular basis before the experiments commencement to ensure the repeatability of gas phase flow and composition. MFCs were calibrated, using a bubble flow meter. The HCl-FTIR analyzer was calibrated, using a HCl/N_2 mixture with known nominal HCl concentration (span calibration) and N_2 (zero level calibration).

- System Saturation (without sample):

  The experimental set-up was saturated with HCl before every group of experiments, when the reactor reached the defined temperature. It had been observed that HCl measurements, using unsaturated set-up demonstrated significant deviations. This could be related to the physical absorption of HCl in quartz reactor, HCl analyzer filter, and gas supply lines.

- Flushing with N_2 (without sample):

  The set-up was flushed with N_2 in order to remove HCl gas from the reactor-gas supply lines and for the reactor bottom removal to be safe. This stage had short duration ($\sim$5min) in order to prevent system desaturation. In the end of this step the gas flow was set to zero.

- Sample placement:

  The bottom of fixed-bed reactor was removed for the sample placement. A layer of glass wool was inserted between the sample and sintered quartz plate to prevent its contamination or blocking by sample particles. The wool layer compaction should be minimized in order to decrease the extra flow resistance. Then, the bed-reactor with sample, either pure or mixed with diluent particles, was sealed and experiment started, using the selected gas phase composition and flow.

5.1.3 Materials and Experimental Conditions of Fixed-bed Tests

This section presents the used gas phase compositions, experimental conditions, and materials characterization. Emphasis was given to the study of the mechanism of HCl absorption by two industrial raw meals (raw meal A (RM-A) and raw meal B (RM-B)) at temperatures between 100^oC and 180^oC. Furthermore, the effect of gas phase moisture content on HCl absorption by raw meal was investigated. O_2 and CO_2 effects were also studied. Fused silica particles with sizes between $50\mu m$ and $100\mu m$ were used as inert diluent in order to break up raw meal agglomerates and eliminate flow channelling phenomena. An overview of the used materials and experimental conditions in fixed-bed tests is shown in Table 5.2.

Table 5.2: Overview of the used experimental conditions and materials in fixed-bed tests.

Sample material	raw meal A (RM-A), raw meal B (RM-B) and fused silica
Temperature (^{o}C)	100, 150, or 180
Pressure (Pa)	$1.01325 \cdot 10^5$
Gas phase composition	
HCl(ppmv)	52, 100 or 200
CO_2 (% v/v)	0 or 30
O_2 (% v/v)	0 or 3
H_2O (% v/v)	0 or 5
N_2	Balance
Sample mass (g)	0.3 to 16
Sample layer height (m)	$3 \cdot 10^{-3}$ to $6.7 \cdot 10^{-2}$
Gas phase flow (Nl/min)	1.5

Gas Phase Characterization

Table 5.3 shows the feed stream compositions in the fixed-bed experiments. In particular, composition 1-3 were used in the study of HCl concentration effect on the mechanism of HCl absorption by raw meal in the case of dry gas phase. Composition 2 and composition 4 were used in the evaluation of gas phase moisture content and temperature effects (comparison of the test results from composition 2 and composition 4). The investigation of O_2 and CO_2 effects was based on tests using composition 2 and composition 5.

Table 5.3: Tested feed gas compositions in fixed-bed tests.

	HCl (ppmv)	CO_2 (% v/v)	O_2 (% v/v)	H_2O (% v/v)	N_2
Composition 1	50	-	-	-	Balance
Composition 2	100	-	-	-	Balance
Composition 3	200	-	-	-	Balance
Composition 4	100	-	-	5	Balance
Composition 5	100	30	3	-	Balance

Sample Characterization

The experimental activities were conducted using two industrial raw meals (RM-A and RM-B) supplied by FLSmidth A/S, and fused silica (min SiO_2: 99.9%) supplied by Quarte Inc. as inert diluent. The used weight ratios of fused silica to raw meal varied between 0 and 49.

Table 5.4 presents the compositional analysis of raw meals. The comparison of raw meals composition shows that they have similar CaO content. RM-B has higher content of chlorine, organic matter and MgO than RM-A. RM-A has higher content of Al_2O_3 and Fe_2O_3. The term LOI (Loss on Ignition) comprises the weight losses by $CaCO_3$ and $MgCO_3$ calcination, raw meal dehydration, organic matter desorption, and pyrite oxidation at 975^oC in air atmosphere.

Table 5.4: RM-A and RM-B compositional analyses [6].

Component	RM-A (% w/w)	RM-B (% w/w)
SiO_2	14.55	13.22
Al_2O_3	3.12	2.72
Fe_2O_3	2.22	1.59
CaO	43.07	43.25
MgO	0.87	1.66
K_2O	0.6	0.66
Na_2O	0.31	0.06
TiO_2	0.16	0.14
LOI-975^oC	34.54	35.77
Cl	0.015	0.019
Org.C	0.13	0.21

The raw meal particle size distribution analysis was based on Laser Scattering (L.S.) measurements, using Malvern Mastersizer 3000. Furthermore, the specific surface areas were determined using L.S. and BET measurements. The raw meal particle agglomeration resulted in many difficulties in the application of L.S. method. The use of a wet(ethanol) L.S. method probably did not break up the raw meal agglomerates.

Table 5.5 and Figure 5.3 - A show the measured particle size distributions of RM-A and RM-B using L.S. method. It is clearly seen that raw meal particle size distributions are between $1.5\mu m$ and $100\mu m$ with a mass-median-diameter ($D_{50\%L.S.}$) close to 13 μm. However, SEM analysis of RM-A in Figure 5.3 - B shows that a significant fraction of raw meal particles has smaller diameter than $10\mu m$. Furthermore, the two raw meals have almost the same specific surface area based on L.S. method. L.S. method assumes that the particles are spheres; its results are affected by raw meal agglomerates. Hence, it can significantly underestimate the specific surface area. On the other hand, RM-B has 26% larger BET area than RM-A.

Table 5.5: Particle size distributions and specific surface areas of the tested raw meals.

	$D_{10\%L.S.}(\mu m)$	$D_{50\%L.S.}(\mu m)$	$D_{90\%L.S.}(\mu m)$	L.S. (m^2/g)	BET(m^2/g)
RM-A	1.39	12.9	90.3	1.45	7.67
RM-B	1.41	13.5	96.8	1.4	9.67

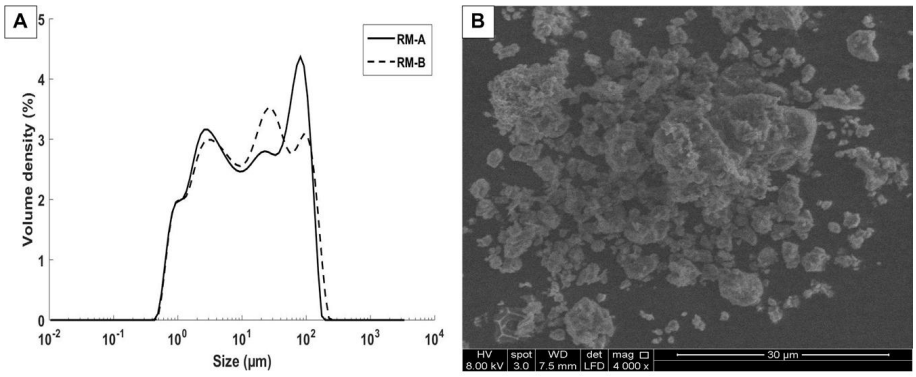

Figure 5.3: A) Particle size distributions of RM-A and RM-B; B) SEM picture of pure RM-A.*

5.2 Experimental Activities - Ramping Temperature Tests & In-situ HCl Release

TGA-FTIR set-up Perseus STA 449 F1 allows the study of HCl absorption based on thermogravimetry and IR spectrometry. The purposes of these experiments were: (i) the evaluation of HCl absorption capacity of industrial raw meals, reagent grade $CaCO_3$ and simulated raw meals, and (ii) the detection of the raw meal compounds that affect HCl absorption, using ramping temperature conditions (15^oC/min) and a solid, thermally degradable HCl source ($AlCl_3 \cdot 6H_2O$) in N_2 environment. These activities did not simulate the industrial conditions due to the use of a solid HCl source with a standard thermal decomposition temperature window (100-350^{o}C) and phase transition at 100^oC (melting point). However, the obtained results may be utilized for the fast screening of raw meal HCl absorption capacity and raw meal components effect at temperatures between 100^oC and 350^oC.

5.2.1 TGA-FTIR Set-up

The equipment is shown in Figure 5.4. The main parts of device are: (i) the thermogravimetric analysis system (furnace, balance, etc.), (ii) the vacuum pump, (iii) FTIR analyzer (Alpha) from Bruker, and (iv) the cooling system of balance. The set-up can detect the changes in carrier gas composition (IR spectrometry), and testing sample mass at dynamic and static temperature conditions. The sample heating releases gases, which are carried by the carrier gas flow from the furnace chamber to FTIR analyzer, and the sample mass change is simultaneously measured by the mass balance (see Figure 5.4 - B). The user can set the experimental temperature program (dynamic

*Figure 5.3 - B is intended to be published in a scientific article with the title: "Experimental evaluation of hydrogen chloride (HCl) absorption by cement raw meal at low temperatures, using fixed-bed tests", written by Pachitsas, S., Wedel, S., Skaarup Jensen, L., Boll Illerup, J, and Dam-Johansen, K..

and/or static) and carrier gas parameters (composition and flow).

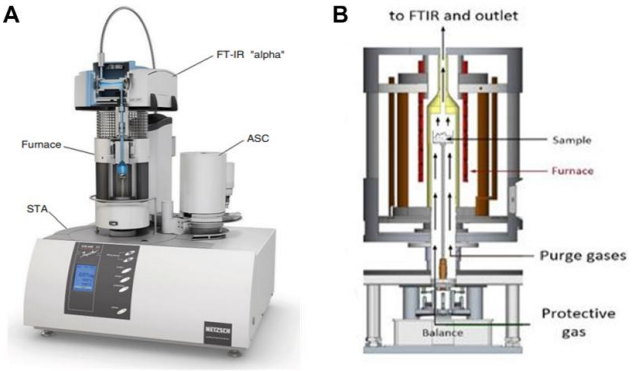

Figure 5.4: A) NETZSCH Perseus STA 449 F1 [7]; B) A cross sectional view of the thermogravimetric analyzer [8].

The technical characteristics of FTIR anlyzer (Alpha) are shown in Table 5.6. The FTIR cell has nominal operating temperature 200^{o}C, optical path length 7cm, and total cell volume 5.8cm^3. The measuring spectral range and selected resolution were 6000-500cm^{-1} and 4cm^{-1}, respectively. The connection tube of sample chamber and FTIR was heated to 250^{o}C to prevent the condensation of gas compounds and potential temperature deviation in FTIR cell.

Table 5.6: FTIR-Analyzer (Alpha) technical characteristics [9].

Parameter	Value
Selected resolution	4cm^{-1}
Optical path length	7cm
Cell volume	5.8 cm^3
Spectral range	6000-500 cm^{-1}
Cell temperature	200 ^{o}C

5.2.2 Experimental Procedure of TGA-FTIR Test

The experimental activities were carried out at dynamic temperature conditions, using a standard experimental protocol and N_2 as carrier gas. This set-up is characterized by accurate control of the carrier gas flow and composition. However, the presence of HCl absorption spots in the internal gas supply system (steel tubes at environmental temperature) did not allow the conduction of experiments using a HCl gas supply from gas cylinder. Therefore, a solid, thermally degradable HCl

source was used in the study of HCl absorption by raw meals and raw meal compounds.

An experimental protocol was defined in order to ensure the reliability of results. This comprises a series of activities for the reference and actual measurements:

- Reference measurements: The experimental set-up requires the conduction of reference measurements without sample at the selected experimental conditions (temperature program, carrier gas flow and empty crucible mass) for evaluation of system response. Therefore, reference measurements were conducted after the experimental program determination. High accuracy reference measurements required removal of the trapped air from the sample chamber before each measurement. The sample chamber was sealed and a vacuum pump was used for the removal of the trapped air in sample chamber. Then, the sample chamber was filled with N_2 and system internal pressure became equal to the atmospheric.

- Experimental measurements: The experiments conduction requires the presence of reference measurements, which correspond to the same experimental conditions (temperature program, carrier gas flow and crucible mass). The device software extracts the reference measurement data from the experimental records, and gives the actual weight balance and FTIR measurements. Therefore, after the reference measurements the sample was placed in the crucible, the trapped air was removed from the sample chamber using the vacuum pump, and test program execution started.

5.2.3 Materials and Experimental Conditions of TGA-FTIR Tests

The TGA-FTIR tests were conducted using ramping temperature conditions with constant heating rate 15^oC/min in the temperature range 25-900^oC. HCl was provided by the thermal decomposition at temperatures between 90^oC end 350^oC (5.1) [10, 11] of $AlCl_3 \cdot 6H_2O$ supplied by Fluka Analytical. It is noteworthy that in these experiments, the low melting point of $AlCl_3 \cdot 6H_2O$ (100^oC [12]) can affect the HCl absorption. In particular, any formed liquid phase wets the raw meal particles and increases the contact interface of reactants. This can result in HCl absorption enhancement.

$$AlCl_3 \cdot 6H_2O(s) \xrightarrow{heat} 1/2 \cdot Al_2O_3(s) + 3 \cdot HCl(g) + 4.5 \cdot H_2O(g) \tag{5.1}$$

Table 5.7 shows the experimental conditions. The fast screening of the HCl absorption capacity of industrial raw meals was conducted using 512 mg of the tested sample and 62mg of HCl source. The study of raw meal compounds effect on HCl absorption was conducted using 1450mg of the tested material and 100mg of HCl source. The mass increase of the tested material and HCl source made more discernible the differences in HCl absorption capacity of the tested materials.

Table 5.7: Experimental conditions of TGA-FTIR tests.

Parameter	Value
Temperature range (^{o}C)	25 up to 900
Heating rate (^{o}C/min)	15
Pressure (Pa)	$1.01325 \cdot 10^5$
Tested sample mass (without HCl source) (mg)	512 or 1450
HCl source mass (mg)	62 or 100
Carrier gas flow rate (Nml/min)	50

Figure 5.5 shows the two sample types used in TGA-FTIR activities. The majority of experimental activities were conducted using a layered sample structure where the tested material is placed on the top of the HCl source layer. However, a small number of experiments were conducted using homogenized samples (mixture of the tested material with HCl source) for the study of HCl source dispersion effect on HCl absorption.

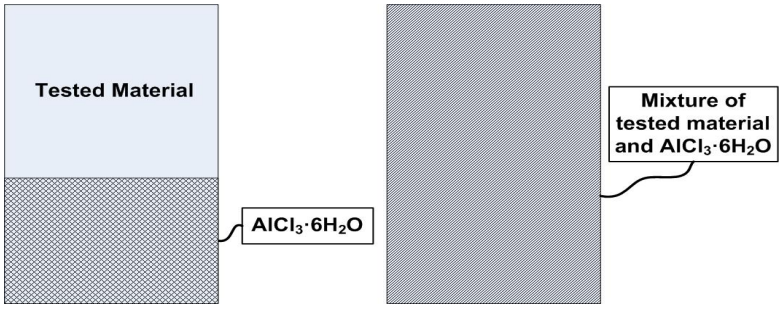

Figure 5.5: TGA-FTIR sample types.

Samples Characterization

The study of the HCl absorption by cement raw meals using TGA-FTIR tests was based on the measurement of HCl absorption capacities of two industrial raw meals (RM-A and RM-B), reagent grade raw meal compounds ($CaCO_3$, Al_2O_3, Fe_2O_3 and SiO_2), and different mixtures of reagent grade compounds. Table 5.8 illustrates the nomenclature, composition, and available physical properties of the tested materials and mixtures. The prepared mixtures were produced by mechanical mixing of reagent grade chemicals ($CaCO_3$, SiO_2, Al_2O_3 and Fe_2O_3) supplied by Sigma Aldrich.

Table 5.8: Nomenclature, composition, and physical properties of the tested materials and mixtures.

	$CaCO_3$ % w/w	Al_2O_3 % w/w	SiO_2 % w/w	Fe_2O_3 % w/w	BET (m^2/g)	Particle sizes (μm)	Supplier
$CaCO_3$	100	-	-	-	0.44	14.9 ($D_{\%50L.S.}$)	Sigma Aldrich
Al_2O_3	-	100	-	-	-	< 32-45	Sigma Aldrich
SiO_2	-	-	100	-	-	< 32-45	Sigma Aldrich
Fe_2O_3	-	-	-	100	-	< 32-45	Sigma Aldrich
CaAl	94.7	5.3	-	-	0.78	-	Prepared
CaFe1	98	-	-	2	0.63	-	Prepared
CaFe2	95.4	-	-	4.6	0.98	-	Prepared
CaAlFe	90.3	5.1	-	4.6	-	-	Prepared
SR	81.92	2.54	13.3	2.24	0.97	-	Prepared
RM-A [3]	∼82	14.55	3.12	2.22	7.67	12.9 ($D_{\%50L.S.}$)	FLSmidth A/S
RM-B [3]	∼82	13.22	2.72	1.59	9.67	13.5 ($D_{\%50L.S.}$)	FLSmidth A/S

5.2.4 Data Processing of TGA-FTIR Tests

The TGA-FTIR system records the measured data using determined time spans. In the case of FTIR, the system records the measured spectra from 500 cm^{-1} to 6000 cm^{-1} in absorbance. The quantitative calculations are based on the measured trace curves of tests and calibrations (see Appendix B). The user selects the integration wavenumber band (for instance HCl: 2600-3100 cm^{-1} and CO_2: 2200-2450 cm^{-1}) and OPUS software gives the spectra integral vs time (trace) in absorbance units. Additionally, the ratio of trace surface areas $A_{measurement}/A_{calibration}$ is proportional to the concentration ratio $C_{measurement}/C_{calibration}$ when they correspond to the same experimental conditions. The conversion of traces to concentrations was obtained, using a calibration process (see Appendix A).

5.3 References

[1] Heterogeneous Quartz Drawings, Internal document Technical University of Denmark, Copenhagen, 2018.

[2] Brix, J., Navascué s, L.G., Nielsen, J.B., Bonnek, P. L., Larsen, Clausen, S., Glarborg, P., and Jensen, A.D., Oxy-fuel Combustion of Millimeter - Sized Coal Char: Particle Temperatures and NO Formation, Fuel, vol. 160, pp.72-78, 2013.

[3] Sørensen, O.C., Johnsson, J.E., and Jensen, A., Reduction of NO over Wheat Straw Char, Energy & Fuels, vol.15, pp.1359-1368, 2001.

[4] Sengeløv, L.W., Hansen, T.B., Bartolomé, C., Wu, H., Pedersen, K.H., Frandsen, J. F., Jensen, D. A., and Glarborg, P., Sulfation of Condensed Potassium Chloride by SO_2, Energy & Fuels, vol.27, pp.3283-3289, 2013.

[5] Servomex-Servotough 2510 series Operating manual, Servomex, 2010.

[6] Compositional Analysis of Raw Meals, Internal report FLSmidth A/S, Copenhagen, 2016.

[7] Schindler, A., Neumann, G., Rager, A., Fueglein, E., Blumm, J., and Denner, T., A Novel Direct Coupling of Simultaneous Thermal Analysis (STA) and Fourier Transform-Infrared (FT-IR) Spectroscopy, Journal of thermal Analysis and Calorimetry, vol.113, pp.1091-1102, 2013.

[8] Netzsch Products & Solutions from NETZSCH Analyzing & Testing, Netzsch Group Group.[25 September 2016] URL http://www.netzsch-thermal-analysis.com/en/products-solutions.

[9] ALPHA FTIR Analyzer-Manual, Bruker OPTIK GmbH, 2nd Edition, 2011.

[10] Hartman H., Trnka O. and Solcova O.,Thermal Decomposition of Aluminum Chloride Hexahydrate, Industrial & Engineering Chemistry Research, vol.44, pp.6591-6598, 2005.

[11] Naumann, R., Petzold, D., Paulik, F., and Paulik, J., Studies on Themal-Decomposition of Aluminium Chloride Hexahydrate Under Dynamic and Quasi-Isothermic Conditions, Journal of Thermal Analysis, vol. 15, pp.47-53, 1979.

[12] Lide, D.R., (editor), CRC Handbook of Chemistry and Physics, 90th Edition, CRC Press, pp. 4.45, 2009, ISBN: 10987654321.

Chapter 6

Experimental Results on HCl Absorption

This chapter presents the obtained experimental results on HCl absorption by raw meals and raw meal compounds using fixed-bed and TGA-FTIR set-ups. The interpretation of fixed-bed experimental data described the mechanism of HCl absorption by raw meal at low temperatures (less than 200^{o}C). Furthermore, a number of parameters potentially affecting HCl absorption, e.g., temperature and gas phase moisture content, were studied. The analysis of TGA-FTIR data focuses on the evaluation of raw meal compound effects, e.g., Fe_2O_3, on the HCl absorption by reagent grade $CaCO_3$. The potential use of TGA-FTIR method for the fast screening of HCl absorption capacity of industrial raw meals was evaluated.

6.1 Fixed-bed Experimental Results

This section presents the obtained experimental data by fixed-bed tests. An interpretation of the mechanism of HCl absorption by raw meal in the temperature range 100-180^{o}C is given. The section is split into three parts: (i) the evaluation of the experimental set-up behaviour and test methodology, (ii) the determination of HCl absorption mechanism and HCl saturation capacities of the tested raw meals, and (iii) the evaluation of parameters that potentially affect the HCl absorption.

The main body of this section (fixed-bed experimental results) is intended to be published in a scientific article (see Appendix F) with the title: "Experimental evaluation of hydrogen chloride (HCl) absorption by cement raw meal at low temperatures, using fixed-bed tests", written by Pachitsas, S., Wedel, S., Skaarup Jensen, L., Boll Illerup, J., and Dam-Johansen, K..

6.1.1 Experimental Set-up Behaviour and Test Methodology

Evaluation of Set-up Behaviour

Figure 6.1 shows the HCl response curve and standard deviation determined based on four repetitions of pure fused silica tests (inert sample), using HCl concentration: 100 ppmv, gas phase moisture content: 0 % v/v, temperature: 100°C, and gas volumetric flow: 1.5 Nl/min - HCl/N_2. It is clearly seen that no HCl concentration breakthrough takes place in the first 45s. This breakthrough time of inert samples is called t_B. Furthermore, an extended transient section exists after the first 45s.

This breakthrough time (t_B) corresponds to the Mass Flow Controllers' (MFCs) response delay, filling of set-up empty space, and physical absorption phenomena in set-up compartments. It is noteworthy, that the observed response delay was affected by the HCl concentration and gas flow rate, however, it did not depend on the reactor temperature. Hence, the response delay t_B determined by fused silica tests at the tested conditions, was subtracted from raw meal test data which are presented in the subsequent figures.

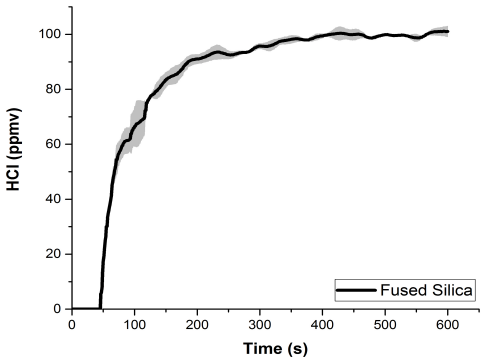

Figure 6.1: HCl response curve and standard deviation (shaded area) of pure fused silica (9g), using HCl concentration: 100 ppmν, gas phase moisture content: 0 % ν/ν, temperature: 100℃, and gas volumetric flow: 1.5 Nl/min - HCl/N_2.

The transient section of the HCl response curve in Figure 6.1 is mainly related to the response characteristics of the HCl-FTIR analyzer. Figure 6.2 illustrates the transient sections of response curves from fused silica and reactor by-pass tests at the same experimental conditions. The small deviations between the transient sections (within uncertainties) show that the transient section shape is not significantly affected by the fixed-bed reactor.

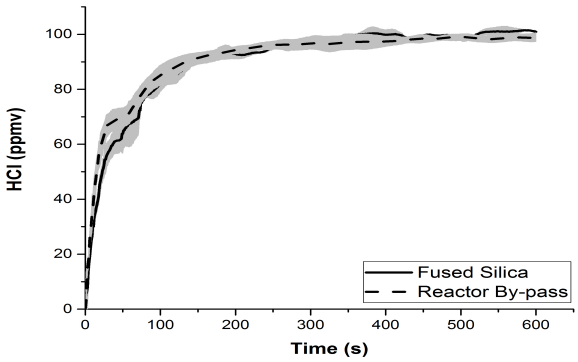

Figure 6.2: The transient sections of HCl response curves of pure fused silica (9g) and reactor by-pass tests, using HCl concentration: 100 ppmν, temperature: 100℃, gas phase moisture content: 0% ν/ν, and gas volumetric flow: 1.5 Nl/min - HCl/N_2.

The additional time to breakthrough (in excess of t_B) Δt_B caused by raw meal samples is the basis for the reported results in this work. It is assumed that the nominal feed HCl content is completely absorbed by the raw meal sample in the additional time. Therefore, the absorbed volume of HCl is equal to the product of the nominal HCl concentration in the feed (expressed as v/v), volumetric flow, and increase in breakthrough time Δt_B. The results are reported as degree of conversion of the assumed raw meal active compound ($CaCO_3$).

Samples Dilution - Real HCl Absorption Capacity Determination

Elimination of raw meal particle agglomeration and flow channelling in the sample layer in fixed-bed reactor has been found to be necessary for the study of HCl absorption by raw meal and accurate determination of the real HCl absorption capacity of raw meal. The presence of agglomerates and flow channelling gives an apparent HCl capacity of raw meal based on the increase of Δt_B in breakthrough time that it is lower than the real HCl absorption capacity of raw meal. Dilution of raw meal samples using fused silica particles with particle size between 50μm and 100μm was applied to break up raw meal agglomerates and to minimize the risk of channelling.

The study of the sample dilution effect was based on an evaluation of HCl absorption by pure and diluted raw meal A (RM-A) samples at 100^{o}C, using dry gas phase and fused silica as diluting agent. Figure 6.3 - A illustrates the HCl response curves and standard deviation (shaded area) of pure fused silica (inert material), pure RM-A, and diluted RM-A samples. In Figure 6.3 - A no HCl is detected until a certain time which is defined as breakthrough time Δt_B. The raw meal dilution, using weight ratio of fused silica to RM-A equal to 29, gives an extended breakthrough time even though the pure and diluted RM-A samples have the same RM-A content of 0.3g.

Figure 6.3 - B illustrates the transient section of HCl response curves of pure fused silica, pure RM-A and diluted RM-A samples when translated to a common starting time. It is discernible that the pure RM-A curve lies below the pure fused silica and diluted RM-A. The transient for the diluted RM-A initially lies close to the transient for fused silica, but later pure RM-A and diluted RM-A samples have nearly coinciding transient sections. The observations indicate that after the first, fast reactions before breakthrough there remains a residual absorption capacity. For pure RM-A, due to agglomeration, this residual capacity probably includes some of the initial capacity observed for diluted samples. However, the transients are so affected by the response characteristics of the FTIR analyzer that further attempts at quantification have not been done.

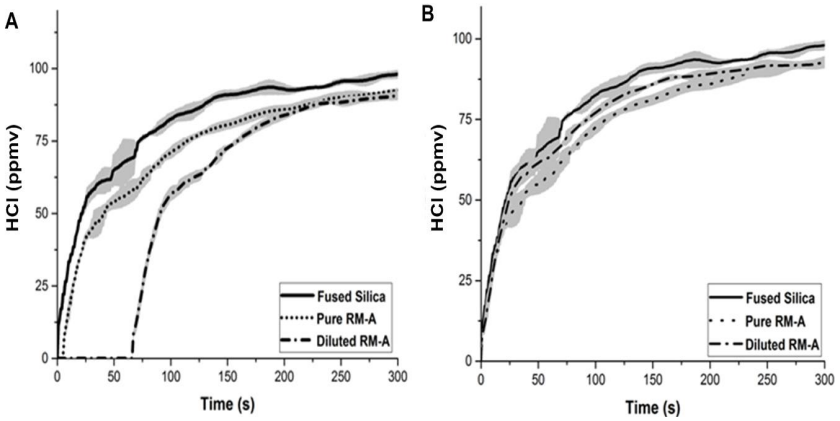

Figure 6.3: A) HCl response curves and standard deviation (shaded area) of pure fused silica (9g), pure RM-A (0.3g), and diluted RM-A (weight ratio of fused silica to RM-A: 29) samples using HCl concentration: 100 ppmν, gas phase moisture content: 0% ν/ν, temperature: 100℃, and gas volumetric flow: 1.5 Nl/min - HCl/N_2; B) The transient parts of HCl response curves of pure fused silica (9g), pure RM-A (0.3g), and diluted RM-A (weight ratio of fused silica to RM-A: 29) samples using HCl concentration: 100 ppmν, gas phase moisture content: 0% ν/ν, temperature: 100℃, and gas volumetric flow: 1.5 Nl/min - HCl/N_2.

Figure 6.4 presents the effect of dilution on breakthrough time Δt_B using weight ratios of fused silica to RM-A between 0 and 49, and constant sample RM-A content 0.3g. It is seen that a fused silica content of 8.7g (weight ratio of fused silica to RM-A: 29) results in an almost 10 times longer breakthrough time than pure RM-A samples. The increase of fused silica content above 8.7g has only a minor effect on breakthrough time - HCl absorption capacity. Therefore, the minimum weight ratio of fused silica to RM-A for the determination of real HCl absorption capacity is 29.

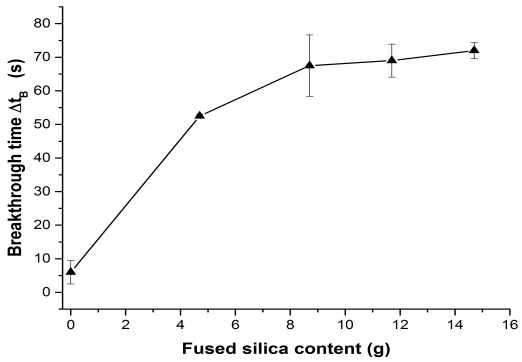

Figure 6.4: Breakthrough time Δt_B as function of sample diluent agent mass content using RM-A mass: 0.3g, HCl concentration: 100 ppmν, temperature: 100℃, gas phase water content: 0% ν/ν, and gas flow rate: 1.5Nl/min - HCl/N_2.

Figure 6.5 shows the SEM - EDS micrographs of the pure RM-A (A), pure fused silica (B), and diluted RM-A samples (C and D). Figure 6.5 - A documents that RM-A particles agglomerate strongly. The presence of agglomerates with size larger than 100μm and very few individual particles are clearly seen. Figure 6.5 - B shows that the particles of diluent have nearly planar surfaces. Furthermore, Figure 6.5 - C and Figure 6.5 - D show that sample dilution results in the breaking of RM-A agglomerates and covering of fused silica particles' surfaces with raw meal agglomerate fragments. It is clearly seen that the fragments are significantly smaller than 100μm and within the particle size distribution range of raw meal. Moreover, individual particles are discernible. The origin of the precipitated fragments from raw meal is confirmed by the calcium elemental map in Figure 6.5 - D.

It is commonly accepted that fine particles tend to develop strong inter-particle cohesive forces that result in a severe agglomeration [1-5] which can cause flow channelling. The observed breakthrough time dependence on sample dilution in conjunction with SEM - EDS analysis results show that the presence of agglomeration phenomena leads to apparent HCl absorption capacities of raw meals lower than the real at temperatures below 180^{o}C. Similar observations were also reported in other studies [2-3, 5] on acidic gases absorption by Ca-based sorbents.

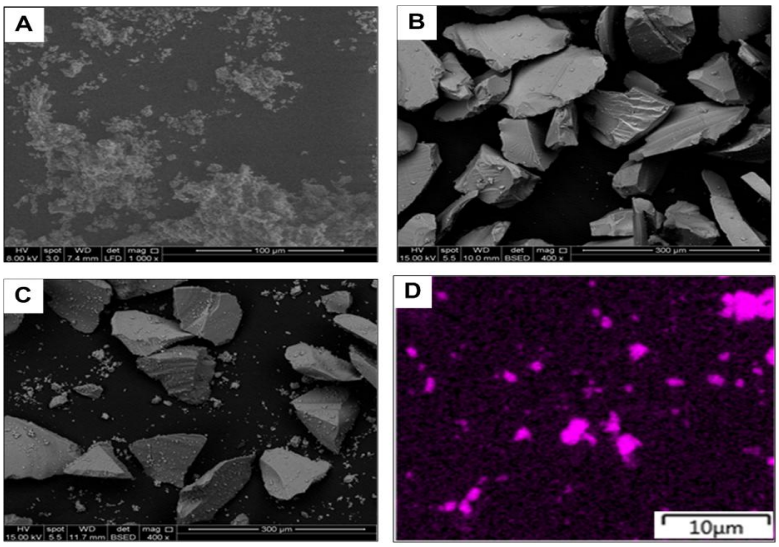

Figure 6.5: A) SEM picture of pure RM-A sample; B) SEM picture of pure fused silica particles; C) SEM picture of diluted RM-A sample (fused silica: 4.7g and RM-A: 0.3g); and D) EDS-calcium elemental map of the surface of a fused silica particle from diluted RM-A sample (fused silica:4.7g and RM-A: 0.3g).

6.1.2 Determination of HCl Absorption Mechanism and Capacities

The determination of the mechanism of HCl absorption by raw meal comprises two stages: (i) the confirmation of raw meal behaviour as HCl sorbent, and (ii) the analysis of HCl concentration effect on HCl absorption by raw meal.

Evaluation of Raw Meal Sample Mass Effect on HCl Absorption

The evaluation of raw meal as HCl sorbent was conducted using diluted raw meal samples with constant total mass 9g and varying raw meal content between 0.15g and 0.6g, and dry gas phase at 100^{o}C. Figure 6.6 - A shows that the only discernible effect of RM-A content increase on HCl response curves is the extension of breakthrough time.

Figure 6.6 - B shows the experimental and corrected breakthrough times of the varying raw meal content tests of RM-A and RM-B. The high raw meal content tests (raw meal mass: 0.3g and 0.6g) were conducted using mass ratios of fused silica to raw meal ≤ 29 that do not ensure complete breaking up of agglomerates. Hence, the experimental results were corrected using the obtained data from the dilution effect analysis of RM-A (see 6.1.1 - Figure 6.4) and a linear proportionality of breakthrough time Δt_B correction with the fused silica content of sample. Figure 6.6 - B shows that the corrected breakthrough time Δt_B is proportional to raw meal content considering that the trend lines are forced through the origin. Based on the amount of HCl absorbed from the start to

the breakthrough time Δt_B and slopes of the linear regressions of the corrected breakthrough time Δt_B as function of the raw meal content, the specific HCl absorption capacities of RM-A and RM-B are $2.9{\cdot}10^{-5}$ mol/g and $3.86{\cdot}10^{-5}$ mol/g, respectively. Therefore, RM-B seems to have higher HCl absorption capacity than RM-A at the tested conditions.

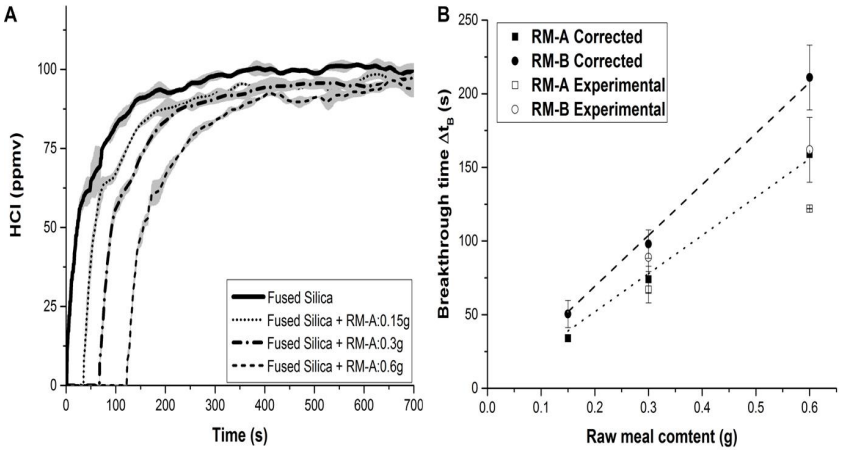

Figure 6.6: A) HCl response curves and standard deviation (shaded area), using diluted raw meal samples of total mass 9g and RM-A content: 0.15g, 0.3g and 0.6g, HCl concentration: 100 ppmν, gas phase moisture content: 0% ν/ν, temperature: 100℃, and gas volumetric flow: 1.5 Nl/min - HCl/N_2; B) Breakthrough times as function raw meal content for RM-A and RM-B using total diluted sample mass: 9g, HCl concentration: 100 ppmν, temperature: 100℃, gas phase moisture content: 0% ν/ν, and flow rate: 1.5 Nl/min - HCl/N_2.

The behavior of raw meals as HCl sorbents at low temperatures was verified by the obtained data.The tested raw meals were characterized by a specific HCl absorption capacity that varies between raw meals. This variation may be related to properties such as BET area, but other properties such as those reported in Chapter 5, e.g. raw meal composition, and homogeneity of the tested samples may have influence on HCl absorption capacity. Table 6.1 shows a strong correlation between BET area and HCl absorption capacity of the tested raw meals. The HCl absorption capacity of RM-B is 33% higher than RM-A and the BET area of RM-B is 26% larger than RM-A. On the other hand, no correlation between the HCl absorption capacity and specific surface area by Laser Scattering (L.S.) method can be distinguished. The permanent accumulation of chlorine in the case of raw meal samples exposed to HCl was verified by X-ray Photoelectron Spectroscopy (XPS) analysis (see Appendix B). In particular, the XPS spectra analysis indicated that the captured chlorine could correspond to formation of $CaCl_2$.

Table 6.1: HCl absorption capacity, BET area, and L.S. area ratios of RM-A and RM-B.

$\frac{Capacity_{RM-B}}{Capacity_{RM-A}}$	$\frac{BET_{RM-B}}{BET_{RM-A}}$	$\frac{L.S.-Area_{RM-B}}{L.S.-Area_{RM-A}}$
1.33	1.26	1

BET area is the sum of the particles external surface area and pore area. The HCl absorption capacity of raw meal is determined using diluted samples, where the smaller size constituents of agglomerates are well dispersed. The outer surface area of the small dispersed particles was part of the pore area of the agglomerates by BET measurements. The L.S. method considers the particles as spheres and measures the external surface of agglomerates as particle external surface. As shown in Chapter 5 - section 5.1.3, the BET area of both raw meals is 5-7 times larger than the L.S. area. This makes it likely that the surface area of the small dispersed particles is measured as 'pore area' by the BET method. Hence, the underestimation of the particles external surface by L.S. method is possible.

Evaluation of HCl Concentration Effect on Active Compound Conversion

The analysis of the effect of HCl concentration on the detected complete absorption stage is based on the comparison of breakthrough time Δt_B and the conversion of the assumed active compound ($CaCO_3$) in raw meal due to the absorbed amount of HCl in the period of length Δt_B.

Table 6.2 shows the experimentally obtained breakthrough times at 100^oC and corresponding $CaCO_3$ conversion (6.1), assuming the formation stoichiometry of $CaCl_2$. A dry gas phase of varying HCl content, and diluted RM-A samples with weight ratio of fused silica to RM-A equal to 49 and RM-A content 0.3g were used. The obtained results showed that the $CaCO_3$ conversion is not affected by gas phase HCl concentration at the tested conditions. The active compound conversion being independent of gas phase HCl concentration in conjunction with the very low $CaCO_3$ conversion indicates that the HCl absorption by raw meal approximates a surface saturation phenomenon.

$$X_{CaCO_3} = \frac{C_{HCl} \cdot \nu_{feed} \cdot \Delta t_B \cdot M_{CaCO_3}}{2 \cdot m_{CaCO_3}} \tag{6.1}$$

Table 6.2: Breakthrough times and $CaCO_3$ conversions using diluted RM-A samples (weight ratio of fused silica to RM-A: 49 and RM-A content: 0.3g), HCl concentration: 52, 100 and 200 ppmv, temperature: 100℃, dry gas phase, and gas flow: 1.5Nl/min - HCl/N_2.

HCl (ppmv)	Breakthrough time Δt_B(s)	$CaCO_3$ Conversion (%)
52	133 ± 7	0.157 ± 0.008
100	75 ± 6.6	0.170 ± 0.015
200	36 ± 1.5	0.163 ± 0.007

The theoretical conversion of a thin active surface layer with thickness equal to a calcite unit cell height (17.06 Å [8]) and surface area defined by BET and laser scattering measurements can be calculated. The corresponding active layer conversions are 4.2% and 22% for BET and laser scattering determined surface areas. Therefore, it may be concluded that only a fraction of the available active surface area reacts with HCl, even if the smallest measured surface area is used.

6.1.3 Evaluation of Parameters Affecting HCl Absorption Capacity

This section presents the fixed-bed experimental results that are related to the evaluation of parameters that potentially affect the HCl absorption capacity in the temperature range 100-180^{o}C. It comprises the effects of temperature in the case of dry and moist gas phases, samples thermal treatment at 115^{o}C and 200^{o}C, and presence of O_2 and CO_2 in gas phase.

Temperature Effect Using Dry Gas Phase

Figure 6.7 shows the HCl response curves and standard deviation (shaded area) from tests in the temperature range 100-180^{o}C, using diluted RM-A samples (dilution ratio: 29) and dry gas phase. It is clearly seen that the temperature has a very minor effect on breakthrough time Δt_B and no discernible effect on the post-breakthrough response section. The HCl absorption capacity represented by Δt_B is seen to be greater at 100^{o}C than at 150^{o}C and 180^{o}C.

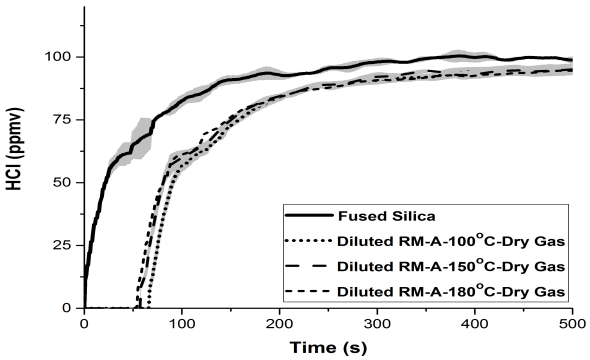

Figure 6.7: HCl response curves and using HCl concentration: 100 ppmν, gas phase moisture content: 0% ν/ν, temperature: 100℃, 150℃ and 180℃, diluted RM-A samples: fused silica-8.7g and RM-A-0.3g (undried), and gas volumetric flow: 1.5 Nl/min - HCl/N_2.

In order to determine if the water content of the raw meal samples had any influence on HCl absorption a series of experiments was carried out with diluted RM-A samples dried at different temperatures. Table 6.3 shows the experimentally determined mass loss of RM-A samples due to the thermal treatment. Drying of pure RM-A samples at 115^{o}C, 200^{o}C and 300^{o}C for 5 hours

caused reversible mass loss close to 1.7 ± 0.8 % w/w, 3.5 ± 1.3 % w/w and 4.5 ± 1 % w/w (samples gained the lost mass after 1hr of exposure in ambient air), respectively. These values correspond to the release of 4.5, 9 and 11.6 monolayers of water if the H_2O absorption by raw meal follows a BET-isotherm (multilayer absorption) and sorbent surface is defined by BET measurements. The H_2O absorption by limestone based on BET-isotherms is also reported [3, 9, 10].

Table 6.3: Mass loss of RM-A samples (assuming that the mass loss corresponds to H_2O release) due to the thermal treatment at 115℃, 200℃, and 300℃.

Drying	Mass loss-115^{o}C		Mass loss-200^{o}C		Mass loss-300^{o}C	
(hr)	(%w/w)	(mol/g)	(%w/w)	(mol/g)	(%w/w)	(mol/g)
5	1.7±0.8	$9{\cdot}10^{-4}$ $\pm 4{\cdot}10^{-4}$	3.5±1.3	$1.9{\cdot}10^{-3}$ $\pm 7{\cdot}10^{-4}$	4.5±1	$2.5{\cdot}10^{-3}$ $\pm 6{\cdot}10^{-4}$
12	-	-	3.8±1.4	$2.1{\cdot}10^{-3}$ $\pm 8{\cdot}10^{-4}$	-	-

Figure 6.8 shows the breakthrough time Δt_B and the equivalent HCl saturation capacity of RM-A as function of fixed-bed test temperature and temperature at which samples were dried for 5 hours. It is clearly seen that the drying of samples reduces the HCl saturation capacity of RM-A. In particular, the tests at 150^{o}C and 180^{o}C showed that the molar ratio of the HCl saturation capacity decrease (mol/g) to the released H_2O (Table 6.3 - mol/g) is close to $6.3{\cdot}10^{-3}$ at both drying temperatures (115^{o}C and 200^{o}C). This clearly indicates a proportional relation between the raw meal water content and HCl absorption capacity which corresponds to the absorption of 1 molecule of HCl per $\sim$ 160 molecules of H_2O. It is also seen that the obtained breakthrough times (Δt_B) at 100^{o}C tend to be slightly longer than at 150^{o}C and 180^{o}C in case of samples that are undried or dried at 115^{o}C. In contrast with this, the obtained breakthrough times are almost identical at all fixed-bed temperatures for the samples dried at 200^{o}C.

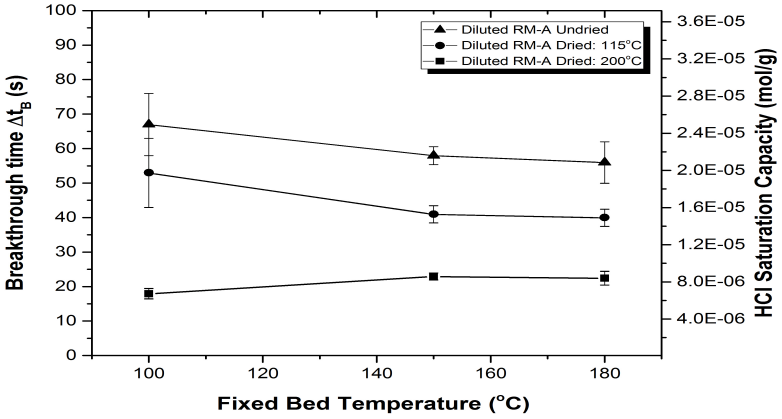

Figure 6.8: Breakthrough time Δt_B and equivalent HCl saturation capacity of RM-A as function of temperature using HCl concentration: 100 ppmν, gas phase moisture content: 0% ν/ν, temperature: 100℃, 150℃, and 180℃, drying temperature: 115℃ and 200℃, diluted RM-A samples: fused silica-8.7g and RM-A-0.3g, and gas volumetric flow: 1.5 Nl/min - HCl/N_2.

The dependence of breakthrough time Δt_B on sample thermal treatment mass loss shows that the raw meal moisture content significantly affects the HCl absorption by raw meal. In addition, the used drying temperatures cannot cause structural or chemical changes in active compound, e.g., calcination [11] and sintering [12]. Furthermore, it is well known that clay minerals demonstrate reversible hydration - dehydration behavior in the tested temperature range [13, 14]. The promotion of acidic gases absorption by Ca-based sorbents due to the presence of bound moisture on silicates surface was also suggested by Jozewicz et al.[15]. Therefore, the variation of breakthrough times at 100^oC (fixed bed temperature) could be related to the hydration - dehydration properties of clay minerals in raw meal.

The absorbed amount of HCl by undried RM-A at 100^oC (product of specific HCl saturation capacity of RM-A: $2.49 \cdot 10^{-5}$ mol/g and RM-A mass: 0.3g) is ~ 13 times larger than the HCl saturation capacity of the water content of raw meal expressed in moles. The calculations assume RM-A mass: 0.3 g, H_2O content of RM-A: 4.5% w/w (mass loss by drying at 300^oC for 5hr), and HCl equilibrium saturation capacity of pure water at 100^oC when the HCl concentration in gas phase is 100ppmv: $1.43 \cdot 10^{-4}$ mol/g (calculated based on the model of Takeshi et al.[16]). This in conjunction with the active compound conversion being independent of the HCl concentration in gas phase supports that the HCl absorption by raw meal is not simply determined by HCl saturation equilibrium of water.

Temperature Effect Using Moist Gas Phase

Figure 6.9 - A shows the HCl response curves from HCl absorption tests in the fixed-bed temperature range 100-180^oC, using diluted RM-A samples and gas phase moisture content 5% v/v. It is clearly seen that the breakthrough time $\Delta t_{B,moist}$ decreases as the temperature is raised. The fluctuations in the HCl signal also increases substantially as the increased standard deviation shows. Furthermore, the fluctuations are more pronounced at lower fixed-bed temperature.

Figure 6.9 - B shows the increase on moist breakthrough time $\Delta t_{B,moist}$ (proportional to HCl absorption enhancement) by gas phase moisture content relative to dry breakthrough time $\Delta t_{B,dry}$ in the fixed-bed temperature range 100-180^oC. The presence of 5% v/v H_2O increased the HCl absorption capacity by 25% at 180^oC and 61% at 100^oC. The water effect rapidly weakens with temperature.

The present observations on gas phase moisture content effect on HCl absorption by raw meal are consistent with previous works on Ca-based sorbents chlorination at low temperatures in the presence of water (Weinell et al. [17], Jozewicz et al. [15], Fonseca et al.[7] and Chisholm and Rochelle [18]). These studies were, however, done with much higher HCl concentrations where saturation of water with HCl may occur. Furthermore, the obtained results can be related to the literature data for SO_2 absorption by limestone at low temperatures which claim that SO_2 absorption occurs only in presence of H_2O monolayers on the sorbent surface and increases with relative humidity [3, 9, 10].

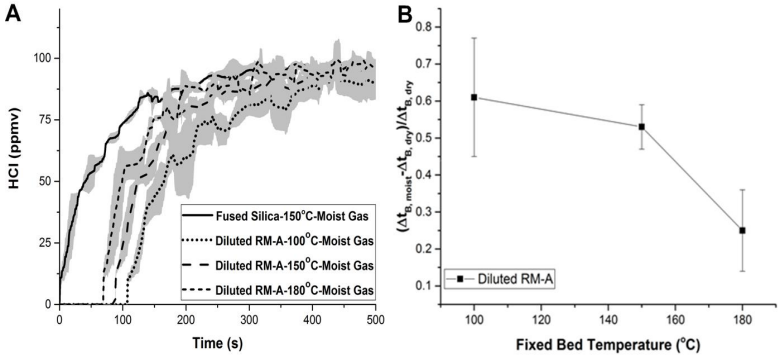

Figure 6.9: A) HCl response curves and standard deviation (shaded area) using diluted RM-A samples of total mass 9g and RM-A content: 0.3g, HCl concentration: 100ppmν, gas phase moisture content: 5% ν/ν, temperature: 100℃, 150℃, and 180℃, and gas volumetric flow: 1.5 Nl/min - HCl/N_2; B) HCl absorption enhancement by gas phase moisture content relative to dry breakthrough time $\Delta t_{B,dry}$ ($\Delta t_{B,dry}$: breakthrough time Δt_B using dry gas phase and $\Delta t_{B,moist}$: breakthrough time Δt_B using moist gas phase), using diluted raw meal samples of total mass 9g and RM-A content: 0.3g, HCl concentration: 100ppmν, gas phase moisture content: 0% ν/ν and 5% ν/ν, temperature: 100℃, 150℃, and 180℃, and gas volumetric flow: 1.5 Nl/min - HCl/N_2.

CO_2 and O_2 Effects

Figure 6.10 compares the obtained average HCl response curves using pure RM-A samples (no dilution by fused silica) and dry gas phase with and without O_2 and CO_2 at 100^{o}C. It is observed that the presence of 3% v/v O_2 and 30% v/v CO_2 in gas phase has no effect on HCl absorption by raw meal at the used experimental conditions. These results are consistent with the observations of Mura and Lallai [19] and Gullett et al.[20] at much higher HCl concentrations. It is especially noteworthy that together with the literature results of Murra and Lallai [19] it can be concluded that O_2 and CO_2 have no effect on HCl absorption in the range of operating temperatures of post-preheater tower units.

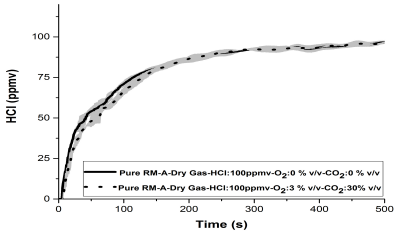

Figure 6.10: HCl response curves and standard deviation (shaded area) of pure RM-A samples: 0.3g, using gas phase composition: HCl: 100ppmν-H_2O: 0%ν/ν-O_2: 0%ν/ν-CO_2: 0%ν/ν and HCl: 100ppmν-H_2O: 0%ν/ν-O_2:3%ν/ν-CO_2:30%ν/ν, temperature: 100℃, and gas volumetric flow: 1.5 Nl/min.

6.1.4 Conclusions on Fixed-bed Data

This work has shown that cement raw meals absorb HCl in the temperature range 100-180^{o}C. Furthermore, the fast HCl absorption rates and very low active compound conversion degree seem consistent with a fast surface reaction that leads to a saturation phenomenon. The apparent HCl absorption capacity depends on raw meal type and other experimental conditions such as the water content in gas phase, raw meal, and degree of dilution. The active compound conversion is significantly less than 1%. The HCl absorption by raw meal depends only slightly on the temperature in the case of dry gas phase.

The presence of moisture in the gas phase significantly enhances the HCl absorption by raw meal at temperatures below 180^{o}C. The presence of 5% v/v H_2O in the gas phase increased the HCl absorption capacity of RM-A at temperatures of 180^{o}C (25% increase), 150^{o}C (53% increase) and 100^{o}C (61% increase). Furthermore, the gas phase moisture content effect rapidly weakens with temperature. The moisture content of the raw meal also strongly promotes the HCl absorption in the case of dry gas phase. These results suggest that the initial HCl absorption (breakthrough time) is mainly dependent on a combined interaction with the water on the raw meal surface and solid constituents in the raw meal rather than on a direct interaction with $CaCO_3$.

Agglomeration of the raw meal particles potentially accompanied by flow channelling gives low apparent HCl absorption capacity. The dilution of raw meal samples using inert material with larger particles size gave almost 10 times higher HCl absorption capacity of raw meals, due to elimination of these effects.

The presence of 3% v/v O_2 and 30% v/v CO_2 in gas phase has no apparent effect on HCl absorption by raw meal at the tested experimental conditions.

6.2 TGA-FTIR Results

This section presents the obtained experimental results by TGA-FTIR tests on HCl absorption by raw meals and raw meal compounds. The purposes of these activities were the evaluation of TGA-FTIR method for the fast screening of HCl absorption capacity of industrial raw meals, and the study of raw meal compound effects on HCl absorption. This section comprises: (i) the presentation of set-up behaviour and methodology, (ii) the evaluation of the TGA-FTIR method for the fast screening of HCl absorption capacity of raw meals, and (iii) the study of HCl absorption by raw meal compounds.

6.2.1 Experimental Set-up Behaviour

Figure 6.11 shows the obtained HCl signals from pure samples of $AlCl_3 \cdot 6H_2O$, RM-A, and RM-B using constant heating rate: 15^{o}C/min and carrier gas (N_2) flow rate: 50 Nml/min. It is clearly seen that the thermal decomposition of $AlCl_3 \cdot 6H_2O$ results in HCl release in the temperature range 100-380^{o}C (peak area). This is consistent with the literature data [21, 22]. On the other hand, HCl release from pure raw meal samples (RM-A and RM-B) has not been detected.

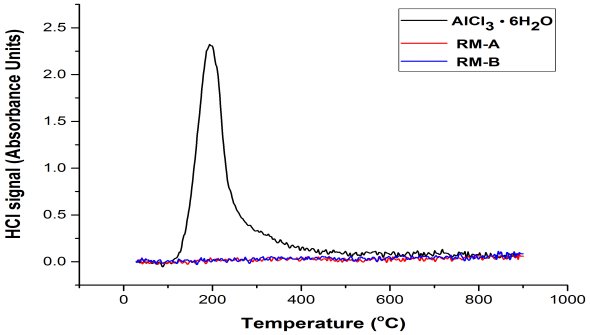

Figure 6.11: HCl signals from $AlCl_3 \cdot 6H_2O$: 13mg, RM-A: 530mg, and RM-B: 502mg, using HCl IR-spectrum band: 2600-3100 cm^{-1}, heating rate: 15 ℃/min, and carrier gas(N_2) flow: 50 Nml/min.

Figure 6.12 illustrates the CO_2 release from pure raw meals (RM-A and RM-B) using constant heating rate: 15^{o}C/min and carrier gas (N_2) flow rate: 50 Nml/min. It is obvious that CO_2 release from raw meals occurs at temperatures above 540^{o}C. This observation is consistent with the limestone calcination [23]. Furthermore, the small differences between CO_2 curves could be related to raw meal composition and physical properties. For instance, the variation of initiation temperature of calcination is governed by the crystal structure and form of the stone [23].

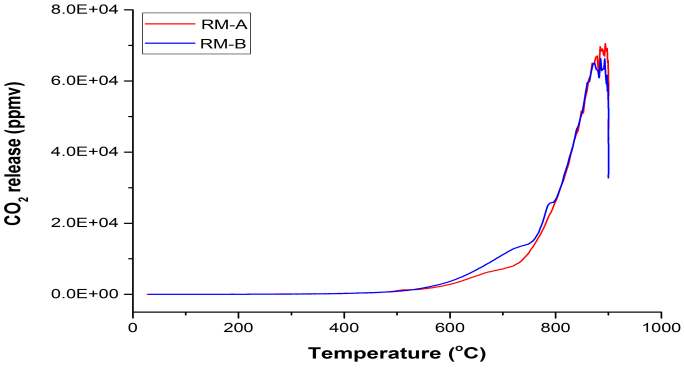

Figure 6.12: CO_2 release from pure RM-A: 530mg and RM-B: 502mg, using CO_2 IR-spectrum band: 2200-2450 cm^{-1}, heating rate: 15 ℃/min and carrier gas (N_2) flow: 50Nml/min.

6.2.2 Fast Screening of HCl Absorption Capacity of Raw Meals

This section presents the evaluation of HCl absorption capacity of RM-A and RM-B using constant heating rate: 15°C/min and carrier gas (N_2) flow rate: 50 Nml/min. In these experimental activities the masses of $AlCl_3 \cdot 6H_2O$ and raw meal were 62mg and 570mg, respectively. These experimental conditions made discernible the differences in the HCl absorption capacity of raw meals. Furthermore, the effect of HCl source dispersion in raw meal sample was investigated. Two types of samples (see Chapter 5, section 5.2.3) were tested: (i) samples with a layered structure (raw meal is placed on the top of the HCl source layer), and (ii) homogenized samples (HCl source and raw meal are mixed).

Figure 6.13 shows the obtained HCl signals of $AlCl_3 \cdot 6H_2O$ (mass: 62mg) and RM-A - $AlCl_3 \cdot 6H_2O$ (layer structure with RM-A: 570mg and $AlCl_3 \cdot 6H_2O$: 62mg) using heating rate: 15 °C/min, and carier gas (N_2) flow rate: 50 Nml/min. The shaded area (green) in Figure 6.13 - A corresponds to the absorbed amount of HCl by raw meal sample. Therefore, the ratio of the shaded area to the total area of the HCl preak of $AlCl_3 \cdot 6H_2O$ sample gives the fraction of the released HCl from HCl source which is absorbed by raw meal sample. The released amount of HCl from the thermal dissociation of $AlCl_3 \cdot 6H_2O$ is calculated by the stoichiometry of the dissociation mechanism (see Appendix A). The observed 'shoulder' is related to the flow rate of carrier gas, heating rate, and mass of $AlCl_3 \cdot 6H_2O$. Appendix A comprises the study on the observed 'shoulder' of HCl signals from $AlCl_3 \cdot 6H_2O$ samples. The analysis of shoulder origin indicated that HCl was absorbed and released again from the experimental set-up.

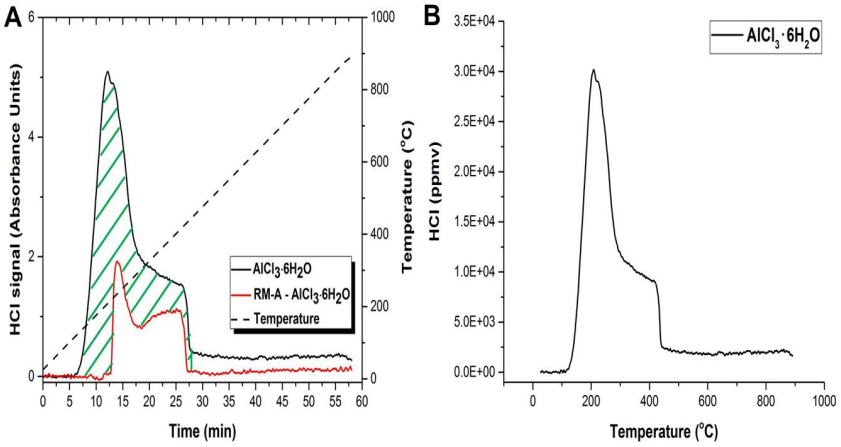

Figure 6.13: A) HCl signals from pure $AlCl_3 \cdot 6H_2O$: 62mg and RM-A - $AlCl_3 \cdot 6H_2O$ (sample with a layered structure): RM-A: 570mg and $AlCl_3 \cdot 6H_2O$: 62mg, using HCl IR-spectrum band: 2600-3100 cm^{-1}, heating rate: 15 ℃/min, and carrier gas (N_2) flow rate: 50 Nml/min; B) HCl release (ppmv) from pure $AlCl_3 \cdot 6H_2O$: 62mg, using HCl IR-spectrum band: 2600-3100 cm^{-1}, heating rate: 15 ℃/min, and carrier gas (N_2) flow rate: 50 Nml/min.

The experimental tests showed incomplete absorption of the released HCl from the thermal dissociation of $AlCl_3 \cdot 6H_2O$ which allows the calculation of HCl absorption capacities of the tested raw meals. Table 6.4 presents the experimentally determined HCl absorption capacities. RM-B has 9% and 17% higher HCl absorption capacities than RM-A in the case of 'layered samples' and homogenized samples, respectively. Furthermore, the corresponding active compound ($CaCO_3$) conversion degrees vary between 5.6% and 7.3%.

Table 6.4: Specific HCl absorption capacities of RM-A and RM-B using TGA-FTIR tests.

Sample Type	RM-A (mol/g)	RM-B (mol/g)
Layer structure	$9.18 \cdot 10^{-4} \pm 4 \cdot 10^{-5}$	$1 \cdot 10^{-3} \pm 6 \cdot 10^{-5}$
Homogenized	$1.03 \cdot 10^{-3} \pm 2 \cdot 10^{-5}$	$1.2 \cdot 10^{-3} \pm 5 \cdot 10^{-5}$

The main differences of raw meals in the composition and physical properties (see Chapter 5, section 5.1.3) are related to BET area, and contents of Fe_2O_3 and MgO. The BET area, Fe_2O_3, and MgO ratios of RM-B to RM-A are 1.26, 0.72 and 1.9, respectively. It may be inferred that the BET area has the strongest effect on HCl absorption at the investigated experimental conditions, assuming that $MgCO_3$ has lower reactivity with HCl than $CaCO_3$ (see Chapter 4, section 4.2). On the other hand, no clear conclusions on the effects of Fe_2O_3 and $MgCO_3$ on HCl absorption can be ascertained.

The TGA-FTIR test data are consistent with fixed-bed test results relative to the raw meals ranking based on HCl absorption capacity (RM-B has higher HCl absorption capacity than RM-A). However, the obtained HCl absorption capacities are more than one order of magnitude higher than those of fixed-bed tests (see section 6.1.2). This indicates that the HCl absorption phenomenon in TGA-FTIR tests does not correspond to a surface saturation phenomenon. Furthermore, the homogenized samples showed between 12% (RM-A) and 19% (RM-B) higher HCl absorption capacity than those of layer structure samples. This observation is probably related to the low melting point of $AlCl_3 \cdot 6H_2O$ (100^oC [23]) and the temperature window (90-350^oC [21, 22]) of the thermal dissociation of $AlCl_3 \cdot 6H_2O$ that has maximum rate close to 240^oC. Therefore, during the ramping temperature tests, the liquefied HCl source initially wets the raw meal particles and in a second stage the main thermal dissociation (HCl release) occurs. It can be claimed that the dispersed $AlCl_3 \cdot 6H_2O$ crystals give a larger contact interface to the reactants, and consequently they increase the raw meal reactivity.

The evaluation of HCl absorption capacity of raw meals using TGA-FTIR method showed that the method can distinguish the raw meal with the higher reactivity with HCl in the temperature range 90-350^oC. However, the obtained HCl absorption capacities by TGA-FTIR tests are more than one order of magnitude higher than those of fixed-bed tests and do not correspond to a surface saturation phenomenon. Therefore, TGA-FTIR data cannot be used in the modelling of the mechanism of HCl absorption at industrial conditions.

6.2.3 Evaluation of Raw Meal Compounds' Effects

This section presents the study of the HCl absorption by different raw meal compounds in comparison with RM-B, using ramping temperature tests, constant heating rate: 15^oC/min (same temperature profile with Figure 6.13 - B), carrier gas (N_2) flow rate: 50 Nml/min, and samples characterized by a layered sample structure. In these experimental activities the masses of the tested materials and $AlCl_3 \cdot 6H_2O$ (HCl source) were $\sim$ 1450mg and 102mg, respectively. The tested materials comprised RM-B, reagent grade $CaCO_3$, reagent grade SiO_2, reagent grade Fe_2O_3, and mixtures of reagent grade compounds (see Chapter 5, section 5.2.3).

HCl Absorption by Raw Meal Compounds

Figure 6.14 illustrates the obtained reduction of HCl release per tested material or mixture in the temperature range 90-350^oC under the same experimental conditions using as reference the HCl release from 102mg of $AlCl_3 \cdot 6H_2O$. The results clearly show that SiO_2 does not react with HCl, Fe_2O_3 reacts with HCl, and RM-B has significantly higher HCl absorption capacity than reagent grade $CaCO_3$ and any other reagent grade compounds mixture. It is also clearly seen that the Fe_2O_3 containing mixtures (CaFe1, CaFe2, SR and CaAlFe) have higher HCl absorption capacity than pure reagent grade $CaCO_3$. This indicates that Fe_2O_3 enhances $CaCO_3$ chlorination in the temperature range 90-350^oC. On the other hand, Al_2O_3 effect on HCl absorption seems negligible. Table 6.5 shows the HCl absorption capacities of the tested samples ($CaCO_3$ containing mixtures) per g of active compound ($CaCO_3$).

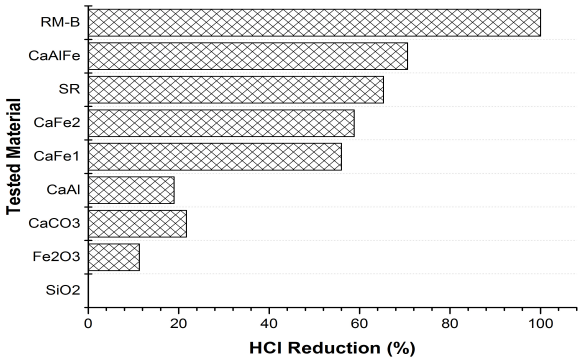

Figure 6.14: Reduction of the HCl release from HCl source per tested material, using tested material mass: $\sim$1450mg, $AlCl_3 \cdot 6H_2O$: 102mg (the samples have layer structure), constant heating rate: 15 ℃/min and carrier gas(N_2) flow: 50 Nml/min.

Table 6.5: Specific HCl absorption capacities of $CaCO_3$ containing mixtures per g of active compound ($CaCO_3$).

	$CaCO_3$	CaAl	CaFe1	CaFe2	SR	CaAlFe	RM-B
$\frac{mol}{g}$	$1.8 \cdot 10^{-4}$	$1.66 \cdot 10^{-4}$	$4.73 \cdot 10^{-4}$	$5.11 \cdot 10^{-4}$	$6.6 \cdot 10^{-4}$	$6.48 \cdot 10^{-4}$	$1.01 \cdot 10^{-3}$

Table 6.6 shows the specific HCl absorption capacity and BET area ratios of the $CaCO_3$ containing mixtures to reagent grade $CaCO_3$. It is clearly seen that the CaAl mixture (94.7% w/w $CaCO_3$ - 5.3%w/w Al_2O_3) has 8% lower HCl absorption capacity than the reagent grade $CaCO_3$ even though it has 77% larger BET area. This supports that Al_2O_3 does not promote the $CaCO_3$ chlorination at the tested conditions. The Fe_2O_3 containing mixtures have significantly higher HCl absorption capacities than reagent grade $CaCO_3$. Furthermore, HCl absorption ratios of CaFe1 and SR to reagent grade $CaCO_3$ are significantly larger than the corresponding BET area ratios. It may be concluded that the $CaCO_3$ chlorination is enhanced in presence of Fe_2O_3.

Table 6.6: Specific HCl absorption capacity and BET area ratios of $CaCO_3$ containing mixtures to reagent grade $CaCO_3$.

	$\frac{CaAl}{CaCO_3}$	$\frac{CaFe1}{CaCO_3}$	$\frac{CaFe2}{CaCO_3}$	$\frac{SR}{CaCO_3}$	$\frac{CaAlFe}{CaCO_3}$	$\frac{RM-B}{CaCO_3}$
BET	1.77	1.43	2.22	2.2	-	22
HCl absorption capacity	0.92	2.64	2.85	3.68	3.61	5.63

It is noteworthy that the thermogravimetric data showed that the exposure of pure Fe_2O_3 to HCl results in a decrease of Fe_2O_3 mass that indicates formation of gaseous iron chlorides, e.g., Fe_2Cl_6, $FeCl_3$, etc.. Table 6.7 shows reactions that can explain the formation of iron chlorides by HCl - Fe_2O_3 system in the temperature range 100-350^{o}C. These reactions were found in literature or determined based on Gibbs energy minimization at equilibrium state (FactSage 7 - Software).

Table 6.7: Iron chlorides formation by Fe_2O_3 - HCl reactions in the temperature range 100-350 ℃.

Reaction	Source
$1/2Fe_2O_3(s) + 3HCl(g) \rightarrow \ FeCl_3(s) + 3/2H_2O(g) \qquad T < 235^oC$	FactSage 7
$1/2Fe_2O_3(s) + 3HCl(g) \rightarrow \ FeCl_3(g) + 3/2H_2O(g) \qquad T > 316^oC$	FactSage 7
$Fe_2O_3(s) + 6HCl(g) \rightarrow \ Fe_2Cl_6(g) + 3H_2O(g)$	Gregory [24]
$Fe_2O_3(s) + 2HCl(g) \rightarrow \ 2FeOCl(s) + H_2O(g)$	Gregory [24]
$6FeOCl(s) \rightarrow \ 2Fe_2O_3(s) + Fe_2Cl_6(g)$	Gregory [24]
$Fe_2O_3(s) + 6HCl(g) \rightarrow \ 2H_2OFeCl_3(g) + H_2O(g)$	Gregory [24]
$Fe_2Cl_6(g) \rightarrow \ 2FeCl_3(g) \qquad T > 300^oC$	Rustad and Gregory [25]
$Fe_2Cl_6(g) \rightarrow \ 2FeCl_2(s) + Cl_2(g)$	Rustad and Gregory [25]

An investigation on solid iron chlorides formation by HCl - Fe_2O_3 reaction in the temperature range 90-350^{o}C was conducted based on XPS analysis of Fe_2O_3 and Fe_2O_3 - $AlCl_3 \cdot 6H_2O$ (layered structure samples - mass ratio of $AlCl_3 \cdot 6H_2O$ to Fe_2O_3: 4.54) samples heated to 350^{o}C using heating rate: 15^{o}C/min (see Appendix B). The XPS spectra (Fe-2p and Cl-2p) supported the chlorine capture and a potential formation of solid iron chlorides in the case of Fe_2O_3 - $AlCl_3 \cdot 6H_2O$ samples. The enhancement of Cl-2p double peak and Fe-2p multiple peak shifting close to the electron binding energies of iron chlorides indicated the reaction of HCl with Fe_2O_3. However, the identification of the formed species was not possible.

Figure 6.15 shows the CO_2 release as function of temperature in the case of pure RM-B and RM-B - $AlCl_3 \cdot 6H_2O$ tests. Three CO_2 peaks in the temperature ranges 100-350^{o}C, 450-620^{o}C, and 640-800^{o}C were detected in the case of RM-B - $AlCl_3 \cdot 6H_2O$ samples. Furthermore, these peaks indicate a similar CO_2 release. The observed CO_2 release ($\sim 3 \cdot 10^{-4}$ mol) in the temperature range 100-350^{o}C corresponds to the temperature range of $AlCl_3 \cdot 6H_2O$ thermal dissociation (HCl release between 90 and 350^{o}C), and consequently it is related to the HCl reaction with raw meal compounds. The molar ratio of the absorbed HCl to the released CO_2 is 4; the stoichiometry of the direct reaction of HCl with $CaCO_3$ ($CaCl_2$ formation based on equation 4.28 - Chapter 4) corresponds to 2. This implies that only a fraction of the absorbed HCl reacts directly with $CaCO_3$ and/or the produced CO_2 is consumed by the sample. It is noteworthy that XRD analysis detected formation of $CaCl_2 \cdot 2H_2O$ (sinjarite) and ankerite ($Ca(Fe,Mg,Mn)(CO_3)_2$) at the contact interface of RM-B and $AlCl_3 \cdot 6H_2O$ in the case of RM-B - $AlCl_3 \cdot 6H_2O$ samples heated to 310^{o}C and 380^{o}C (see Appendix C). Therefore, the experimental data support the simultaneous formation of $CaCl_2$ and CO_2 release due to the reaction of raw meal with the released HCl from the thermal dissociation of $AlCl_3 \cdot 6H_2O$.

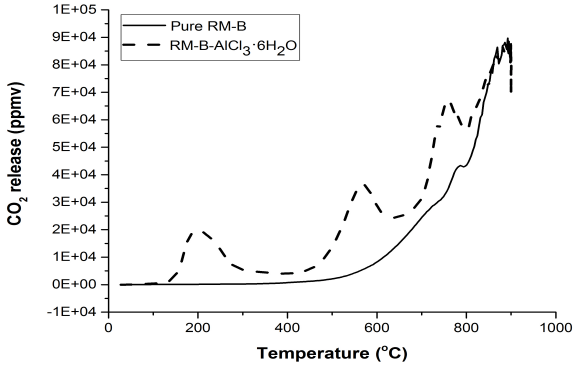

Figure 6.15: CO_2 release from pure RM-B: 1411mg and RM-B - $AlCl_3 \cdot 6H_2O$ (RM-B: 1475mg and $AlCl_3 \cdot 6H_2O$: 102mg), using CO_2 IR-spectrum band: 2200-2450 cm^{-1}, heating rate: 15 ℃/min, and carrier gas (N_2) flow rate: 50 Nml/min.

The presence of CO_2 release in the temperature ranges 450-620^{o}C and 640-800^{o}C indicates that the HCl - raw meal reaction products react again and/or decompose at temperatures above 400^{o}C and release CO_2. For instance, the CO_2 release between 450^{o}C and 620^{o}C can be explained by a secondary HCl release from $CaCl_2$ reactions (6.2 - 6.3) [26], considering the presence of H_2O vapour, CO_2, and HCl reaction with $CaCO_3$ and CaO.

$$CaCl_2(s) + H_2O(g) \rightarrow \ Ca(OH)Cl(s) + HCl(g) \quad (410 - 740^oC) \tag{6.2}$$

$$Ca(OH)Cl(s) + CO_2(g) \rightarrow \ CaCO_3(s) + HCl(g) \quad (410 - 740^oC) \tag{6.3}$$

Similarly, the CO_2 release between 640^{o}C and 800^{o}C can be related to a secondary release of HCl (6.4 - 6.6) [26, 27] and/or thermal dissociation of formed $Ca(Fe,Mg,Mn)(CO_3)_2$ compounds. Thermal analysis studies of dolomites - feroan dolomites showed the presence of multi-stage thermal decomposition mechanisms and relatively high decomposition temperatures between 660^{o}C and 950^{o}C for $CaMg(CO_3)_2$ and $Ca(MgFe)(CO_3)_2$, which are affected by CO_2 partial pressure [28, 29].

$$Ca(OH)Cl(s) \rightarrow \ CaO(s) + HCl(g) \quad (640 - 740^oC) \tag{6.4}$$

$$CaCl_2(s) + H_2O(g) + CO_2(g) \rightarrow \ CaCO_3(s) + 2HCl(g) \quad (> 410^oC) \tag{6.5}$$

$$CaCl_2(s) + 2H_2O(g) + SiO_2(s) \rightarrow \ CaSiO_3(s) + 2HCl(g) \quad (> 600^oC) \tag{6.6}$$

Figure 6.16 illustrates the CO_2 release curves from HCl absorption tests using RM-B, reagent grade $CaCO_3$, CaFe2, SR, and CaAlFe. The Fe_2O_3 containing samples showed a wide CO_2 peak in the temperature range 100-300^{o}C in contrast with reagent grade $CaCO_3$ that has two separated CO_2 release peaks at 160^{o}C and 300^{o}C. This is a strong indication that Fe_2O_3 participates in the HCl absorption mechanism through a HCl - Fe_2O_3 - Fe_yCl_x - $CaCO_3$ reaction system, where iron chlorides are formed as intermediate products by HCl - Fe_2O_3 reaction and react with $CaCO_3$ in a

second stage . The presence of only two CO_2 release peaks in the case of lab prepared mixtures (SR, CaFe2, and CaAlFe) in contrast with the three peaks of RM-B is also discernible. Furthermore, the temperature range of the second CO_2 peak varies with the tested mixture composition. The SiO_2 containing mixture (SR) has a wide second CO_2 release peak corresponding to the temperature range 480-700^{o}C. The SiO_2 free mixtures (CaFe2 and CaAlFe) showed the second CO_2 release between 580^{o}C and 750^{o}C.

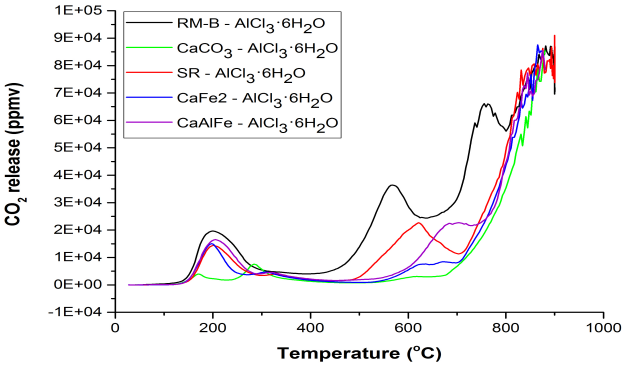

Figure 6.16: CO_2 release curves of TGA-FTIR absorption tests, using RM-B, reagent grade $CaCO_3$, SR, CaFe2, CaAlFe, tested material mass: $\sim$ 1450mg, $AlCl_3 \cdot 6H_2O$: 102mg heating rate: 15 ℃/min and carrier gas (N_2) flow rate: 50 Nml/min.

It is well known in the case of PVC dehydroclorination that metal oxides with large metal ion radius, e.g., Fe_2O_3, attract chlorine and weaken C-Cl bonds [30]. Furthermore, the formation of Fe_yCl_x species as HCl - Fe_2O_3 reaction products in the temperature range 140-400^{o}C was reported [24-25, 30-31]. In applications of CaO - Fe_2O_3 and $CaCO_3$ - Fe_2O_3 catalysts, the formation of intermediated iron chloride species , which react via ion exchange with CaO and $CaCO_3$ in the temperature range 200-500^{o}C was also reported [32, 33]. Table 6.8 presents potential reactions, which can explain the HCl absorption between 100^{o}C and 350^{o}C, involvement of Fe_2O_3, and formation of iron chlorides and $Fe_x(CO_3)_y$ species ($FeCO_3$ thermal dissociation: 400-580^{o}C [34]).

The presented data support the enhancement of $CaCO_3$ chlorination in presence of Fe_2O_3. Table 6.9 shows the BET area, Fe_2O_3 content, and HCl absorption capacity ratios of Fe_2O_3 containing mixtures to CaFe1. It is concluded that the Fe_2O_3 content cannot quantitatively be connected with the HCl absorption capacities of the tested mixtures.

Table 6.8: Potential HCl reactions that can explain the HCl absorption between 100 ℃ and 350 ℃, involvement of iron chloride species, and formation of $CaCl_2$ and $Fe_x(CO_3)_y$ species.

Reaction	Source
$2HCl(g) + CaCO_3(s) \rightarrow\ CaCl_2(s) + H_2O(g) + CO_2(g)$	FactSage 7
$2FeCl_3(g) + 3CaCO_3(s) \rightarrow\ 3CaCl_2(s) + Fe_2O_3(s) + 3CO_2(g)$	FactSage 7
$2FeCl_3(s) + 3CaCO_3(s) \rightarrow\ 3CaCl_2(s) + Fe_2(CO_3)_3(s)$	-
$FeCl_2(s) + CaCO_3(s) \rightarrow\ CaCl_2(s) + FeCO_3(s)$	FactSage 7
$FeCO_3(s) + 2HCl(g) \rightarrow\ FeCl_2(s) + H_2O(g) + CO_2(g)$	FactSage 7

Table 6.9: HCl absorption capacity, Fe_2O_3 content and BET area ratios of Fe_2O_3 containing mixtures to CaFe1.

Ratio	$\frac{CaFe2}{CaFe1}$	$\frac{SR}{CaFe1}$	$\frac{CaAlFe}{CaFe1}$	$\frac{RM-B}{CaFe1}$
BET area	1.55	1.54	-	15.35
Fe_2O_3 content	2.3	1.12	2.3	0.8
HCl absorption capacity	1.08	1.39	1.37	6.05

6.2.4 Conclusions on TGA-FTIR Data

The purposes of TGA-FTIR activities were the evaluation of TGA-FTIR method for the fast screening of HCl absorption capacity of industrial raw meals and investigation of the effects of raw meal compounds on $CaCO_3$ chlorination. The main conclusions can be summarized as follows:

- Fast Screening of HCl Absorption Capacity: The obtained TGA-FTIR data showed that the absorption mechanism of HCl in TGA-FTIR tests significantly differs from that in fixed-bed tests. The evaluation of HCl absorption by raw meals gave active compound conversion between 5.6% and 7.3%; consequently, the mechanism of HCl absorption in TGA-FTIR tests does not correspond to a surface saturation phenomenon. However, TGA-FTIR method detected that RM-B has higher reactivity with HCl than RM-A which is consistent with fixed-bed results. Furthermore, the TGA-FTIR study showed that the Fe_2O_3 content of industrial raw meals cannot directly be connected with the HCl absorption capacity of raw meal. On other

hand, the industrial raw meal with the larger BET area also had higher HCl absorption capacity.

- Evaluation of the Effects of Raw Meal Compounds: The experimental activities showed that SiO_2 and Al_2O_3 did not enhance the chlorination of reagent grade $CaCO_3$ in the temperature range 90-350^oC. SiO_2 behaved as an inert material in the aforementioned temperature range. On the other hand, the presence of Fe_2O_3 significantly enhanced the $CaCO_3$ chlorination. However, a quantitative relation between Fe_2O_3 content and HCl absorption could not be established.

6.3 References

[1] Kobayashi, Y., Method of Purifying Exhaust Gas, U.S. patent: 4726940 A, 1986.

[2] Karlsson, H.T., Klingspor, J., and Bjele, I., Absorption of Hydrochloric Acid on Solid Slaked Lime for Fluel Gas Clean Up, Air Pollution Control Association, vol.31, pp.1177-1180, 1981.

[3] Klingspor, J., Karlsson, H.T., and Bjerle, I., A Kinetic Study of the Dry SO_2 - Limestone Reaction at Low Temerature, Chemical Engineering Communication, vol.22, pp.81-103, 1983.

[4] Kunii, D. and Levenspiel, O., Fluidization Engineering, Butterworth-Heinemann, 2nd Edition, pp.77-78, 1991, ISBN: 0-409-90233-0.

[5] Linee, M., Klingspor, J., Karlsson, H.T., and Bjerle, I., Limestone Based Wet - Dry Scrubbing to Form Gypsum, Chemical Engineering Science, vol.37, pp.807, 1982.

[6] Duo, W., Kirkby, N.F., Seville, J.P.K., Kiel, J.H.A., Bos, A. and Den Uil, H., Kinetics of HCl Reactions with Calcium and Sodium Sorbents for IGCC Fuel GAs Cleaning, Chemical Engineering Science, vol.51, pp.2541-2546, 1996.

[7] Fonsenca, A.M., Órfaõ, J.J., and Salcedo, R.L., Kinetic Modelling of the Reaction of HCl and Solid Lime at Low Temperatures, Industrial & Engineering Chemistry Research, vol.37, pp.4570-4576, 1998.

[8] Gregg, J.M., Bish, D.L., Kaczmarek, S.E., and Machel, H.G., Mineralogy, Nucleation and Growth of Dolomite in the Laboratory and Sedimentary Environment: A review, International Association of Sedimentology, vol.62, pp.1749-1769, 2015.

[9] Hansen, P.J., SO_2 Emissions from Cement Plant Production, PhD Dissertation, Technical University of Denmark, 2003, ISBN: 87-90142-96-9.

[10] Klingspor, J., Stromberg, A.M., Karlson, H.T., and Bjerle, I., Similarities between Lime and Limestone in Wet - Dry Scrubbing, Chemical Engineering and Processing: Process Intensification, vol.18, pp.239-247, 1983.

[11] Kumar, G.S., Ramakrishman,A., and Hung,Y.T., Advanced Physico-Chemical Treatment Technologies - Handbook of Environmental Engineering, Humana Press, vol.5, pp.611-633, 2007, eISBN: 1-59745-173-8.

[12] Borgwardt, R.H., Calcium Oxide Sintering in Atmospheres Containing Water and Carbon Dioxide, Industrial Engineering & Chemistry Research, vol.28, pp.493-500, 1989.

[13] Grim, R.E, Clay Mineralogy, McGraw-Hill Book Company, Inc., 2nd Edition, 1968, ISBN-10: 0070248362.

[14] Grim, R. E. and Brandley, W.F., Rehydration and Dehydration of the Clay Minerals, American Mineralogist, vol.33, pp.50-59, 1948.

[15] Jozewicz, W., Chang, J.C.S., and Sedman, C.B., Bench-Scale Evaluation of Calcium Sorbents for Acid Gas Emission Control, Environmental Progress, vol. 9, pp. 137-142, 1990.

[16] Takeshi, S., Toshikatsu, H., and Hiroshi, Y., Vapor Pressure of Binary (H_2O-HCl, -$MgCl_2$, and -$CaCl_2$) and Ternary (H_2O-$MgCl_2$-$CaCl_2$) Aqueous Solutions, Journal of Chemical and Engineering Data, vol.30, pp.224-227, 1985.

[17] Weinell, C. E., Jensen, P. I. , Dam-Johansen, K., Livbjerg, H., Hydrogen-chloride reaction with lime and limestone - kinetics and sorption capacity, Industrial & Engineering Chemistry Research, vol.31, pp. 164-171, 1992.

[18] Chisholm, P.N., and Rochelle, G.T., Dry Absorption of HCl and SO_2 with Hydrated Lime from Humidified Flue Gas, Industrial Engineering & Chemistry Research, vol.38, pp. 4068-4080, 1999.

[19] Mura, G. and Lallai, A., Reaction kinetics of gas hydrogen chloride and limestone, Chemical Engineering Science, vol. 49, pp.4491-4500, 1994.

[20] Gullett, B.K., Jozewicz, W. and Stefanski, L.A., Reaction Kinetics of Ca-Based Sorbents with HCl, Industrial & Engineering Chemistry Research, vol.31, pp.2437-2446, 1992.

[21] Hartman, H., Trnka O. and Solcova O., Thermal Decomposition of Aluminum Chloride Hexahydrate, Industrial & Engineering Chemistry Research, vol.44, pp.6591-6598, 2005.

[22] Naumann, R., Petzold, D., Paulik, F., and Paulik, J., Studies on Themal-Decomposition of Aluminium Chloride Hexahydrate Under Dynamic and Quasi-Isothermic Conditions, Journal of Thermal Analysis and Calorimetry, vol. 15, pp.47, 1979.

[23] Lide, D.R., and Haynes, W.M., CRC Handbook of Chemistry and Physics, 90th Edition, Taylor and Francis Group, pp.4.45, 2009, ISBN-13: 978-1-4200-9084-0.

[24] Gregory, N.W., Evidence for Volatile Compounds in Fe_2O_3-HCl-H_2O-$FeCl_3$ System, Inorganic Chemistry, vol.22, pp.3750-3754, 1983.

[25] Rustad, D.S. and Gregory, N.W., Vapor Pressure of Iron (III) Chloride, Journal Chemical Engineering Data, vol.28, pp.151-155, 1983.

[26] Fraissler, G., Jller, M., Brunner, T., and Obernberger, I., Influence of Dry and Humid Gaseous Atmosphere on the Thermal Decomposition of Calcium Chloride and its Impact on the Remove of Heavy Metals, Chemical Engineering and Processing, vol.48, pp.380-388, 2009.

[27] Matsuda, H., Ozawa, S., Naruse, K., Ito, K., Kojima,Y., and Yanase, T., Kinetics of HCl Emission from Inorganic Chlorides in Simulated Municipal Wastes Incineration Conditions, Chemical Engineering Science, vol.60, pp.545-552, 2005.

[28] Milodowski, A.E., Morgan, D.J., and Warne, S.S.J., Thermal Analysis Studies of the Dolomite-Ferroan-Domite-Ankerite Series, II Decomposition Mechanism in Flowing CO_2 Atmosphere, Thermochimica Acta, vol.152, pp.279-297, 1989.

[29] Valverde, J.M., Perejon, A., Medina, S., Perez-Maqueda, L.A., Thermal Decomposition of Dolomite Under CO_2: Insights from TGA and in Situ XRD Analysis, Physical Chemistry Chemical Physics, vol.17, pp.30162-30176, 2015.

[30] Blazo, M., and Jakab, E., Effect of Metal Oxides and Caboxylates on the Thermal Decomposition Processes of Poly(vinylchloride), Journal of Analytical and Applied Pyrolysis, vol.49, pp.125-143, 1999.

[31] Iida,T., and Goto, K., Investigations on Poly(vinyl chloride). III. Effects of Metal Oxides Upon Thermal Decomposition of Poly(vinyl chloride), Journal of Polymer Science, vol.15, pp.2427-2433, 1977.

[32] Decjer, S., Klabunde,J., Khaeel, A., and Klaubunde,K.J., Catalyzed,Destructive Adsorption of Environmental Toxins with Nanocrystalline Metal Oxides. Fluoro-, Chloro-, Bromocarbons, Sulfur, and Organophosophorus Compounds, Environmental Science and Technology, vol.36, pp.762-768, 2002.

[33] Ma, X., Sun, Q., Feng, X., He, X., Guo, J., Sun, H., Cao,H., Catalytic Oxidation of 1,2-dichlorobenzene over $CaCO_3$/a-Fe_2O_3 Nanocomposite Catalysts, Applied Catalysis A: General, vol.450, pp. 143-151, 2013.

[34] Gallagher, P.K., and Warne, S.S.J., Thermomagnetometry and Thermal Decomposition of Siderite, Thermocimica Acta, vol.43, pp.253-267, 1981.

Chapter 7

Modelling of HCl Absorption in Fixed-bed Tests

This section presents the modelling of HCl absorption data from fixed-bed tests. The experimental results analysis showed that the mechanism of HCl absorption by raw meal at low temperatures (less than 180^oC) seems consistent with a surface saturation phenomenon. Raw meal is characterized by a HCl absorption capacity that is affected by the temperature, gas phase moisture content, and raw meal moisture content. In addition, the HCl absorption by raw meal is controlled by the mass transfer through the external gas film of particles and active surface conversion. Furthermore, the model assumes that the reaction of HCl with raw meal is irreversible. The fixed-bed model must take into account the aforementioned characteristics and simulate the influence of parameters that affect HCl saturation capacity of raw meal.

7.1 Fixed-bed Model Principles

The basic principles and assumptions of the fixed-bed model are presented in this section. The experimental results (see Chapter 6, section: 6.1.3) indicated the involvement of absorbed water in the mechanism of HCl absorption by raw meal at low temperatures. This work assumes that the mechanism of HCl absorption by raw meal corresponds to a rapid irreversible surface reaction that can be expressed as a consumption of active sites on the external surface of raw meal particles (HCl absorption only occurs on active sites). Moreover, raw meal is characterized by a HCl saturation capacity determined by the physical and chemical properties of raw meal and experimental conditions (temperature, gas phase moisture content and raw meal moisture content). The ratio of specific active surface area to specific HCl saturation capacity is constant and independent of the experimental conditions. The effect of the absorbed water is taken into account as an equivalent active sites (active surface) generation. Therefore, it affects only the HCl saturation capacity of raw meal, and consequently it does not influence the reaction rate.

Table 7.1 summarizes the basic assumptions of the fixed-bed model.

Table 7.1: Basic assumptions of the fixed-bed model.

- HCl absorption by raw meal is based on a rapid and irreversible surface reaction.
- Reaction only occurs on active sites on the external surface of raw meal particles
- Active sites correspond to a certain HCl saturation capacity and active surface area.
- The ratio of specific active surface area to specific HCl saturation capacity of raw meal is constant and independent of the experimental conditions.
- Water effect corresponds to change in the HCl saturation capacity.
- The absorption of water does not influence the reaction rate.
- Spherical active particles with diameter equal to that of the mean raw meal particles size.
- Spherical inert particles (diluting agent-fused silica).
- Gas film diffusion and active surface (active sites) conversion control the HCl absorption reaction.
- Uniform gas phase and isotropic solids.
- The particles size and shape are unaffected by the HCl exposure.
- No axial dispersion.
- Incompressible gas phase.
- Sample has constant and homogeneous temperature.

7.2 Mathematical Model Description

The mathematical fixed-bed model description is based on the mass balance in a control volume of sample bed (Figure 7.1), assuming that the reaction is controlled by gas film diffusion and conversion of active surface with exposure time. Therefore, the mathematical description is based on the mass balance in gas and solid phases and presented in Appendix D.

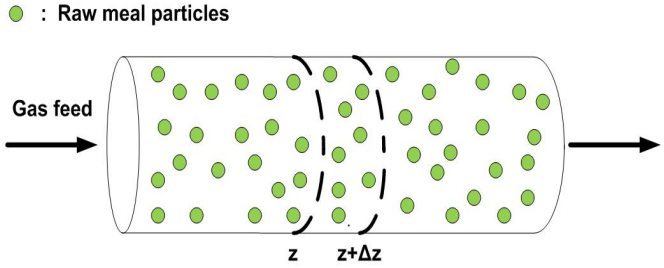

Figure 7.1: Shematic illustration of a packed bed reactor.

The HCl reaction rate as function of the position(z) in sample and exposure time (t) considering that the reaction only occurs on the external surface of particles:

$$r_{HCl}(z,t) = k_g \cdot C_{HCl}(z,t) \cdot (1 - X_s(z,t)) \qquad [\frac{mol}{m^2_{solid-active} \cdot s}] \tag{7.1}$$

where k_g is the mass transfer coefficient, C_{HCl} (z,t) is the HCl concentration in gas phase, and X_s (z,t) is the conversion of active surface (layer).

The HCl concentration in gas phase as function of the position in sample and exposure time:

$$\epsilon \cdot \frac{\partial C_{HCl}(z,t)}{\partial t} + U \cdot \frac{\partial C_{HCl}(z,t)}{\partial z} = -r_{HCl}(z,t) \cdot \rho_{bed} \cdot X_{RM} \cdot S_{act.} \tag{7.2}$$

where ϵ is the void fraction of sample bed, C_{HCl} (z,t) is the HCl concentration in gas phase, U is the fitration velocity (free stream velocity), r_{HCl}(z,t) is the reaction rate, ρ_{bed} is the density of sample bed, X_{RM} is the raw meal mass fraction of the tested sample (diluted samples), and $S_{act.}$ is the specific active surface area of raw meal particles.

As shown in Chapter 6 (section 6.1.2), the breakthrough time Δt_B corresponds to a very fast reaction (almost instantaneous), and its duration is determined by the feed rate of HCl and HCl saturation capacity of raw meal. The conversion rate of the active surface area (layer) as function of the position in the sample and exposure time:

$$\frac{\partial X_s(z,t)}{\partial t} = k_g \cdot C_{HCl}(z,t) \cdot (1 - X_s(z,t)) \cdot \frac{S_{act.}}{k_{ws} \cdot k_{wg} \cdot Cap_{ref.}} \tag{7.3}$$

where Cap_{ref} is the specific HCl saturation capacity of raw meal at reference conditions (raw meal moisture content, gas phase moisture, and fixed-bed temperature), k_{ws} is the sample moisture

content coefficient that represents the sample moisture content effect on the reference HCl saturation capacity, and k_{wg} is the gas phase moisture content coefficient that represents the gas phase moisture effect on the reference HCl saturation capacity.

Table 7.2 shows the initial, boundary, and continuous flow conditions that were used in the fixed-bed model numerical solution (see Appendix D).

Table 7.2: Initial, boundary and continuous flow conditions of fixed-bed model.

Initial conditions:	t=0	C_{HCl}(z,0)=0	X_s(z,0)=0
Boundary conditions:	z=0	C_{HCl}(0,t)=$C_{HCl-feed}$	X_s(0,t)=1
Continuous flow:	$0 < t < \infty$	C_{HCl}(0,t)=$C_{HCl-feed}$	

7.3 Calculation of Mass Transfer Coefficient

The determination of mass transfer coefficient was required for the simulation of fixed-bed experimental data. This was based on the selection of an appropriate Sherwood number expression which considered the flow dynamic parameters and presence of a sample bed characterized by low content of active compound (the raw meal particles are dispersed in diluted samples). It is noteworthy that the experimental tests were characterized by very low particle Reynolds number ~ 0.1.

7.3.1 Flow Dynamic Parameters

This section presents the basic expressions which were used in the calculation of the experimental flow dynamic parameters. The physical properties of dry nitrogen [1], e.g., dynamic viscosity, were used for the simulation of gas phase. The value of the diffusion coefficient of HCl in N_2 [2] was also used.

Particle Reynolds number:

$$Re = \frac{U \cdot \rho_{fluid} \cdot d_p}{\mu} \tag{7.4}$$

where U is the free stream velocity of fluid in the reactor tube, ρ_{fluid} is the density of fluid, d_p is the particle diameter, and μ is the dynamic viscosity of fluid.

Prandtl number:

$$Pr = \frac{\mu \cdot C_p}{k_t} \tag{7.5}$$

where μ is the dynamic viscosity of fluid, C_p is the specific heat capacity of fluid, and k_t is the thermal conductivity of fluid.

Schmidt number:

$$Sc = \frac{\nu}{D_{HCl-N_2}} \tag{7.6}$$

where ν is the kinematic viscosity of fluid and D_{HCl-N_2} is the diffusion coefficient of component HCl in medium N_2.

Péclet number:

$$Pe = Re \cdot Sc \tag{7.7}$$

where Re is the particle Reynolds number and Sc is the Schmidt number.

Sherwood number:

$$Sh = \frac{k_g \cdot d_p}{D_{HCl-N_2}} \tag{7.8}$$

where k_g is the mass transfer coefficient of an active sphere in fluid flow, d_p is the particle diameter, and D_{HCl-N_2} is the diffusion coefficient of component HCl in medium N_2.

7.3.2 Selection of Sherwood Number Expression

The calculation of mass transfer coefficient in fixed-beds in presence of very low Reynolds numbers is a difficult and controversial issue [3-5]. The minimum value of Sh in the case of an isolated active sphere in a stagnant fluid is 2 [6]. However, Cornish [7] suggested that when an active sphere is entirely surrounded by other active spheres the value of Sh approaches zero. Similarly, the work of Scala [8] on the mass transfer around freely moving active particles in fluidized bed of inert particles argued for a correction of Sh limiting value 2 when the active sphere is in a bed of inert particles due to the decrease in the available fluid volume, and the effect of the moving inert particles on the fluid flow and boundary layer formation. Furthermore, the mass transfer model of Nelson and Galloway [9] for packed and fluidized beds of fine particles predicted that at low Reynolds numbers the value of Sh is much lower than 2 and approaches zero when $Re \rightarrow 0$.

Scala [5] proposed models for the calculation of effective (Sh_{eff}) and local Sherwood numbers (Sh^*) in the case of multiparticle systems (mixtures of active and inert particles). Sh^* depends only on the geometrical and fluid-dynamics parameters. On the contrary, Sh_{eff} also depends on the assumptions made in deriving the mass balance equations across the bed and corresponds to the bed average Sherwood number [5].

The calculation of Sh^* is based on a concentration difference close to the active particle and the dividing of unit bed volume into a number of "non-overlapping cells with an active bed particle at their centers" [5]. Scala [5] suggested the Sh^* calculation as follows:

$$Sh^* = \frac{2 \cdot \frac{\epsilon}{\tau}}{1 - \sqrt[3]{(1-\epsilon) \cdot \Omega}} + b \cdot (\frac{Re}{\epsilon})^c \cdot Sc^d \tag{7.9}$$

where, ϵ is the void fraction of bed sample, τ is the tortuosity, Ω is the volume fraction of active bed particles with respect to the total volume occupied by inert and active solids, Re is the particle Reynolds number, Sc is the Schmidt number, and b, c and d are parameters of a Frössling-type equation for fixed bed. In this work the calculation of Sh^* is based on 7.9, with ϵ=0.5 [5], τ=1.4[10], b=0.6 [11], c=0.5 [11], and d=1/3 [11].

Sh_{eff} [5] was calculated as follows:

$$Sh_{eff} = \frac{Pe^2}{12 \cdot (1-\epsilon) \cdot \Omega \cdot \frac{\epsilon}{\tau}} \cdot (\sqrt{1 + \frac{24 \cdot (1-\epsilon) \cdot \Omega \cdot \frac{\epsilon}{\tau} \cdot Sh^*}{Pe^2}} - 1) \tag{7.10}$$

where ϵ is the void fraction of sample bed, τ is the tortuosity, Ω is the volume fraction of active bed particles with respect to the total volume occupied by inert and active solids, Pe is the P*éclet* number, and Sh^* local Sherwood number.

The present fixed-bed model uses Sh_{eff} (bed average Sh) for the determination of k_g due to the fact that both the fixed-bed absorption model and Sh_{eff} consider the fixed bed as a plug flow reactor. The values of Sh^* and Sh_{eff} at 100^{o}C for RM-A considering Ω equal to 0.075 and the aforementioned bed characteristics are 1.32 and 0.28, respectively.

7.4 Fixed-bed Model Evaluation

The evaluation of fixed-bed model performance is based on its ability to predict the experimental breakthrough time Δt_B (see Chapter 6, section 6.1) as function of the raw meal content of sample, physical and chemical characteristics of raw meal, e.g., HCl saturation capacity and specific active surface area, and moisture content of gas phase and solids. Furthermore, an analysis of the sensitivity of fixed-bed model to Sh values and discretization grid was done.

7.4.1 Model Performance at 100^{o}C - Dry Gas Phase

The fixed-bed model was evaluated based on the prediction of breakthrough time Δt_B in the case of diluted raw meal samples characterized by constant total mass (9g) and varying raw meal content (0.15g, 0.3g and 0.6g) using dry gas phase at 100^{o}C. The simulation results were compared with the presented experimental data in Chapter 6 (section 6.1.2). Furthermore, the model application was tested for RM-A and RM-B considering the differing physical properties (specific surface area and mean particle size) and HCl saturation capacity. The reference HCl saturation capacities (Cap_{ref}) were $2.9 \cdot 10^{-5}$ mol/g and $3.86 \cdot 10^{-5}$ mol/g for RM-A and RM-B, respectively (see Chapter 6, section 6.1.2). These values correspond to experimental activities using undried samples and dry gas phase at 100^{o}C which were also the conditions of the experiments. Therefore, k_{ws} and k_{wg} coefficients (7.3) are equal to 1. The ratio of the specific active surface area to specific HCl saturation capacity was determined based on the experimental data at 100^{o}C - dry gas phase, assuming that the active surface layer depth was equal to calcite unit cell hight (see Chapter 6, section 6.1.2).

Figure 7.2 - A shows the simulated HCl - time responses at the outlet of fixed-bed reactor as function of RM-A content using diluted raw meal samples with total mass equal to 9g. It is clearly seen that the calculated responses have a step shape. The breakthrough time Δt_B seems proportional to the raw meal content of samples.

Figure 7.2 - B shows the corrected experimental (see Chapter 6, section 6.1.2) and simulated breakthrough times as function of raw meal content in the diluted raw meal samples with total mass equal to 9g. It is clearly seen that the model gives almost identical breakthrough times to the corrected experimental values.

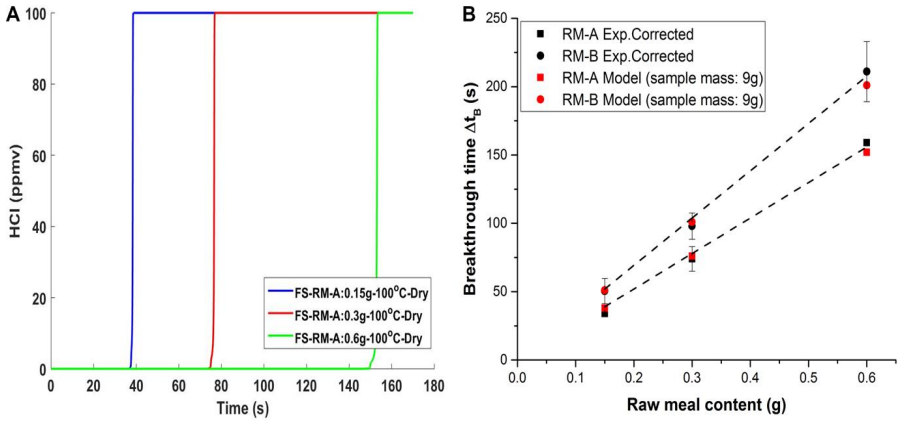

Figure 7.2: A) HCl - time response curves obtained by fixed-bed model, using diluted raw meal samples with total mass 9g and varying RM-A content: 0.15g, 0.3g and 0.6g, ϵ: 0.5, τ: 1.4, Sh: Sh_{eff}-model ,HCl concentration: 100ppmν, T: 100 ℃, dry gas phase, Δz: $8 \cdot 10^{-6}$s, Δt: $5 \cdot 10^{-6}$s, and volumetric gas flow: 1.5Nl/min; B) Experimental and simulated breakthrough times as function of raw meal content, using diluted raw meal samples (total mass: 9g), HCl concentration: 100ppmν, ϵ: 0.5, τ: 1.4, Sh: Sh_{eff}-model, T: 100 ^oC, dry gas phase, Δz: $8 \cdot 10^{-6}$s, Δt: $5 \cdot 10^{-6}$s, and volumetric gas flow: 1.5 Nl/min. The experimental results are corrected for agglomeration effects (see Chapter 6 - section 6.1.1).

Figure 7.3 shows the propagation of HCl concentration and active surface conversion fronts in fixed-bed sample as function of time. The reacted zone is characterized by complete active surface conversion (X_s: 1) and HCl concentration equal to that of the feed (HCl: 100ppmv).

The fixed-bed model evaluation at 100^{o}C showed that the model has acceptable performance in the case of diluted samples using dry gas phase. Furthermore, it was shown that the consideration of the raw meal related parameters: (i) specific HCl saturation capacity, (ii) specific active surface area and (iii) mean particles size (through Sherwood number), allows the model use for the prediction of HCl absorption by different raw meals at varying conditions.

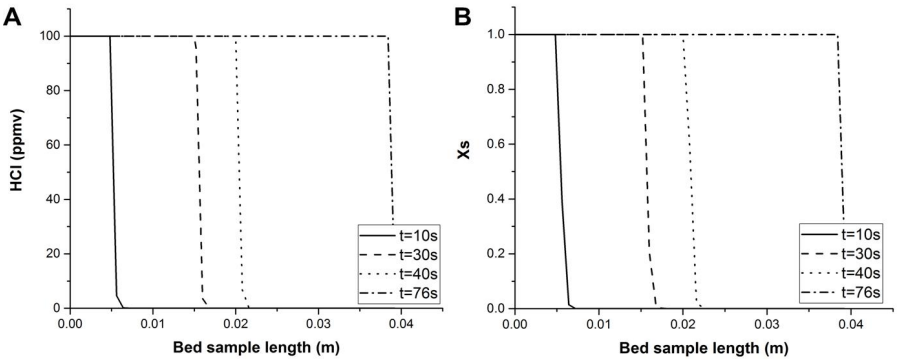

Figure 7.3: A) HCl front propagation as function of time, using diluted raw meal samples with total mass 9g and varying RM-A content: 0.3g, ϵ: 0.5, τ: 1.4, Sh: Sh_{eff} - model, HCl concentration: 100ppmν, T: 100 ℃, dry gas phase, bed sample length: 0.04m, Δz: $8 \cdot 10^{-6}$s, Δt: $5 \cdot 10^{-6}$s, and volumetric gas flow: 1.5Nl/min; B) Active surface conversion as function of time, using diluted raw meal samples with total mass 9g and varying RM-A content: 0.3g, ϵ: 0.5, τ: 1.4, Sh: Sh_{eff} - model, HCl concentration: 100ppmν, T: 100 ℃, dry gas phase, bed sample length: 0.04m, Δz: $8 \cdot 10^{-6}$s, Δt: $5 \cdot 10^{-6}$s, and volumetric gas flow: 1.5Nl/min.

7.4.2 Model Performance Using Moist Gas Phase

The prediction of HCl absorption by raw meal as function of temperature using moist gas phase is a challenging issue due to the interaction of solids moisture content and gas phase moisture content. The moisture effects enter the model as two correction factors to the HCl saturation capacity. These correction factors, k_{ws} and k_{wg}, need to be determined before the use of fixed-bed model at non-dry conditions. k_{ws} is function of the fixed-bed temperature (T_{FB}) and raw meal moisture content (Y_{ws}) at dry gas phase conditions (Y_{wg}=0 % v/v). k_{wg} is function of the fixed-bed temperature, gas phase moisture content (Y_{wg}), and raw meal moisture content(Y_{ws}). This study uses the experimentally determined HCl saturation capacities (see Chapter 6, section 6.1.3) using dried samples at 200^{o}C (assuming: Y_{ws}=0%w/w) and dry gas phase (Y_{wg}=0%v/v) as a reference for HCl saturation capacities ($Cap_{ref}(T_{FB},Y_{ws},Y_{wg})$). The values of HCl saturation capacities of raw meal were corrected for the presence of agglomerates (see Chapter 6, section 6.1.2). The correction factor is assumed only to depend on the dilution ratio (dilution ratio: 29 - correction factor: 1.1), and consequently it is common to all tested conditions.

k_{ws} is expressed as follows:

$$k_{ws}(T_{FB}, Y_{ws}, Y_{wg} = 0\%\nu/\nu) = \frac{Cap(T_{FB}, Y_{ws}, Y_{wg} = 0\%\nu/\nu)}{Cap_{ref}(T_{FB}, Y_{ws} = 0\%w/w, Y_{wg} = 0\%\nu/\nu)} \tag{7.11}$$

where T_{FB} is the fixed-bed temperature, Y_{ws} is the solids moisture content, Y_{wg} is the gas phase moisture content, Cap(T_{FB}, Y_{ws}, Y_{wg}=0% v/v) is the HCl saturation capacity of raw meal with dry gas phase, Cap_{ref} (T_{FB}, Y_{ws}=0% w/w, Y_{wg}=0%v/v) is the reference HCl saturation capacity of dry raw meal at the same conditions.

The gas phase moisture content effect is negligible above 200^{o}C based on the experimental and literature data (see Chapter 6, section: 6.1.3). The model takes into account the gas phase moisture effect through the factor k_{wg}:

$$k_{wg}(T_{FB}, Y_{ws}, Y_{wg}) = \frac{Cap(T_{FB}, Y_{ws}, Y_{wg})}{Cap(T_{FB}, Y_{ws}, Y_{wg} = 0\%\nu/\nu)} \tag{7.12}$$

where Cap(T_{FB}, Y_{ws}, Y_{wg}) is the HCl saturation capacity of raw meal at the indicated temperature, gas phase moisture content and solids moisture content.

The model performance is evaluated using HCl concentration: 100 ppmv, gas phase moisture content: 5% v/v, undried fused silica-RM-A samples (fused silica: 8.7g and RM-A: 0.3g), and gas volumetric flow: 1.5 Nl/min at 100^{o}C, 150^{o}C and 180^{o}C. Table 7.3 shows the values of k_{ws} coefficient for RM-A based on equation 7.11 and the corrected fixed-bed experimental data (see Chapter 6, section 6.1.3).

Table 7.3: k_{ws} coefficient for undried raw meal samples and the corrected HCl saturation capacities of RM-A in the case of fixed-bed experiments.

	Y_{wg}	T_{FB}		
		100^{o}C	150^{o}C	180^{o}C
k_{ws}	0% v/v	3.72	2.51	2.49
Cap (mol/g)	0% v/v	$2.74 \cdot 10^{-5}$	$2.37 \cdot 10^{-5}$	$2.29 \cdot 10^{-5}$
Cap_{ref} (mol/g)	0% v/v	$7.36 \cdot 10^{-6}$	$9.41 \cdot 10^{-6}$	$9.2 \cdot 10^{-6}$

Table 7.4: k_{wg} coefficient for undried raw meal samples and the corected HCl saturation capacities of RM-A in the case of fixed-bed experiments.

	Y_{wg}	T_{FB}		
		100^{o}C	150^{o}C	180^{o}C
k_{wg}	5% v/v	1.61	1.53	1.23
Cap (mol/g)	5% v/v	$4.41 \cdot 10^{-5}$	$3.62 \cdot 10^{-5}$	$2.82 \cdot 10^{-5}$
Cap(mol/g)	0% v/v	$2.74 \cdot 10^{-5}$	$2.37 \cdot 10^{-5}$	$2.29 \cdot 10^{-5}$

Table 7.4 shows the values of k_{wg} coefficient based on equation 7.12 and the corrected HCl saturation capacities of RM-A for undried fused silica - RM-A samples (fused silica: 8.7g and RM-A: 0.3g) and gas phase moisture content: 0%v/v and 5%v/v.

The fixed-bed model simulations and corrected experimental values of breakthrough time Δt_B with moist gas phase are shown in Figure 7.4. It is clearly seen that the fixed-bed model gives a good prediction of Δt_B, although there is a small systematic underestimation. In particular, the differences between the corrected experimental values and model results increase from 2% at 100^{o}C to 5% at 180^{o}C. This is acceptable taking into account that the physical properties of gas phase correspond to dry nitrogen, the bed void (0.5 [5]) and tortuosity (1.4 [10]) were determined by literature data for spherical particles, and the correction factor for particles agglomeration was determined based on the dry gas phase tests. Therefore, the overall model performance for moist gas phase is good.

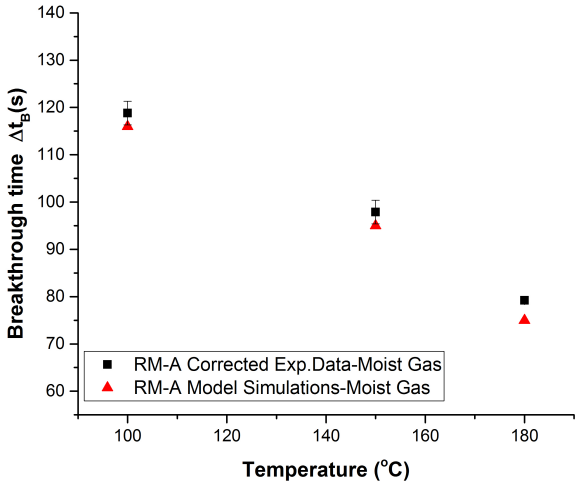

Figure 7.4: Experimental breakthrough times (corrected) and model simulations (ϵ=0.5 and τ=1.4) as function of temperature using nominal HCl concentration: 100 ppm$v$, gas phase moisture content: 5% v/v, Sh: Sh_{eff} - model, temperature: 100 °C, 150 °C and 180 °C, undried diluted RM-A samples (fused silica: 8.7g and RM-A: 0.3g), Δz: $8 \cdot 10^{-6}$s, Δt: $5 \cdot 10^{-6}$s, and gas volumetric flow: 1.5 Nl/min - HCl/N_2.

7.4.3 Model Sensitivity to Sherwood Number and Discretization Grid

This section presents the results of an analysis of model sensitivity with respect to Sherwood number and discretization steps on HCl - time responses. The model performance was studied using gas phase HCl content 100 ppmv, moisture content of gas phase: 5% v/v, temperature: 150°C, undried diluted RM-A samples (total mas: 9g and dilution ratio: 29), spatial discretization step: $4 \cdot 10^{-4}$ - $2 \cdot 10^{-3}$m, time discretization step: $5 \cdot 10^{-6}$ - $5 \cdot 10^{-5}$s , and Sh values: 0, 0.26 (Sh_{eff} - model), 1.31 (Sh* - model) and 2.

Figure 7.5 illustrates the model results for different Sh values. It is clearly seen in Figure 7.5 - A that the use of Sh values between 0.26 (Sh_{eff}) and 2 (sphere at stagnant conditions [6]) gives almost identical breakthrough times. However, Figure 7.5 - B shows that the increase of the values of Sh close to 2 results in a steeper front. Furthermore, the fixed-bed model gives breakthrough time equal to 0 for Sh equal to 0 that corresponds to absence of mass transfer, and consequently absence of reaction. The values of breakthrough time for Sh values between Sh_{eff} and 2 correspond well with the experimental results as shown in Figure 7.4. Therefore, the Sherwood number model for diluted packed beds (7.9 and 7.10) can be used for the determination of the minimum values of Sh which can be used in the fixed-bed model.

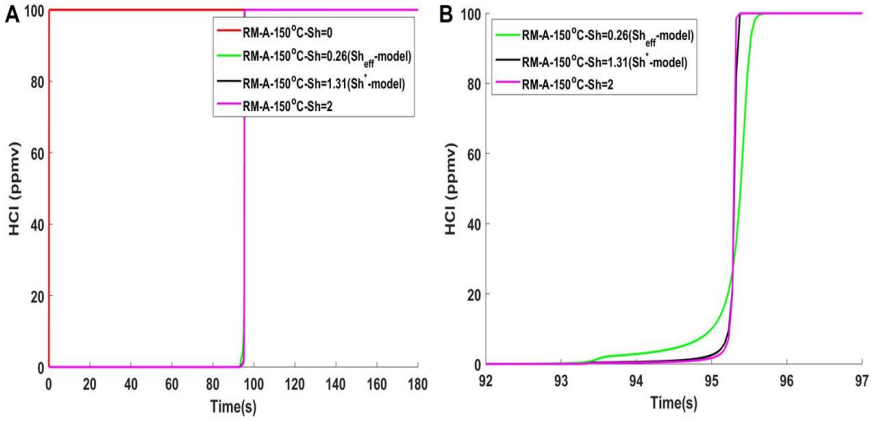

Figure 7.5: A) Model sensitivity analysis with respect to Sherwood number using HCl concentration: 100 ppmν, gas phase moisture content: 5% ν/ν, temperature: 150 °C, undried diluted RM-A samples (9g) with dilution ratio: 29, Sh: 0, 0.26 (Sh_{eff} - model), 1.31 (Sh^* - model) and 2, Δt: $5 \cdot 10^{-6}$s, Δz: $8 \cdot 10^{-4}$m and gas volumetric flow: 1.5 Nl/min - HCl/N_2; B) HCl - time response front with respect to Sherwood number using HCl concentration: 100 ppmν, gas phase moisture content: 5% ν/ν, temperature: 150 °C, undried diluted RM-A samples (9g) with dilution ratio: 29, Sh: 0.26 (Sh_{eff} - model), 1.31 (Sh^* - model) and 2, Δt: $5 \cdot 10^{-6}$s, Δz: $8 \cdot 10^{-4}$m and gas volumetric flow: 1.5 Nl/min - HCl/N_2.

Figure 7.6 shows the model sensitivity to the spatial discretization step using a constant time discretization step equal to $5 \cdot 10^{-6}$s and Sh values: 0.26 (Figure 7.6 -A) and 2 (Figure 7.6 - B). It is clearly seen that a decrease in the spatial discretization step gives longer breakthrought times and steeper fronts. However, the effect of spatial discretization step weakens with step decrease and becomes negligible for Δz close to $5 \cdot 10^{-4}$m. Furthermore, the comparison of Figure 7.6 - A and Figure 7.6 - B indicates that the effect of spatial discretization on breakthrough time does not depend on Sh value. The only discernible effect of Sh is that the simulations with Sh=2 gave sharper response fronts than the simulations with Sh=0.26.

Figure 7.7 shows the model sensitivity to time discretization step using a constant spatial discretization step equal to $8 \cdot 10^{-4}$s, and Sh equal to 2. It is clearly seen that the decrease in the time discretization step gives longer breakthrought times. However, no effect of time discretization step on the breakthrough time is observed for $\Delta t \leq 1 \cdot 10^{-5}$s.

The sensitivity analysis showed that the fixed-bed model simulates sufficiently well the experimental data using Sherwood number values between Sh_{eff} (0.26) and 2, spatial discretization step: $\leq 8 \cdot 10^{-4}$ m, and time discretization step: $1 \cdot 10^{-5}$s. Therefore, the presented simulation results (Sh_{eff}, Δz: $8 \cdot 10^{-4}$m, and Δt: $5 \cdot 10^{-6}$s) in sections 7.4.1 and 7.4.2 were not significantly affected by the discretization grid and values of Sh.

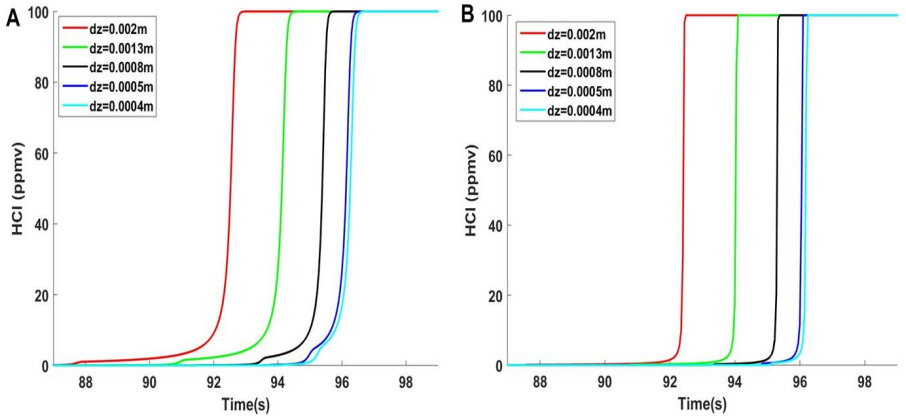

Figure 7.6: A) HCl - time response front as function of the space discretization step, using HCl concentration: 100 ppmν, gas phase moisture content: 5% ν/ν, temperature: 150 °C, undried diluted RM-A samples (9g) with dilution ratio: 29, Sh: 0.26 (Sh_{eff} - model), Δt: $5{\cdot}10^{-6}$s, Δz: $4{\cdot}10^{-4}$ - $2{\cdot}10^{-3}$m, and gas volumetric flow: 1.5 Nl/min - HCl/N_2; B) HCl - time response front as function of the space discretization step, using HCl concentration: 100 ppmν, gas phase moisture content: 5% ν/ν, temperature: 150 °C, undried diluted RM-A samples (9g) with dilution ratio: 29, Sh: 2, Δt: $5{\cdot}10^{-6}$s, Δz: $4{\cdot}10^{-4}$ - $2{\cdot}10^{-3}$m, and gas volumetric flow: 1.5 Nl/min - HCl/N_2.

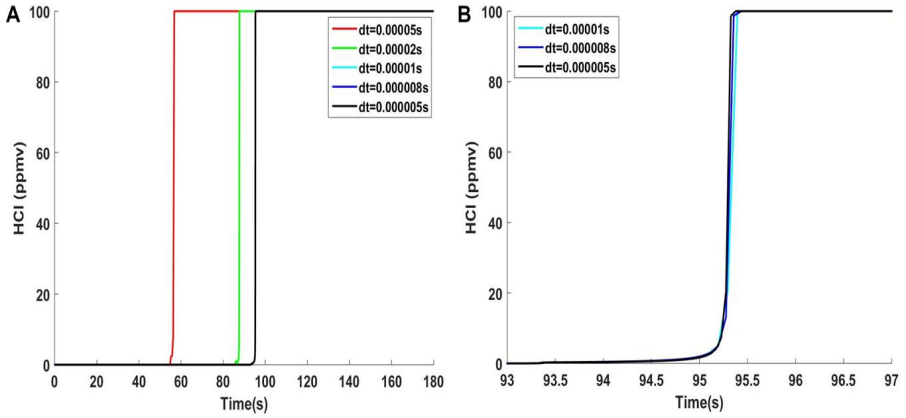

Figure 7.7: A) HCl - time response as function of the time discretization step, using HCl concentration: 100 ppmν, gas phase moisture content: 5% ν/ν, temperature: 150 °C, undried diluted RM-A samples (9g) with dilution ratio: 29, Sh: 2, Δt: $5{\cdot}10^{-6}$ - $5{\cdot}10^{-5}$s, Δz: $8{\cdot}10^{-4}$, and gas volumetric flow: 1.5 Nl/min - HCl/N_2; B) HCl - time response front as function of the time discretization step, using HCl concentration: 100 ppmν, gas phase moisture content: 5% ν/ν, temperature: 150 °C, undried diluted RM-A samples (9g) with dilution ratio: 29, Sh: 2, Δt: $5{\cdot}10^{-6}$ - $1{\cdot}10^{-5}$s, Δz: $8{\cdot}10^{-4}$, and gas volumetric flow: 1.5 Nl/min - HCl/N_2.

7.5 Conclusions on Fixed-bed Model

The developed fixed-bed model was based on the assumption that the HCl absorption by raw meal was a surface saturation phenomenon that was strongly affected by the moisture content of gas phase and sorbent. The raw meal was characterized by a specific HCl saturation capacity that depended on the experimental conditions, physical and chemical properties of raw meal, gas phase moisture content, and raw meal moisture. The model evaluation supports:

- The developed fixed-bed model can predict with sufficient accuracy HCl absorption by diluted raw meal samples in the temperature range 100-180^{o}C based on specific active surface area of raw meal particles, mean particles diameter, specific HCl saturation capacity of raw meal at the tested conditions, and diluted fixed-bed sample characteristics, e.g., the volume ratio of active particles to inert particles.

- Determination of the individual raw meal capacity is required for the simulation of the HCl absorption.

- The inclusion of gas phase moisture content and solids moisture content effects is important for the reliable model performance.

- The model has provided confirmation that that HCl absorption for short contact times may be interpreted as mass transfer controlled saturation reaction.

7.6 References

[1] Physical properties of dry nitrogen, [15 April 2018],
http://www.peacesoftware.de/einigewerte/stickstoff_e.html.

[2] Mian, A.A., Coates, J., and Cordiner, J.B., Binary Gaseous Diffusion Coefficients of N_2-HCl, A-HBr, and N_2-HBr Systems as a Function of Temperature, The Canadian Journal of Chemical Engineering, vol.47, pp. 499-502, 1969.

[3] Dwivedi, P.N., and Upadhyay, S.N., Particle-Fluid Mass Transfer in Fixed and Fluidized Beds, Industrial & Engineering Chemistry Process Design and Development, vol.16, pp. 157-165, 1977.

[4] Glicksman, L.R., and Joos, F.M., Heat and Mass Transfer in Fixed Beds at Low Reynolds Numbers, Journal of Heat Transfer, vol.102, pp. 736-741, 1980.

[5] Scala, F., Particles-Fluid Mass Transfer in Multiparticle Systems at low Reynolds Number, Chemical Engineering Science, vol.91, pp. 90-101, 2013.

[6] Scala, F., Fluidized Bed Technologies for Near Zero Emission Combustion and Gasification, Elsevier-Woodhead Publishing Limited, pp.226, 2013, ISBN: 0857098802.

[7] Cornish, A.R.H., Note on Minimum Possible Rate of Heat Transfer from a Sphere When Other Spheres Are Adjacent to It, Transactions of the Institution of Chemical Engineers and the Chemical Engineer, vol.43, pp.T332-T333, 1965.

[8] Scala, F., Mass Transfer Around Freely Moving Active Particles in the Dense Phase of a Gas Fluidized Bed of Inert Particles, Chemical Engineering Science, vol.62, pp. 4159-4176, 2007.

[9] Nelson, P.A., and Galloway, T.R, Particle-to-Fluid Heat and Mass Transfer in Dense Systems of Fine Particles, Chemical Engineering Science, vol.30, pp.1-6, 1975.

[10] Gunn, D.J., Axial and Radial Dispersion in Fixed Beds, Chemical Engineering Science, vol.42, pp. 363-373, 1987.

[11] Ranz W.E. and Marshall W.R., Evaporation from Drops I, Chemical Engineering Progress, vol.48, pp. 141-146, 1952.

Chapter 8

Industrial HCl Absorption Models for Cement Plants

This chapter presents industrial models that simulate the HCl scrubbing phenomena in cement plant units, utilizing the conclusions of the study on HCl absorption by raw meal at low temperatures. The developed models take into account the operating principles of cement plant units, e.g., flow patterns, and characteristics of the mechanism of HCl absorption by raw meal, e.g., surface saturation phenomenon. Furthermore, the results of industrial model simulations are compared with those of industrial measurements. Emphasis is given to the modelling of HCl scrubbing phenomena in particle filters (bag filters) and vertical raw mills for which industrial data are available.

8.1 Basic Principles of Cement Plant Unit Models

This section presents the basic operating principles of the particle filters, vertical raw mills and gas conditioning towers that were taken into account by the developed industrial models. These data determined the type of chemical reactor model which was used in this modelling work.

8.1.1 Particle Filters

The HCl scrubbing phenomena in particle filters were industrially investigated in cement plant A, equipped with bag filters, as function of filter outlet temperature (see Chapter 3, section 3.4). Raw meal from plant A has been used as basis for some of the results presented in the following sections. This raw meal is called RM-A. The temperature operating range of particle filters is between 120^{o}C and 250^{o}C, and inlet flue gas moisture content varies between 3% v/v and 20% v/v. The HCl sorbent is dust from the preheater tower that is dispersed in flue gas.

Figure 8.1 illustrates the basic operating principles of bag filters for the filtration and regeneration stages, and an example of internal gas flow patterns for a raw mill filter unit based on CFD simulations of the filtration stage. The dust laden flue gas enters the particle filter's compartment bottom, where its velocity decreases below 3m/s, and propagates toward the filtration bags' top. The flue gas passes through the filtration bags, using pressure difference as driving force, while solids are captured on filtration bag surface, where a dust cake layer (2-3mm) builds up [3,4]. Empirical relations indicate that the majority of particles follow the gas phase flow having the same velocity as the gas phase (at least all the particles less than 50μm) [3].

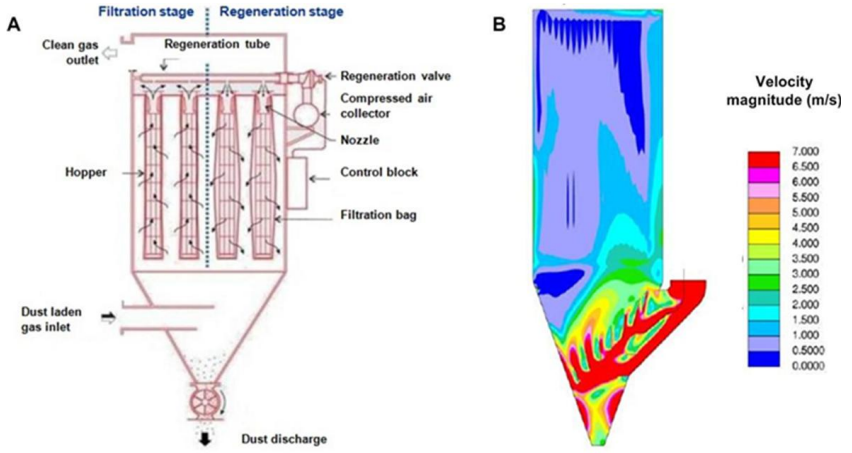

Figure 8.1: A) Operating principles of bag filters [1]; B) Gas flow patterns based on CFD simulations of raw mill filters at filtration stage [2].

The pressure drop increases with dust layer thickness, and when it reaches a certain level (1400-1500Pa) the filtration bag regeneration takes place. The average filtration velocity is sustained close to $1.67 \cdot 10^{-2}$ m/s [3]. It is assumed that the dust free bags have two times higher filtration velocity than that of the dust saturated bags just before cleaning. Furthermore, industrial inspections showed that the dust layer is homogeneously distributed along the filtration bags [3]. The dust layer is periodically removed (regeneration stage), using reverse air injection, reverse air pulse injection or mechanical shaking. The detached dust is collected in the hopper (conical section-Figure 8.1 - A) and removed. The filtration bag cleaning frequency is mainly determined by the inlet flue gas dust load. In typical operating conditions only the 5-10% of the total filtration bags are regenerated (in group of rows), simultaneously [3]. Table 8.1 presents characteristic values of the operating parameters of bag filter units.

Table 8.1: Typical values of the operating parameters of bag filter units [3, 4].

Parameter	Unit	Value
Dust load in inlet flue gas	g/Nm^3	50
Operating inlet flue gas temperature	^oC	120-250
Inlet - Outlet gas phase temperature difference	^oC	3
Average filtration velocity in filters unit	m/s	$1.67 \cdot 10^{-2}$
Filtration velocity of clean bags	m/s	$2.22 \cdot 10^{-2}$
Filtration velocity of saturated bags	m/s	$1.11 \cdot 10^{-2}$
$\triangle P_{cleaning-limit}$	Pa	1400-1500
Maximum dust layer thickness	mm	2-3
Cleaning interval per bag	min	30-60

Figure 8.2 illustrates the configuration of a parallel bag filter unit (top view) and compartment unit structure. It is clearly seen that the bag filter unit consists of an even number of structural blocks - compartments, which are characterized by a 'standard' internal structure. The bag filter unit sizes are determined by the inlet flue gas flow rate, so that the average filtration velocity per bag is close to $1.67 \cdot 10^{-2}$ m/s, and a standard compartment configuration. Each compartment is split into two symmetrical filtration bag subgroups, which are configured rectangularly with 10×20 array of single filtration bags. The filtration bags have standardized diameter: 127mm and length: 10 meter [3, 4].

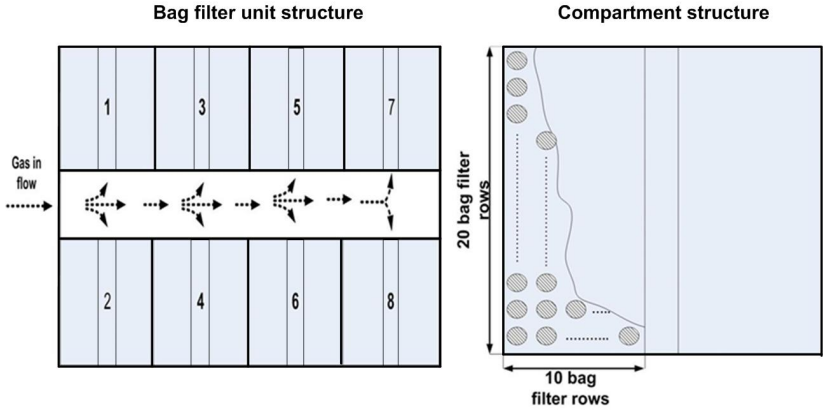

Figure 8.2: A typical structure of a parallel bag filter unit (8 compartments) and single compartment structure consisted of two identical filtration bag sub-blocks.

The particle filter modelling approach assumes that the HCl absorption occurs before the filtration bags in the dispersion and not in the dust layer on filtration bags. This assumption is mainly based on our experimental fixed-bed results. They showed that the HCl absorption by raw meal at low temperatures is very fast and leads to a surface saturation phenomenon in the case of dispersed particles of raw meal. Furthermore, the particles of raw meal tend to agglomerate and give very low apparent HCl saturation capacities when they form cake layers. Hence, the developed model for bag filter units assumes that the HCl absorption approximates a gas - solid reaction in an entrained flow reactor where the sorbent particles are moving with the same velocity as the flue gas. The gas phase and solids have the same residence time that is equal to 1.9s [3]. This results in a PFR like model, where the conversions of gas phase HCl content and particle active surface continuously change along the reactor.

The volume of the equivalent entrained flow reactor is calculated based on the inlet actual flue gas volumetric rate assuming a standard residence time (1.9s).

8.1.2 Vertical Raw Mill

The vertical raw mill is the most common type of raw materials mill in the cement industry. Industrial measurements showed the presence of a strong HCl removal in vertical raw mills that reduced the HCl concentration in outlet gas stream to the detection limit of the used FTIR analyzer (see Chapter 3). An extensive study on HCl absorption in raw mill unit was conducted at cement plant A. The determination of the internal flow patterns, operating parameters, and flue gas dust load are considered important for the modelling of HCl scrubbing phenomena in raw mill units. Typically, the raw mill section comprises the raw mill unit, raw mill cyclone, and raw mill cyclone - raw mill connection pipeline. However, the modelling work only includes the raw mill unit and the raw mill cyclone - raw mill connection pipeline.

Figure 8.3 shows the raw mill section which is considered to be the area of primary interest for HCl scrubbing. The raw mill unit, raw mill cyclone for flue gas and raw meal separation, false air inlet streams (m_{FA-RM} and m_{FA-RMC}), water injection in raw mill ($m_{w-inj.}$), flue gas recirculation ($m_{re,SG}$), and raw materials external recirculation (m_{re-S}) are illustrated. The consideration of flue gas recirculation (B - C gas stream) is important due to the dilution of the flue gas stream coming from preheater that determines the HCl concentration in the inlet gas stream of raw mill. A similar effect (flue gas dilution) is anticipated by the false air streams in the raw mill unit and raw mill cyclone. Typically, the false air corresponds to 10-15% v/v and 2% v/v of the inlet gas streams of raw mill and raw mill cyclone, respectively [5].

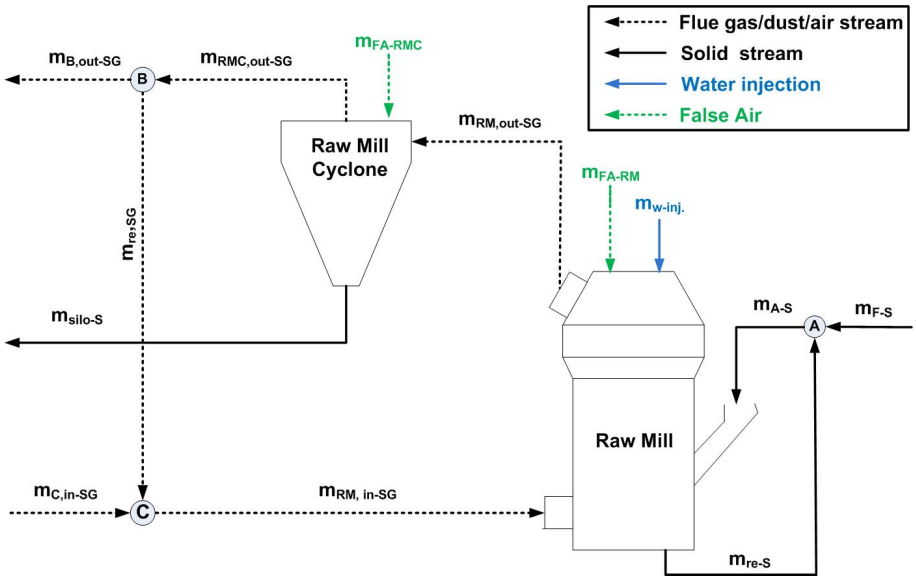

Figure 8.3: Schematic illustration of the raw mill section and relevant mass flows.

Indicative raw mill internal flow patterns of gas phase and solids were obtained using CFD simulations of OK-46-6 (vertical type) raw mill and a determined particle size distribution for particles leaving grinding table. Table 8.2 shows the particle size distribution which was used in the CFD simulation of internal flow patterns. It is clearly seen that the feed particle sizes vary between $4.5{\cdot}10^{-5}$m and $3{\cdot}10^{-2}$m.

Table 8.2: Particle size distribution for particles leaving grinding table used in CFD simulations [6].

Particles Diameter (m)	Mass Fraction (%)
$3 \cdot 10^{-2}$	4.66
$2 \cdot 10^{-2}$	3.465
$1 \cdot 10^{-2}$	1.815
$5 \cdot 10^{-3}$	7.095
$2 \cdot 10^{-3}$	14.3
$1 \cdot 10^{-3}$	14.41
$5 \cdot 10^{-4}$	16.585
$3.55 \cdot 10^{-4}$	12.055
$2 \cdot 10^{-4}$	11.805
$9 \cdot 10^{-5}$	6.025
$4.5 \cdot 10^{-5}$	7.785

The CFD simulations correspond to raw mill compartments from the grinding table to the separator inlet. They assume a constant temperature equal to that of the inlet gas stream of raw mill unit (no temperature decrease in raw mill unit). In addition, CFD model neglects the potential effects of separator operation and water injection (flue gas volume increase) on the gas streamlines and solids trajectory. Therefore, the particles grinding and separator effects are not considered in the residence time estimation. The CFD simulations were conducted considering two main particle size groups: (i) small particles: $9{\cdot}10^{-5}$ - $2{\cdot}10^{-4}$m, and (ii) large particles: $2{\cdot}10^{-2}$ - $3{\cdot}10^{-2}$m. This approach allows the separate study of the fine particles, which are characterized by large specific surface area and relatively short residence times, and the large particles that are characterized by long residence times.

Figure 8.4 illustrates the trajectories of solids as function of the particle sizes and residence time that is indicated by color. In particular, fine particles (Figure 8.4 - A) have similar flow patterns with the gas phase in the space above grinding table and are characterized by residence times between 0.5s and 0.75s. However, the separator operation, temperature decrease and presence of a dense dispersion may give longer residence times than simulated by CFD models. On the other hand, the large particles (Figure 8.4 - B) return to the grinding table and are characterized by trajectory residence times between 5s and 7s, without considering the grinding and separator effects. This is consistent with the reported high mass of internally recirculating solids in raw mill units [7].

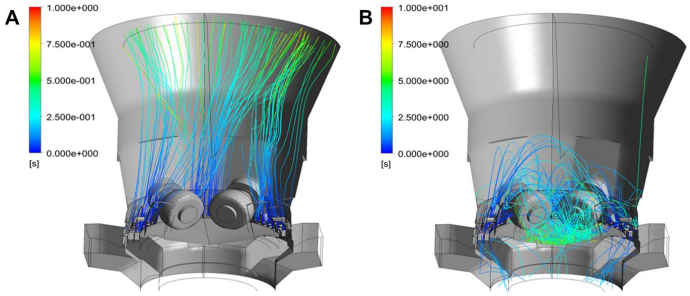

Figure 8.4: A) Trajectories and residence times of fine particles ($9{\cdot}10^{-5}$ - $2{\cdot}10^{-4}$m; B) Trajectories and residence times of large particles ($2{\cdot}10^{-2}$ - $3{\cdot}10^{-2}$m) [6].

Figure 8.5 - A shows the raw mill unit split into three sections which correspond to three PFRs characterized by varying solids load. The selection of PFRs for the raw mill model was mainly based on the internal flow patterns of solids and flue gas [5, 7]. It is clearly seen in Figure 8.5 - B that the flue gas solids load and its physical properties, e.g., particles size, vary significantly from the grinding table towards the raw mill outlet. Furthermore, a significant quantity of solid materials recirculates in raw mill unit. The solids are categorized into three groups: (i) the fine particles that pass through the separator (final raw meal product: 1-90μm), (ii) the intermediate particles (90-200μm) that fail to pass through the separator and return to grinding table, and (iii) the coarse particles (300μm-3mm) that immediately return to the grinding table [5, 6].

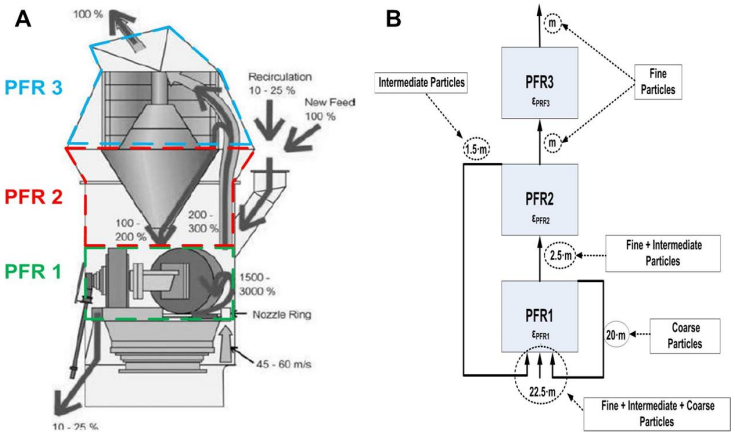

Figure 8.5: A) Schematic illustration of vertical raw mill unit and PFRs (adapted) [7]; B) Solids mass flow diagram in the raw mill unit where 'm' stands for solids mass flow out of PFR3 (raw mill separator).

PFR1 has height equal to the grinding rollers diameter and corresponds to the annular volume determined by raw mill walls and grinding table diameter. PFR1 volume:

$$V_1 = \pi \cdot \frac{(Din_{wall}^2 - D_{table}^2)}{4} \cdot h_1 \tag{8.1}$$

where Din_{wall} is the internal diameter of raw mill walls, D_{table} is the grinding table diameter , and h_1 is the grinding rollers diameter.

PFR2 occupies the annular volume that is delimited by the grinding rollers top, separator blades inlet, raw mill walls, and an equivalent internal diameter which takes into account the grinding table diameter and separator lower part shape. PFR2 volume:

$$V_2 = \pi \cdot \frac{(Din_{wall}^2 - D_{equiv.}^2)}{4} \cdot h_2 \tag{8.2}$$

where $\mathrm{D}_{equiv.}$ is the equivalent internal boundary diameter, and h_2 is the distance between grinding rollers top and separator blades inlet.

PFR3 corresponds to the volume of raw mill outlet - raw mill cyclone connection pipeline and separator upper part. In this work the PFR3 is considered to be a cylindrical PFR with cross-sectional diameter equal to the diameter of the connection pipeline. Therefore, the separator upper part volume corresponds to an equivalent length of pipeline. The separator upper part equivalent pipeline length:

$$l_{sep} = \frac{V_{sep.-upper}}{\pi \cdot \frac{D_{pipe}^2}{4}} \tag{8.3}$$

where $V_{sep.-upper}$ is the volume of separator upper part and D_{pipe} is the diameter of separator - raw mill cyclone connection pipeline.The total effective length of PFR3 becomes

$$l_3 = l_{pipe} + l_{sep.} \tag{8.4}$$

where l_{pipe} is the length of the raw mill outlet - raw mill cyclone connection pipeline.

PFR3 volume:

$$V_3 = \pi \cdot \frac{D_{pipe}^2}{4} \cdot l_3 \tag{8.5}$$

The total external surface areas of solids in PFRs are calculated by 8.6-8.8 (the parameters are descried in):

$$s_1 = (x_{fine,1} \cdot S_{fine} + x_{inter.,1} \cdot S_{inter.} + x_{coarse,1} \cdot S_{coarse}) \cdot \varepsilon_1 \cdot \nu_1 \cdot t_{1,res.} \tag{8.6}$$

$$s_2 = (x_{fine,2} \cdot S_{fine} + x_{inter.,2} \cdot S_{inter.}) \cdot \varepsilon_2 \cdot \nu_2 \cdot t_{2,res.} \tag{8.7}$$

$$s_3 = S_{fine} \cdot \varepsilon_3 \cdot \nu_3 \cdot t_{3,res.} \tag{8.8}$$

Table 8.3: Parameters used in the calculation of total external surface areas of solids in raw mill PFRs.

Symbol	Parameter	Unit
S_{coarse}	Specific surface area of coarse particles	m^2_{solid} /g_{coarse}
S_{fine}	Specific surface area of fine particles	m^2_{solid} /g_{fine}
$S_{inter.}$	Specific surface area of intermediate particles	m^2_{solid} /$g_{inter.}$
s_i	Total external surface area of raw meal in PFR_i	m^2_{solid}
$t_{i,res.}$	The residence time of dispersion in PFR_i	s
v_i	The actual volumetric flow of dispersion in PFR_i	m^3_{gas} /s
$x_{coarse,i}$	The mass fraction of coarse particles in PFR_i	g_{coarse}/g_{total}
$x_{fine,i}$	The mass fraction of fine particles in PFR_i	g_{fine}/g_{total}
$x_{inter.,i}$	The mass fraction of intermediate particles in PFR_i	$g_{inter.}/g_{total}$
ε_i	The dust load of dispersion in PFR_i	g_{total} / m^3_{PFR}

The splitting of the raw mill into three PRFs characterized by varying dust load of dispersion is consistent with the internal flow patterns and solids recirculation. Furthermore, industrial measurements showed an instantaneous flue gas temperature drop at grinding table plane [5]. Hence, the temperature and moisture content of flue gas in PFRs will be considered constant and equal to those of the outlet stream of raw mill.

8.1.3 Gas Conditioning Tower

The GCT designing - operation depends on the cement plant layout. GCT can be used as (i) cooler - humidifier of preheater flue gas, (ii) cooler - humidifier of a preheater flue gas fraction and mixing point with raw mill gas stream, and (iii) mixing chamber for the preheater and raw mill gas streams. The designing concept is mainly based on the presence of an evaporation region (temperature transient zone along GCT), where the injected water evaporation and flue gas cooling occur, before the potential mixing with the raw mill outlet gas stream in GCT bottom part.

The presence of HCl scrubbing phenomena in GCT have not been investigated using industrial measurements. However, the presence of dispersed dust particles in conjunction with gas phase moisture content between 5%v/v and 20%v/v makes possible the HCl absorption by dust particles in the temperature range 150-400°C. Therefore, the modelling of HCl absorption in GCT can be simulated using a PFR characterized by varying temperature and gas phase moisture content profiles along its length.

It is anticipated that the entrained flow reactor model which is presented in the next section (section 8.2) can be used for the simulation of HCl absorption in GCT if appropriate functions for temperature and moisture profiles are included (see Chapter 3, section 3.2). However, this work does not present simulations of HCl scrubbing phenomena in GCTs due to the lack of industrial data for comparative analysis.

8.2 Entrained Flow Reactor Model Description

This section presents the mathematical description of the entrained flow reactor model that can be applied in the simulation of HCl absorption in post-preheater tower units (particle filters and raw mill). The model considers that the HCl absorption is controlled by mass transfer to the external surface of dust particles (gas film diffusion) and conversion of the active surface.

The mechanism of HCl absorption by dust particles corresponds to a surface saturation phenomenon that is characterized by a certain HCl saturation capacity determined by sorbent chemical and physical properties, and unit operating conditions (temperature, gas phase moisture content and solids moisture content). As it was described in Chapter 7, HCl absorption only occurs on specific active points where HCl molecules react with $CaCO_3$ on dust particles external surface based on the direct $CaCO_3$ chlorination. The liquid aqueous phase formation is taken into account as an equivalent active points generation. Solid particles are - as approximation - assumed to be of one size only with diameter equal to the mean diameter of the dispersed particles. The particles are also assumed to have the same velocity as the gas phase. Table 8.4 shows the basic assumptions of the entrained flow reactor model.

The mathematical description is based on the mass balance in a control volume of the entrained flow reactor (see Appendix F). Figure 8.6 illustrates the flue gas HCl concentration change through a plug flow reactor of length l, constant temperature, and constant dispersion velocity. F_{HCl} represents the molar flow rate of HCl, C_{HCl} is the HCl concentration in gas phase, X_{HCl} is the HCl conversion, and v is the volumetric flow rate of gas phase.

Reaction rate expression:

$$r_{HCl} = k_g \cdot C_{HCl} \cdot (1 - X_s) \qquad [\frac{mol}{m^2_{solid-active} \cdot s}] \tag{8.9}$$

where k_g is the mass transfer coefficient, C_{HCl} is the HCl concentration in gas phase, and X_S is the active surface conversion.

Mass transfer coefficient:

$$k_g = \frac{Sh \cdot D_{HCl-N_2}}{d_p} \tag{8.10}$$

where Sh is the Sherwood number of an active sphere in stagnant gas phase (Sh=2 [8]), D_{HCl-N_2} is diffusion coefficient of HCl in N_2, and d_p is the mean diameter of dust particles.

Table 8.4: Basic assumptions of the entrained flow reactor model.

- HCl absorption by raw meal is based on a rapid irreversible surface reaction.
- Reaction only occurs on active sites on the external surface of raw meal particles.
- Active sites correspond to certain HCl saturation capacity and active surface area - ratio of specific active surface area to specific HCl saturation capacity is constant.
- Spherical active particles in stagnant gas - Sherwood number equal to 2. [8]
- Water effect corresponds to change in the HCl saturation capacity.
- Spherical dust particles with diameter equal to that of the mean raw meal particle size.
- Gas film diffusion and active surface (active sites) conversion control the HCl absorption reaction.
- Uniform dispersion of particles in gas.
- The particles size and shape are unaffected by the exposure to HCl.
- Dust particles have the same velocity as gas phase.
- Constant velocity along the entrained flow reactor.
- No axial dispersion.
- Incompressible gas phase.
- Entrained flow reactor has constant and uniform temperature and gas phase moisture content.

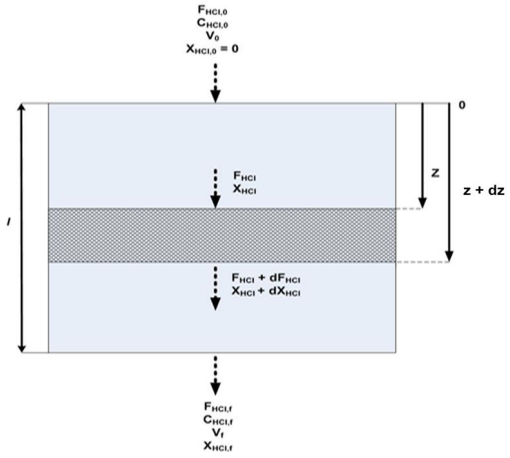

Figure 8.6: Schematic illustration of a control volume in the entrained flow reactor.

The mass balance of gas phase gives an expression for the HCl conversion along the entrained flow reactor:

$$\frac{dX_{HCl}}{dz} = \frac{S_{act.} \cdot \varepsilon \cdot A_{PFR}}{F_{HCl,0}} \cdot k_g \cdot C_{HCl,0} \cdot (1 - X_{HCl}) \cdot (1 - X_s) \tag{8.11}$$

where $S_{act.}$[†] is the specific external active surface area of dust, ε is the dust load of gas phase, A_{PFR} is the reactor cross sectional area, $F_{HCl,0}$ is the molar flow rate of HCl at the reactor inlet, $C_{HCl,0}$ is the HCl concentration at the reactor inlet, and X_{HCl} is the HCl conversion.

The mass balance of solid phase gives an expression for the active surface conversion along the entrained flow reactor:

$$\frac{dX_s}{dz} = \frac{1}{U_{PFR}} \cdot k_g \cdot C_{HCl,0} \cdot (1 - X_{HCl}) \cdot (1 - X_s) \cdot \frac{S_{act.}}{k_{ws} \cdot k_{wg} \cdot Cap_{ref.}} \tag{8.12}$$

where U_{PFR} is the dispersion velocity in the reactor, $Cap_{ref.}$ is the specific HCl saturation capacity of dust, and k_{ws} and k_{wg} are correction factors of HCl saturation capacity that correspond to moisture content effect of solids and gas phase (see Chapter 7 - section 7.4.2).

8.3 Industrial Models Evaluation

This section presents the industrial models application in the prediction of the HCl absorption in post-preheater units (particle filters and raw mill). The used operating parameters, e.g., temperatures, flue gas mass flows, were determined by the process design diagrams [9] and industrial measurements [10] of cement plant A (see Figure 8.7). Furthermore, the RM-A physical properties and experimentally determined HCl saturation capacities were used in these simulations.

[†]The active surface area corresponds to a fraction of the external surface area of particles. This work assumes that the ratio of active surface area to HCl saturation capacity of dust is constant and independent on operating conditions. Therefore, the active surface area is determined by HCl saturation capacity of dust.

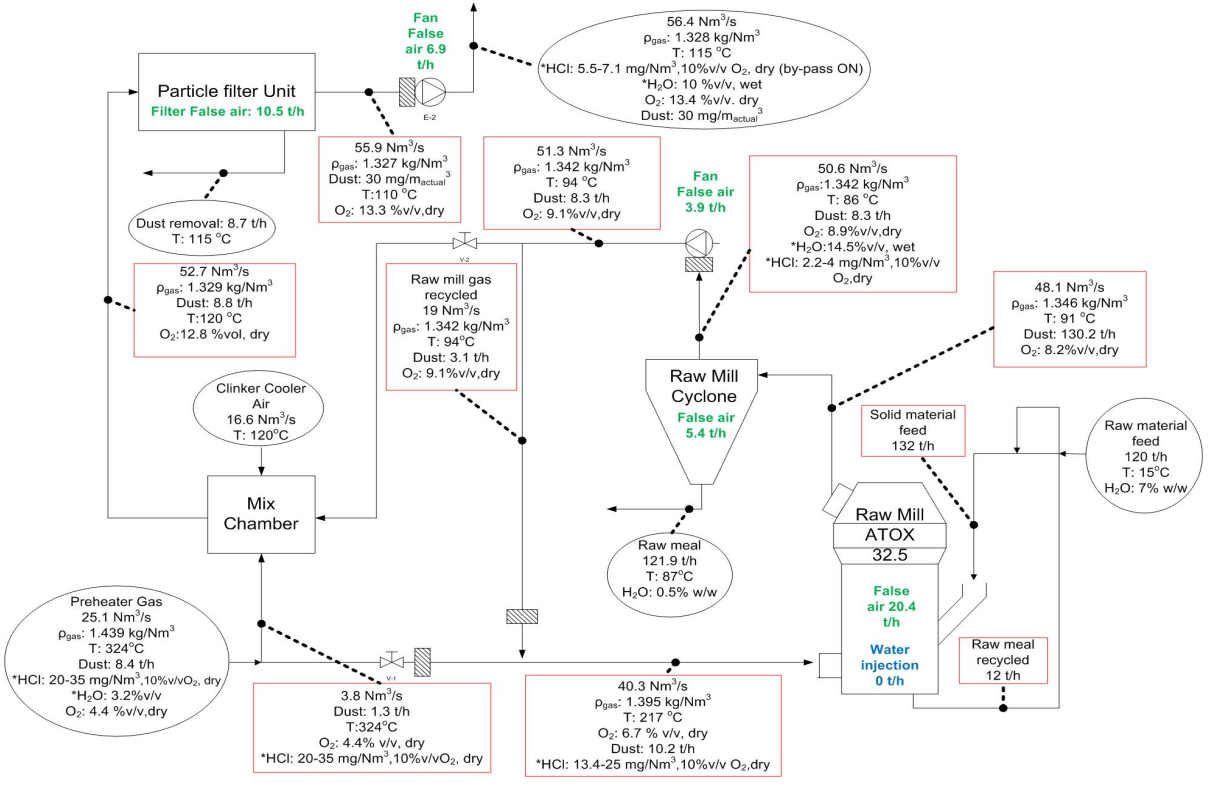

Figure 8.7: Process design diagram of cement plant A (flows correspond to By-pass: OFF) and some indicative values (*) of HCl and H_2O levels during cement plant operation (these values correspond to the operating conditions) [9, 10]. Black ellipses: inlet and outlet streams; red rectangular: stream conditions at indicated point; green text: false air; and blue text: water injection.

8.3.1 Particle Filters

The industrial evaluation of particle filter scrubbing effect when raw mill is OFF was conducted in cement plant A. The simultaneous decrease in operating temperature from 210^{o}C to 151^{o}C and the increase in water content from 3.5% v/v to 6% v/v , both caused by fresh air and water injections, resulted in an enhancement of the HCl reduction from 51% to 63%, with inlet HCl concentration 32 mg/Nm^{3*} at 210^{o}C and 35 mg/Nm^{3*} at 151^{o}C [10]. The preheater flue gas cooling to 210^{o}C was done using fresh air from the clinker cooler with temperature close to 120^{o}C. The additional cooling to 151^{o}C was achieved with the injection of 1.22 kg/s H_2O in downcomer before the mixing chamber. The water injection resulted in increase of the actual flue gas volumetric flow close to 2.34 m^3 $_{actual}$/s.

The entrained flow reactor volume:

$$V_{PFR} = \nu_{actual-FG} \cdot t_{res.} \tag{8.13}$$

where $\nu_{actual-FG}$ is the actual flue gas volumetric flow rate at the inlet of particle filters unit and t_{res} is the flue gas residence time from the filter inlet to the filtration bags ($\sim$ 1.9s).

The length of entrained flow reactor is estimated assuming that it has cylindrical shape with cross sectional diameter equal to that of flue gas pipeline (2.24m):

$$L_{PFR} = \frac{4 \cdot V_{PFR}}{\pi \cdot D^2_{pipe}} \tag{8.14}$$

The physical properties and experimentally determined HCl saturation capacities of RM-A were used as inputs in 8.11 and 8.12. Furthermore, the moisture content coefficients (k_{ws} and k_{wg}) of flue gas and dust were determined based on the experimental data of RM-A (see Chapter 6, section 6.1.3). The dust particles of flue gas were heated to temperatures close to 350-400^{o}C before the particle filters unit. Hence, the dust moisture content is very low and can be approximated the moisture content of the raw meal particles dried at 200^{o}C for 5hr.

Table 8.5: Reference HCl saturation capacities (corrected for partial dilution (see Chapter 6, section 6.1.2)) and moisture coefficients at the conditions of industrial measurements.

Temperature (^{o}C)	Cap$_{ref.}$ (mol/g)	k_{ws}	Gas Phase H_2O (%v/v)	k_{wg}
151	$9.41 \cdot 10^{-6}$	1	6	1.84
210	$9.2 \cdot 10^{-6}$	1	3.5	1

Table 8.5 shows the used reference HCl saturation capacities and moisture coefficients in the industrial tests simulation. The reference HCl saturation capacities correspond to the experimentally determined values for RM-A samples dried at 200^{o}C, considering fixed-bed temperatures 150^{o}C and 180^{o}C. The preheater dust is considered to be dry due to the exposure to high temperatures in preheater tower. Hence, the solid phase moisture content coefficient is assumed equal to 1 (absence

*in dry flue gas at 10% v/v O_2

of solids moisture content effect). The gas phase moisture content effect is neglected (k_{wg}=1) at temperatures above 200^{o}C [11, 12]. On the other hand, the gas phase moisture content effect at 150^{o}C - 6%v/v H_2O is estimated based on the experimental data from 150^{o}C - 5%v/v H_2O tests assuming that k_{wg} is linearly proportional to the gas phase moisture content and an independence of the gas phase moisture effect on solids moisture content. The ratio of Cap(150^{o}C, Y_{ws}=3.8 %w/w, Y_{wg}=5 %v/v) to Cap(150^{o}C, Y_{ws}=3.8 %w/w, Y_{wg}=0 %v/v) is 1.53 (see Chapter 6, section 6.1.3). Therefore, it is assumed that if 5%v/v H_2O gives k_{wg}=1.53 then 6%v/v H_2O gives k_{wg}=1.84.

Table 8.6: Input parameters to the particle filter model.

Parameter	Unit	151^{o}C	210^{o}C
Inlet HCl concentration [10]	mg/Nm^3	35	32
Inlet dust mass rate [9]	t/h	8.4	8.4
Flue gas flow	Nm^3/s	34.8	33.3
Flue gas H_2O [10]	%v/v	6	3.5
D_{HCl-N_2} [13]	m^2/s	$3.41 \cdot 10^{-5}$	$4.22 \cdot 10^{-5}$
Active specific surface area†	m^2/g	0.192	0.102
Mean particles diameter of dust	μm	12.9	12.9

Table 8.6 shows the input parameters to the model for the simulation of industrial tests. The HCl concentration, dust mass rate and H_2O content in the inlet gas stream were obtained by the industrial measurements [10] and process design diagrams of cement plant A (see Figure 8.7) [9]. The flue gas flow rate was determined as the sum of the preheater gas stream at 90% of the nominal production (90% of the process diagrams value [9, 10]), fresh air from clinker cooler (120^{o}C), and injected water vapour.

Table 8.7: HCl reductions based on the industrial tests and the required capacity factor (CF) values for their simulation, using the model parameters and operating conditions listed in Table 8.5 and Table 8.5.

Temperature (^{o}C)	Gas Phase H_2O (% v/v)	HCl reduction (industrial data) (%)	CF
151	6	63	0.52
210	3.5	51	0.69

The inclusion of a capacity factor (CF) in equation 8.12 was necessary. The capacity factor changes the value of $Cap_{ref.}$ to CF $\cdot$ $Cap_{ref.}$. Table 8.7 shows the results of simulations of industrial measurements in terms of HCl reduction and used capacity factor values. The use of CF=1 in the industrial model gives HCl reduction equal to 100% and 73% at 151^{o}C and 210^{o}C, respectively. However, the developed model was able to predict the HCl reduction at 151^{o}C and 210^{o}C using CF equal to 0.52 and 0.69, respectively. Therefore, the correction is equivalent to an overestimation between 31% and 48% of the determined HCl saturation capacities of preheater dust. This was anticipated considering

†The active surface areas were calculated based on: (i) total external area equal to BET area of RM-A, (ii) external area of $CaCO_3$ fraction: 82% of BET , (iii) active surface area of undried RM-A at 100^{o}C-0%v/v H_2O: 4.2% of BET area (see Chapter 6, section 6.1.2), (iv) constant ratio of active surface to HCl saturation capacity, and (v) HCl saturation capacity of RM-A at the investigated conditions.

the exposure 'history' of the preheater dust particles. The flue gas dust is already exposed to HCl in preheater tower at temperatures between 360^{o}C and 900^{o}C. Hence, it is characterized by a very low moisture content and a potential partial HCl saturation in preheater tower. Furthermore, particle filter model used experimental data (HCl saturation capacities) from RM-A tests for the simulation of preheater dust performance as HCl sorbent. The variation of CF value at the simulated conditions can be explained by the uncertainty in the determination of moisture content coefficients (k_{ws} and k_{wg}). For instance, the industrial data simulation at 151^{o}C - 6%v/v H_2O using k_{wg} equal to 1.53 (150^{o}C - 5%v/v H_2O) requires CF equal to 0.63.

Figure 8.8 illustrates the simulated conversions of HCl and active surface at the tested industrial conditions. It is clearly seen that the steady state is reached in the first $\sim$ 4 meters of the reactor (total reactor length: $\sim$ 25-28m). This is consistent with the lab results, which showed that the HCl absorption by raw meals is a very fast reaction controlled by gas film diffusion.

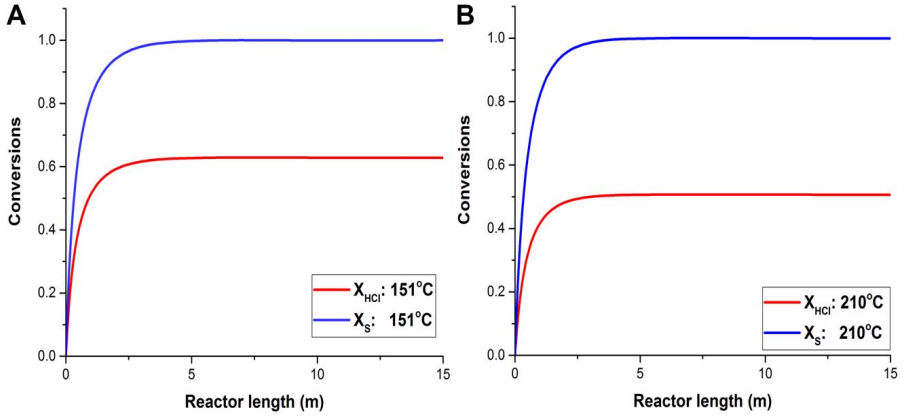

Figure 8.8: A) Simulation of HCl and active surface conversions in the particle filters unit, using inlet HCl concentration: 35mg/Nm^3, temperature: 151^{o}C, active specific surface area: 0.1 m^2/g, mean particles diameter: 12.9µm, flue gas flow rate: 34.8 Nm^3/s, CF=0.52, and dust mass rate: 8.4 t/h; B) Simulation of HCl and active surface conversions in the particle filter unit, using inlet HCl concentration: 32mg/Nm^3, temperature: 210^{o}C, active specific surface area: 0.07 m^2/g, mean particles diameter: 12.9µm, flue gas flow rate: 33.3 Nm^3/s, CF=0.69, and dust mass rate: 8.4 t/h.

It is concluded that the developed model can sufficiently predict the HCl reduction in particle filter units assuming that the dust is already saturated when it deposits on filtration bags. Since the preheater dust has been exposed to HCl prior to entering the filter unit, the experientially determined HCl capacity of RM-A may not be appropriate of the remaining capacity at the entrance to the filter unit. This makes the values of CF lower than 1 acceptable.

8.3.2 Vertical Raw mill

An extensive industrial evaluation of raw mill scrubbing effect was conducted in cement plant A which is equipped with a vertical raw mill. The industrial tests comprised the evaluation of raw mill operating conditions (outlet temperature: 80-115^{o}C and water injection: 1-5.5 t/h) effect on raw mill scrubbing efficiency with HCl concentration in inlet gas stream 25mg/Nm^{3*} [10]. The industrial evaluation showed that raw mill effectively scrubs HCl and gave outlet HCl concentrations in the range 2-4mg/Nm^{3*} that correspond to the detection limit of the used FTIR analyzer [10, 14]. Furthermore, the raw mill scrubbing efficiency was independent on operating conditions [10]. Figure 8.7 illustrates the process design diagram of cement plant A in the case of raw mill operation without injection of water on grinding table.

Table 8.8: Operating conditions of raw mill in cement plant A used in HCl scrubbing effect simulation [10].

Parameter	Unit	Value
HCl concentration in inlet gas stream	mg/Nm^{3*}	25
Temperature of inlet gas stream	^{o}C	288
Inlet flue gas flow rate	Nm^3/s	40.7
Injected water mass rate	t/h	2.8
Temperature of outlet gas stream	^{o}C	84
Outlet flue gas flow rate	Nm^3/s	60.5
Outlet dust mass rate	t/h	131.4
HCl concentration in outlet gas stream	mg/Nm^3	2-4
H_2O content in outlet gas stream	% v/v	14.5

Table 8.8 shows the operating conditions used in the simulations of raw mill tests. It should be kept in mind that the flue gas temperature drop and moisture content increase occur instantaneously at the grinding table plane. Therefore, the temperature, flue gas moisture content and flue gas volumetric flow are constant along the raw mill and equal to the values of the outlet stream.

The HCl saturation capacity of fine raw meal particles at raw mill conditions (Table 8.8) was determined using the fixed-bed experimental data for undried RM-A samples. Generally, the raw mill simulations are characterized by a conservative approach related to the gas phase moisture content effect. In particular, it is assumed that the HCl saturation capacity of fine raw meal particles at 84^{o}C - 14.5% v/v H_2O is equal to that of undried raw meal at 100^{o}C - 5% v/v H_2O. This assumption underestimates the HCl saturation capacity of RM-A considering the anticipated increase of HCl saturation capacity with gas phase moisture content at temperatures less than 200^{o}C.

*in dry flue gas at 10% v/v O_2

Table 8.9: Reference HCl saturation capacity (RM-A) and moisture content coefficients used in raw mill simulations at 84^{o}C-14.5% v/v H_2O.

Cap_{ref} (mol/g)	k_{ws}	k_{wg}
$2.9 \cdot 10^{-5}$	1	1.61

Table 8.9 shows the values of the reference HCl saturation capacity of RM-A and moisture content coefficients of gas phase and solids. The HCl saturation capacity of undried RM-A at 100^{o}C - 0% v/v H_2O content in gas phase was used as a reference HCl saturation capacity. It was assumed that the moisture content of fine raw meal particles was the same as the used undried RM-A in lab tests (3.8% w/w H_2O); hence, k_{ws} was equal to 1. k_{wg} was assumed equal to 1.61 that corresponded to the ratio of Cap(100^{o}C,Y_{ws}=3.8% w/w,Y_{wg}=5% v/v) and Cap(100^{o}C,Y_{ws}=3.8% w/w,Y_{wg}=0% v/v). However, the expected k_{wg} value at the raw mill conditions is above 1.61 due to the potential increase of HCl saturation capacity with gas phase moisture at temperatures less 200^{o}C.

The total HCl saturation capacity of fine particles mass rate (product of dust outlet mass rate and specific HCl saturation capacity at 84^{o}C - 14.5% v/v H_2O) is 55 times larger than the inlet HCl molar rate. The developed raw mill model can be further simplified assuming that only the fine particles contribute to HCl reduction. The raw mill unit is simulated as a cylindrical PFR with cross - sectional area equal to that of the raw mill - raw mill cyclone connection pipeline. The reactor volume is determined by the product of actual flue gas volumetric flow at the outlet of raw mill and flue gas residence time. The total flue gas residence time in raw mill unit and raw mill - raw mill cyclone connection line is approximately 2s. These assumptions remove uncertainties related to the physical properties and HCl absorption capacities of coarse and intermediate size particles, which have not been determined by lab tests.

Figure 8.9 illustrates the conversion of gas phase HCl in raw mill as function of the HCl concentration in inlet gas stream using the operating conditions listed in Table 8.8 and Table 8.9. It is clearly seen that the model predicts complete HCl absorption in raw mill at the industrially tested conditions (25 mg/Nm^3). Furthermore, it showed that raw mill is able to remove significantly higher HCl concentrations, e.g., 400 mg/Nm^3, at the same operating conditions. It is noteworthy that the present simulation results correspond to a conservative determination of HCl saturation capacity of the fine particles and no consideration of the potential effects of coarse and intermediate size particles.

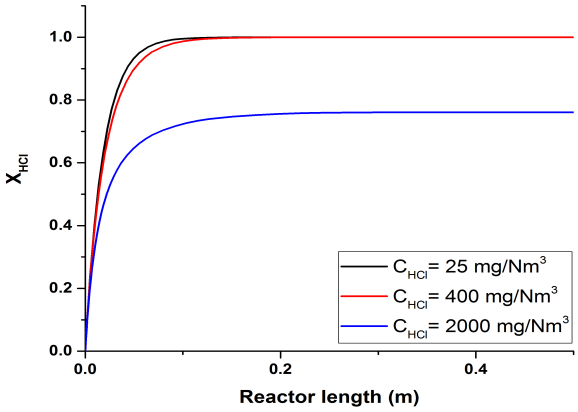

Figure 8.9: Simulated conversion of HCl (X_{HCl}) in raw mill using inlet fine dust mass rate: 131.4 t/h, inlet flue gas flow rate: 40.7, outlet flue gas flow rate: 60.5 Nm^3/s, residence time: 1.9s, CF=1, HCl concentration in the inlet stream: 25, 400 and 2000 mg/Nm^3, outlet temperature: 84^{o}C, main particles size: 12.9 μm, HCl saturation capacity of RM-A at 84^{o}C-14.5 % v/v H_2O: 4.67 $\cdot$ 10^{-5} mol/g, flue gas velocity: 23.14 m/s, total length of entrained reactor: 44 m, and active specific surface area: 0.52 m^2/g.

8.3.3 Sensitivity Analysis of the Entrained Flow Reactor Model

This section presents the sensitivity analysis of the entrained flow reactor model related to the dust load of flue gas and inlet HCl concentration. The analysis is based on the simulations of particle filters scrubbing effect at 210^{o}C. Table 8.10 shows the input parameters that were kept constant in this study. The values of the reference HCl saturation capacity, moisture effect coefficients, and correction factor of HCl saturation capacity at 210^{o}C - H_2O: 3.5% v/v were determined in section 8.3.1.

Table 8.10: Constant input parameters for the filter model sensitivity analysis.

Parameter	Unit	Value
Temperature	^{o}C	210
Inlet flue gas flow rate	Nm^3/s	33.3
Flue gas H_2O content [10]	%v/v	3.5
D_{HCl-N_2} [13]	m^2/s	$4.22 \cdot 10^{-5}$
Cap_{ref}	mol/g	$9.2 \cdot 10^{-6}$
CF		0.69
k_{ws}	-	1
k_{wg}	-	1
Total reactor length	m	28.42
Active specific surface area †	m^2/g	$7 \cdot 10^{-2}$
Mean particles diameter	μm	12.9

Effect of Flue Gas Dust Load

Figure 8.10 illustrates the simulated conversions of HCl (X_{HCl}) and active surface (X_S) in particle filter units as function of the inlet dust mass rates. It is clearly seen that the HCl conversion increases with flue gas dust load. This is an anticipated result considering that the dust load increase is equivalent to the addition of sorbent with a standard HCl saturation capacity. Furthermore, the simulations showed a linear proportionality of the inlet dust mass rate to HCl conversion. The obtained active surface conversions are equal to 1 due to the sufficient supply of HCl for the saturation of the available sorbent.

†The active surface areas were calculated based on: (i) total external area equal to BET area of RM-A, (ii) external area of $CaCO_3$ fraction: 82% of BET , (iii) active surface area of undried RM-A at 100^{o}C-0%v/v H_2O: 4.2% of BET area (see Chapter 6, section 6.1.2), (iv) the ratio of active surface to HCl saturation capacity is constant, and (v) HCl saturation capacity of RM-A at the investigated conditions.

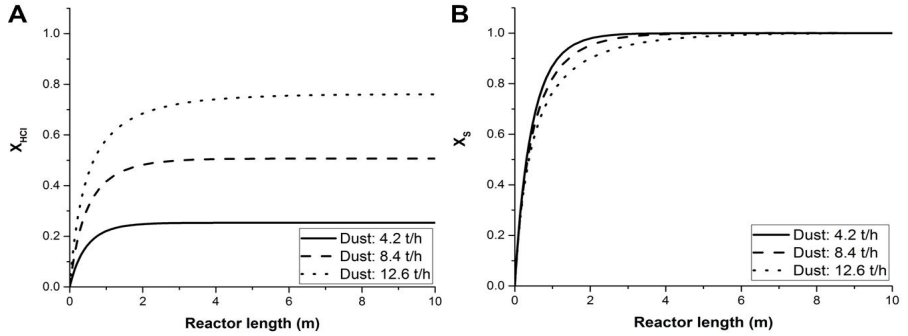

Figure 8.10: A) Simulated conversion of HCl (X_{HCl}) in particle filters unit, using the input parameters listed in Table 8.10, inlet HCl concentration: 32mg/Nm^3, and inlet dust mass rate: 4.2 t/h, 8.4 t/h and 12.6 t/h; B) Simulated conversion of active surface (X_S) in particle filters unit, using the input parameters listed in Table 8.10, inlet HCl concentration: 32mg/Nm^3, and inlet dust mass rate: 4.2 t/h, 8.4 t/h and 12.6 t/h.

Effect of Inlet HCl Concentration

Figure 8.11 illustrates the simulated conversions of HCl (X_{HCl}) and active surface (X_S) in particle filters unit as function of the inlet HCl concentration. It is clearly seen that the final HCl conversion decreases with the flue gas HCl concentration increase. This result was anticipated considering that the model treats the HCl absorption as a surface saturation phenomenon which is characterized by a standard maximum HCl absorption capacity proportional to the dust load of flue gas. Furthermore, the simulations showed that the system reaches faster the steady state in the case of high HCl concentrations (32 mg/Nm^3 and 64 mg/Nm^3). This is as expected when the absorption is proportional to HCl concentration.

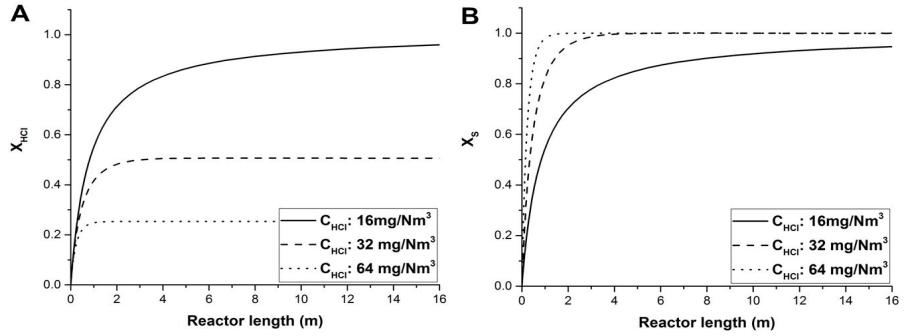

Figure 8.11: A) Simulated conversion of HCl (X_{HCl}) in particle filters unit, using the input parameters listed in Table 8.10, inlet HCl concentration: 16mg/Nm^3, 32mg/Nm^3 and 64mg/Nm^3, and inlet dust mass rate: 8.4 t/h; B) Simulated conversion of active surface (X_s) in particle filters unit, using the input parameters listed in Table 8.10, inlet HCl concentration: 16mg/Nm^3, 32mg/Nm^3 and 64mg/Nm^3, and inlet dust mass rate: 8.4 t/h.

The sensitivity analysis of the entrained flow reactor model in the case of particle filters unit showed that the model can follow the changes in HCl concentration and flue gas dust load.

8.4 Conclusions on Industrial Models Evaluation

This chapter showed the utilization of the obtained experimental results from HCl absorption tests using industrial raw meals in industrial models. It was shown that the models are able to predict the HCl absorption in post-preheater units. The industrial models took into account the operating conditions of the cement plant units and the obtained experimental data which indicated that the HCl absorption by raw meal at low temperatures approximated a surface saturation phenomenon. The main conclusions from the comparative analysis of the simulation results and available industrial data, and models sensitivity analysis can be summarized as follows:

- The developed industrial model for particle filter unit simulated this as an entrained flow reactor taking into account that the HCl absorption by preheater dust occurred in the dispersion before the filtration bags. The HCl absorption mechanism was based on the surface saturation of dust particles and controlled by the mass transfer through the gas film around the particles and active surface conversion. The dust particles were characterized by a specific HCl saturation capacity that was affected by the operating conditions, and physical and chemistry properties of the preheater dust. The developed model was able to simulate the industrial observation of the HCl scrubbing in particle filters using the lab determined HCl saturation capacities of raw meal. However, it was necessary to correct the inlet HCl saturation capacity with a factor CF $\sim 1/2$.

- The developed industrial model simulated the raw mill unit as three entrained flow reactors in a series configuration considering the internal flow patterns, solids recirculation and HCl absorption as a surface saturation phenomenon. The raw mill model evaluation was based on a simplified model which considered only fine particles and treated the raw mill as a single entrained flow reactor. The simulation results were consistent with the industrial measurements that indicated a complete scrubbing of HCl in raw mill. Furthermore, they showed that raw mill is able to remove significantly higher HCl concentrations, e.g., 400 mg/Nm^3, than those usually encountered industrially at the used operating conditions.

- The sensitivity analysis of particle filters model showed that it can follow the changes in the inlet HCl concentration and dust load of flue gas according to its basic principles and mathematical description.

8.5 References

[1] Bag Filters Operating Principles, AirpolGroup [25 November 2016] http://www.airpol.com.pl/site.php/en/products/177/Bag%20filters

[2] Nielsen, N.F., Skriver, K.G., and Castañ̃o, L.J., Fabric Filter Optimization Using Computational Fluid Dynamics, Report, FLSmidth Airtech, FLSmidth A/S, Copenhagen, 2012. [20 May 2018] http://youornot.com/isespscreensv8/papers/xii/fabricfilter.pdf

[3] Personal communication: Andersen, B.O., CFD and Fluid Dynamic Specialist, FLSmidth Airtech, FLSmidth A/S, Copenhagen,2018.

[4] Personal communication: Nielsen, N.F., Development Engineer-Fabric Filter Product Management, FLSmidth Airtech, FLSmidth A/S, Copenhagen, 2016.

[5] Personal communication: Folsberg, J., Regional Chief Engineer, Raw Mill Department, FLSmith A/S, Copenhagen, 2018.

[6] Personal communication: Zakrzewski, S., CFD Specialist, Research & Development Cement, FLSmidth A/S, Copenhagen, 2018.

[7] ATOX Raw Mill Structure and Solid Material Flows, Internal training material, FLSmidth A/S, Copenhagen, 2013.

[8] Scala, F., Fluidized Bed Technologies for Near Zero Emission Combustion and Gasification, Elsevier-Woodhead Publishing Limited, pp.226, 2013, ISBN:0857098802.

[9] Process Diagrams of Cement Plant A, Internal report FLSmidth A/S, Copenhagen, 2005.

[10] Emission Measurements of Cement Plant A,Internal report FLSmidth A/S, Copenhagen, 2012.

[11] Weinell, C.E., Jensen, P.I., Dam-Johansen, K., and Livbjerg, H., Hydrogen-Chloride Reaction with Limeans Limestone-Kinetics and Sorption Capacity, Industrial and Engineering Chemistry Research, vol.31, pp.164-171, 1992.

[12] Mura, G. and Lallai, A., Reaction Kinetics of Gas Hydrogen Chloride and Limestone, Chemical Engineering Science, vol.49, pp.4491-4500, 1994.

[13] Mian, A.A., Coates, J., and Cordiner, J.B., Binary Gaseous Diffusion Coefficients of N_2-HCl, A-HBr, and N_2-HBr Systems as a Function of Temperature, The Canadian Journal of Chemical Engineering, vol.47, pp.499-502, 1969.

[14] Personal communication: Gjedde, L., CEO in C.K. Environment A/S (representative of Gasmet Tenchnologies Inc.), Copenhagen, 2018.

Chapter 9

Conclusions & Recommendations

This section summarizes the thesis conclusions on the project objectives in the introduction chapter. The main purposes of this project were the understanding of the mechanism of HCl absorption by raw meal at the conditions of post-preheater tower units, development of industrial models for the simulation of HCl scrubbing phenomena in post-preaheater tower units, and suggestion of a method that potentially allows the fast screening of HCl absorption capacity of industrial raw meals. Furthermore, recommendations for future work will be given.

9.1 Understanding of HCl Absorption Mechanism

The knowledge that has been gained in this project regarding to HCl absorption by raw meals at the conditions of post-preheater tower units can be summarized as follows:

- Cement raw meals absorb HCl at temperatures less than 200^{o}C. The observed high HCl absorption rates and the very low active compound conversion degrees seem consistent with a surface saturation phenomenon which is characterized by a specific HCl saturation capacity. The HCl saturation capacity depends on the physical and chemical properties of raw meal, and experimental and operating conditions. The obtained data showed that HCl absorption is controlled by the mass transfer through the gas film around raw meal particles and active surface conversion. The observed active compound conversion degrees were significantly less than 1%.

- The presence of moisture in gas phase significantly enhances the HCl absorption by raw meal at temperatures less than 200^{o}C. The gas phase moisture content effect rapidly weakens with temperature. The moisture content of raw meal particles promotes HCl absorption in the case of dry gas phase. The data support that the observed HCl absorption is mainly dependent on a combined interaction with water on the raw meal surface and solid constituents in the raw meal rather than on a direct interaction with $CaCO_3$.

- Temperature has significant effect on HCl absorption in the case of moist gas phase. In particular, the HCl absorption weakens with temperature in the range 100-180^{o}C. On the other hand, the HCl absorption by raw meal depends only slightly on temperature in the case of dry gas at low temperatures (less than 200^{o}C).

- The industrial concentrations of O_2 (3%v/v) and CO_2 (30% v/v) were found not to significantly influence the HCl absorption by raw meal at temperatures less than 200^{o}C. These data in conjunction with the literature data [1, 2] support that O_2 and CO_2 have no effect on HCl absorption in the range of operating temperatures of post-preheater tower units.

- Agglomeration of raw meal particles and potential channelling phenomena lower the apparent HCl saturation capacity of raw meals in the case of fixed-bed tests. The elimination of agglomerates and channelling phenomena is required for the optimal determination of HCl saturation capacity with our fixed-bed method.

- Fe_2O_3 promotes the chlorination of reagent grade $CaCO_3$ in the temperature range 90-350^{o}C according to TGA-FTIR tests. However, these tests correspond to significantly different conditions than those of the cement plant and fixed-bed tests. Therefore, the Fe_2O_3 effect on HCl absorption should be further investigated using fixed-bed tests.

9.2 Fixed-bed Model

The developed fixed-bed model simulated the obtained fixed-bed experimental data sufficiently well. The model assumed that the HCl absorption by raw meals approximated a surface saturation phenomenon. Furthermore, the HCl reaction was controlled by the mass transfer through the gas film around raw meal particles and active surface conversion. The dependence of HCl saturation capacity on temperature, gas phase moisture content, and raw meal moisture content was taken into account. The use of an appropriate Sherwood number expression for multiparticle fixed-beds (mixtures of active and inert particles) and a numerical solution method with sufficiently fine discretization steps for the model equations allowed the simulation of the experimental data without using any correction factor.

9.3 Simulation of Industrial HCl Scrubbing Phenomena

The development of industrial models for the prediction of HCl reduction in post-preheater tower units corresponds to the industrial utilization of the obtained fixed-bed experimental data. The industrial models take into account the principles of the mechanism of HCl absorption by raw meals as they were determined by the lab experiments, and the operating principles of post-preheater tower units. These models assume that the HCl absorption by raw meal is a surface saturation phenomenon controlled by the mass transfer to the particle surfaces (through the gas film) and active surface conversion. The reactor models were selected based on the flow patterns of gas phase and solids in cement plant units. Emphasis was given to the simulation of HCl scrubbing in particle filters and raw mills due to the presence of available data from industrial measurements [3].

The particle filter model assumes that the HCl absorption occurs in the dispersion before filtration bags. This assumption was supported by the fixed-bed experimental data that showed a very fast HCl absorption reaction, and decrease of the apparent HCl saturation capacity of raw meals due to the formation of agglomerates and presence of channelling phenomena. The model assumes the particle filter unit as a PFR characterized by flue gas residence time equal to 1.9s. Furthermore, the solids follow the flue gas flow and have the same velocity as flue gas. The model successfully simulated the industrially determined scrubbing efficiency of particle filter unit at the tested operating conditions using acceptable values for the correction factor of HCl saturation capacity of dust. The determination of HCl saturation capacity of preheater dust was based on the fixed-bed data of raw meal from the investigated cement plant.

The vertical raw mill model splits the raw mill section into three sub-sections in order to take into account the changes in dispersion dust load and available solids' external surface area from the grinding table plane towards the raw mill cyclone. The raw mill section (excluding raw mill cyclone) was simulated by a configuration of three PFRs in series having the same temperature and moisture content as the raw mill outlet stream [4]. The selection of PFRs was based on CFD simulations of the flow patterns of gas phase and solids in the raw mill unit [5]. The model results were consistent with the industrial evaluation of raw mill HCl scrubbing efficiency [3]. The model predicted the complete HCl absorption at the tested conditions. Furthermore, it showed that raw mill is able to remove significantly higher HCl concentrations than those measured in the investigated cement plant.

The HCl scrubbing phenomena in gas conditioning towers were not simulated in this work due to the lack of industrial data for comparative analysis. However, the developed entrained flow reactor model can be applied using appropriate functions for the simulation of temperature and moisture profiles along gas conditioning tower length.

9.4 Method for Fast Screening of HCl Absorption Capacity

A secondary objective of this work was the suggestion of a simplified method for the fast screening of HCl absorption capacity of industrial raw meals. The used fixed-bed method was able to determine the HCl absorption capacity of raw meal at conditions that approximate those of cement plant. However, it cannot be considered as fast screening method due its complexity. On the other hand, the used TGA-FTIR method was able to distinguish the raw meal with the higher HCl absorption capacity. However, this method corresponds to experimental conditions significantly different from those of cement plant in terms of HCl concentration, active compound conversion (no surface saturation phenomenon in TGA-FTIR tests), and formation of a liquid HCl source that wets the raw meal particles. Therefore, TGA-FTIR method is not suggested for the fast screening of HCl absorption capacity of industrial raw meals.

9.5 Recommendations for Future Work

This work identified a number of topics for which further study could be fruitful for the control of HCl emission from cement plants and optimization of the industrial HCl scrubbing methods. The main topics are:

- The study of gas phase moisture content effect on HCl absorption by raw meal using H_2O concentrations above 5%v/v will determine the type of the relation, e.g., linear, between the gas phase moisture content and HCl saturation capacity of raw meals.

- The evaluation of HCl absorption by dried (0%w/w H_2O) raw meal samples using moist gas phase will give significant information related to the simultaneous HCl and H_2O absorption by industrial raw meals.

- HCl absorption tests using raw meal samples from the same cement plant that are characterized by different specific surface area will clarify the degree of dependence of the HCl absorption capacity on the specific surface area of raw meal.

- The evaluation of the HCl absorption capacity of mixtures of clay minerals and Ca-sorbents at low temperatures could be fruitful for the optimization of available industrial HCl scrubbing techniques. The hydration and dehydration properties of clay minerals in conjunction with the detected promotion of HCl absorption with the moisture content of sorbents make such a study reasonable.

- The study of Fe_2O_3 effect on Ca-based sorbents chlorination using fixed-bed tests is promising for the optimization of the industrial HCl scrubbing methods at low temperatures.

9.6 References

[1] Mura, G. and Lallai, A., Reaction Kinetics of Gas Hydrogen Chloride and Limestone, Chemical Engineering Science, vol. 49, pp.4491-4500, 1994.

[2] Gullett, B.K., Jozewicz, W. and Stefanski, L.A., Reaction Kinetics of Ca-Based Sorbents with HCl, Industrial & Engineering Chemistry Research, vol.31, pp.2437-2446, 1992.

[3] Emission Measurements of Cement Plant A,Internal report FLSmidth A/S, Copenhagen, 2012.

[4] Personal communication: Folsberg, J., Regional Chief Engineer in Raw Mill Department, FLSmith A/S, Copenhagen, 2018.

[5] Personal communication: Zakrzewski, S., CFD Specialist, Research & Development Cement, FLSmidth A/S, Copenhagen, 2018.

Notation

Latin

A: Cross-sectional area of fixed-bed reactor [m^2]

$A_{abs.}$: Absorbance

$A_{calibration}$: Area of calibration trace peak - TGA-FTIR [s]

$A_{measurement}$: Area of measurement trace peak - TGA-FTIR [s]

A_{PFR}: Cross-sectional area of PFR reactor (entrained flow reactor) [m^2]

BET: Brunauer-Emmett-Teller theory

b: Parameter of Frössling-type equation for Sherwood number calculation

CaAl: $CaCO_3$ - Al_2O_3 mixture

CaAlFe: $CaCO_3$ - Al_2O_3 - Fe_2O_3 mixture

CaFe1, CaFe2: $CaCO_3$ - Fe_2O_3 mixtures

Cap, Cap(T, Y_{ws},Y_{wg}): HCl saturation capacity of raw meal [mol/g]

$Cap_{ref.}$, $Cap_{ref.}$(T, Y_{ws},Y_{wg}): Reference HCl saturation capacity of raw meal [mol/g]

$C_{calibration}$: Concentration in gas phase - calibration [ppm]

C_{HCl}, $C_{HCl,0}$: HCl concentration in gas phase (main report body (models), Appendix D, Appendix E : [mol/m^3] - Figure legends: [mg/Nm^3] - Appendix A: [ppmv]

CF: Correction factor of HCl saturation capacity of raw meals (industrial models)

$C_{measurement}$: Concentration in gas phase [ppm]

C_{CO_2}: Concentration of CO_2 [mol/Nm^3]

$C^*_{CO_2}$: Concentration of CO_2 [$Nm^3_{CO_2}/Nm^3$]

C_2S: Dicalcium silicate (Belite)

C_3A: Tricalcium aluminate

C_3S: Tricalcium silicate (Alite)

C_4AF: Tetracalcium aluminoferrite

c: Parameter of Frössling-type equation for Sherwood number calculation

$D_{equiv.}$: Equivalent inner diameter of the annular cross-section of PFR2 (raw mill model) [m]

D_{HCl-N_2}: Diffusion coefficient of gas HCl in gas N_2 [m^2/s]

Din_{wall}: Internal wall diameter of raw mill [m]

D_{pipe}: Cross-sectional diameter of the flue gas supply pipeline [m]

D_{table}: Grinding table diameter of raw mill [m]

$D_{10\%,L.S.}$, $D_{50\%,L.S.}$, $D_{90\%,L.S.}$: Diameters of raw meal particles determined using laser scattering method [μm]

d: Parameter of Frössling-type equation for Sherwood number calculation

d_p: Particle diameter [m]

ESP: Elecrostatic precipitator

EDS: Energy-dispersive X-ray spectroscopy

F_{HCl}, $F_{HCl,f}$, $F_{HCl,0}$: HCl molar rate (general, entrained flow reactor outlet and entrained flow reactor inlet) [mol/s]

FTIR: Fourier transform infrared spectroscopy

GCT: Gas conditioning tower

$\dot{HCl}_{input}$, $\dot{HCl}_{outlet}$, $\dot{HCl}_{consumption}$, $\dot{HCl}_{accumulation}$: HCl molar rate (inlet, outlet, consumption and accumulation in PFR control volume) [mol/s]

h_1: Diameter of grinding rollers [m]

h_2: The distance between grinding rollers top and separator blades inlet [m]

I: Integral of Lambert-Beer relation

IR: Infrared

K: The conversion factor of I (absorbance) to CO_2 concentration [$Nm^3_{CO_2}$]

K*: The conversion factor of I (absorbance) to CO_2 concentration [ppmv]

k_g: Mass transfer coefficient $[\frac{\frac{mol}{m^2_{solid} \cdot s}}{\frac{mol}{m^3_{gas}}}]$

k_{wg}, k_{wg} (T_{test}, Y_{ws}, Y_{wg}): Gas phase moisture content coefficient

k_{ws}, k_{ws} (T_{test}, Y_{ws}, Y_{wg}): Solids moisture content coefficient

LOI: Loss on ignition [%w/w]

L_{RPF}: Length of the equivalent particle filters PFR [m]

L.S.: Laser scattering

l_{pipe}: Length of raw mill outlet-raw mill cyclone connection pipeline [m]

l_{sep}: Length of separator equivalent pipeline [m]

l_3: Length of PFR3 in raw mill model [m]

M_{CaCO_3}, M_{CO_2}, M_{HCl}: Molar weights of $CaCO_3$, CO_2 and HCl [g/mol]

MFC: Mass flow controller

m: Mass of fine particles of raw meal in raw mill [g]

m_{HCl}, $m_{HCl,consumption}$, $m_{HCl,accumulation}$: Mass of HCl [mol, kg]

m_{F-S}, m_{A-S}, m_{re-S}, m_{silo-S}: Mass flows of solids in raw mill section of interest [g/s]

$m_{C,in-SG}$, $m_{RM,in-SG}$, $m_{RM,out-SG}$, $m_{RMC,out-SG}$, $m_{B,out-SG}$, $m_{re,SG}$: Mass flows of dispersions in raw mill section of interest [g/s]

m_{FA-RMC}, m_{FA-RM}: Mass flows of false air in raw mill section units [g/s]

m_{CaCO_3}: Mass of $CaCO_3$ in fixed bed sample [g]

m_{CO_2}: Mass of CO_2 [g]

N_{CO_2}: Number of CO_2 moles [mol]

P: Pressure [Pa]

$P_{cleaning-limit}$: Pressure (filter model - cleaning pressure drop limit)[Pa]

$P^e_{CO_2}$: Equilibrium pressure of CO_2 [atm]

Pe: P*élect* number

PM10: Particulate matter $< 10\mu$m

Pr: Prandtl number

PRF: Plug flow reactor

PRF1, PFR2, PFR3: PFRs of the raw mill section

R: Ideal gas constant [kg·m^2/(mol·K·s^2)]

Re: Particle Reynolds number

RM-A: Raw meal from cement plant A

RM-B: Raw meal from cement plant B

r_{HCl}, r_{HCl}(z,t): Reaction rate [mol/(m$^2_{solid}$ ·s)]

$S_{act.}$: Active specific surface area of raw meal [m^2/g]

Sh: Sherwood number

Sh_{eff}: Effective Sherwood number

Sh*: Local Sherwood number

Sc: Schmidt number

SEM: Scanning electron microscope

S_{fine}, $S_{inter.}$, S_{coarse}: Specific surface areas of fine, intermediate and coarse raw meal particles in raw mill [m^2/g]

SR: Simulated raw meal

s_1, s_2, s_3: Total external surface areas of particles in raw mill PFRs (PFR1, PFR2 and PFR3) [m^2]

T: Temperature [K]

T_{FB}: Temperature of fixed-bed [^{o}C]

TGA: Thermogravimetric analysis

TOC: Total organic carbon

t: Time [s]

t_B: Breakthrough time in the case of inert samples [s]

Δt_B: Breakthrough time from active compound (t_B is subtracted) [s]

$\Delta t_{B,dry}$, $\Delta t_{B,wet}$: Breakthrough times from active compound using dry and moist gas phase [s]

Δt_{peak}: Duration of the injection peak in CO_2 calibration of TGA-FTIR [s]

$t_{res.}$, $t_{1,res.}$, $t_{2,res.}$, $t_{1,res.}$: Residence times in particle filters equivalent PFR and raw mill PFRs (RFR1, PFR2 and PFR3) [s]

U: Filtration velocity in fixed-bed [m/s]

U_{PFR}: Dispersion velocity in PFR [m/s]

$\dot{V}_{carrier}$: Volumetric flow of carrier gas [Nm^3/s]

V_{CO_2}: Volume of CO_2 [Nm^3]

V_{HCl}: Volume of HCl [Nm^3]

V_{N_2}: Volume of N_2 [Nm^3]

V_{PFR}, V_1, V_2, V_3: Volumes of PFR and PFRs of raw mill (PFR1, PFR2 and PFR3) [m^3]

$V_{sep.-upper}$: Volume of separator upper part [m^3]

VOCs: Volatile Organic Compounds

X_{CaCO_3}: Mass fraction of $CaCO_3$ in raw meal

X_{HCl}, $X_{HCl,f}$, $X_{HCl,0}$: Conversions of gas phase HCl content

XPS: X-ray photoelectron spectroscopy

XRD: X-ray diffraction

X_{RM}: Mass fraction of raw meal in fixed-bed samples

X_S, X_S(z,t): Conversion of active surface of particles

$x_{fine,1}$, $x_{fine,2}$, $x_{inter.,1}$, $x_{inter.,2}$, $x_{coarse,1}$: Mass fractions of fine , intermediate and coarse raw meal particles in the raw mill PFRs

Y_{wg}: Moisture content of gas phase [%v/v]

Y_{ws}: Moisture content of solids [%w/w]

z: Distance variable

Greek

Ω : Volumetric fraction of active bed particles with respect to the total volume occupied by inert and active solids.

ϵ: Void fraction of the tested samples in fixed-bed tests

ε: Gas phase dust load [g/m^3_{actual}]

ε_1, ε_2, ε_3: Gas phase dust load in raw mill PFRs [g/m^3_{actual}]

μ: Dynamic viscosity of gas phase [kg/(m·s)]

$\nu_{actual-FG}$: Inlet actual flue gas volumetric flow of particle filters unit [m^3_{actual}/s]

ν_f: Dispersion volumetric flow at the outlet of entrained flow reactor model [m^3_{actual}/s]

ν_{feed}: Gas phase volumetric flow of fixed-bed tests [Nm^3/s]

ν_0, ν_1, ν_2, ν_3: Dispersion volumetric flows in raw mill PFRs [m^3_{actual}/s]

ρ_{bed}: Density of sample bed in fixed-bed tests [kg/m^3]

ρ_{fluid}: Density of gas phase [kg/m^3]

τ: Tortuosity

ν: Kinematic viscosity of gas phase [m^2/s]

$\bar{\nu}$: Wavenumber (infrared spectroscopy) [cm^{-1}]

Appendix A

TGA-FTIR Calibration Examples

A.1 HCl Calibration

This HCl calibration example is based on the thermal decomposition of 100mg of $AlCl_3 \cdot 6H_2O$ (Figure A.1) using constant heating rate: 5°C/min and carrier gas flow (N_2): 100 Nml/min.

$$AlCl_3 \cdot \ 6H_2O(s) \rightarrow \ 1/2Al_2O_3(s) + 3HCl(g) + 4.5H_2O(g) \tag{A.1}$$

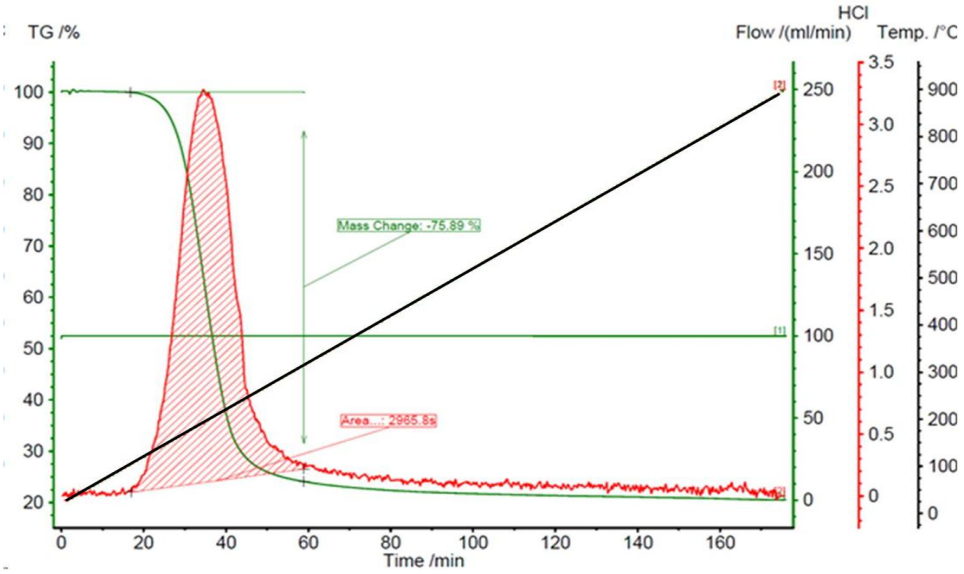

Figure A.1: Thermogravimetric sample mass change (% - green curve), HCl trace (absorbance units - red curve) and temperature (°C - black curve) as function of time, using 100mg of $AlCl_3 \cdot 6H_2O$, heating rate: 5°C/min, carrier gas flow N_2: 100 Nml/min, and HCl wavenumber band: 2600-3100cm^{-1}.

The mass of the released HCl is calculated by the thermogravimetric results (Figure A.1) and equation A.2, where the M_{HCl} is the molecular weight of HCl and the M_{H_2O} is the molecular weight of H_2O.

$$HCl_{Release} = \frac{3 \cdot M_{HCl}}{3 \cdot M_{HCl} + 4.5 \cdot M_{H_2O}} \cdot Total\ Mass\ loss = 43.6 \cdot 10^{-3} g \tag{A.2}$$

The spectral absorbance of a given wavenumber zone and corresponding compound concentration are linearly related according Lambert-Beer law. The Lambert-Beer relation in integral form for a characteristic wavenumber zone:

$$I = \int_{\overline{\upsilon_1}}^{\overline{\upsilon_2}} A_{abs.}(\overline{\upsilon}) \cdot d\overline{\upsilon} \tag{A.3}$$

where $A_{abs.}$ is the measured absorbance and $\overline{\upsilon}$ is the wavenumber.

Conversion of HCl Trace to Concentrations:

The area under two consecutive measurement points of I - time curve (trace - red curve in Figure A.1) is calculated by application of the trapezoid method:

$$Area_i = \frac{I_i + I_{i+1}}{2} \cdot (t_{i+1} - t_i) \tag{A.4}$$

where the I_i is the value of Lambert-Beer relation integral at the measurement point i, I_{i+1} is the value of Lambert-Beer relation integral at measurement point i+1, t_i is the time at the measurement point i, and t_{i+1} is the time at measurement point i+1.

The released HCl mass between two consecutive measurement points:

$$m_{HCl,i} = \frac{Area_i}{\sum Area} \cdot Total\ mass\ released\ HCl \tag{A.5}$$

where the $m_{HCl,i}$ is the mass of the released HCl between two consecutive measurement points, $Area_i$ is the area between two consecutive measurement points of trace curve, and $\sum Area_i$ is the total area under the trace curve.

The carrier gas (N_2) volume at the reference conditions (1atm - 0^oC) which passes through the FTIR between two consecutive measurement points:

$$V_{N_2,i} = (t_{i+1} - t_i) \cdot \dot{V}_{carrier} \qquad [Nm^3] \tag{A.6}$$

where $\dot{V}_{carrier}$ is the volumetric flow of carrier gas [Nm^3/s]
The volume of the released HCl in the time interval i:

$$V_{HCl,i} = \frac{(\frac{m_{HCl,i}}{M_{HCl}}) \cdot R \cdot T}{P} \qquad [Nm^3] \tag{A.7}$$

where $V_{HCl,i}$ is the released volume of HCl in the time interval i, $m_{HCl,i}$ is the mass of the released HCl in the time interval i, the P is the pressure in FTIR cell (1atm=$1.01325 \cdot 10^5$Pa), T is the reference temperature (273K) and R is the gas constant 8.314 $J{\cdot}K^{-1}mol^{-1}$.

The HCl release in ppmv:

$$C_{HCl,i} = \frac{V_{HCl,i}}{V_{N_2,i} + V_{HCl,i}} \cdot 10^6 \tag{A.8}$$

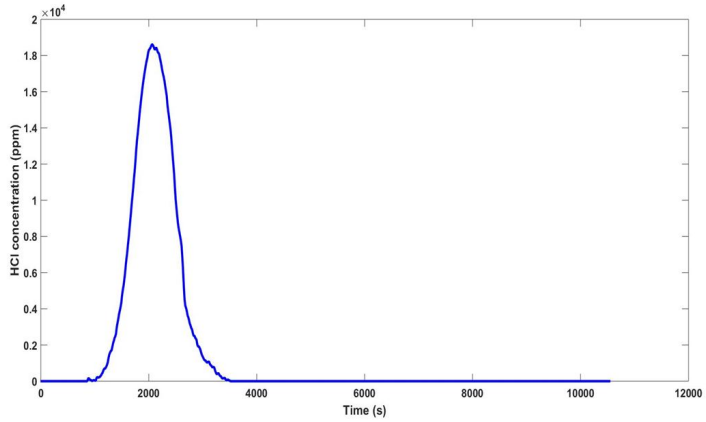

Figure A.2: HCl concentration (ppmv) - time curve, using 100mg of $AlCl_3 \cdot 6H_2O$, heating rate: $5^oC/min$, carrier gas flow N_2: 100 Nml/min, and HCl wavenumber band: 2600-3100cm^{-1}.

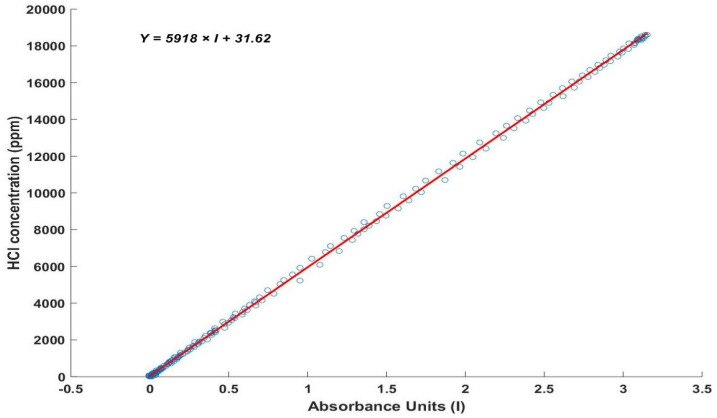

Figure A.3: HCl calibration curve that expresses the relation between HCl concentration (ppm) and absorbance (I).

A.2 CO_2 Calibration

The CO_2 calibration of TGA-FTIR system was based on the injection of CO_2 pulses (volume: 1ml at 25^{o}C, concentration: 19000 ppm) during a ramping temperature test of inert sample (SiO_2). The CO_2 was injected using 50 Nml/min carrier gas (N_2) flow in the injection device. The total carrier gas flow was 150 Nml/min in the sample chamber. Figure A.4 shows the CO_2 traces (I-time curve) in the case of CO_2 pulse injection at differing sample chamber temperature. It is clearly seen that the CO_2 peaks have identical surface areas. Furthermore, the chamber temperature does not affect the FTIR sensitivity.

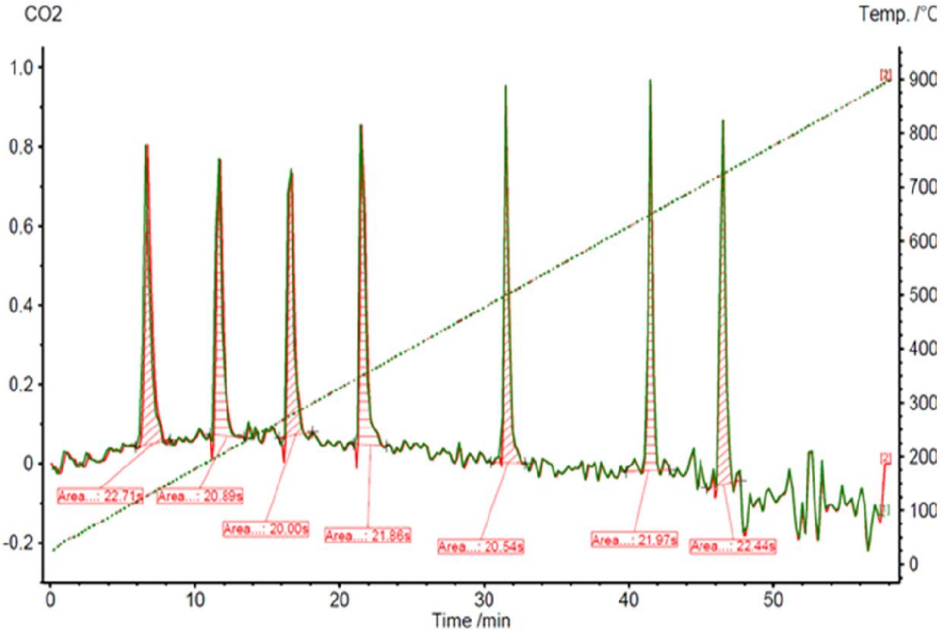

Figure A.4: CO_2 pulse injection test (I - time curve), using inert sample (SiO_2), heating rate: 15^{o}C/min, total carrier gas flow: 150 Nml/min, and CO_2 wavenumber band: 2200-2450cm^{-1}.

The mass of the injected CO_2:

$$m_{CO_2} = \frac{PV_{CO_2,25^oC}}{RT} \cdot M_{CO_2} = 34.2 \cdot 10^{-6} g \tag{A.9}$$

where P is the pressure($1.01325 \cdot 10^5$ Pa), $V_{CO_2,25^oC}$ is the volume of the injected CO_2 at 25^{o}C [m^3], R is the gas constant (8.314 J·K^{-1}mol^{-1}), M_{CO_2} is the molar weight of CO_2 and T is the injection temperature temperature (298K).

The injected CO_2 in each injection:

$$N_{CO_2} = \int_0^{\Delta t_{peak}} C_{CO_2} \cdot \dot{V_{carrier}} \cdot dt \qquad [mol] \tag{A.10}$$

where Δ t_{peak} is the duration of the peak [s], and C_{CO_2} is the CO_2 concentration [mol / Nm^3].

The assumed linear relation between CO_2 concentration and I (absorbance):

$$C^*_{CO_2} = C_{CO_2} \cdot \frac{R \cdot T}{P} = K \cdot I \qquad [\frac{Nm^3_{CO_2}}{Nm^3}] \tag{A.11}$$

where T is the reference temperature (273K) and K is conversion factor of I to concentration

Equatio A.10 can be expressed as follow:

$$N_{CO_2} = \frac{P \cdot K \cdot \dot{V}_{carrier}}{R \cdot T} \cdot \int_0^{\Delta t_{peak}} I \cdot dt = \frac{P \cdot K \cdot \dot{V}_{carrier}}{R \cdot T} \cdot Area \tag{A.12}$$

The conversion factor of I to HCl concentration in ppmv based on the calibration data is:

$$K^* = K \cdot 10^6 = \frac{N_{CO_2} \cdot R \cdot T}{P \cdot \dot{V}_{carrier} \cdot Area} \cdot 10^6 = 339 ppm\nu. \tag{A.13}$$

A.3 $AlCl_3 \cdot 6H_2O$ Dissociation Tests

This section presents the effects of sample mass, flow rate of carrier gas (N_2), and heating rate on the HCl signals from the thermal dissociation of $AlCl_3 \cdot 6H_2O$.

Sample Mass Effect:

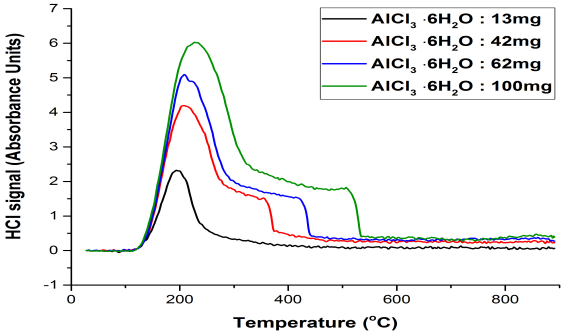

Figure A.5: HCl signals from the thermal dissociation tests of $AlCl_3 \cdot 6H_2O$, using HCl IR-spectrum band: 2600-3100 cm^{-1}, sample mass: 13mg, 42mg, 62mg and 100mg, heating rate: 15 ^oC/min, and carrier gas (N_2) flow rate: 50 Nml/min.

Carrier Gas Flow Rate Effect:

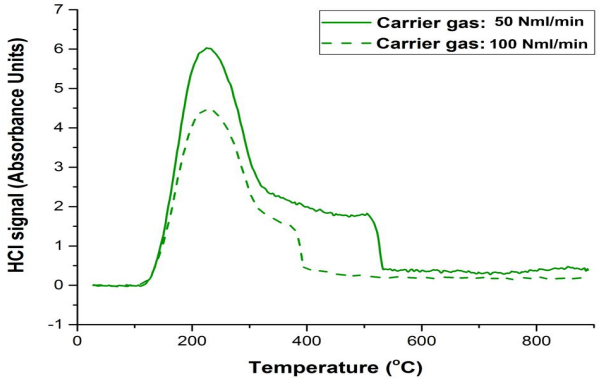

Figure A.6: HCl signals from the thermal dissociation tests of $AlCl_3 \cdot 6H_2O$, using HCl IR-spectrum band: 2600-3100 cm^{-1}, sample mass: 100mg, heating rate: 15 ^oC/min, and carrier gas (N_2) flow rate: 50 Nml/min and 100 Nml/min.

Heating Rate Effect:

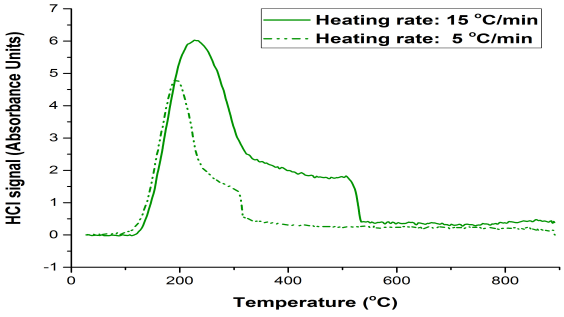

Figure A.7: HCl signals from the thermal dissociation tests of $AlCl_3 \cdot 6H_2O$, using HCl IR-spectrum band: 2600-3100 cm^{-1}, sample mass: 100mg, heating rate: 5 ^oC/min and 15 ^oC/min, and carrier gas (N_2) flow rate: 50 Nml/min.

Thermogravimetric data and Shoulder Origin:

The comparison and interpretation of the thermogravimetric and FTIR data give significant information related to the observed shoulder in HCl signals. Figure A.8 shows that the measured total mass loss by the thermal decomposition of 100mg $AlCl_3 \cdot 6H_2O$ was equal to 76.06 mg, which is close to the expected (78.8 mg) based on the stoichiometric decomposition (A.1). The total HCl release based on the experimental mass loss and stoichiometric decomposition is 43.7mg which corresponds to the total area of the HCl peak (4265.2s). The thermogravimetric data show that the the shoulder area corresponds to mass loss close to 4.79 mg. The linear relation between the HCl signal area and the released HCl mass allows the calculation of the HCl mass that corresponds to the shoulder area based on FTIR data. In particular, the shoulder area corresponds to 16.43mg of HCl.

The difference in the released HCl mass based on the thermogravimetric and FTIR data indicates that the shoulder region was not released from the crucible. Probably, the shoulder corresponds to HCl that was released in an earlier stage and trapped in the sample chamber due to the low flow rate of carrier gas and/or physical absorption. The thermogravimetric data analysis makes it unlikely that the speciation of $AlCl_3 \cdot 6H_2O$ is related to the shoulder area.

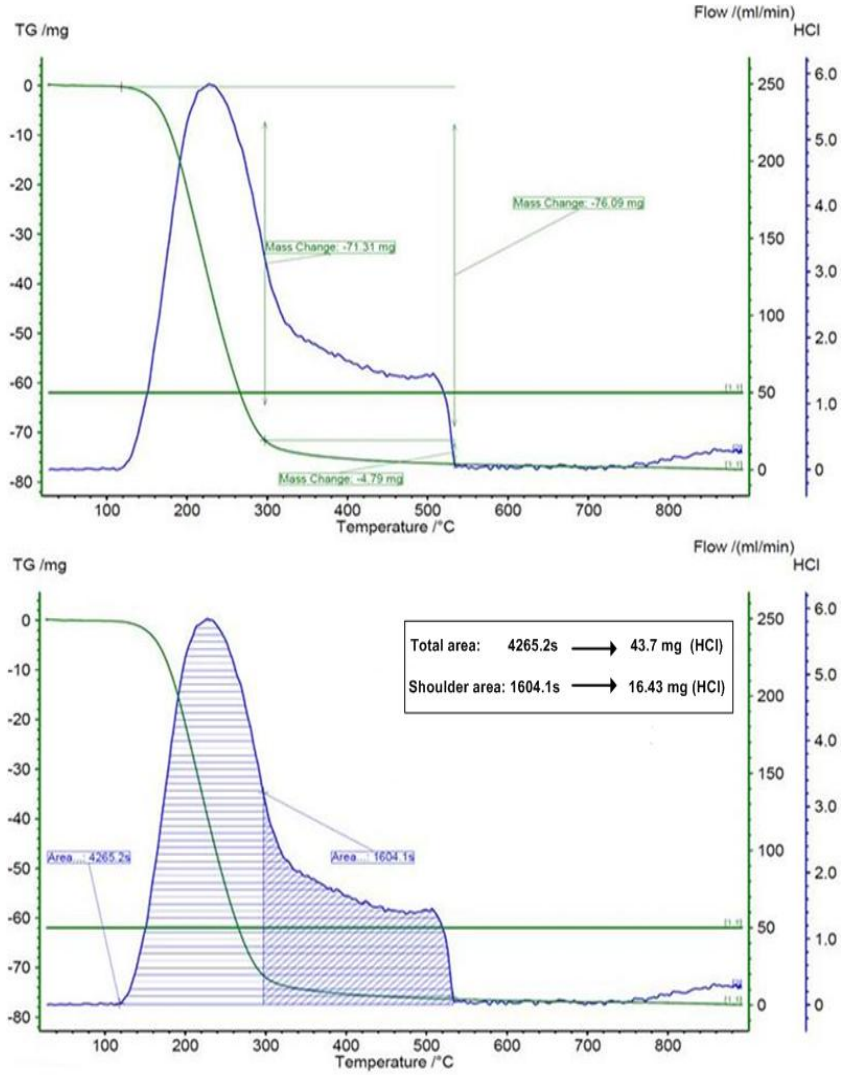

Figure A.8: Thermogravimetric data and HCl signal from thermal dissociation of $AlCl_3 \cdot 6H_2O$, using HCl IR-spectrum band: 2600-3100 cm^{-1}, sample mass: 100mg, heating rate: 15 °C/min, and carrier gas (N_2) flow rate: 50 Nml/min.

Appendix B

XPS Analysis Results

B.1 RM-A Samples Unexposed and Exposed(fixed-bed) to HCl

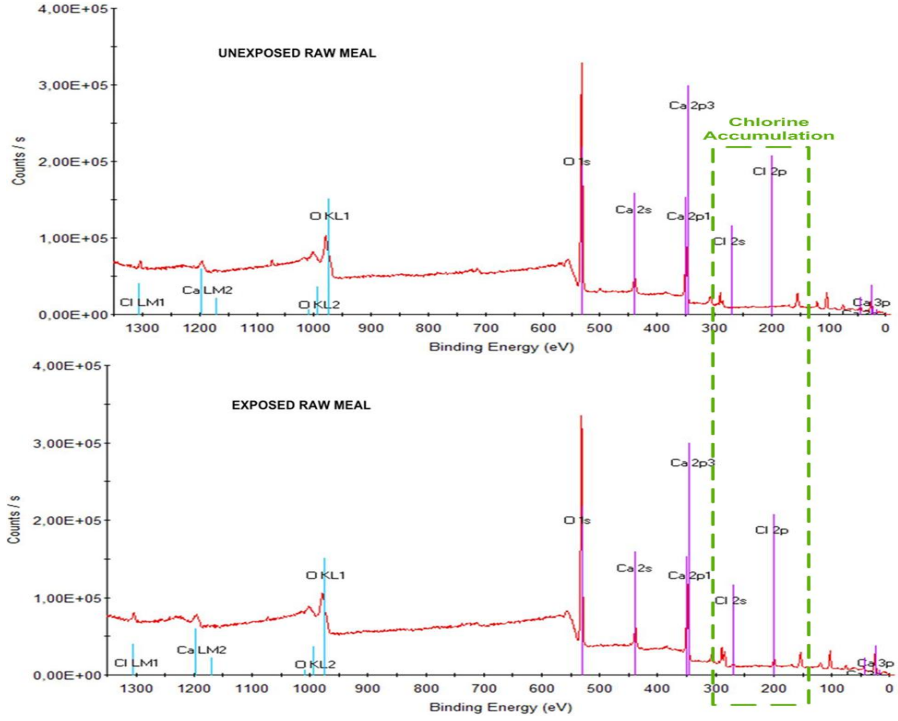

Figure B.1: XPS spectra of pure RM-A samples unexposed and exposed (HCl: 100ppmv, temperature: 100°C, dry gas phase, and exposure time: 16min) to HCl.

*Table B.1: Characteristic XPS spectra lines - binding energies for $CaCO_3$ *.*

Element	Spectra lines	Binding Energy (eV)
C	1s	289.8
C	1s	290.1
C	1s	289.7
C	1s	289.4
C	1s	289.6
Ca	AP-2p3/2,L2M23M23(1D)	638.7
Ca	AP-2p3/2,L2M23M23(1D)	638.8
Ca	2p3/2	347.7
Ca	2p1/2	346.8
Ca	2p3/2	346.8
Ca	2p3/2	347
Ca	2p3/2	346.7
Ca	3p	25.3
Ca	3s	44.2
Ca	2p3/2	347.4
Ca	2p1/2	351.1
Ca	2s	439.2
Ca	L2M23M23 (1D)	291.8
Ca	L2M23M23 (1D)	292
Ca	DS-2p	3.5
O	AP-1s, KL23L23(1D)	1041
O	1s	531.7
O	KVV	509.7
O	1s	531.4
O	1s	531.2
O	1s	531.3

*Table B.2: Reported XPS spectra lines and electron binding energies for $CaCl_2$ *.*

Element	Spectra lines	Binding Energy (eV)
Ca	2p3/2	348.7
Ca	2p3/2	347.8
Ca	L2M23M23(1D)	291.9
Ca	AP2p3/2L2M23M23(1D)	640.2
Ca	2p3/2	348.3
Cl	2p3/2	199

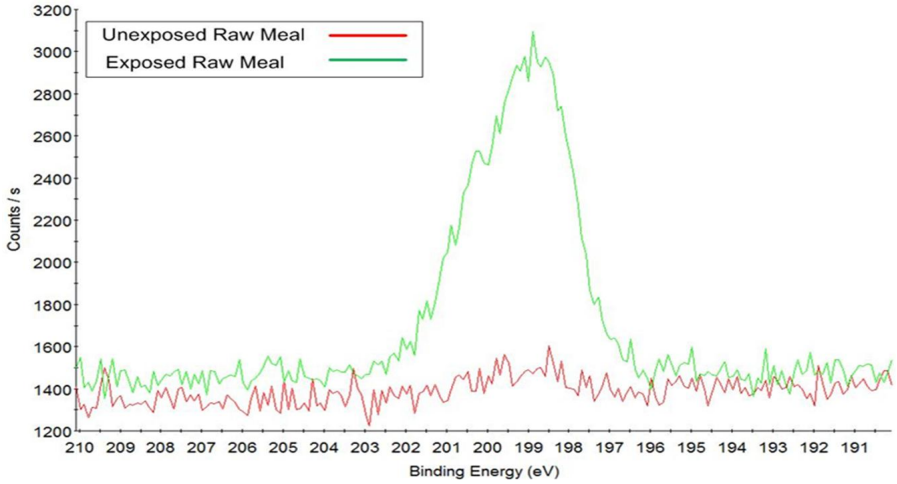

Figure B.2: XPS spectra of the HCl exposed (HCl: 100ppmv, temperature: 100°C, dry gas phase, and exposure time: 16min) and unexposed pure RM-A samples based on Cl-2p electrons energy state scanning.

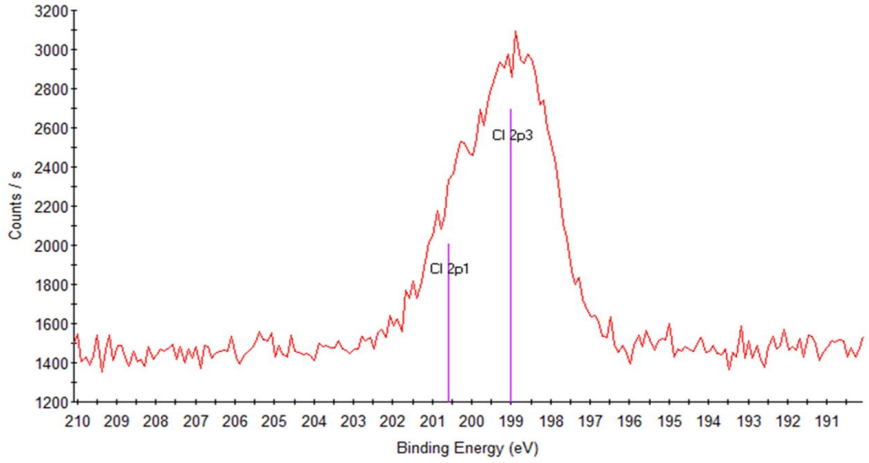

Figure B.3: XPS spectra of the HCl exposed RM-A sample (HCl: 100ppmv, temperature: 100°C, dry gas phase, and exposure time: 16min) based on Cl-2p stationary stage scanning and the characteristic Cl-2p spectra lines (elemental).

B.2 Fe_2O_3 Samples Unexposed and Exposed to HCl

Table B.3: Characteristic Cl-2p photoelectron lines - binding energies of Fe_2O_3, $FeCl_2$, $FeCl_3$, and Fe_2O_3 - $AlCl_3 \cdot 6H_2O$ heated to 350°C using heating rate 15°C/min.

Cl-2p		
	C-2p1 (eV)	Cl-2p3 (eV)
Sample Fe_2O_3 (fitted)	200.27	198.67
Heated Fe_2O_3-$AlCl_3 \cdot 6H_2O$ (fitted)	200.98	199.38
$FeCl_2$†	201	199.3
$FeCl_3$†	201.4	199.7

Table B.4: Characteristic Fe-2p photoelectron lines - binding energies of Fe_2O_3, FeO, $FeCl_2$, and $FeCl_3$.

Fe-2p				
Compound	Peak 1 (eV)	Peak 2 (eV)	Preak 3 (eV)	Peak 4 (eV)
α-Fe_2O_3†	709.8	710.7	711.4	712.3
γ-Fe_2O_3 †	709.8	710.8	711.8	713
FeO†	708.4	709.7	713.3	-
$FeCl_3$†	711.3	712.4	711.5	714.2
$FeCl_2$ †	709.8	710.5	710.9	-

*NIST XPS spectra database [June 22, 2017] https://srdata.nist.gov/xps/chem_name.aspx.

†Grosvenor,A.P., Kobe, B.A., Biesinger, M.C. and Mclntyre, N.S., Investigation of Multiplet Splitting of Fe-2p XPS Spectra and Bonding in Iron Compounds, Journal of Surface and Interface Analysis, vol.36, pp.1564-1574, 2004.

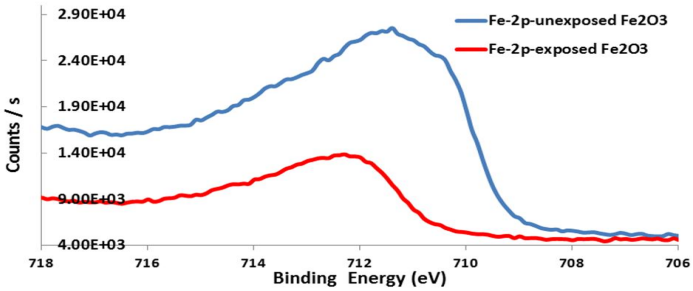

Figure B.4: Fe-2p XPS spectra of Fe_2O_3 and Fe_2O_3 - $AlCl_3 \cdot 6H_2O$ heated to 350°C using heating rate 15°C/min.

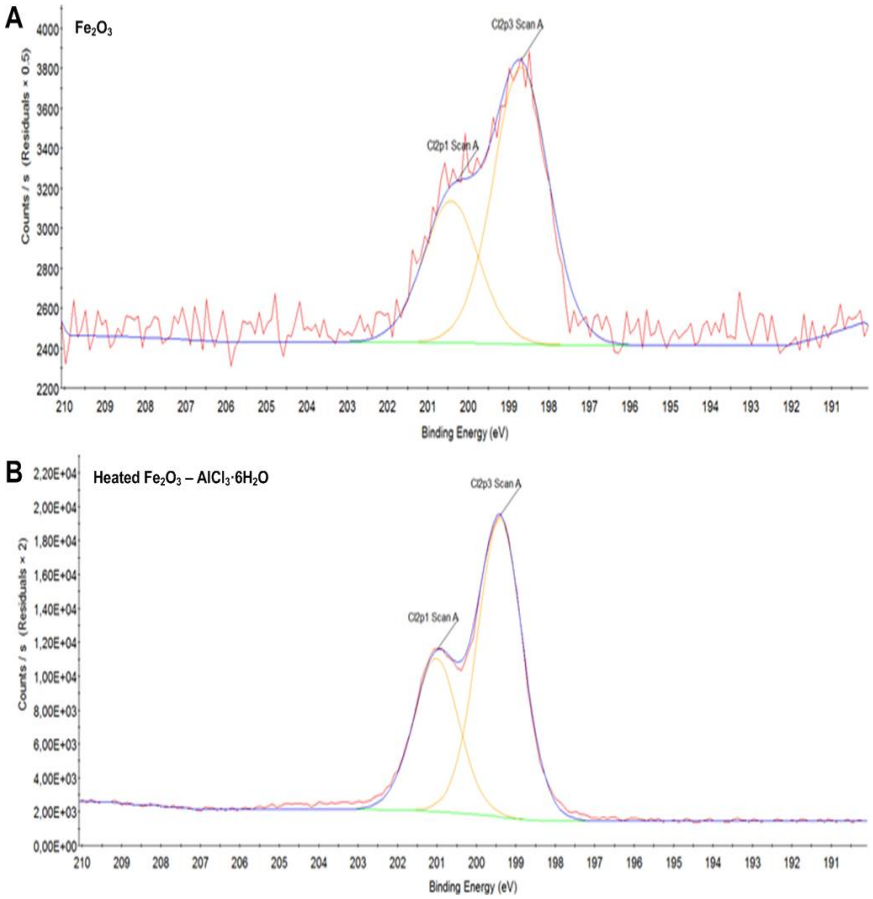

Figure B.5: A) Cl-2p XPS spectra (red) and the fitted photoelectron lines (yellow) of Fe_2O_3 (unexposed); B) Cl-2p XPS spectra (red) and the fitted photoelectron lines (yellow) of Fe_2O_3 - $AlCl_3 \cdot 6H_2O$ heated to 350°C using heating rate 15°C/min (exposed to HCl).

Appendix C

XRD Analysis of RM-B and RM-B-$AlCl_3 \cdot 6H_2O$ Samples Heated at 310^oC and 380^oC

C.1 Detection of $CaCl_2$ Formation

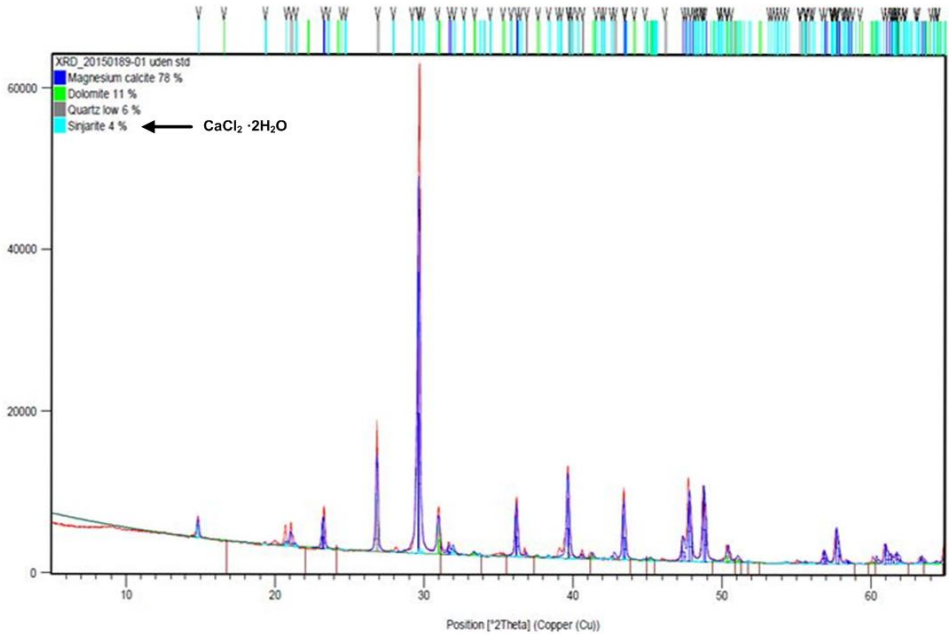

Figure C.1: XRD analysis of RM-B-$AlCl_3 \cdot 6H_2O$ sample (interface - a layered structure sample), $AlCl_3 \cdot 6H_2O$ content:6.6% w/w, heating rate: 15 ^oC/min, heated to 380^oC (FLSmidth A/S).

C.2 Detection of $Ca(MgFe)(CO_3)_2$ Formation

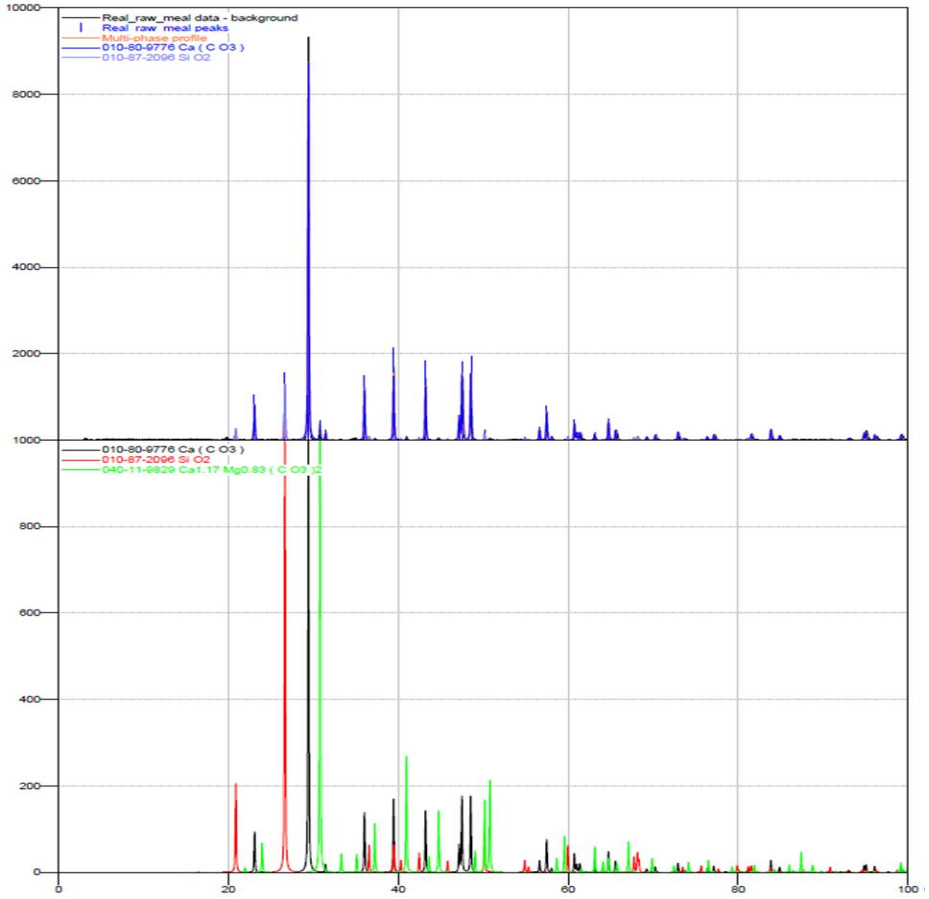

Figure C.2: XRD analysis results (spectra matching) of pure RM-B sample heated to 310°C (Chemistry Department of DTU).

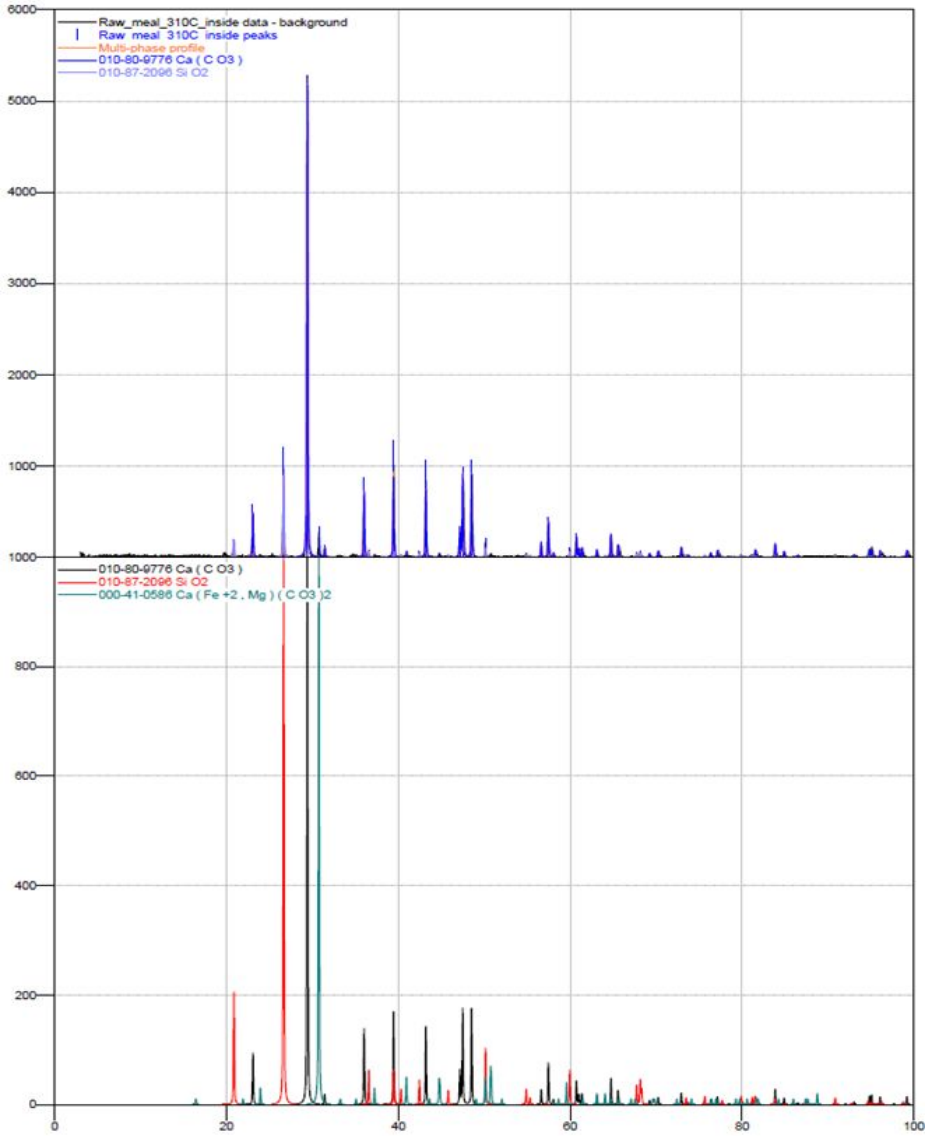

Figure C.3: XRD analysis results (spectra matching) of RM-B-$AlCl_3 \cdot 6H_2O$ sample (formed interface solid disc) heated to 310° C (Chemistry Department of DTU).

Appendix D

Mass Balance & Numerical Solution of Fixed-bed Model

D.1 Mass Balance

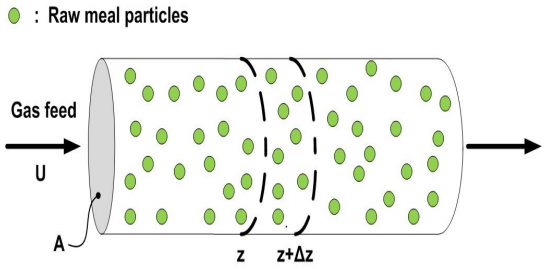

Figure D.1: Shematic illustration of a packed bed reactor.

Gas Phase:

Reaction rate:

$$r_{HCl}(z,t) = k_g \cdot C_{HCl}(z,t) \cdot (1 - X_s(z,t)) \tag{D.1}$$

Mass transfer coefficient:

$$k_g = \frac{Sh \cdot D_{HCl-N_2}}{d_p} \tag{D.2}$$

The gas phase mass balance of the control volume in Figure D.1:

$$m_{HCl}\mid_z - m_{HCl}\mid_{z+\Delta z} - m_{HCl,consumption} = m_{HCl,accumulation} \tag{D.3}$$

HCl enters the control volume during the time span Δt:

$$m_{HCl} \mid_z = C_{HCl}(z,t) \cdot A \cdot U \mid_z \cdot \Delta t \tag{D.4}$$

HCl permeates the control volume during the time span Δt:

$$m_{HCl} \mid_{z+\Delta z} = C_{HCl}(z,t) \cdot A \cdot U \mid_{z+\Delta z} \cdot \Delta t \tag{D.5}$$

HCl consumed during the time span Δt:

$$m_{HCl,consumption} = A \cdot \Delta z \cdot r_{HCl}(z,t) \cdot \Delta t \cdot \rho_{bed} \cdot X_{RM} \cdot S_{act.} \tag{D.6}$$

HCl accumulated in gas phase during the time span Δt:

$$m_{HCl,accumulation} = \epsilon \cdot A \cdot \Delta z \cdot (C_{HCl}(z,t+\Delta t) - C_{HCl}(z,t)) \tag{D.7}$$

The substitution of D.4-D.7 in D.3:

$$A{\cdot}U{\cdot}\frac{C_{HCl}(z,t) \mid_z - C_{HCl}(z,t) \mid_{z+\Delta z}}{\Delta z} - A{\cdot}r_{HCl}(z,t){\cdot}\rho_{bed}{\cdot}X_{RM}{\cdot}S_{act.} = \epsilon{\cdot}A{\cdot}\frac{C_{HCl}(z,t+\Delta t) - C_{HCl}(z,t)}{\Delta t} \tag{D.8}$$

$$\epsilon \cdot \frac{\partial C_{HCl}(z,t)}{\partial t} + U \cdot \frac{\partial C_{HCl}(z,t)}{\partial z} = -r_{HCl}(z,t) \cdot \rho_{bed} \cdot X_{RM} \cdot S_{act.} \tag{D.9}$$

$$\epsilon \cdot \frac{\partial C_{HCl}(z,t)}{\partial t} + U \cdot \frac{\partial C_{HCl}(z,t)}{\partial z} = -k_g \cdot C_{HCl}(z,t) \cdot (1 - X_s(z,t)) \cdot \rho_{bed} \cdot X_{RM} \cdot S_{act.} \tag{D.10}$$

Solid Phase:

The solid phase mass balance gives an expression for the active surface conversion along PFR:

$$\frac{\partial X_s(z,t)}{\partial t} = r_{HCl}(z,t) \cdot \frac{S_{act.}}{k_{ws} \cdot k_{wg} \cdot Cap_{ref.}} \tag{D.11}$$

$$\frac{\partial X_s(z,t)}{\partial t} = k_g \cdot C_{HCl}(z,t) \cdot (1 - X_s(z,t)) \cdot \frac{S_{act.}}{k_{ws} \cdot k_{wg} \cdot Cap_{ref.}} \tag{D.12}$$

D.2 Numerical Solution Using Explicit Discretization

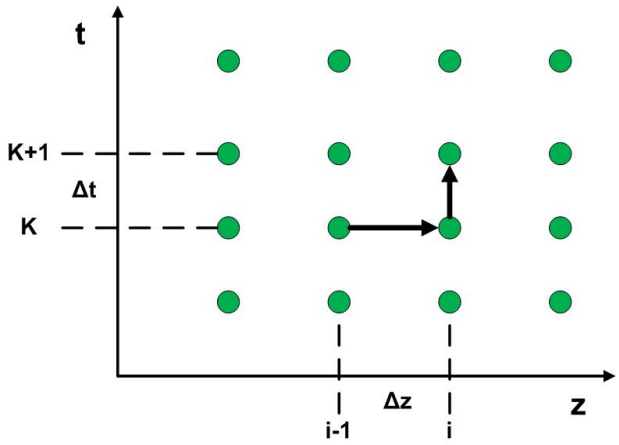

Figure D.2: Shematic illustration of the explicit scheme.

Gas Phase:

$$\frac{C_{HCl,i}^{K+1} - C_{HCl,i}^{K}}{\Delta t} + \frac{U}{\epsilon} \cdot \frac{C_{HCl,i}^{K} - C_{HCl,i-1}^{K}}{\Delta z} = -\frac{\rho_{bed} \cdot X_{RM} \cdot S_{act.}}{\epsilon} \cdot k_g \cdot C_{HCl,i}^{K} \cdot (1 - X_{S,i}^{K}) \quad \text{(D.13)}$$

$$C_{HCl,i}^{K+1} = C_{HCl,i}^{K} - \frac{U \cdot \Delta t}{\epsilon \cdot \Delta z} \cdot (C_{HCl,i}^{K} - C_{HCl,i-1}^{K}) - \frac{\rho_{bed} \cdot X_{RM} \cdot S_{act.} \cdot \Delta t}{\epsilon} \cdot k_g \cdot C_{HCl,i}^{K} \cdot (1 - X_{S,i}^{K}) \quad \text{(D.14)}$$

Solid Phase:

$$\frac{X_{S,i}^{K+1} - X_{S,i}^{K}}{\Delta t} = \frac{S_{act.}}{k_{ws} \cdot k_{wg} \cdot Cap_{ref.}} \cdot k_g \cdot C_{HCl,i}^{K} \cdot (1 - X_{S,i}^{K}) \quad \text{(D.15)}$$

$$X_{S,i}^{K+1} = X_{S,i}^{K} + \frac{S_{act.} \cdot \Delta t}{k_{ws} \cdot k_{wg} \cdot Cap_{ref.}} \cdot k_g \cdot C_{HCl,i}^{K} \cdot (1 - X_{S,i}^{K}) \quad \text{(D.16)}$$

Stability Condition:

$$\frac{U \cdot \Delta t}{\epsilon \cdot \Delta z} \leq 1 \quad \text{(D.17)}$$

*The discretization method and explicit scheme were based on the the teaching material of the DTU course: 28361 Chemical Engineering Model Analysis (professor: Associate Professor Alexander Shapiro).

Appendix E

Mass Balance - Entrained Flow Reactor Model

E.1 Mass Balance

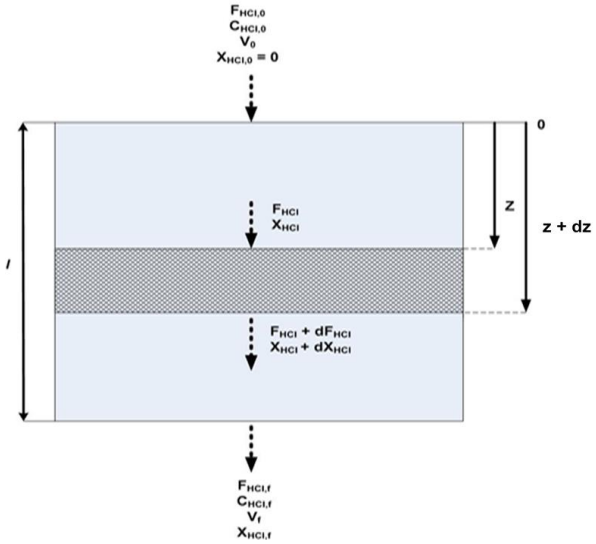

Figure E.1: Schematic illustration of a control volume in the entrained flow reactor.

Reaction rate:

$$r_{HCl} = k_g \cdot C_{HCl} \cdot (1 - X_s) \qquad [\frac{mol}{m^2_{solid-active} \cdot s}] \tag{E.1}$$

The mass balance of gas phase of the control volume (Figure D.1) gives:

$$\dot{HCl}_{input} = \dot{HCl}_{output} + \dot{HCl}_{consumption} + \cancelto{0}{\dot{HCl}_{accumulation}} \tag{E.2}$$

$$F_{HCl} = F_{HCl} + dF_{HCl} + \dot{HCl}_{consumption} \tag{E.3}$$

The term dF_{HCl}:

$$dF_{HCl} = d(F_{HCl,0} \cdot (1 - X_{HCl}) = -F_{HCl,0} \cdot dX_{HCl} \tag{E.4}$$

where $F_{HCl,0}$ is the HCl molar rate at the reactor inlet and X_{HCl} is the conversion of the gas phase HCl content.

The substitution of D.4 in D.3 gives:

$$F_{HCl,0} \cdot dX_{HCl} = \dot{HCl}_{consumption} \tag{E.5}$$

The HCl consumption rate:

$$\dot{HCl}_{consumption} = r_{HCl} \cdot S_{act.} \cdot \varepsilon \cdot dV \tag{E.6}$$

where r_{HCl} is the reaction rate, $S_{act.}$ is the specific external active surface area of the dust, ε is the dust load of flue gas , and dV is the control volume.

The substitution of E.6 in E.5 gives:

$$F_{HCl,0} \cdot dX_{HCl} = r_{HCl} \cdot S_{act.} \cdot \varepsilon \cdot dV \tag{E.7}$$

The consideration of a cylindrical PFR allows the expression of E.7 as follows:

$$F_{HCl,0} \cdot dX_{HCl} = r_{HCl} \cdot S_{act.} \cdot \varepsilon \cdot A_{PFR} \cdot dz = k_g \cdot C_{HCl,0} \cdot (1 - X_{HCl}) \cdot (1 - X_s) \cdot S_{act.} \cdot \varepsilon \cdot A_{PFR} \cdot dz \tag{E.8}$$

$$\frac{dX_{HCl}}{dz} = \frac{S_{act.} \cdot \varepsilon \cdot A_{PFR}}{F_{HCl,0}} \cdot k_g \cdot C_{HCl,0} \cdot (1 - X_{HCl}) \cdot (1 - X_s) \tag{E.9}$$

The mass balance of solid phase gives an expression for the active surface conversion along the entrained flow reactor:

$$\frac{dX_s}{dt} = k_g \cdot C_{HCl,0} \cdot (1 - X_{HCl}) \cdot (1 - X_s) \cdot \frac{S_{act.}}{k_{ws} \cdot k_{wg} \cdot Cap_{ref.}} \tag{E.10}$$

$$\frac{dX_s}{dz} = \frac{1}{U_{PFR}} \cdot k_g \cdot C_{HCl,0} \cdot (1 - X_{HCl}) \cdot (1 - X_s) \cdot \frac{S_{act.}}{k_{ws} \cdot k_{wg} \cdot Cap_{ref.}} \tag{E.11}$$

Appendix F

Scientific Article on HCl Absorption by Raw Meal (Draft)

Experimental Evaluation of Hydrogen Chloride (HCl) Absorption by Cement Raw Meals at Low Temperatures, using Fixed-Bed Tests

Authors:

Stylianos Pachitsas[a*], Stig Wedel[a], Lars Skaarup Jensen[b], Jytte Boll Illerup[a], and Kim Dam-Johansen[a]

[a] Department of Chemical and Biochemical Engineering, CHEC, Technical University of Denmark, Søltofts Plads, Building 229, DK-2800, Kgs. Lyngby, Denmark

[b] FLSmidth A/S, Vigerslev Allé 77, 2500 Valby, Denmark

Keywords: HCl; Absorption; Emission; Cement; Limestone; Low temperatures

Abstract

The HCl absorption by cement raw meals was experimentally evaluated in the temperature range 100-180°C, using a fixed-bed set-up and gas phase HCl content between 50 ppmv and 200 ppmv. In particular, the effects of temperature, gas phase composition and dispersion of raw meal particles on HCl absorption capacity of raw meals were studied. The obtained data are consistent with our interpretation of HCl absorption mechanism based on a surface saturation phenomenon that corresponds to a certain specific HCl absorption capacity of raw meal. The experimentally observed active compound conversions were significantly less than 1%. The dilution of raw meal samples using fused silica with particle size range 50-100μm increased the apparent HCl absorption capacity of raw meal 10 times due to the elimination of raw meal particle agglomerates. The HCl absorption was slightly enhanced as the temperature was decreased from 180°C to 100°C in the case of dry gas phase tests. A dependence of raw meal HCl absorption capacity on raw meal moisture content was detected at the same experimental conditions. The presence of 5% v/v H_2O in gas phase increased the absorption capacity of raw meal A by 25% at 180°C and by 61% at 100°C relative to the absorption capacity from dry gas phase. The presence of 3% v/v O_2 and 30% v/v CO_2 in gas phase did not have any apparent effect on the HCl absorption in the investigated temperature range.

1. Introduction

HCl is a gaseous pollutant of concern in the cement industry with serious environmental impact. A significant number of cement plants are challenged on their compliance with the emission regulations, e.g., 3 ppmv in dry flue gas at 7% v/v O_2 [1]. Therefore, the minimization of the cost of HCl emission control and optimization of the prediction of HCl emission are considered as high priority issues for cement producers and equipment suppliers. Efficient addressing of HCl

emission issues requires detailed understanding of HCl release and absorption mechanisms in cement plants.

The identification of HCl sources is a challenging issue due to the simultaneous release and absorption of chlorine species, low raw meal chlorine content, e.g., 0.03% w/w, and complex raw meal composition. Generally, the raw meal term denotes the fine (1μm-90μm) mixed raw material product produced by grinding in raw mill units. Industrial scale measurements have identified the presence of HCl release and absorption zones in the cement manufacturing process (Fig.1) [2, 3]. In particular, the two detected HCl formation zones are the low temperature (360-600°C) preheater tower cyclones, and the rotary kiln [4, 5]. In addition, industrial tests in cement plants with high HCl emissions showed that the HCl content in stack gas was not dependent on fuel chlorine content [3] and kiln formation zone in the absence of a bypass stream from kiln to stack [2,3]; This points to HCl release from raw materials in the preheaters as a primary source.

HCl scrubbing phenomena have been detected in raw mill and particle filter units at temperatures between 90°C and 220°C [2,3]. It is noteworthy that the industrial evaluation of particle filters and raw mill HCl scrubbing efficiencies [2] showed active compound ($CaCO_3$ content of preheater dust in particle filters and raw meal in raw mill) conversions close to $4 \cdot 10^{-2}$ % and $5 \cdot 10^{-3}$ %, respectively .

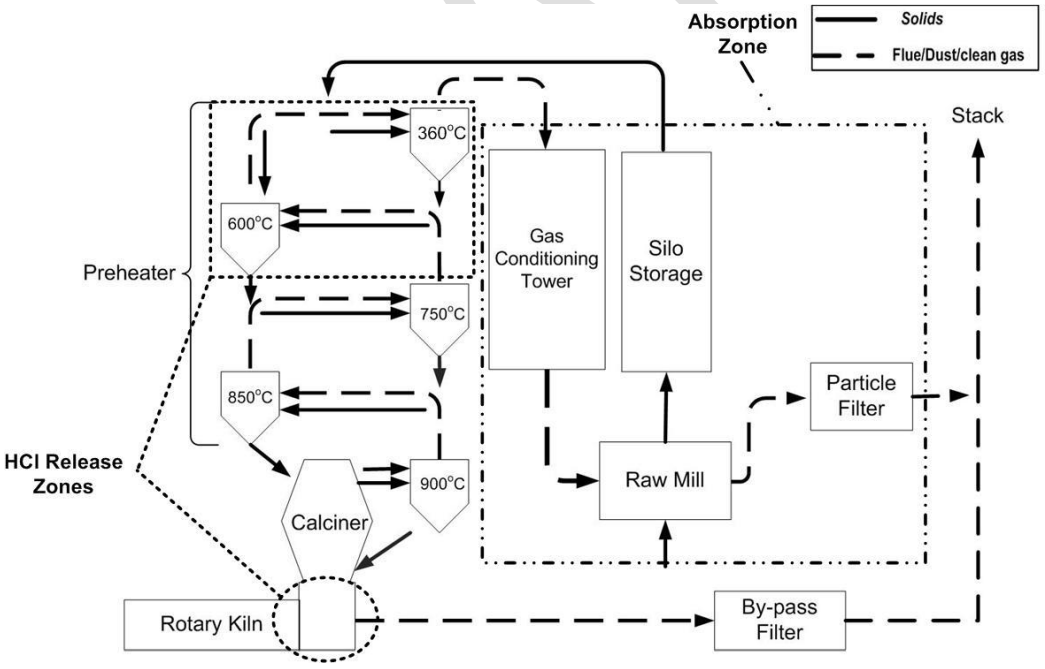

Fig.1 Simplified cement plant layout diagram.

The industrial flue gas at preheater tower outlet is characterized by HCl concentrations less than 100ppmv and moisture content between 5%v/v and 19%v/v [2, 3] .Typically, the HCl absorption temperature window is considered to be between 90℃ and 400℃. However, the main interest is focused on the temperature ranges 90-120℃ and 120-220℃ that correspond to the scrubbing conditions in raw mill and particle filter, respectively. Raw meal is a multicomponent mixture of natural products, e.g., clay, limestone, sand, with particle sizes predominantly between 1μm and 100μm, large specific surface area 7-9 m^2/g. The flue gas residence times in particle filter (bag filter) and raw mill (vertical roller mill) are approximately 2s and 1.5s, respectively. The fine particles are dispersed in the flue gas; and consequently, flue gas and particles have approximately similar residence times in the gas conditioning tower and raw mill units. However, fine particles have significantly longer residence times than flue gas in particle filters.

The existing HCl emission control methods are based on the empirical utilization of raw mill scrubbing effect [2,3], $Ca(OH)_2$ injection in particle filter, gas conditioning tower and preheater outlet flue gas stream [6-9], and acidic gases scrubber installations, e.g., wet scrubbers and gas suspension absorber semi-dry scrubbers (lime slurry spraying) [10-13]. The most widely used method for the control of HCl emission is the flue gas passing through the raw mill when it is in operation. However, this method is limited by the process operating flue gas and solids mass flows (not necessarily all flue gas passes through the raw mill) and raw mill operating time.

It is concluded that the prediction of HCl emission, optimization of HCl control methods and operating cost reduction require the understanding of the mechanism of HCl absorption by raw meal. Despite many researchers [14-29] having investigated the HCl absorption by gas solid reactions on Ca-based sorbents, the direct utilization of these results in the HCl emission control from cement plants demonstrates many challenges. These are related to the different physical properties of raw meals, and relevant process conditions, e.g., low HCl concentration in flue gas and low temperatures. Therefore, the study of HCl absorption by raw meal at experimental conditions similar to cement plants is necessary. This work is focused on the study of the mechanism of HCl absorption by cement raw meal, using a fixed bed-FTIR set-up, low HCl concentrations, and isothermal tests.

2. Previous Studies

It is well known that absorption of acidic gasses by Ca-based sorbents can be affected by the temperature, gas phase composition and sorbent physical properties, e.g., specific surface area and particle size. Therefore, the selection of experimental conditions relevant to industrial environment is required for the simulation of HCl absorption in cement plant units.

Table 1 shows studies relevant to HCl absorption by Ca-based sorbents considering common direct gas-solid reactions (eq. 1-3).

$$CaCO_3(s) + 2HCl\,(g) \rightleftharpoons CaCl_2(s) + H_2O\,(g) + CO_2\,(g) \quad (1)$$

$$CaO(s) + 2HCl\,(g) \rightleftharpoons CaCl_2(s) + H_2O\,(g) \quad (2)$$

$$Ca(OH)_2(s) + 2HCl(g) \rightleftharpoons CaCl_2\,(s) + 2H_2O(g) \quad (3)$$

The previous studies insufficiently account for HCl absorption under conditions relevant to the cement plant absorption zone in terms of temperature, gas phase composition, exposure time, and sorbent composition-physical properties outlined in section 1. In the following sections a more detailed review of results from previous studies will be presented with the aim of extracting information of relevance for the present work.

Appendix F

Table 1: Studies related to HCl absorption by Ca-based sorbents.

T (°C)	HCl (ppmv)	Particle Size Range	BET (m^2/g)	Gas Phase H_2O (% v/v)	Tested Materials	Method	
60-1000	1000	20.5-2.12μm (CaO)	8.8-19.7 ($Ca(OH)_2$) 1.2-1.85 (limestone)	0, 5, 15	Limestone, CaO, $Ca(OH)_2$	Fixed-bed	Weinell et al.[14]
350-600	13000-40000	0.2-2mm	-	0	Limestone	Fixed-bed	Petrini et al.[15]
450-550	20000-240000	<0.25mm	-	0	Limestone	Fixed-bed	Ketov et al.[16]
300-600	2000	46.5μm-190μm	~5	0 and 5	Limestone	Fixed-bed	Mura and Lallai [17]
750	1000	32-75μm, 250-355μm, 710-1000 μm	- - -	0	Calcined limestone	Fluidized bed	Matsukata et al. [18]
310-600	21000	<10μm-720μm	11-13	0	Calcined limestone	Thermogravimatric balance	Daoudi and Walters [19]
300-600	900	125-500μm	1-2 (limestone) 4.1 (CaO) 24 ($Ca(OH)_2$)	1.8-24.2	$CaCO_3$, CaO, $Ca(OH)_2$	Fixed-bed	Duo et al. [20]
150-250 ($CaOH_2$) 400-600 (CaO-$CaCO_3$)	1000	<0.125μm	- -	1.3	Limestone, Calcined limestone, $Ca(OH)_2$	Fixed-bed	Wang et al. [21]
150-350	1000-7500	3-59μm	5	0	Calcined limestone, $Ca(OH)_2$	Fixed-bed	Gullett et al.[22]
200-600	1000	0.188-925mm	-	0	CaO	Fixed-bed	Mura and Lallai [23]
650-850	2000	200-250μm	-	0 and 14	Calcined limestone	Thermogravimetric balalce	Partanen et al.[24]
310-670	5000-50000	<45μm	-	0	Calcined limestone	Thermogravimetric balance	Daoudi and Walters[25]
54-177	1000	-	12.4	~0- 10	$Ca(OH)_2$	Fixed-bed	Jozewicz et al.[26]
50-127	150-1000	0.05-3μm	10	0-11	$Ca(OH)_2$	Fixed-bed	Fonseca et al.[27]
150-400	630	<0.09mm	-	0-10	$Ca(OH)_2$	Fixed-bed	Karlsson et al.[28]
120	250-1000	92%<45μm	21.1	0-19	$Ca(OH)_2$	Fixed-bed	Chisholm and Rochelle [29]

* The presented works do not include information related to the experimental pressure, and consequently it was considered close to atmospheric.

2.1 ***Temperature Effect***

The temperature can significantly affect the HCl absorption by Ca- based sorbents. The study of Weinell et al. [14] on HCl absorption by limestone at temperatures between 60℃ and 1000℃ showed that HCl binding capacity is largest in the range 500-600℃ and decreases above 600℃. They also reported a similar behavior from $Ca(OH)_2$ except from an increase of HCl binding capacity below 150℃ in presence of wet gas phase. Petrini et al. [15] using limestone at temperatures between 350℃ and 600℃, showed increase of $CaCO_3$ chlorination with temperature. Ketov et al. [16] reported an optimal HCl absorption temperature for limestone in the range 450-500℃ under comparable experimental conditions. Furthermore, the works of Daoudi and Walters [19, 25] and Duo et al.[20] on HCl absorption, using different Ca-based sorbents in the temperature range 300-600℃, showed increase of the conversion levels with temperature. Therefore, the available studies clearly support that the HCl absorption by Ca-based sorbents increases with temperature in the range 300-600℃. It should be kept in mind that these observations of the temperature effect correspond to much higher HCl concentrations than those present in the absorption zone of cement plants (see Fig.1). It should also be considered that only two studies [14, 22] used limestone in the relevant temperature range 90-220℃.

An interpretation of the HCl absorption enhancement with temperature and detected incomplete active compound conversion between 300℃ and 600℃ was given by Duo et al.[20] and Daoudi and Walters [19, 25]. They suggested that the HCl absorption dependence on temperature and incomplete active compound conversion can be related to changes in reaction kinetics and sintering phenomena. In particular, the temperature increase up to 600℃ results in increase of reaction constant and diffusion coefficient. However, the formation of a solid product with larger molar volume [30] leads to pore closure. Partanen et al. [24] presented a different approach to the enhancement of Ca-based sorbents chlorination at temperatures close to 650℃. According to this, the gaseous H_2O release from $CaCO_3$/CaO chlorination opens the solid reactant pores, and consequently enhances the HCl diffusion to the inner particle part at temperatures up to 670℃. The attenuation of Ca-based sorbents chlorination above a certain temperature around 600℃, was reported by many researchers [14, 19, 20, 24, 25]. In particular, Weinell et al.[14] supported that, in the case of limestone, the diminishing HCl binding capacity above 500℃ is related to the chemical equilibrium between gas and solid (eq. 1-2). Partanen et al.[24] connected the overall conversion decrease at 850℃ with formation of $CaCO_3$- $CaCl_2$ liquid phase. Daoudi and Walters [19,25] supported that the reduction of limestone conversion at 650℃ was related to the diffusion resistance increase by sintering phenomena. Duo et al.[20] also suggested that sintering at high temperatures [31] results in increase of diffusion resistance and reduction of particles porosity. Generally, the aforementioned diffusion resistance increasing mechanisms (pore blocking and sintering) and gas – solid phase chemical equilibrium are the most common explanations for the Ca-based sorbents overall incomplete conversion [15, 17, 19, 20, 23, 25]. However, the view of

Duo et al. [32] was that the observed incomplete conversion is insufficiently explained by the aforesaid causes.

2.2 *Gas Phase Moisture Content Effect*

The effect of gas phase moisture content on acidic gases absorption by Ca-based sorbents was investigated by many researchers. The presented studies concluded that absorption of acidic gases is enhanced by the presence of moisture at temperatures less than 300℃. [14,17,26,27,29,33,34] In particular, Weinell et al. [14] reported enhancement of HCl absorption by $Ca(OH)_2$ in presence of H_2O in gas phase at temperatures less than 200°C. Moreover, the water effect weakens with temperature and disappears above 200℃. The beneficial effect of gas phase moisture content on HCl absorption by $Ca(OH)_2$ at temperatures between 54℃ and 177℃ was also found by many other research groups [14,26,27,29]. The absence of gas phase moisture effect on HCl absorption by limestone in the temperature range 300-600℃ was confirmed by Mura and Lallai [17].

The mechanism which the gas phase moisture affects the HCl absorption by Ca-based sorbents is not completely understood. Weinell et al. [14] and Fonseca et al.[27] suggested that the moisture effect is based on the fracturing of sorbent crystal lattice or product layer by a saturated aqueous phase. Furthermore, Jozewicz et al.[26] reported that calcium silicate sorbents (mixture of flyash and $Ca(OH)_2$) have higher reactivity with acidic gases in presence of a wet gas phase in comparison to reagent grade Ca-based sorbents due to the bonding of water molecules on silicates surface. Raw meal contains a significant amount of clay minerals, to which H_2O molecules and OH^- groups can be bonded up to 550℃ and 550-950℃, respectively [35-37]. Based on Jozewicz's results it is likely that H_2O molecules and OH^- groups contribute to HCl absorption by calcium silicate sorbents at low temperatures.

2.3 *CO_2 and O_2 Effects*

CO_2 and O_2 are primary rotary kiln flue gas components. Mura and Lallai [17] reported that limestone reactivity with HCl was unaffected by the presence of 30 %v/v CO_2 in gas phase at temperatures less than 500°C. However, reactivity was reduced by CO_2 at temperatures above 500°C. Partanen et al. [24] supported that in the case of calcined limestone the presence of CO_2 enhances chlorination at 650°C due to the simultaneous re-carbonation; on the other hand, HCl absorption was unaffected by CO_2 at 850°C.

Gullett et al.[22] reported that a change of gas phase O_2 content between 0% v/v and 5% v/v. did not have any apparent effect on HCl absorption by CaO between 150°C and 350°C. Although pertaining to higher HCl concentrations than in absorption zone, these results point to no or only very small effects on HCl absorption at low temperatures (less than 350℃).

2.4 *Particle Size and Specific Surface Area Effects*

Solid reactant particle size and specific surface area are important parameters for solid-gas reactions. Weinell et al. [14] and Matsukata et al.[18] pointed out that the effect of particle size on CaO and limestone final conversion and chlorination rates was limited. On the other hand, Petrini et al.[15], Daoudi and Walters [19], Wang et al.[21], Gullett et al.[22], Mura and Lallai [17], and Partanen et al.[24] supported that small particle size and large specific surface area are beneficial for the HCl absorption. Therefore, the majority of the researchers support that the large surface area-small particle size of Ca-based sorbents promotes the HCl absorption.

2.5 *HCl Absorption Mechanism Modeling and Reaction Limiting Step*

The unreacted grain core model and shrinking unreacted core model are mainly applied in the simulation of HCl absorption by Ca-based sorbents. In particular, Weinell et al.[14], Mura and Lallai [23] and Fonseca et al.[27] studied the HCl absorption mechanism using grain models in the temperature range 60-1000℃. Mura and Lallai [17] proposed the grain model for porous particles, and the unreacted core shrinking model in the case of less porous particles. The shrinking core model is also used by Wang et al.[21] and Gullett et al. [22] in the temperature range 150-350℃. The previous studies report that the sorption rate initially is very fast and decreases with the particle conversion until the reaction rate becomes zero [14, 17, 21-23, 27]. Furthermore, they state that the reaction rates are limited by reaction kinetics and HCl diffusion resistance in particles. Solid diffusion [17, 23, 27], pores diffusion [17, 21] and gaseous HCl diffusion through product layer [22] are suggested as potential reaction control resistances. A group of researchers [14, 22, 23] consider that the reaction is mainly controlled by HCl diffusion in solid phase. However, Mura and Lallai [17, 23], Wang et al.[21], and Fonseca et al.[27] suggested chemical reaction and HCl diffusion in solid phase as control mechanisms depending on reaction stage. They state that the chemical reaction is the rate controlling step in the initial or early stages of the reaction. Furthermore, the reported active compound final conversions vary between 0% and 98% depending on the experimental conditions and tested sorbent.

It is commonly accepted that the HCl absorption by Ca-based sorbents is characterized by first order reaction kinetics with respect to HCl concentration [14 (60-1000℃), 17 (300-600℃), 19-23 (150-600℃), 25 (310-670℃), 27-29 (50-400℃)]. Furthermore, the works of Gullett et al.[22] and Fonseca et al.[27] on CaO and $Ca(OH)_2$ respectively, found that the HCl absorption is described by first order reaction kinetics relative to HCl concentration.

2.6 Literature Study Summary

The available information related to HCl absorption by Ca-based sorbents corresponds to experimental conditions and tested sorbents that significantly differ from relevant cement plant conditions. Furthermore, the given HCl absorption mechanism interpretations cannot explain the industrially detected fast HCl absorption that is characterized by extremely low active compound conversions ($5 \cdot 10^{-3}$ - $4 \cdot 10^{-2}$ %). Therefore, a direct utilization of the literature data in prediction of the HCl emission from cement plants does not seem possible.

The previous studies support that the HCl absorption by Ca-based sorbents is characterized by two steps: a first very fast initial reaction step and a second where the reaction rate decreases down to zero with time. The first step may be controlled by the chemical reaction. The second step is controlled by the HCl diffusion in solid phase. Furthermore, the available data indicate that the reaction is characterized by first order reaction kinetics with respect to HCl concentration.

Literature references support that the temperature can significantly affect HCl absorption by Ca-based absorbents. In addition, enhancement of HCl absorption in presence of moisture in gas phase was reported for temperatures less than 200°C. Independence of the HCl absorption on O_2 and CO_2 was reported at temperatures up to 350°C.

3. Materials and Methods

A quartz fixed-bed reactor set-up (Fig.2) was used in the study of HCl absorption by raw meals, using isothermal experiments in the temperature range 100-180°C, and 1.5 Nl/min gas flow (normal conditions: T=273K and P=1.01326× 10^5 Pa). The quartz reactor is based on a standard design used by CHEC group [38-40]. It consists of an external quartz tube that is immobilized in the furnace, a sample tube reactor with 1.6cm internal diameter, reactor top seal, and reactor bottom part seal. The gas flow control system comprises five mass flow controllers Bronkhost EL-Flow for regulation of gas stream components supply and gas stream composition. The steam supply system consists of a water evaporator, a high accuracy peristaltic pump (Messgaspumpe N5 Kp18, MC TechGroup A/S), and a water tank. The gas and steam supply lines to fixed-bed reactor and FTIR analyser are heated to 115-130°C to prevent condensation of H_2O and HCl. The quartz fixed-bed reactor temperature is controlled by a furnace with an automatic temperature control system. The measurement of HCl concentration in the gas stream after the reactor is conducted using an HCl - FTIR analyzer (Servomex Sercotough 2510 series), which gives the HCl concentration in ppmv.

The fixed-bed reactor was loaded with a quartz wool layer on top of which test sample was placed. The loaded reactor tube was placed and sealed in the pre-heated furnace. Each experiment's duration was 800s. The sample removal stage comprises system flushing using 1.5Nl/min N_2 for 600s to remove residual HCl.

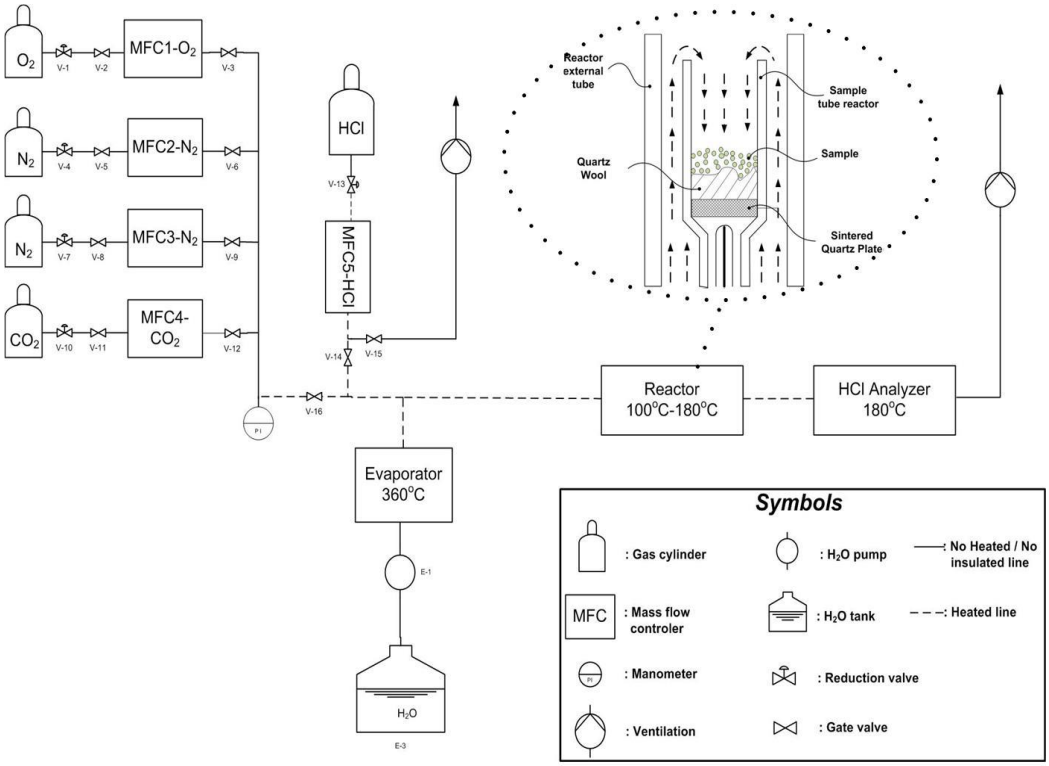

Fig.2 Fixed-bed experimental set-up apparatus.

The feed gas stream (Table2) used in this work was prepared by mixing of certified O_2/N_2, CO_2/N_2 and HCl/N_2 mixtures supplied by AGA A/S. The water vapor fraction of gas stream was prepared by deionized water evaporation. The experimental activities were conducted using two industrial raw meal samples (RM-A and RM-B) supplied by FLSmidth A/S. The composition and physical properties of the used raw meals are shown in Table 3. The most important differences between RM-A and RM-B are in BET area and iron oxide content where RM-B has 26% larger BET area than RM-A and 28% lower iron oxide content than RM-A. The raw meals have almost identical surface

area according to laser scattering method; however, laser scattering can be sensitive to particle agglomeration. The SEM analysis of RM-A samples (Fig.3) shows the presence of strong agglomeration phenomena and a significant fraction of particles smaller than 10µm. In the same experiments fused silica (min SiO_2: 99.9%) supplied by Quarte Inc. , with particles size between 50µm and 100µm, was used as inert diluting agent for raw meal samples. This dilution was used to break up agglomerates.

Table 2 Gas stream composition.

Component	ppmv or % v/v
HCl	52, 100 or 200ppmv
O_2	0 or 3% v/v
CO_2	0 or 30% v/v
H_2O	0 or 5% v/v
N_2	Balance

Table 3 Composition and physical properties of the used raw meals.

	$CaCO_3$ %w/w	Fe_2O_3 %w/w	Al_2O_3 %w/w	Si_2O%w/w	BET- m^2/g	L.S.*- m^2/g	L.S*.-D_{50} -µm
RM-A	~82	2.22	3.12	14.55	7.67	1.45	12.9
RM-B	~82	1.59	2.72	13.21	9.67	1.4	13.5

*Wet laser scattering measurements using ethanol as dispersion medium

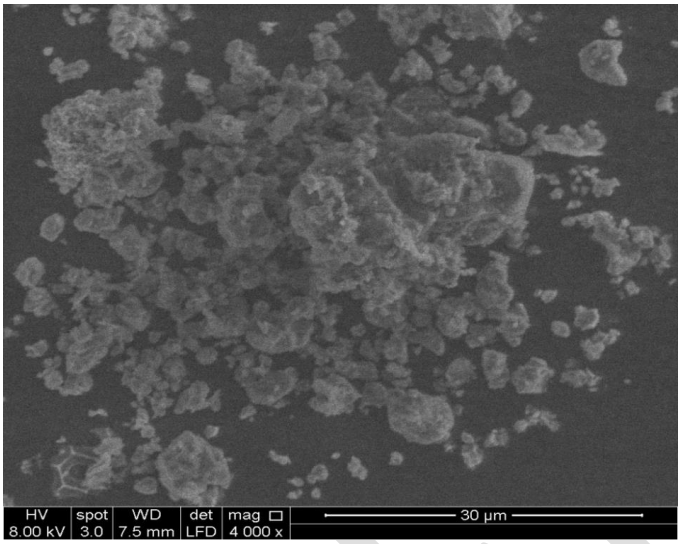

Fig.3 SEM picture of pure RM-A sample.

All experiments were done at least four times to confirm repeatability of results. The standard deviation [41] for each experimental condition was calculated.

4. Results and Discussion

4.1 Experimental Set-Up Behavior and Tests Methodology

4.1.1 Evaluation of Set-Up Behavior & HCl Absorption Calculation Method

Fig.4 shows the HCl response curve and standard deviation determined based on four repetitions of pure fused silica tests (inert sample), using nominal HCl concentration: 100ppmv, gas phase moisture content: 0%v/v, temperature: 100℃, and gas volumetric flow: 1.5 Nl/min – HCl/N_2. It is clearly seen that no HCl breakthrough takes place in the first of 45s. This breakthrough time of inert samples is called t_B. Furthermore, an extended transient section exists after the first 45s.

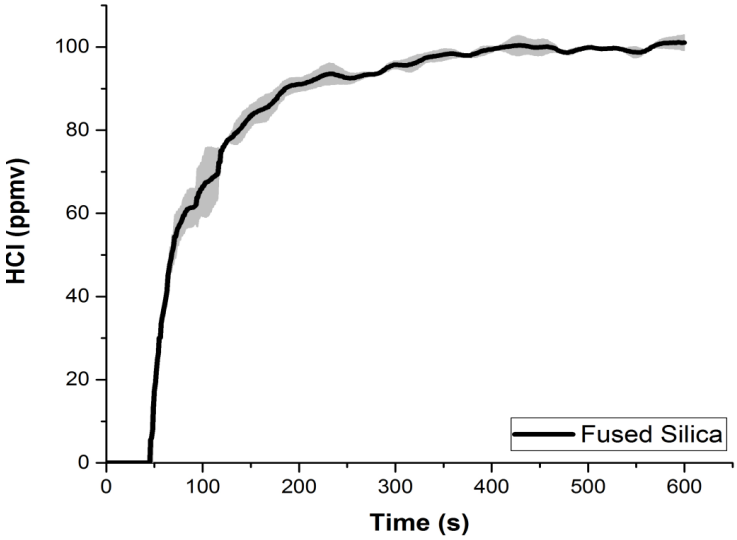

Fig.4 HCl response curve and standard deviation (shaded area) of pure fused silica (9g), using nominal HCl concentration: 100ppmv, gas phase moisture content: 0% v/v, temperature: 100℃, and gas volumetric flow: 1.5 Nl/min - HCl/N_2. t_B shows the breakthrough time.

This breakthrough time (t_B) corresponds to the Mass Flow Controllers (MFCs) response delay, filling of set-up empty space, and physical absorption phenomena in set-up compartments. It is noteworthy, that the observed response delay was affected by the HCl concentration and gas flow rate, however, it did not depend on the reactor temperature. Hence, the response delay t_B determined by fused silica tests at the tested conditions, was subtracted from the raw meal test data which are presented in the subsequent figures.

The transient section of the HCl response curve in Fig.4 is mainly related to the response characteristics of the HCl FTIR analyzer. Fig.5 illustrates the transient sections of response curves from fused silica and reactor by-pass tests at the same experimental conditions. The small deviations between the transient sections (within uncertainties) show that the transient section shape is not significantly affected by the fixed-bed reactor.

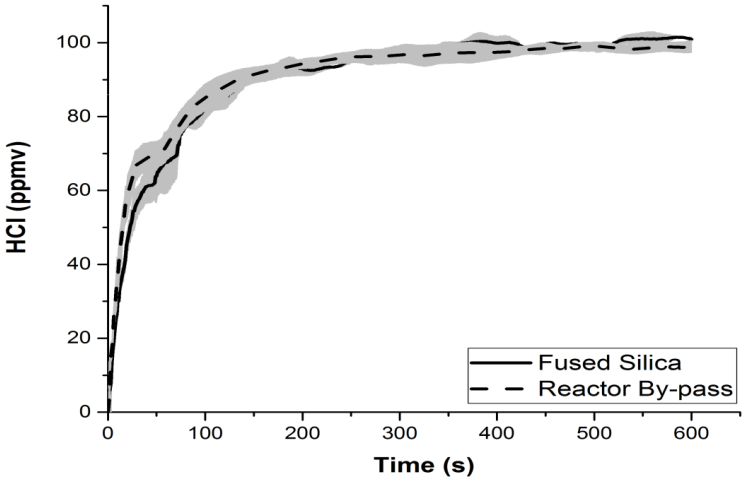

Fig.5 The transient parts of HCl response curves of pure fused silica (9g) and reactor by-pass tests, using nominal HCl concentration: 100ppmv, temperature: 100°C, gas phase moisture content: 0% v/v, and gas volumetric flow: 1.5 Nl/min - HCl/N_2.

The additional time to breakthrough (in excess of t_B) Δt_B caused by raw meal samples is the basis for the reported results in this work. It is assumed that the nominal feed HCl content is completely absorbed by the raw meal sample in the additional time. Therefore, the absorbed volume of HCl is equal to the product of the nominal HCl concentration in the feed (expressed as v/v), volumetric flow and increase in breakthrough time Δt_B. The results are reported as degree of conversion of the assumed raw meal active compound ($CaCO_3$).

4.1.2 Samples Dilution – Real HCl Absorption Capacity Determination

Elimination of raw meal particle agglomeration and flow channeling in the sample layer in the fixed bed reactor has been found to be necessary for the study of HCl absorption by raw meal and accurate determination of the real HCl absorption capacity of raw meal. In particular, the presence of agglomerates and any flow channeling gives an apparent HCl capacity of raw meals based on increase Δt_B in breakthrough time that it is lower than the real HCl absorption capacity of raw meal. Dilution of raw meal samples using fused silica particles with particle size between 50μm and 100μm was applied to break up raw meal agglomerates and to minimize the risk of channeling.

The study of the sample dilution effect was based on an evaluation of HCl absorption by pure and diluted raw meal samples at 100°C, using dry gas phase and fused silica as diluting agent. Fig.6-A illustrates the HCl response curves and standard deviation (shaded area) of pure fused silica (inert

material), pure RM-A, and diluted RM-A samples. In Fig.6-A no HCl concentration is detected until a certain time which is defined as breakthrough time Δt_B. The raw meal dilution, using a weight ratio of fused silica to RM-A equal to 29, gives an extended breakthrough time even though the pure and diluted RM-A samples have the same RM-A content of 0.3g.

Fig.6-B illustrates the transient section of HCl response curves of pure fused silica, pure RM-A and diluted RM-A samples when translated to a common starting time. It is discernible that the pure RM-A curve lies below the pure fused silica and diluted RM-A. The transient for the diluted RM-A initially lies close to the transient for fused silica, but later pure RM-A and diluted RM-A samples have nearly coinciding transient sections. The observations indicate that after the first, fast reactions before breakthrough there remains a residual absorption capacity. For pure RM-A, due to agglomeration, this residual capacity probably includes some of the initial capacity observed for diluted samples. However, the transients are so affected by the response characteristics of the FTIR – analyzer that further attempts at quantification have not been done.

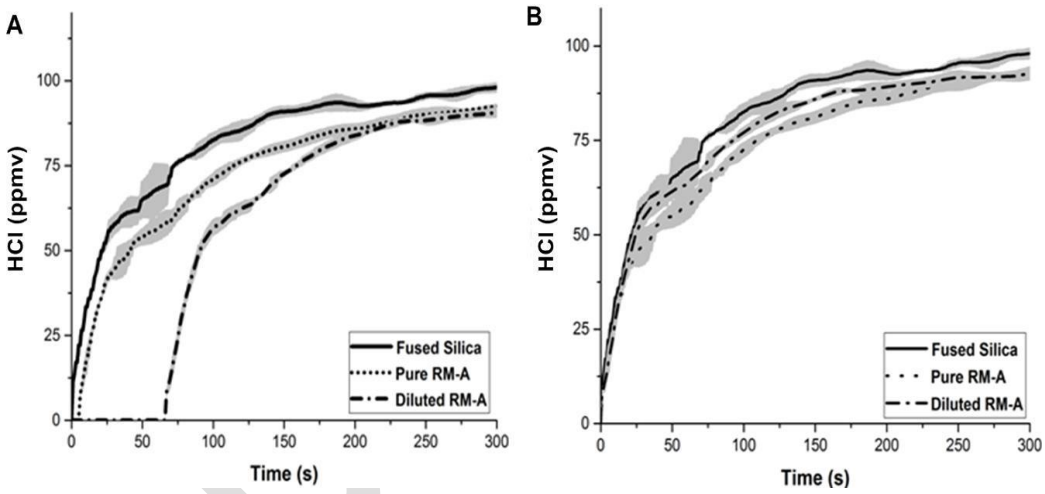

Fig.6 A) HCl response curves and standard deviation (shaded area) of pure fused silica (9g), pure RM-A (0.3g) and diluted RM-A (weight ratio of fused silica to RM-A: 29) samples using nominal HCl concentration: 100ppmv, gas phase moisture content: 0% v/v, temperature: 100℃, and gas volumetric flow: 1.5 Nl/min - HCl/N_2; B) The transient parts of HCl response curves of pure fused silica (9g), pure RM-A (0.3g) and diluted RM-A (weight ratio of fused silica to RM-A: 29) samples using nominal HCl concentration: 100ppmv, gas phase moisture content: 0% v/v, temperature: 100℃, and gas volumetric flow: 1.5 Nl/min - HCl/N_2.

Fig.7 presents the effect of dilution on breakthrough time Δt_B using weight ratios of fused silica to RM-A between 0 and 49 and constant sample RM-A content 0.3g. It is seen that a fused silica content of 8.7g (weight ratio of fused silica to RM-A: 29) results in an almost 10 times longer breakthrough time than pure RM-A samples. The increase of fused silica content above 8.7g has only a minor effect on breakthrough time/HCl absorption capacity. Therefore, the minimum weight ratio of fused silica to RM-A for the determination of real HCl absorption capacity is 29.

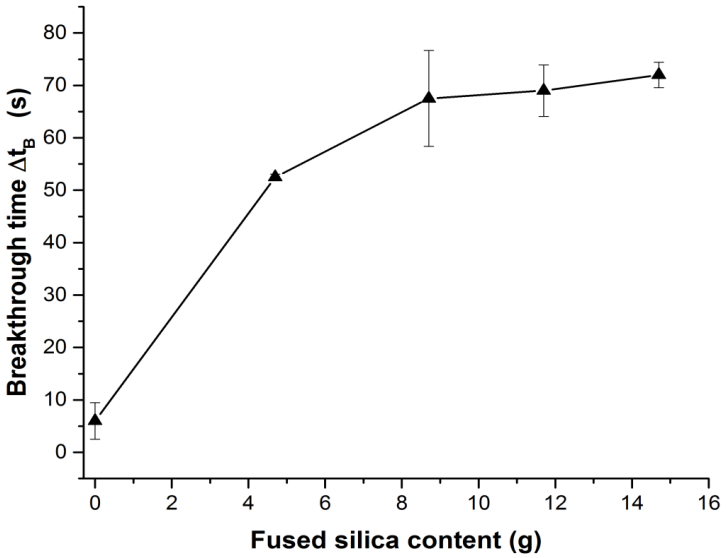

Fig.7 Breakthrough time Δt_B as function of sample diluent agent mass content using RM-A mass: 0.3g, gas phase HCl content: 100ppmv, temperature: 100°C, gas phase water content: 0% v/v, and gas flow rate: 1.5Nl/min - HCl/N_2.

Fig.8 shows the SEM-EDS micrographs of the pure RM-A (A), pure fused silica (B) and diluted RM-A samples (C and D). Fig.8-A documents that RM-A particles agglomerate strongly. The presence of agglomerates with size larger than 100µm and very few individual particles are clearly seen. Fig.8-B shows that the particles of diluent have nearly planar surfaces. Furthermore, Fig.8-C and Fig.8-D show that sample dilution results in the breaking of RM-A agglomerates and in the covering of fused silica particles' surfaces with raw meal agglomerate fragments. It is clearly seen that the fragments are significantly smaller than 100µm and within the particle size distribution range of raw meal. Moreover, individual particles are discernible. The origin of the precipitated fragments from raw meal is confirmed by the calcium elemental map in Fig.8-D.

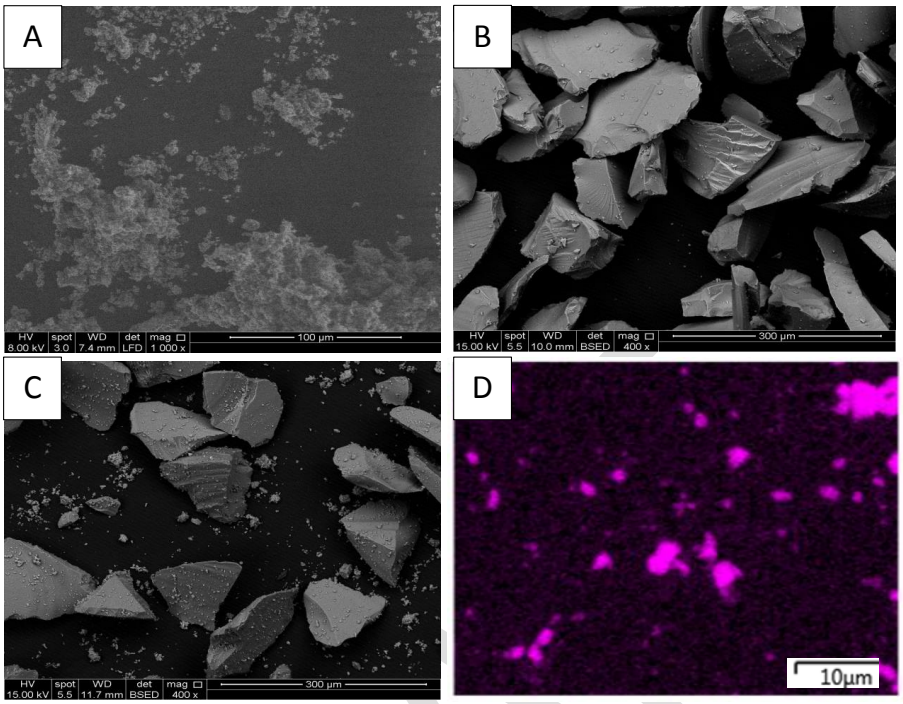

Fig.8 A) SEM picture of pure RM-A sample; B) SEM picture of pure fused silica particles; C) SEM picture of diluted RM-A sample (fused silica: 4.7g and RM-A: 0.3g); D) EDS-calcium elemental map of the surface of a fused silica particle from diluted RM-A sample (fused silica:4.7g and RM-A: 0.3g).

It is commonly accepted that fine particles tend to develop strong inter-particle cohesive forces that result in severe agglomeration [10, 28, 33, 42, 43] which can cause flow channeling. The observed breakthrough time dependence on sample dilution in conjunction with SEM-EDS analysis results show that the presence of agglomeration phenomena leads to apparent HCl absorption capacities of raw meals lower than the real at temperatures below 180℃. Similar observations were also reported in other studies on acidic gases absorption by Ca-based sorbents at temperatures less than 600℃ [20, 27, 28, 33].

4.2 Determination of HCl Absorption Mechanism and Capacities

4.2.1 Evaluation of Raw Meal Sample Mass Effect on HCl Absorption

The evaluation of raw meal as HCl absorber was conducted using diluted raw meal samples with constant total mass 9g and varying raw meal content between 0.15g and 0.6g, and dry gas phase

at 100°C. Fig.9-A shows that the only discernible effect of RM-A content increase on HCl response curves is the extension of breakthrough time.

Fig.9-B shows the experimental and corrected breakthrough times of the varying raw meal content tests of RM-A and RM-B. The high raw meal content tests (raw meal: 0.3g and 0.6g) were conducted using mass ratios of fused silica to raw meal ≤ 29 that do not guarantee the complete agglomerates breaking up. Hence, the experimental results were corrected using the obtained data from the dilution effect analysis of RM-A (see 4.1.2-Fig.7) and a linear proportionality of breakthrough time Δt_B correction with the fused silica content of sample. Furthermore, Fig.9-B shows that the corrected breakthrough time Δt_B is proportional to raw meal content considering that the trend lines are forced through the origin. Based on the amount of HCl absorbed from the start to the breakthrough time Δt_B and slopes of the linear regressions of the corrected breakthrough time Δt_B as function of the raw meal content, the specific HCl absorption capacities of RM-A and RM-B are $2.9 \cdot 10^{-5}$ mol/g and $3.86 \cdot 10^{-5}$ mol/g, respectively. Therefore, RM-B seems to have higher HCl absorption capacity than RM-A at the tested conditions.

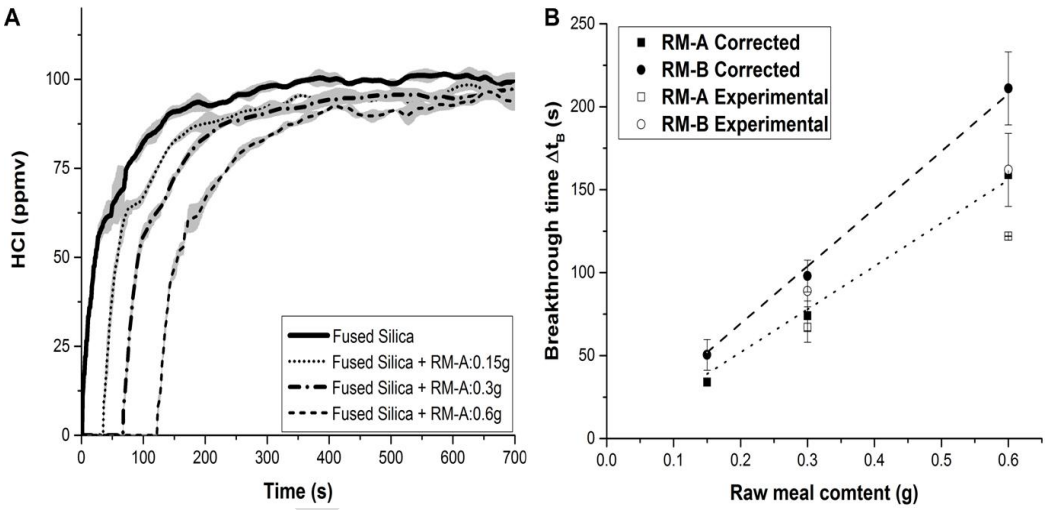

Fig.9 A) HCl response curves and standard deviation (shaded area), using diluted raw meal samples of total mass 9g and RM-A content : 0.15g, 0.3g and 0.6g, nominal HCl concentration: 100ppmv, gas phase moisture content: 0% v/v, temperature: 100°C, and gas volumetric flow: 1.5 Nl/min - HCl/N_2; B) Experimental and corrected breakthrough times as function raw meal content for RM-A and RM-B using total diluted sample mass: 9g, HCl concentration: 100ppmv, temperature: 100°C , gas phase moisture content: 0% v/v, and flow rate: 1.5 Nl/min - HCl/N_2.

The behavior of raw meals as HCl absorbents at low temperatures was verified by the obtained data. The tested raw meals were characterized by a specific HCl absorption capacity that varies between raw meals. This variation may be related to properties such as BET area, but other properties such as those reported in Table 3 and homogeneity of the tested samples may have influence on HCl absorption capacity. Table 4 shows a strong correlation between BET area and HCl absorption capacity of the tested raw meals. The HCl absorption capacity of RM-B is 33% higher than RM-A and the BET area of RM-B is 26% larger than RM-A. On the other hand, no correlation between the HCl absorption capacity and specific surface area by laser scattering method can be distinguished.

Table 4 HCl absorption capacity, BET area and L.S. area ratios of RM-A and RM-B.

$\frac{Capacity_{RM-B}}{Capacity_{RM-A}}$	$\frac{BET_{RM-B}}{BET_{RM-A}}$	$\frac{L.S.-Area_{RM-B}}{L.S.-Area_{RM-A}}$
1.33	1.26	1

BET area is the sum of the particles external surface area and pore area. The HCl absorption capacity of raw meal is determined using diluted samples, where the smaller size constituents of agglomerates are well dispersed. The outer surface area of the small dispersed particles was part of the 'pore area' of the agglomerates by BET measurements. The L.S. method considers the particles as spheres and measures the external surface of agglomerates as particle external surface. As shown in Table 3, the BET area of both raw meals is 5-7 times larger than the L.S. area. This makes it likely that the surface area of the small dispersed particles is measured as ''pore area'' by the BET method. Hence, the underestimation of the particles external surface by L.S. method is possible.

4.2.2 Evaluation of HCl Concentration Effect on Active Compound Conversion

The analysis of the effect of HCl concentration on the detected complete absorption stage is based on comparison of breakthrough time Δt_B and the assumed raw meal active compound ($CaCO_3$) conversion due to the absorbed amount of HCl in the period of length Δt_B.

Table 5 shows the experimentally obtained values of breakthrough time Δt_B at 100°C and corresponding raw meal active compound ($CaCO_3$) conversion considering the formation stoichiometry of $CaCl_2$. A dry gas phase of varying HCl content and diluted RM-A samples with weight ratio of fused silica to RM-A equal to 49 and RM-A content 0.3g were used. The obtained results showed that the $CaCO_3$ conversion is not affected by gas phase HCl concentration at the tested conditions. The active compound conversion being independent of gas phase HCl

concentration in conjunction with the very low $CaCO_3$ conversion indicates that the HCl absorption by raw meal is a surface saturation phenomenon.

Table 5 Breakthrough times and $CaCO_3$ conversions using diluted RM-A samples (weight ratio of fused silica to RM-A: 49 and RM-A content: 0.3g), HCl concentration: 52, 100 and 200ppmv, temperature: 100°C, dry gas phase, and gas flow: 1.5Nl/min- HCl/N_2.

HCl (ppmv)	Breakthrough time Δt_B(s)	$CaCO_3$ Conversion (%)
52	133 ± 7	0.157 ± 0.008
100	75 ± 6.6	0.170 ± 0.015
200	36 ± 1.5	0.163 ± 0.007

The theoretical conversion of a thin active surface layer with thickness equal to a calcite unit cell height (17.06 Å [44]) and surface area defined by BET and laser scattering measurements can be calculated. The corresponding active layer conversions are 4.2% and 22%, respectively. Therefore, it may be concluded that only a fraction of the available active surface area reacts with HCl, even if the smallest measured surface area is used.

4.3 Evaluation of HCl absorption Capacity Affecting Parameters

4.3.1 Temperature Effect using Dry Gas Phase

Fig.10 shows the HCl response curves and standard deviation (shaded area) from tests in the temperature range 100-180°C, using diluted RM-A samples (dilution ratio: 29) and dry gas phase. It is clearly seen that the temperature has a very minor effect on breakthrough time Δt_B and no discernible effect on the post-breakthrough response section. The HCl absorption capacity is seen to be greater at 100°C than at 150°C and 180°C.

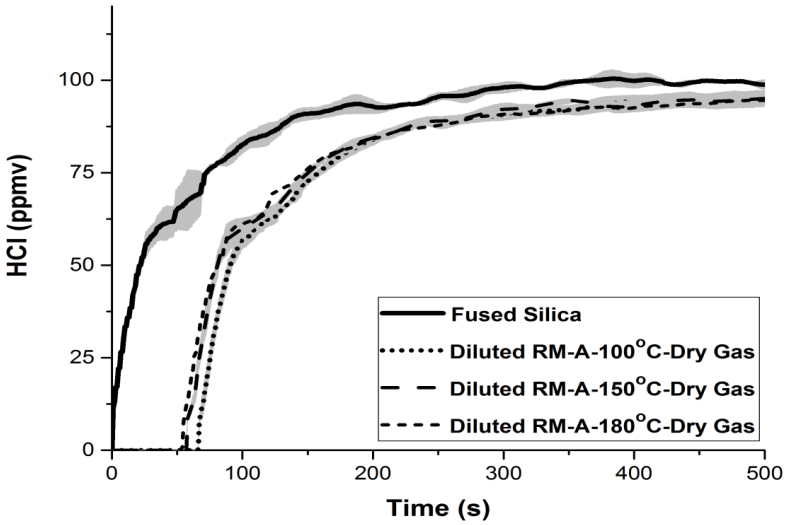

Fig.10 HCl response curves and using nominal HCl concentration: 100 ppmv, gas phase moisture content: 0% v/v, temperature: 100°C, 150°C and 180°C, diluted RM-A samples: fused silica-8.7g and RM-A-0.3g (un-dried), and gas volumetric flow: 1.5 Nl/min - HCl/N_2.

In order to determine if the water content of the raw meal samples had any influence on HCl absorption a series of experiments was carried out with diluted RM-A samples dried at different temperatures. Table 6 shows the experimentally determined mass loss of RM-A samples due to the thermal treatment. It is noteworthy that drying of pure RM-A samples at 115°C, 200°C and 300°C for 5 hours caused reversible mass loss close to 1.7 ± 0.8 % w/w, 3.5 ± 1.3 % w/w and 4.5 ± 1 % w/w (samples gained the lost mass after 1hr of exposure in ambient air), respectively. These values correspond to the release of 4.5, 9.0 and 11.6 monolayers of water if the H_2O absorption by raw meal follows a BET-isotherm (multilayer absorption), and the sorbent surface is defined by BET measurements. The H_2O absorption by limestone based on BET-isotherms is also reported [33, 34, 45].

Table 6 Mass loss of RM-A samples (assuming that the mass loss corresponds to H_2O release) due to the thermal treatment at 115°C, 200°C and 300°C.

Drying Period	Mass loss - 115°C		Mass loss - 200°C		Mass loss - 300°C	
(hr)	(% w/w)	(mol/g)	(%w/w)	(mol/g)	(%w/w)	(mol/g)
5	1.7 ± 0.8	$9 \cdot 10^{-4} \pm 4 \cdot 10^{-4}$	3.5 ± 1.3	$1.9 \cdot 10^{-3} \pm 7 \cdot 10^{-4}$	4.5 ± 1	$2.5 \cdot 10^{-3} \pm 6 \cdot 10^{-4}$
12	-	-	3.8 ± 1.4	$2.1 \cdot 10^{-3} \pm 8 \cdot 10^{-4}$	-	-

Fig.11 shows the breakthrough time Δt_B and the equivalent HCl saturation capacity of RM-A as function of fixed-bed test temperature and temperature at which samples were dried for 5 hours. It is clearly seen that the drying of samples reduces the HCl saturation capacity of RM-A. In particular, the tests at 150℃ and 180℃ showed that the molar ratio of the HCl saturation capacity decrease (mol/g) to the released H_2O (Table 6-mol/g) is close to $6.3 \cdot 10^{-3}$ at both drying temperatures (115℃ and 200℃). This clearly indicates a proportional relation between the raw meal water content and HCl absorption capacity which corresponds to the absorption of 1 molecule of HCl per 160 molecules of H_2O. It is also seen that the obtained breakthrough times (Δt_B) at 100℃ tend to be slightly longer than at 150℃ and 180℃ in case of samples that are undried or dried at 115℃. In contrast with this, the obtained breakthrough times are almost identical at all fixed bed temperatures for the samples dried at 200℃.

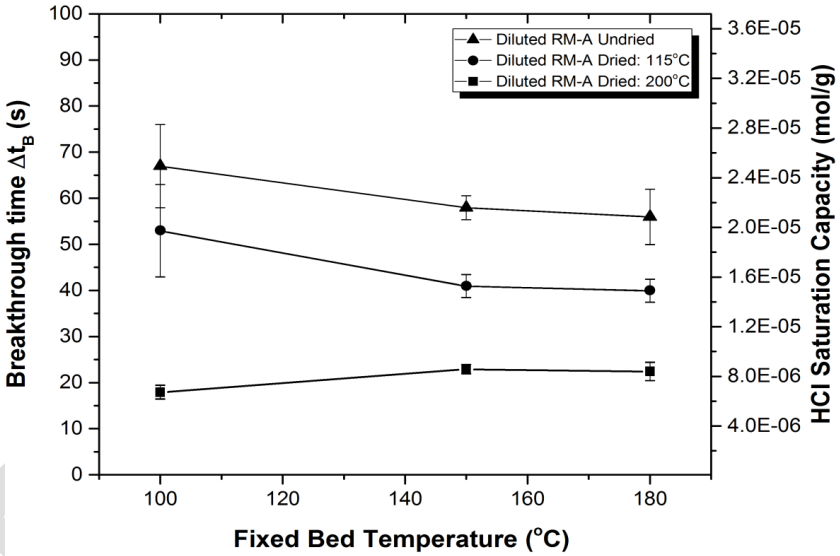

Fig.11 Breakthrough time Δt_B and equivalent HCl saturation capacity of RM-A as function of temperature using nominal HCl concentration: 100 ppmv, gas phase moisture content: 0% v/v., fixed bed temperature: 100℃, 150℃ and 180℃, drying temperature: 115℃ and 200℃, diluted RM-A samples: fused silica-8.7g and RM-A-0.3g, and gas volumetric flow: 1.5 Nl/min - HCl/N_2.

The dependence of breakthrough time Δt_B on sample thermal treatment mass loss shows that the raw meal moisture content significantly affects the HCl absorption by raw meal. In addition, the used drying temperatures cannot cause structural or chemical changes in active compound, e.g., calcination [46] and sintering [31]. Furthermore, it is well known that clay minerals containing silicates demonstrate reversible hydration–dehydration behavior in the tested temperature range [35, 36]. The promotion of acidic gases absorption by Ca-based sorbents due to the presence of bound moisture on silicates surface was also suggested by Jozewicz et al.[26]. Therefore, the

variation of breakthrough times at 100°C (fixed bed temperature) could be related to the hydration-dehydration properties of raw meal clay minerals.

The absorbed amount of HCl by undried RM-A at 100°C, (the product of specific HCl saturation capacity of RM-A: $2.49 \cdot 10^{-5}$ mol/g and RM-A mass: 0.3g) is ~ 13 times larger than the HCl saturation capacity of the water content of raw meal in moles. The calculations assume RM-A mass: 0.3 g, H_2O content of RM-A: 4.5% w/w - mass loss by drying at 300°C for 5hr, and HCl equilibrium saturation capacity of pure water at 100°C when the HCl concentration in gas phase is 100ppmv: $1.43 \cdot 10^{-4}$ mol/g (it is calculated based on the model of Takeshi et al.[47]). This observation in conjunction with the lack of dependence between the HCl concentration in gas phase and active compound conversion supports that the HCl absorption by raw meal is not simply determined by the HCl saturation equilibrium of water.

4.3.2 Temperature Effect using Moist Gas Phase

Fig.12-A shows the HCl response curves from HCl absorption tests in the temperature range 100-180°C, using diluted RM-A samples and gas phase moisture content 5% v/v. It is clearly seen that the breakthrough time $\Delta t_{B,\,moist}$ decreases as the temperature is raised. The fluctuations in the HCl signal also increases substantially as the increased standard deviation shows. Furthermore, the fluctuations are more pronounced at lower fixed-bed temperature.

Fig.12-B shows the increase on moist breakthrough time $\Delta t_{B,\,moist}$ (proportional to HCl absorption enhancement) by gas phase moisture content relative to dry breakthrough time $\Delta t_{B,\,dry}$ in the fixed-bed temperature range 100-180°C. The presence of 5% v/v H_2O increased the HCl absorption capacity by 25% at 180°C and by 61% at 100°C. The water effect rapidly weakens with temperature.

The present observations on gas phase moisture content effect on HCl absorption by raw meal are consistent with previous works on Ca-based sorbents chlorination at low temperatures in the presence of water (Weinell et al. [14], Jozewicz et al. [26], Fonseca et al.[27] and Chisholm and Rochelle [29]). These studies were, however, done with much higher HCl concentration where saturation of water with HCl may occur. Furthermore, the obtained results can be related to the literature data for SO_2 absorption by limestone at low temperatures which claim that SO_2 absorption occurs only in presence of H_2O monolayers on the sorbent surface and increases with relative humidity [33, 34, 45].

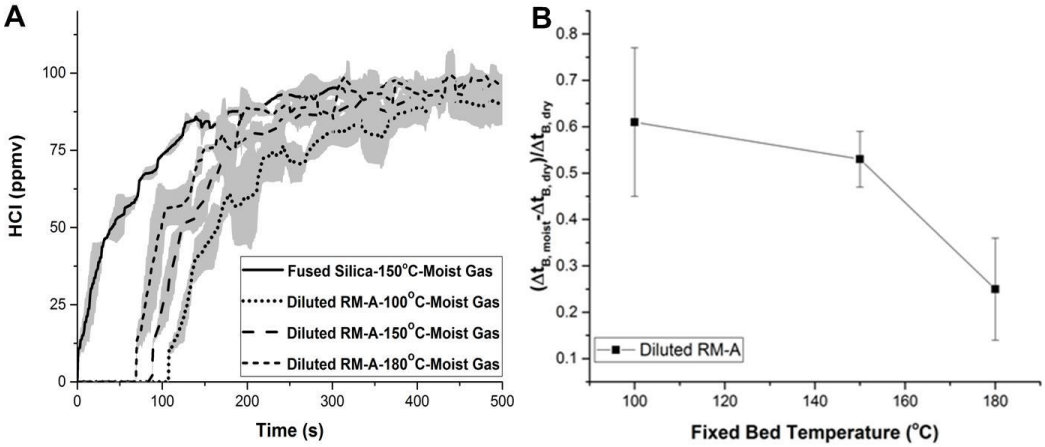

Fig.12 A) HCl response curves and standard deviation (shaded area) using diluted RM-A samples of total mass 9g and RM-A content: 0.3g, nominal HCl concentration: 100ppmv, gas phase moisture content: 5% v/v, temperature: 100℃, 150℃ and 180℃ and gas volumetric flow: 1.5 Nl/min - HCl/N_2; B) HCl absorption enhancement by gas phase moisture content relative to dry breakthrough time $\Delta t_{B,dry}$ ($\Delta t_{B,dry}$: breakthrough time Δt_B using dry gas phase and $\Delta t_{b,moist}$: breakthrough time Δt_B using moist gas phase), using diluted raw meal samples of total mass 9g and RM-A content: 0.3g, nominal HCl concentration: 100ppmv, gas phase moisture content: 0% v/v and 5% v/v, temperature: 100℃ , 150℃ and 180℃ , and gas volumetric flow: 1.5 Nl/min - HCl/N_2.

4.3.3 CO_2 and O_2 Effects

Fig.13 compares the obtained average HCl response curves using pure RM-A samples (no dilution by fused silica) and dry gas phase with and without O_2 and CO_2 at 100℃. It is observed that the presence of 3% v/v O_2 and 30% v/v CO_2 in gas phase has no effect on HCl absorption by raw meal at the used experimental conditions. These results are consistent with the observations of Mura and Lallai [17] and Gullet et al.[22] at much higher HCl concentrations. It is especially noteworthy that together with the literature results of Murra and Lallai [17] it can be concluded that O_2 and CO_2 have no effect on HCl absorption in the range of operating temperatures of post-preheater units.

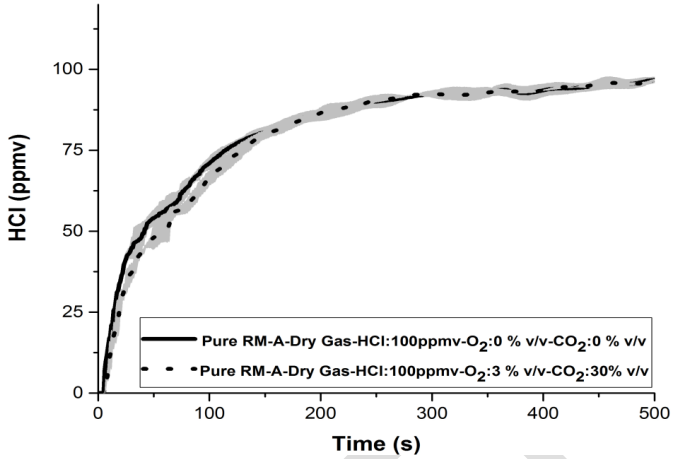

Fig.13 HCl response curves and standard deviation (shaded area) of pure RM-A samples: 0.3g, using gas phase composition: HCl: 100ppmv-H_2O:0%v/v-O_2:0%v/v-CO_2:0%v/v and HCl: 100ppmv-H_2O:0%v/v-O_2:3%v/v-CO_2: 30%v/v, temperature: 100℃, and gas volumetric flow: 1.5 Nl/min.

5. Conclusions

This work has shown that cement raw meals absorb HCl in the temperature range 100-180℃. The HCl absorption rates and the very low active compound conversion degree seem consistent with a fast surface reaction that leads to a saturation phenomenon. The apparent HCl absorption capacity depends on raw meal type and other experimental conditions such as the gas water content, raw meal, and degree of raw meal dilution. The active compound conversion is significantly less than 1%. The HCl absorption by raw meal depends only slightly on the temperature in the case of dry gas phase.

The presence of moisture in the gas phase significantly enhances the HCl absorption by raw meal at temperatures below 180℃. In particular, the presence of 5% v/v H_2O in the gas phase increased the HCl absorption capacity of RM-A at temperatures of 180℃ (25% increase), 150℃ (53% increase) and 100℃ (61% increase). The gas phase moisture content effect rapidly weakens with higher temperatures. The moisture content of the raw meal also strongly promotes the HCl absorption in the case of dry gas phase. Together, these results suggest that the initial HCl absorption is mainly dependent on a combined interaction with water on the raw meal surface and solid constituents in the raw meal rather than on a direct interaction with $CaCO_3$.

Agglomeration of the raw meal particles, possibly accompanied by gas channeling, gives low apparent HCl absorption capacity. The dilution of raw meal samples using inert material with larger particles size gave almost 10 times higher HCl absorption capacity of raw meals, due to elimination of these effects.

The presence of 3% v/v O_2 and 30% v/v CO_2 in gas phase has not any apparent effect on HCl absorption by raw meal at the tested experimental conditions.

Acknowledgements
This work is part of the advanced technology platform 'Minerals and Cement Process Technology – MiCeTech' funded by the Innovation Fund Denmark, FLSmidth A/S, Hempel and the Technical University of Denmark (Grant No. 39-2013-2). Furthermore, we gratefully acknowledge DTU-Center of Electron Nanoscopy, which made the SEM-EDS analyses.

References

[1] U.S. Environmental Protection Agency (EPA), ''National Emission Standards for Hazardous Air Pollutants for the Portland Cement Manufacturing Industry'', 40 CFR Part 63, § 63.1343, pp.405, 2013.

[2] Emission Measurements of Cement plant A, Internal report FLSmidth A/S, Copenhagen, 2012.

[3] Emission Measurements of Cement plant B, Internal report FLSmidth A/S, Copenhagen, 2013.

[4] Saint-Jeana, S. J., Jønsb, E. , Lundgaardb, N. ,and Hansena, S., '' Chlorellestadite in the Preheater System of Cement Kilns as an Indicator of HCl Formation'', Cement and Concrete Research, 2005, vol.35, pp. 431-437.

[5] Jøns, E.S. and Østergård, M.J.L., ''Investigation into Shell Corrosion of Rotary Cement Kilns'', ZKG International, 1999, vol.52, pp.68-79.

[6] Emission Compliance for Cement Production, Commercial report FLSmidth A/S, Copenhagen, 2014.

[7] Laird, C.P., Smith, K.J., and Looney B.,'' Results of Dry Sorbent Injection Testing to Reduce HCl, Journal of Air and Waste Management Association - Power Plant Air Pollutant Control "mega" Symposium 2012, 2012, vol.1, pp. 136-147.

[8] Dry Sorbent Injection for Better HCl and SO_2 Control, Commercial Report Sorbacal S.A., 2016.

[9] Dry Hydrated Lime Injection for Coal-Fired Boiler Flue Gas Desulfurization (FGD), Commercial report SORB-N-JECT Technology & NOL-TEC SYSTEMS, pp.1-10, 2002.

[10] Kobayashi, Y., 'Method of Purifying Exhaust Gas', U.S. patent: 4726940 A, 1986.

[11] Schwab, J.,'' Method Apparatus for Controlling Acid Gas Emissions from Cement Plants'', U.S. patent: 8383073 B2, 2013.

[12] Bhatia, K.V., ''Method for Removing Sulfur oxides from Hot Flue Gases'', U.S. patent: 4555390, 1985.

[13] Kisters, T., and Vogler, A., ''Process and Apparatus for the Absorptive Removal of Pollutants from Waste Gases'', U.S. patent: 4208383, 1988.

[14] Weinell, C. E., Jensen, P. I. , Dam-Johansen, K., Livbjerg, H., "Hydrogen-chloride reaction with lime and limestone- kinetics and sorption capacity", Industrial and Engineering Chemistry Research, 1992, vol.31, pp. 164-171.

[15] Petrini, S., Eklund, H., and Bjerle, I., "HCl-Absorption durch Kalkstein", Aufbereit Tech, vol.20, 1979, pp. 309-315.

[16] Ketov, A. N., Kostin, L. P., Terent'eva, E. I., "O vzaimodeistii razlichnykh vidov karbonata kal'taiya s khloristym vodorodom prinagrevanii", Izv, Vyssh. Uchebn. Zaved., Khim. Khim. Tekhnol., 1968, vol.11,pp.680.

[17] Mura, G. and Lallai, A., "Reaction kinetics of gas hydrogen chloride and limestone", Chemical Engineering Science, 1994, vol. 49, pp. 4491-4500.

[18] Matsukata, M., Takeda, K., Miyatani, T. and Ueyama, K., ''Simultaneous Chlorination and Sulphation of Calcined Limestione'', Chemical Engineering Science, 1996, vol.51, pp.2529-2535.

[19] Daoudi, M. and Walters, J.K., ''The Reaction of HCl Gas with Calcined Commercial Limestone Particles: the Effect of Particle Size'', Chemical Engineering Journal, 1991, vol.47, pp.11-16.

[20] Duo., W., Kirkby, N.F., Seville, J.P.K, Kiel, J. H. A., Bos, A. and Den Uil, H., "Kinetics of HCl Reactions with Calcium and Sodium Sorbents for IGCC Fuel Gas Cleaning", Chemical Engineering Science, 1996, vol. 51, pp. 2541-2546.

[21] Wang, W., Ye, Z. and Bjerle, I., ''The Kinetics of the Reaction of Hydrogen Chloride with Fresh and Spent Ca-Based Desulfurization Sorbents'', Fuel, 1996, vol.75, pp.207-212.

[22] Gullett, B.K., Jozewicz, W. and Stefanski, L.A., "Reaction Kinetics of Ca-Based Sorbents with HCl ", Industrial & Engineering Chemistry Research, 1992, vol. 31, pp.2437-2446.

[23] Mura, G. and Lallai, A., ''On the Kinetics of Dry Reaction between Calcium Oxide and gas Hydrochloric Acid'', Chemical Engineering Science, 1992, vol.47, pp.2407-2411.

[24] Partanen, J., Backman, P., Backman, and Hupa, M.R., "Absorption of HCl by Limestone in Hot Flue Gases. Part I: the Effects of Temperature, Gas Atmosphere and Absorbent Quality", Fuel, 2005, vol.84, pp.1664-1673.

[25] Daoudi, M. and Walters, J.K., "A Thermogravimetric Study of the Reaction of Hydrogen Chloride Gas with Calcined Limestone Determination of Kinetic Parameters", Chemical Engineering, vol.1991, vol.47, pp. 1-9.

[26] Jozewicz, W., Chang, J.C.S., and Sedman, C.B., "Bench-Scale Evaluation of Calcium Sorbents for Acid Gas Emission Control", Environmental Progress, 1990, vol. 9, pp. 137-142.

[27] Fonseca, A.M., Orfao, J.J., and Salcedo, R.L., "Kinetic Modeling of the Reaction of HCl and Solid Lime at Low Temperatures", Industrial and Engineering Chemistry Research, 1998, vol. 37, pp. 4570-4576.

[28] Karlsson, H.T., Klingspor, J., and Bjerle, I., ''Absorption of Hydrochloric Acid on Solid Slaked Lime for flue gas clean up'', Air Pollution Control Association, 1981, vol.31, pp.1177-1180.

[29] Chisholm, P.N., and Rochelle, G.T., ''Dry Absorption of HCl and SO_2 with Hydrated Lime from Humidified Flue Gas'', Industrial Engineering and Chemistry Research, 1999, vol.38, pp. 4068-4080.

[30] Perry, R.H. and Green,D.W., ''Perry's Chemical Engineers' Handbook'', 8th Edition, McGraw-Hill, 2007, pp.2-11, ISBN: 978-0-07-142294-9.

[31] Borgwardt, R.H., ''Calcium Oxide Sintering in Atmospheres Containing Water and Carbon Dioxide'', Industrial Engineering and Chemistry Research, 1989, vol.28, pp.493-500.

[32] Duo, W., Sevill, J.P.K., Kirkby, N.F., and Clift, R., "Formation of Product Layers in Solid-Gas Reactions for Removal of Acid Gases", Chemical Engineering Science, 1994, vol. 49, pp. 4429-4442.

[33] Klingspor, J., Karlsson, H.T., and Bjerle, I., ''A kinetic Study of the Dry SO_2 – Limestone Reaction at Low Temperature '', Chemical Engineering Communication, 1983, vol.22, pp.81-103.

[34] Hansen, P.J., ''SO_2 Emissions from Cement Plant Production'', PhD Dissertation, Technical University of Denmark, 2003, ISBN: 87-90142-96-9.

[35] Grim, R.E, "Clay Mineralogy", McGraw-Hill Book Company, Inc., Second Edition, 1968, ISBN-10: 0070248362.

[36] Grim, R. E. and Brandley, W.F., "Rehydration and Dehydration of the Clay Minerals", American Mineralogist, 1948, vol.33, pp. 50-59.

[37] Bhatty, J., Kosmatka, F., and Miller, S., ''Innovation in Portland Cement Manufacturing '', Portland Cement Association, 2004, pp.58, ISBN: 0-89312-234-3.

[38] Brix, J., Navascués, L.G., Nielsen, J.B., Bonnek, P. L., Larsen, Clausen, S., Glarborg, P., and Jensen, A.D., ''Oxy-fuel Combustion of Millimeter-Sized Coal Char: Particle Temperatures and NO Formation'', Fuel, 2013, vol. 160, pp.72-78.

[39] Sørensen, O.C., Johnsson, J.E., and Jensen, A., ''Reduction of NO over Wheat Straw Char'', Energy & Fuels, 2001, vol.15, pp.1359-1368.

[40] Sengeløv, L.W., Hansen, T.B., Bartolomé, C., Wu, H., Pedersen, K.H., Frandsen, J. F., Jensen, D. A., and Glarborg, P., Sulfation of Condensed Potassium Chloride by SO_2, Energy and Fuels, vol.27, pp.3283-3287.

[41] Skoog,D.A., West, D.M., and Holler, F.J., ''Fundamentals of Analytical Chemistry'', Saunders College Publishing, Fifth Edition, 1988, pp.8, ISBN: 0-03-14828-6.

[42] Kunii, D. and Levenspiel, O., ''Fluidization Engineering '', Butterworth-Heinemann, Second Edition, 1991, pp.77-82, ISBN: 0-409-90233-0.

[43] Linee,M., Klingspor,J., Karlsson, H.T., and Bjerle,I., ''Limestone Based Wet-Dry Scrubbing to Form Gypsum'', Chemical Engineering Science, 1982, vol.37, pp. 807.

[44] Gregg, J.M., Bish, D.L., Kaczmarek, S.E., and Machel, H.G., ''Mineralogy, Nucleation and Growth of Dolomite in the Laboratory and Sedimentary Environment: A review'', International Association of Sedimentology, 2015, vol.62, pp. 1749-1769.

[45] Klingspor,J., Stromberg, A.M., Karlson, H.T., and Bjerle, I., ''Similarities between Lime and Limestone in Wer-Dry Scrubbing'', Chemical Engineering and Processing: Process Intensification, 1983, vol.18, pp.239-247.

[46] Kumar, G.S., Ramakrishman, A., and Hung, Y.-T., "Advanced Physico-Chemical Treatment Technologies-Handbook of Environmental Engineering", 2007,vol.5, pp. 611-633, ISBN: 1588298604.

[47] Takeshi, S., Todhikatsu, H., and Hiroshi, Y., ''Vapor Pressure of Binary (H_2O-HCl, -$MgCl_2$ and –$CaCl_2$) and Ternary (H_2O-$MgCl_2$-$CaCl_2$) Aqueous Solutions, Journal of Chemical and Engineering Data, 1985, vol.30, pp. 224-227.

Department of Chemical and Biochemical Engineering - CHEC
Technical University of Denmark
Søltofts Plads, Building 229
2800 Kgs. Lyngby
Denmark
Phone: +45 45 25 28 00
Web: www.kt.dtu.dk